Institutsbereich Geophysik, Astrophysik und Meteorologie
Institut für Physik
Karl - Franzens - Universität Graz
Universitätsplatz 5, A-8010 Graz, Austria
http://www.uni-graz.at/igam

Wissenschaftlicher Bericht No. 23

Stratospheric Ozone and Temperature Sounding by the Envisat/GOMOS Stellar Occultation Sensor

by
Christian Retscher

December 2004

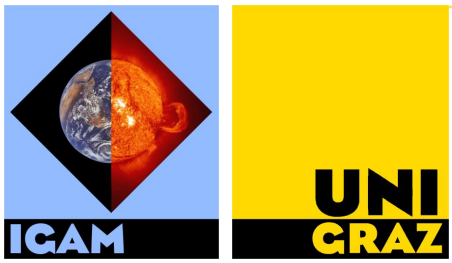

Der Humor ist die Maske der Weisheit.
Maskenlos ist die Weisheit unerbittlich.

F. Dürrenmatt

Acknowledgments

I would like to thank my advisor Prof. G. Kirchengast, who gave me the possibility to participate in a study, which contributes to a better understanding of global climate change. He was open for all kinds of scientific discussions and brought up many interesting scientific issues.

I am grateful to Prof. R. Leitinger for co-reading this thesis, supporting my scientific work and my academic career. As well I am thankful to Prof. H. Biernat for facilitating the finalization of my Ph.D. study.

I gratefully acknowledge discussions with and support by all ARSCliSys group members, especially C. Rehrl, A. Gobiet, M. Schwärz, A. Löscher, U. Foelsche, A. Steiner, J. Fritzer, J. Ramsauer, M. Borsche, and C. Bichler (IGAM, Univ. of Graz, Austria) and by the entire staff of IGAM.

I received financial support from Envisat Project AO-620/Part-I funded by the Austrian Ministry for Traffic, Innovation, and Technology (BMVIT) and carried out under contract with the Austrian Space Agency (ASA). The European Space Agency is thanked for operating the Envisat satellite and for its related Announcement of Opportunity and free access to Envisat data, which was vital for this work.

I am especially grateful to A. Hauchecorne for his co-supervisory support of my Ph.D. thesis and for hosting me for a six month stay in 2001 at SA/CNRS, Verrières-le-Buisson, France. I am thankful to V. Sofieva, J. Tamminen, and Erkki Kyrölä (FMI, Helsinki, Finland) for discussions and their contributions. I acknowledge B. Theodore, G. Barrot, and O. Fanton d'Andon (ACRI-ST, Sophia Antipolis, France) for helping with GOMOS data. I thank C. Zehner and S. Casadio (ESA-ESRIN, Frascati, Italy) for discussions and support related to Envisat atmospheric payload products. Furthermore, I am grateful to J. Wickert and T. Schmidt (GFZ, Potsdam, Germany) for providing CHAMP occultation data. D.-Y. Wang and H. Fischer (IMK, Karlsruhe, Germany) are thanked for their support with MIPAS data.

My warmest thanks go to my parents for being who they are. I am not quite sure if they actually figured out how one can study physics, but they were always there when I needed mental, emotional or financial support.

Last but not least I thank my sister and all my friends for nodding, when I needed laughing, looking puzzled when I needed nodding and laughing when I needed to talk about puzzles.

Contents

Introduction

Our atmosphere is the medium which makes life on Earth possible. It is the transition zone of the Earth's surface to space. The atmosphere is in permanent physical and chemical interaction with incoming solar radiation, with land masses, the oceans, the ice sheets and the biological system. All these factors contribute to the climate system. We know that the climate has undergone a lot of changes in the past and will continue to change in future. The climate is an evolving entity. It is important to understand the physical and chemical processes governing the different components of the Earth system and how mankind contributes to a change in the climate system.

A parameter of special importance to life on Earth is the temperature of the atmosphere. Local changes of the temperature distribution are noticeable as we observe extended periods of droughts, floating icebergs to melt, the sea surface level to rise, or alpine glaciers to disappear and with them a chapter in the history of climate on Earth. But are these local temperature changes observed on a global scale? Do human activities perturb the Earth system in a sustainable manner?

In order to answer this type of questions we need observations of key parameters of the Earth. Observations can be made *in situ* by being in physical contact with the measured quantity, or by remote sensing techniques, which can be set as ground-based, air-borne or space-borne measurements.

Space-borne remote sensing techniques have encountered a vast increase in terms of availability of satellite platforms in the last 30 years, various instruments covering a broad range of the electromagnetic spectrum, and methods to accurately retrieve geophysical information from the measured data. Besides utilization for exploring the atmospheres of planets in our solar system, remote sensing techniques are nowadays widely in use for mapping the Earth's gaseous envelope.

Not only the temperature alone drives the climate system. There exist many processes connected to temperature changes, which results in positive or negative feedback reactions. A key constituent in the atmosphere, influencing also the biological system, is ozone. Ozone is known to be toxic to human beings in the troposphere, but in turn it is the main absorbing species for harmful UV radiation in the stratosphere. Changes in the stratospheric ozone concentration lead to a changing temperature distribution. Cooler temperatures in the stratosphere, moreover, favor a depletion of ozone. Ozone is governed by a series of production and depletion processes, most importantly induced by man-made chlorofluorocarbons. The investigation and protection of the Earth's ozone layer is a hot topic and several instruments account for that with data measured in different wavelength regions and altitude regimes.

A special sensor, which is important for this thesis, is the Global Ozone Monitoring

by Occultation of Stars (GOMOS) instrument on-board Envisat. It is dedicated to perform high-accuracy altitude-resolved global ozone monitoring as well as measurements of other atmospheric trace gases and of temperature. Measurements are carried out within an altitude range of about 15 to 100 km. We present GOMOS ozone profiles, retrieved from GOMOS transmission data and validated with operational GOMOS ozone profiles and ECMWF analysis data.

A second focus lies on the presentation of a GOMOS temperature profile retrieval compared to CHAMP, MIPAS, and ECMWF analysis data. GOMOS temperatures are gained by exploiting pointing data of the GOMOS Steering Front Assembly (SFA) and the Star Acquisition and Tracking Unit (SATU), which provide information on the refraction of the star light in the atmosphere and thus allow to derive refractive bending angle profiles. According to the SFA sampling rate and retrieval algorithm requirements, we performed the retrieval at 10 Hz including down-sampled SATU data from 100 Hz. Bending angles were found with errors of $\sim$3 μrad. Statistical optimization of observed bending angles with model bending angles was used to provide adequate data quality for the Abel transform from the stratopause region upwards, which led to a significant gain in temperature retrieval accuracy up to 40 km height due to suppressed downward propagation of errors induced by Abel transform and hydrostatic integral. Bending angle profiles are then converted via refractivity and pressure profiles to temperature profiles.

A validation setup for a selected period in 2002 and 2003 is based on co-located sets of CHAMP GPS occultation profiles, Envisat/MIPAS temperature profiles and analysis profiles of the European Centre for Medium-Range Weather Forecasts (ECMWF). All three comparison sets for the year 2002 show mean deviations below 2 K from 23 km up to 35 km. Below about 23 km the accuracy of GOMOS bending angle data is degraded, which leads to positive biases. GOMOS data for the year 2003 were only validated with CHAMP GPS and ECMWF analysis data. In comparison to the year 2002 validation, results are degraded in quality, due to different reasons. Nevertheless atmospheric temperature profiles, connected to measurements for some selected stars, have the performance already seen in the year 2002 validation and thus give us the affirmation of an appropriate retrieval algorithm setup.

Together with the SFA/SATU-based refractivity and temperature retrieval, we developed an optimal estimation retrieval scheme for ozone using sensibly selected channels from the Spectrometer A transmission spectra within 260-340 nm and 602-634 nm. GOMOS ozone profiles are discussed and validated with operational GOMOS ozone profiles and ECMWF analysis data for the years 2002 and 2003. Validation results for both years show almost the same performance. Overall profiles over low, mid, and high latitudes have biases smaller than 5% in the validation with operational ozone data. These biases can be explained by the selection of *a priori* error magnitudes of $> 25\%$. The validation with ECMWF errors generally yields large biases of $\sim 30\%$ coming from the ECMWF product. Some bright and hot stars enable excellent quality ozone retrieval throughout all altitudes.

In Chapter 1 we summarize basic thermodynamic concepts and point out their application in atmospheric physics. The structure and the composition of the Earth's atmosphere is discussed as well as the radiative transfer and its importance in understanding processes like absorption, emission, and scattering of radiation by gases. This Chapter closes with an overview of chemical properties of ozone, its production, and

its depletion by chlorofluorocarbons and other species.

Chapter 2 deals with techniques of atmospheric remote sensing. Remote sensing together with numerical models and computer simulations have led to an enormous increase of our understanding of atmospheric processes. Large amounts of data have been processed and interpreted, but there is still is a lot of data available and ready to be processed by the user community. A special concern is the discussion of the stellar occultation techniques amongst others like solar or lunar occultations.

The Envisat polar platform is discussed in detail in Chapter 3. We give an overview of all Envisat instruments, but of major importance are the atmospheric chemistry instruments, GOMOS, MIPAS, and SCIAMACHY. GOMOS, as the main instruments for this thesis is treated in extensive detail. From instrumental properties of the telescope and the optics (the CCD) we come to a description of used algorithms, the provided products, and its possible applications in models.

The retrieval algorithm developed for this thesis is described in Chapter 4. The temperature retrieval follows a classical retrieval concept involving the numerical solution of the Abel integral equation. As input data we use SFA/SATU bending angles from GOMOS measurements. The ozone retrieval was performed with a so-called optimal estimation technique, incorporating *a priori* data.

In Chapter 5 we show the retrieval setup for ozone and temperature sounding data as well as results of our algorithm. GOMOS data were available for a series of days in September, October, and December 2002 as well as in September 2003.

A concise Summary and Conclusions Section, gathering the main findings of the study, completes this thesis.

1

The Atmosphere

The Earth's gaseous envelope is a highly variable system driven by a large number of physical and chemical processes. These involve transport, production, and loss of chemicals due to atmospheric activity itself, biological and anthropogenic influences, volcanic eruptions, exchanges with oceans, radio active decay processes, and depositions from the solid Earth. Depending on their cycles, gas molecules have different lifetimes from a few seconds to millions of years. Production and destruction processes depend on concentrations of gases and the atmospheric altitude or latitude. Several gases may have hardly any effect on the climate system in the troposphere, but in turn become eminently relevant in the stratosphere and vice versa. Water vapor, e.g., has great effects on the regulation of tropospheric temperature and plays, together with carbon dioxide, a key role in the Earth's greenhouse effect. Ozone in turn has its largest influence in the stratosphere, where it absorbs the majority of the solar radiation in the UV and is therefore inevitably necessary for life on Earth. The following description is mainly based on [*Salby* (1995), *Thomas and Stamnes* (1999), *Andrews* (2000)].

1.1 Structure and Composition of the Atmosphere

The atmosphere's prime constituents are molecular nitrogen and molecular oxygen, which comprise 99% of its total volume. Almost all of the atmospheric mass is distributed below an altitude of 30 km. Besides the main species we further find several noble and trace gases (cf. Tab. 1.1), which have, despite their small concentrations in the atmosphere, a high impact on the Earth's climate system. By involving radiative processes, trace gases can control the energy budget of the Earth.

The atmosphere can be classified by several layers (see Fig. 1.2), which are mainly determined by its thermal structures, pressure, and composition of gases. From the Earth's surface upwards one defines the main layers shown in Tab. 1.2 and Fig. 1.1.

The troposphere is the region from Earth's surface up to the tropopause, which lies between 8 km in polar regions and 18 km in the tropics. In the troposphere one finds a negative temperature gradient with increasing height until the tropopause is

Gas	Volume Mixing Ratio	Status
N_2	78.08%	well mixed
O_2	20.94%	well mixed
H_2O	$\sim$1 – 3%	variable with max. in the troposphere
Ar	0.93%	well mixed
CO_2	370 ppmv	well mixed
O_3	10 ppmv	highly variable with max. in the stratosphere

Table 1.1. Summary of the most concentrated and most relevant atmospheric gases [*Salby* (1995)].

Layer	Properties
Troposphere	This region extends from surface to about 8 to 18 km. Temperature decreases with height. It exists a fast vertical mixing.
Stratosphere	In this layer we observe increasing temperatures with height and slow vertical mixing. The stratosphere extends from the tropopause at roughly 8 to 18 km to near 50 km.
Mesosphere	Here temperatures decrease with height and a fast vertical mixing is found. We observe the lowest temperature in the atmosphere. This region reaches a height of about 80 km.
Thermosphere	Due to absorption of short wavelength (EUV) radiation by N_2 and O_2 high temperatures are measured. A fast vertical mixing is found.
Exosphere	Gas molecules having sufficient energy can escape from the Earth's gravitational field. The exospheric temperature can be in the range of 500 K to 2000 K.

Table 1.2. The main atmospheric layers [*Salby* (1995)].

reached. The tropopause is defined such that the temperature shall not decrease with more than 2 K km^{-1} and for the next 2 km the averaged temperature lapse rate has to remain below this value. The troposphere, whose name has its origin in the Greek word *tropos* $\mapsto$ *turning*, can be divided into the planetary boundary layer, reaching from the Earth's surface up to 1 km height and the free troposphere extending from 1 km up to the tropopause. It is a region of ceaseless turbulence and mixing containing about 80% of the atmospheres total mass and almost all of its water content. The forces due to mixing are much larger than the downward gravitational force (strictly speaking the gravitational force does not act downward; it is inherent to every single massive particle and act into all directions) which results in a well-mixed state of the lower atmosphere.

The stratosphere (Latin for *stratum* $\mapsto$ *layer*) extends from the tropopause up to the mesopause, which reaches a height of about 50 km. The temperature in the stratosphere is much higher than expected by an extending of the tropospheric temperature gradient. In contrast to the troposphere here one finds increasing temperatures reaching $\sim$271 K at 50 km. Ozone plays a key role in the heating of this layer, where the absorption of UV radiation is the main source of energy to drive the circulation and the formation of the observed temperature structure.

The key process in atmospheric chemistry is the transport of chemical species from the troposphere to the stratosphere an vice versa [*Visconti* (2001)]. The vertical transport of both layers is very different. In the troposphere the vertical displacement of air masses can occur on a time scale of a few hours, while the stratospheric vertical mo-

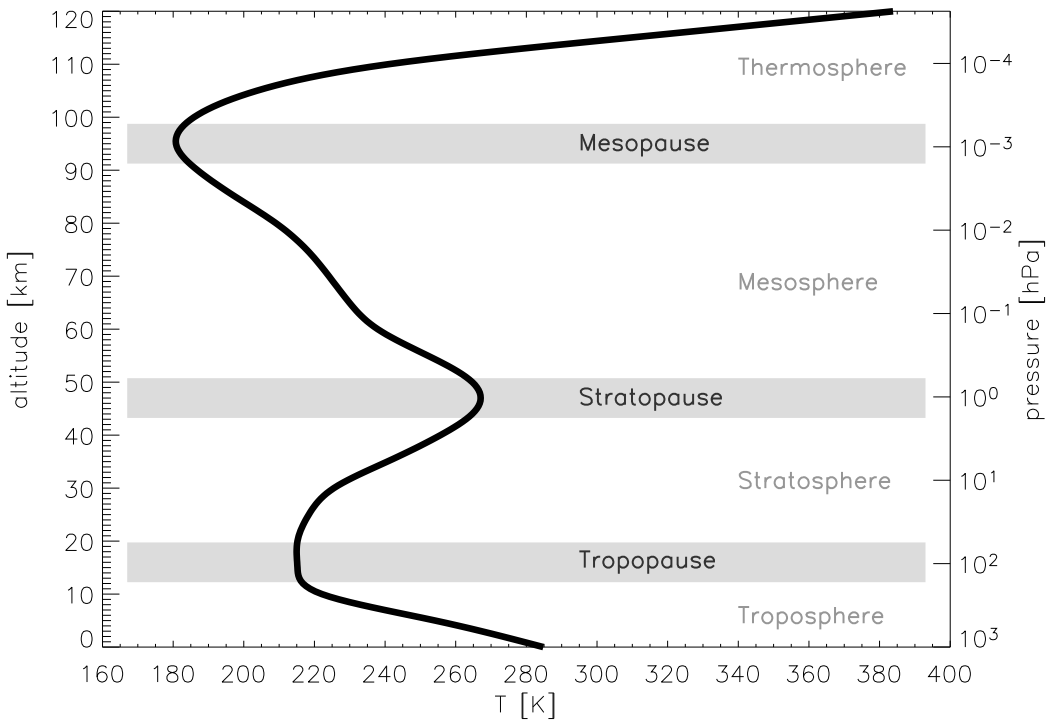

Figure 1.1. Temperature distribution throughout atmospheric layers, such as the troposphere, the stratosphere, the mesosphere, and the thermosphere. The temperature gradient changes its sign at the transition from one layer to another, which are the so-called pauses.

tion is largely inert and it takes months to years to move chemicals over a comparable vertical distance. A large scale ascending of air crossing the tropopause, is possible in the tropics as a result of a persistent seasonally and interannually varying extratropical pumping. The detection of long-lived chemical tracers like N_2O and CH_4 imply such upwelling in the tropics and for continuity a downwelling at mid and high latitudes is required. In the tropical stratosphere air is dispersed upwards and towards the poles, which is an essential component in the stratospheric transport. Such a meridional motion may be responsible for low ozone abundances in the tropics and large absolute concentrations of ozone at higher latitudes. However these processes are still not fully understood. The subject of exchanges of chemicals via the tropopause is crucial to many areas of atmospheric science and impact studies of, e.g., aircraft emissions on the ozone layer. For a more detailed description we refer to [*Salby* (1995)].

1.2 The Ideal Gas Law and the Hydrostatic Equation: An Overview

The atmosphere can be seen as to a good approximation behaving like an ideal gas obeying the law (cf., e.g., [*Andrews* (2000)])

$$pV_m = R^*T, \tag{1.1}$$

where p is the pressure, V_m the volume of one mole, R^* is the universal gas constant and T denotes the absolute temperature. The basic assumption of a perfect gas is that its molecules have only physical interactions due to brief collisions and intermolecular forces can be disregarded. By introducing the mass M_m of one mole and given density $\rho = M_m/V_m$ one finds

$$p = \rho RT, \tag{1.2}$$

with $R = R^*/M_m$ the gas constant per unit mass. This equation is given for an one component gas, but can be easily extended to a mixture of gases like our atmosphere. Daltons law tells us that the pressure for a mixture of gases is the sum of its partial pressures hence Eq. 1.2 can be generalized by taking the sum over R and ρ for all contributing gases. The molar abundance, used for molar fraction, can vary through changes of single gases in the mixture. It is therefore more convenient to introduce the mass and the volume mixing ratio

$$m_i = \frac{M_i}{M},\ v_i = \frac{V_i}{V}, \tag{1.3}$$

where M and V stand for the total mass and the total volume of the mixture. Often mass and volume mixing ratios are used to track the transport of chemicals since it only depends on chemical production and loss and is not affected by changes in volume. The number density, another measure of concentrations of gases, is given by n_i/V, which is the number of molecules per unit volume. The concentration may change by changes in volume or densities of individual species n_i.

The atmosphere is a fluid and is always in a state of vertical and horizontal motion. The main driving force for this motion is a differential heating by the Sun, but it is also influenced by the rotation of the Earth itself and by heterogeneous surface conditions. The atmospheric response time on imposed changes of gas concentration, pressure or temperature is much shorter than for any other climate system component. The response time denotes the time to find a new equilibrium state after some provoked perturbations.

Vertical transportation of air happens with maximum velocities of 10 ms^{-1}, where particles are influenced by upward forces due to pressure gradients balanced with the Earth's attracting gravitational field. Particles having sufficient energy can escape from the outermost atmospheric layer, the so-called exosphere, extending from an altitude of more than 500 km. The atmosphere obeys the basic equation of hydrostatic equilibrium, which is the balance between upward and downward forces. Ideally an equilibrium is reached, if no vertical motion is observed. In a first order approximation for large scale fluctuations the atmosphere fulfills this condition, nevertheless for fast vertical accelerations of air, as may be found in, e.g., thunderstorms, the equilibrium brakes down.

The atmosphere is a highly compressible gas and its density ρ varies with height z, where the air mass above a certain level is supported by the fluid below. The pressure, at each level equaling the weight of the air column above, builds up from the top of the atmosphere down to the Earth's surface. In differential form, the weight of the gas mixture of an air parcel with a volume element dV is gdM, where the incremental mass is

$$dM = \rho dV = \rho\ dA\ dz. \tag{1.4}$$

This has to be in balance with the exerted net force on the air parcel by the surrounding gas

$$-dp\ dA = g\rho\ dA\ dz, \tag{1.5}$$

which then leads to an equation for the differential pressure

$$dp = -g\rho\ dz. \tag{1.6}$$

Substituting Eq. 1.2 now into Eq. 1.6 leads to

$$\frac{dp}{p} = -\frac{dz}{H}, \tag{1.7}$$

where the pressure scale height is given by

$$H(z) = \frac{RT(z)}{g}. \tag{1.8}$$

The scale height is the height over which the pressure falls by a factor e. It is a measure for the characteristic vertical dimension of mass distributions in the atmosphere and varies from 8 km on the Earth's surface to 6 km in very cold regions. Integrating Eq. 1.7 from ground $z' = z_0$ to the height $z' = z$ we obtain a form for the hydrostatic equation

$$p(z) = p(z_0)\exp\left[\int_{z_0}^{z} \frac{dz'}{H(z')}\right]. \tag{1.9}$$

If the temperature T is a function of height z, equivalent descriptions can be found for the density $\rho(z)$ of the gas and for number densities $n(z)$ of individual species as long as they are well mixed. This does not apply to short-lived species like ozone or water vapor. Ozone is chemically created and destroyed on short time scales and water vapor may undergo rapid phase transitions. The equation above is often approximated by an isothermal atmosphere with constant T, g, and mean molecular mass with an exponential decay of pressure and thus we obtain

$$p(z) \approx p(z_0)e^{-(z-z_0)/H}. \tag{1.10}$$

The atmosphere arranges itself into a vertically stratified medium and its horizontal motion favors the tendency to keep physical properties stable along constant pressure levels on a global scale. Horizontal motion occurs on scales much larger than the atmospheric scale height, but observed temperature changes form the origin of weather. The temperature is an atmospheric key parameter and the knowledge of its distribution is essential in an understanding of the bulk structure of the atmosphere.

1.3 Radiative Transfer

1.3.1 The Global Radiation Balance

In general all the radiation that reaches the Earth has its origin in solar activity and is the prime energy supply for the Earth system (cf., e.g., [*Thomas and Stamnes* (1999)]). The energy is chiefly provided at wavelengths between 0.2 and 4 μm, which is in the

ultraviolet, visible, and infrared spectral range. The shortwave (SW) energy flux F_s impinging a surface normal to the incident ray direction is $\sim$1370 Wm^{-2}. This parameter is called the solar constant and characterizes the total solar radiation input on the Earth's atmosphere. The total incoming energy uniformly distributed over the Earth corresponds to only $F_s/4 \simeq 342$ Wm^{-2} (see Fig. 1.2), where 31% or 107 Wm^{-2} are immediately backscattered to space by clouds and the Earth's surface. This amount of solar radiation reflected to space without changes in wavelengths is called albedo. The

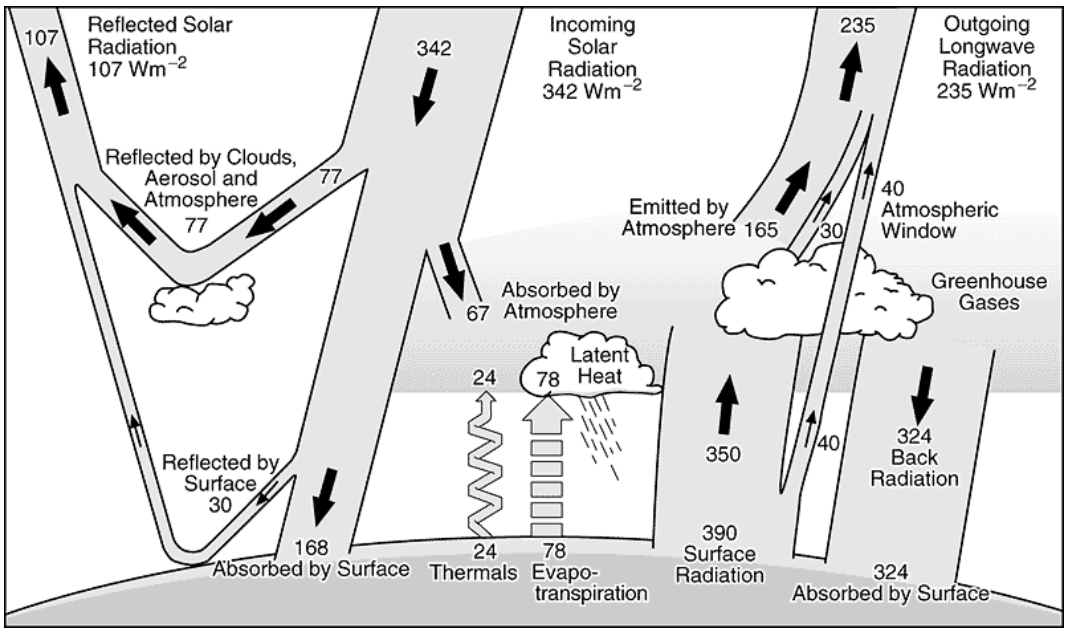

Figure 1.2. A schematic diagram of the global mean energy budget [*Houghton et al.* (2001)]. The net incoming solar radiation of 342 Wm^{-2} is partially reflected by clouds and the atmosphere, or at the surface, but almost the half of this amount of energy is absorbed by the Earth's surface.

albedo of different surfaces varies from 90% for fresh snow to less than 5% for water at specific temperatures or coniferous woodland. The remaining 235 Wm^{-2} are absorbed by the atmosphere and warms the land and the oceans. As main absorbers in the atmosphere act molecular oxygen, ozone, and water vapor. The surface returns the heat to the atmosphere, partially as longwave (LW) radiation, partially as sensible heat and as water vapor. The latter releases the latent energy when it cools down and condensates at high altitudes. For a stable climate, a balance is required between incoming and outgoing radiation and the climate system on average must radiate 235 Wm^{-2} back to space. The intensity of radiation emitted by the Sun is not entirely constant with time. Variations of $\sim$0.1% in the solar constant, due to the 11-year solar cycle, are observed.

An estimate of the Earth's mean temperature is found when considering the Earth and the Sun as black bodies with different temperatures. The Sun does behave like a black body with an effective surface temperature of 5780 K with a maximum SW emission at $\sim$0.48 μm. For a black body the intensity of radiation emitted and the wavelengths distribution only depends on the absolute temperature T and is expressed by the Stefan-Boltzmann law

$$F = \sigma T^4, \tag{1.11}$$

where F is the radiative flux and σ is the Stefan-Boltzmann constant. The outgoing LW radiation from the Earth has its peak at $\sim$10 μm and corresponds to a temperature of 255 K, whereas the observed Earth's mean temperature is about 288 K. The temperature difference is explained by the so-called greenhouse effect (cf. Section 1.3.4) reflecting the fact that the atmosphere processes SW and LW radiation in different ways.

1.3.2 The Radiative Transfer Equation

The understanding of radiative influences on the atmosphere requires a description of the radiative transfer with its three dimensional dependence on wavelength and directionality. Radiative transfer energy traverses a surface with unit normal $\mathbf{n}$ and can have contributions from all directions with unit vector $\hat{\mathbf{\Omega}}$ (see Fig. 1.3). Radiation is

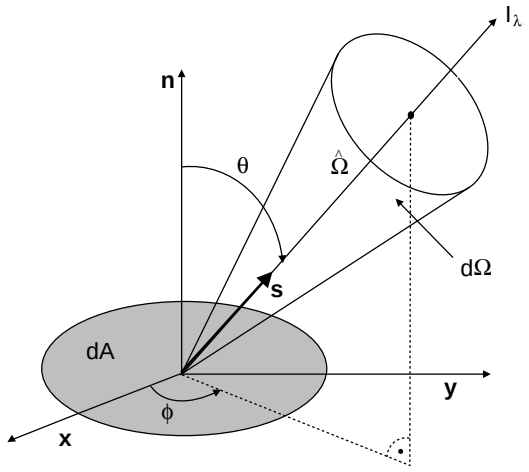

Figure 1.3. Flow of radiative transfer energy carried by a beam in direction Ω traversing the surface element dA with unit normal $\mathbf{n}$. The monochromatic intensity or radiance passing through the pencil is given by $\mathbf{I}_\nu = \mathrm{I}_\nu\hat{\mathbf{\Omega}}$.

called diffuse, if it comes from several directions, whereas incoming photons from a single direction, like from a stellar source, are termed parallel beam radiation. The monochromatic intensity or radiance $\mathbf{I}_\nu = \mathrm{I}_\nu\hat{\mathbf{\Omega}}$ is the rate of energy, depending on frequency ν, traversing a surface at a zenith angle θ, passing through a pencil in direction $\hat{\mathbf{\Omega}}$. Integrating $\mathbf{I}_\nu$ normal to the surface with positive $\mathbf{n}$ direction over the half-space of solid angle gives

$$\mathbf{I}_\nu \cdot \mathbf{n} = I_\nu\hat{\mathbf{\Omega}} \cdot \mathbf{n} = I_\nu \cos\theta, \tag{1.12}$$

and defines the monochromatic flux or irradiance crossing the surface

$$F_\nu^\uparrow = \int_{2\pi} \mathbf{I}_\nu \cdot \mathbf{n} d\Omega^\uparrow \tag{1.13}$$

$$= \int_0^{2\pi}\int_0^{\pi/2} I_\nu(\phi,\theta)\cos\theta\sin\theta\ d\theta\ d\phi. \tag{1.14}$$

The total flux then follows by an integration of the forward flux over all frequencies

$$F^\uparrow = \int_0^\infty F_\nu^\uparrow d\nu. \tag{1.15}$$

Equally, we can find an expression for the backward flux $F_\nu^\downarrow$ by integrating over the opposite half in negative **n** direction. The forward and the backward flux are both nonnegative quantities and the monochromatic net flux in **n** direction follows by taking the difference

$$F_\nu = F_\nu^\uparrow - F_\nu^\downarrow. \tag{1.16}$$

In terms of electromagnetic quantities the net forward irradiance is equal to the vertical component of the Poynting vector. Electromagnetic radiation not always passes mathematically defined surfaces. Photons can physically interact with matter through the three mechanisms absorption, emission, and scattering. The attenuation of a pencil of radiation occupying the solid angle $\mathrm{d}\Omega$ depends on the density and the absorbing characteristics of the medium through which it passes. Energy can also be scattered out of, scattered into, or emitted into the solid angle.

Absorption, Emission, and Scattering

We consider a beam of radiation of unit cross-sectional area moving in a small range of solid angles $\mathrm{d}\Omega$ along an incremental element ds. If the photons are absorbed or scattered by a radiatively active gas the spectral radiance I_ν will be reduced and can be written as

$$dI_\nu = -n\sigma_\nu I_\nu ds, \tag{1.17}$$

where σ_ν is the extinction cross section and n the number density of the gas. This is the so-called Beer-Bouguer-Lambert's law, which states that the decrease of spectral radiance is proportional to the mass of absorbing or scattering material encountered along the ray path. The cross sections denotes the area of the pencil lost by passing an increment of mass. The extinction coefficient σ_ν consists of an absorption and a scattering part

$$\sigma_\nu = \sigma_{a\nu} + \sigma_{s\nu}, \tag{1.18}$$

and generally depends on temperature and pressure. It measures the characteristic length over which energy is attenuated and can be derived from measurements or calculated from quantum mechanic processes. The radiance as a function of direction gives a complete description of the radiative field.

By integrating Eq. 1.17 along the ray path, we obtain

$$\frac{I_\nu(s)}{I_\nu(0)} = \exp\left[-\int_0^s n(s')\sigma_\nu(s')ds'\right], \tag{1.19}$$

where the number density n now depends on the path s reflecting the change in density over altitude in a real atmosphere.

Like for absorption, the emission of energy is proportional to the mass involved. If the gas along the path is also emitting photons of frequency ν, an extra term $J_\nu(s)$ must be added to Eq. 1.17, where $J_\nu(s)$ is called the source function. Having now the extinction and the emission part characterized we obtain

$$dI_\nu = -n\sigma_\nu \left(I_\nu - J_\nu\right) ds, \tag{1.20}$$

which is called the radiative transfer equation (Schwarzschild equation). A formal solution of Eq. 1.20 can be found when introducing the optical thickness τ_ν with

$$\tau_\nu(s) = \int_{s_1}^{s_2} n(s')\sigma_\nu(s')ds' \tag{1.21}$$

and inserting it into the radiative transfer equation

$$\frac{dI_\nu}{d\tau_\nu} + I_\nu = J_\nu. \tag{1.22}$$

By integration of Eq. 1.22 we obtain

$$I_\nu e^{\tau_\nu} = \int J_\nu e^{\tau'_\nu} d\tau'_\nu + C \tag{1.23}$$

and with the imposition of the boundary condition $I_\nu(s_0) = I_{\nu 0}$ we get

$$I_\nu(s) = \int_0^{\tau_\nu} J_\nu(\tau'_\nu) e^{-(\tau_\nu - \tau'_\nu)} d\tau'_\nu + I_{\nu 0} e^{-\tau_\nu}. \tag{1.24}$$

If we neglect the source term J_ν, Eq. 1.24 reduces to an exponential drop-off function over a distance corresponding to unit optical thickness. A photon may be absorbed or scattered in optically thick regions, which are denoted by a total optical thickness of $\tau_\nu > 1$. If the optical thickness is $\tau_\nu < 1$ the medium is called optically thin and particles traverse more likely without being absorbed or scattered.

Under local thermodynamic equilibrium (LTE) conditions and in the absence of scattering, the source function is equal to the black-body monochromatic radiance, or the Planck function

$$B_\nu(T) = \frac{2h\nu^3}{c^2\left(e^{h\nu/kT} - 1\right)}. \tag{1.25}$$

Integration over ν again gives the Stefan-Boltzmann equation (cf. Eq. 1.11). This relation can be verified by Kirchhoff's law asserting, that a gas at given frequency emits radiation as efficient as it absorbs it.

LTE conditions are found in the atmosphere, where at high enough pressures, molecular collisions are sufficient to satisfy the so-called Boltzmann equation (population of energy levels due to the Boltzmann distribution) and therefore give a local value of temperature T.

1.3.3 Absorption of Radiation by Gases

For a gas the absorption spectrum is described by transitions between discrete electronic, vibrational, and rotational energy levels of a molecule, respectively. Vibrational and rotational transitions occur at IR wavelengths, whereas transitions between electronic levels are triggered by the impact of UV and visible radiation. In this wavelength range radiation chiefly interacts with molecular oxygen and ozone. In addition to excitations at singular wavelengths, continuous bands of absorption are encountered at short wavelengths induced by photodissociation and photoionization.

Bonds between atoms in molecules have varying strengths, where it takes different amounts of energy to break them down. The bond between the two oxygen atoms in an

Wavelength	Atmospheric Absorber
121.6 nm	Solar Lyman α line, absorption in the mesosphere
100 - 175 nm	O_2 Schumann Runge continuum, absorption in the thermosphere
175 - 200 nm	O_2 Schumann Runge bands, absorption in the mesosphere and upper stratosphere
200 - 242 nm	O_2 Hertzberg continuum, absorption in the stratosphere; weak absorption in the mesosphere, weak O_3 absorption in the stratosphere
242 - 310 nm	O_3 Hartly band, absorption in the stratosphere
310 - 400 nm	O_3 Huggins band, absorption in the stratosphere and troposphere
400 - 850 nm	O_3 Chappuis bands, absorption in the troposphere

Table 1.3. Spectral regions of photochemical importance in the atmosphere [*Brasseur and Solomon* (1984)].

oxygen molecule is broken down if the molecule absorbs high energy UV-C radiation. The bonds between the oxygen atoms in ozone are weaker and are broken down by absorption of less energetic UV-B radiation. Absorption of this highly energetic, SW radiation by molecular oxygen and ozone in the upper atmosphere prevents it reaching the troposphere. Less energetic radiation passes through the atmosphere without significant absorption and reaches the surface of the Earth.

Tab. 1.3 summarizes the absorption characteristics at UVVIS wavelengths for molecular oxygen and ozone, nevertheless we focus on ozone absorption. Ozone absorbs at longer wavelengths than molecular oxygen and thus radiation penetrates deeper into the atmosphere. The primary absorption of UV by ozone lies between 200 and 310 nm and is called the Hartly band (see Fig. 1.4). The Hartley band merges the Huggins band from 310 to 400 nm. In the troposphere and lower stratosphere ozone also absorbs in the visible at 400 to 850 nm, which is the Chappuis band. The absorption coefficients for ozone are summarized in Fig. 1.5 for several tangent heights. In addition we show absorption coefficients for NO_2 and NO_3 as well as the refraction coefficient for air. These coefficients are important for the forward model which is developed in the scope of this thesis (cf. Section 4.1). SW radiation in these levels is almost absent, since most of the energy is already absorbed in the middle and high stratosphere. The Hartly and the Chappuis band have a continuous character, whereas the Huggins band contains a spectrum of diffuse lines.

The absorption and emission of radiation by atmospheric constituents lead to heating and cooling. The troposphere and the stratosphere exhibit different time scales of stability. The stratosphere is due to less convection and a strong static stability governed by the radiative transfer. Its radiative energy is controlled by SW heating due to the absorption of radiation by ozone and molecular oxygen and LW cooling at 15 μm by the radiative emission due to CO_2 as well as cooling by ozone at 9.6 μm. A small amount of LW heating takes place near 20 km, due to absorption of upwelling radiation by ozone at 9.6 μm. Tropospheric cooling is dominated by water vapor.

1.3.4 The Greenhouse Effect

The Earth's atmosphere contains a couple of trace gases absorbing and emitting infrared radiation. Such radiation coming from the Earth's surface, the atmosphere and clouds is absorbed by so-called greenhouse gases. Greenhouse gases, like water vapor and carbon

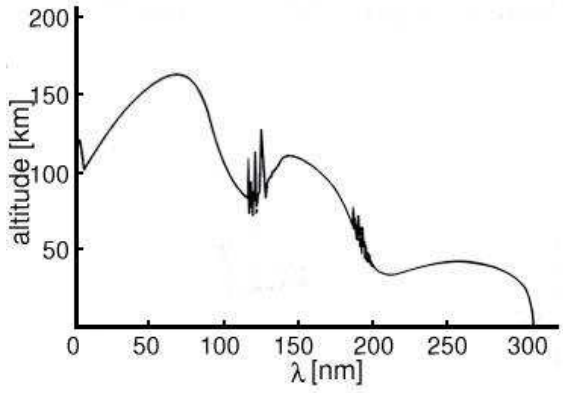

Figure 1.4. Unit optical depth for vertical solar radiation [*Huffmann* (1992)].

dioxide, have volume mixing ratios of only less than 0.1%, but are very important for the Earth's energy budget. The greenhouse gases trap heat within the atmosphere, which is called the natural greenhouse effect. The natural greenhouse effect is responsible for the observed global mean temperature of ∼15°C. Strictly spoken the greenhouse effect is not a trapping of energy in the infrared, but the restriction of convective losses when air is warmed by contact with the Earth's surface.

The increased concentration of absorbing gases in the atmosphere with anthropogenic origin enables an additional heating. The opacity of the atmosphere rises and thus the altitude from which radiation is re-emitted to space is higher. Temperatures at higher altitudes are lower and less energy is emitted, which leads to a positive radiative forcing. This effect is called the enhanced greenhouse effect.

1.4 Ozone Physics and Chemistry

One of the most interesting and important research areas in atmospheric science is the determination of global ozone budgets and related temperature profiles [*Andrews* (2000), *Salby* (1995), *Peixoto and Ooort* (1992)]. Since the 1970s the density of stratospheric ozone has decreased continuously. The most spectacular loss of ozone is reported above the South Pole, where a hole in the so-called ozone layer now opens annually and is a dramatic symbol of our atmosphere's inherent unpredictability. Each year, when temperatures significantly fall in the beginning southern hemispheric winter and favored by singular meteorological circumstances such as the polar vortex, the ozone hole builds up and remains for several months with a minimum of column ozone in the antarctic spring around October. Nonetheless stratospheric ozone loss can be measured as well in the northern hemisphere, where industrialized countries are the main contributors to the global air pollution in general.

The culprits for such dramatic changes, in heights where the atmosphere is very sensitive to variations in the balance of several chemical constituents, were found to be Chlorofluorocarbons (CFCs) once developed as stable, non-polluting chemicals widely used in aerosols and refrigerators. But CFCs turned out to circulate throughout the

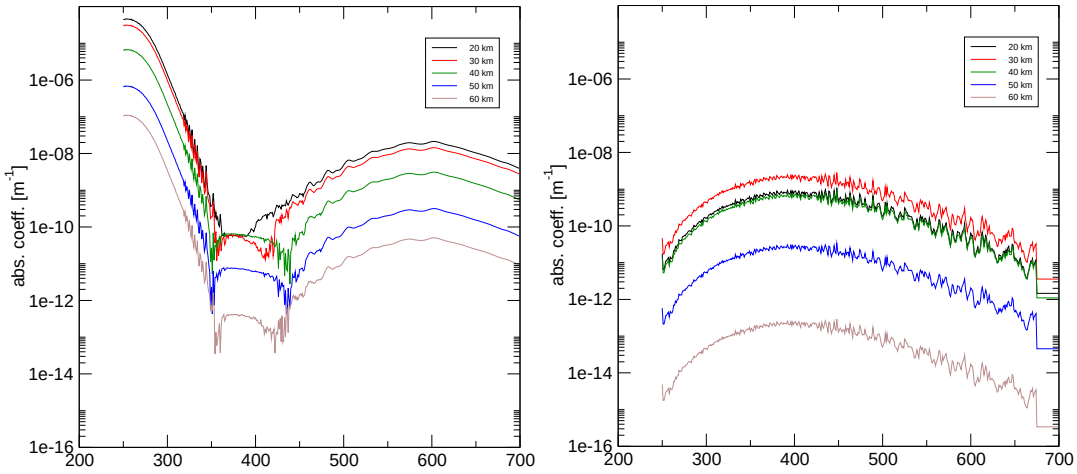

Figure 1.5. Absorption coefficients of ozone (left panel) and NO_2 (right panel) at typical GOMOS wavelengths from 250 - 700 nm at heights of 20, 30, 40, 50, and 60 km. Typical ozone absorption bands are found between 200 and 310 nm (Hartly band), from 310 to 400 nm (Huggins band), and lies at 400 to 850 nm (Chappuis band).

globe and sometimes move up into stratospheric regions. Whereas CFCs seemed to be inert at lower altitudes, they were broken up at high altitudes by intense solar ultraviolet radiation. The ozone layer is highly reactive with chlorine once liberated from CFCs. A single chlorine molecule has a devastating effect, taking apart a large number of ozone molecules.

The ozone layer protects the Earth and its biosphere from harmful UV radiation. It absorbs radiation originating from the Sun between 240 and 290 nm (UV-C) almost completely and reduces the radiative impact on the Earth between 290 and 320 nm (UV-B), which is a biologically very active spectral window. It is believed that an increase of UV-B at the Earth's surface has a strong dermatological influence and increases the occurrence of skin cancer. Life on Earth is thought to be unimaginable without the removal of harmful radiation.

The highest concentration of ozone is typically found between 25 and 35 km, but only reaches a mixing ratio of $\sim$10 ppm. More than 90% of the total atmospheric ozone contains the stratosphere where it is due to the absorption of UV radiation the main heat source. Decreasing ozone densities lead to lower temperatures and have therefore an impact on the climate system as well. The remaining 10% of tropospheric ozone are known to have direct toxic effects on humans and on the vegetation. It plays an important role in the generation of photochemical smog and the formation of acid rain from SO_2 and NO_2, and moreover acts as a greenhouse gas due to the absorption of thermal infrared radiation at wavelengths near 9.6 μm.

The transport of ozone plays a significant role in the stratospheric air circulation, where air experiences a noticeable difference in the radiative environment compared to the troposphere. The trace gas is redistributed from equatorial regions with high ozone production to higher latitudes with low production rates. The time scale for the stratospheric ozone deportation lies at about three months and reflects the fact that ozone, under certain conditions, has a longer lifetime than time is consumed for an intact transport. From below 20 km at the equator up to about 40 km near the poles

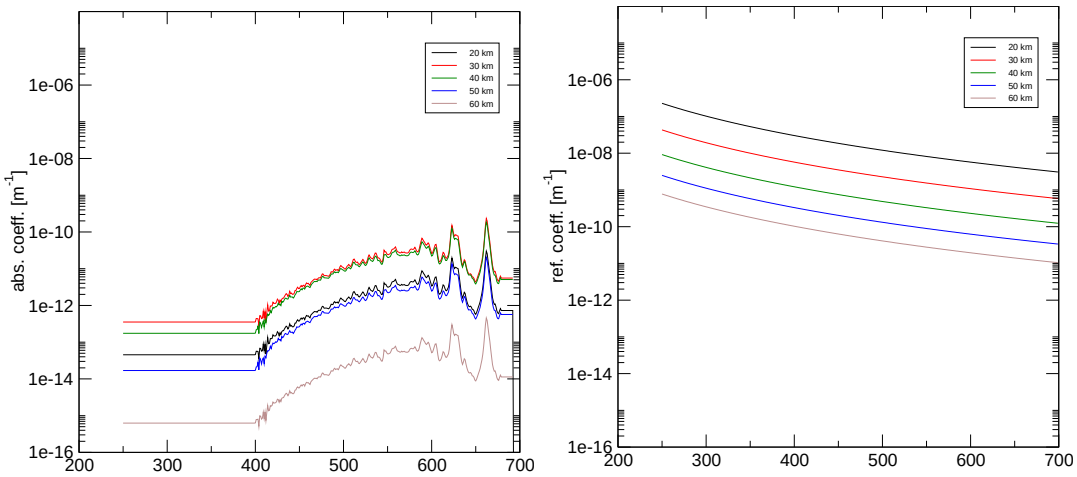

Figure 1.6. Absorption coefficients of NO_3 (left panel) and refraction coefficients of air (right panel) at typical GOMOS wavelengths from 250 - 700 nm at heights of 20, 30, 40, 50, and 60 km.

ozone remains sufficiently long in a stable state.

The total column ozone, as displayed in Fig. 1.7, is the integrated amount of ozone from Earth's surface up to the top of the atmosphere. It is often expressed in Dobson units (DU), where one DU is the thickness of the ozone column at standard pressure and temperature (273.15 K and 1 atm) measured in hundreds of a millimeter. A midrange column density is 300 DU, which would correspond to a total column density of ozone equivalent to 0.3 cm of ozone at standard pressure.

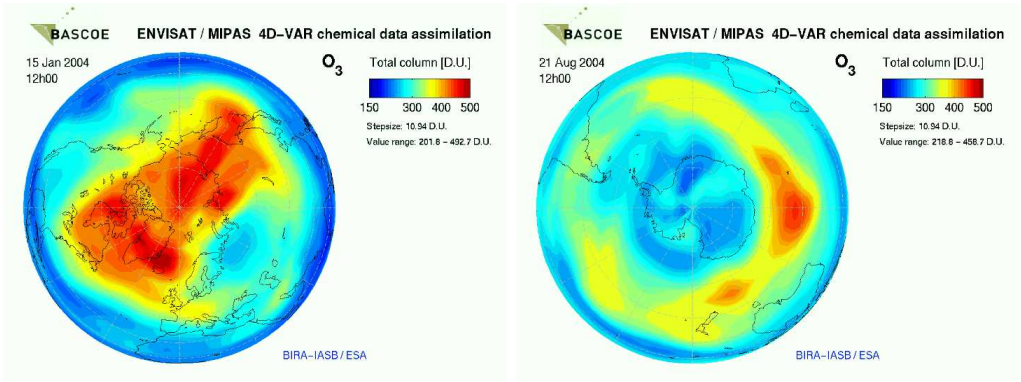

Figure 1.7. Two images of the total ozone column over the North and the South Pole. Data were measured by the Envisat/MIPAS instrument and assimilated by BASCOE, a 4-D VAR chemical assimilation system [*Errera and Fonteyn* (2001)] (http://bascoe.oma.be, August 2004).

From now 17 years ago the Montreal Protocol banned the production and use of CFCs, but too late to stop a 28 million km^2 ozone hole opening over Antarctica each spring. Since then, science teams all over the world are hoping for a response of the ozone layer. The first sign of a reconstruction of stratospheric ozone may have been found in the now famous small-area ozone hole in 2002 followed by a split into two separated holes. In 2003 the ozone hole was back at its extension measured in years before 2002.

1.4.1 Ozone Production and Depletion

The British scientist Sidney Chapman [*Chapman* (1930)] proposed in 1930 that ozone is continuously produced in the atmosphere by a cycle including O_2, a process now named after him. In 1970 it was Paul Crutzen [*Crutzen* (1970)] to bring to light a better understanding of stratospheric ozone cycles by enlightening the role of reactive NO_x, which has a pivotal influence on the ozone chemistry of the troposphere and the stratosphere.

Over time scales of days up to many years, depending on altitude, ozone is in balance between production and destruction. Ozone production occurs in the stratosphere above 30 km height at wavelengths less than 242 nm, where first molecular oxygen is photo-dissociated into two oxygen atoms

$$O_2 + h\nu \rightarrow 2O \tag{1.26}$$

and shortly after reacts with molecular oxygen to form ozone

$$O_2 + O + M \rightarrow O_3 + M, \tag{1.27}$$

where M stands for any third body absorbing liberated excess energy and momentum. This is the only reaction that produces ozone in the stratosphere and even the troposphere. Ozone strongly absorbs radiation between 240 and 320 nm and splits due to dissociation

$$O_3 + h\nu \rightarrow O_2 + O \tag{1.28}$$

into molecular and atomic oxygen, where the latter almost immediately recombines to new ozone. Furthermore ozone can react with atomic oxygen to form two molecules of O_2

$$O_3 + O \rightarrow 2O_2. \tag{1.29}$$

This simple description of ozone photochemistry, also called the Chapman mechanism, constitutes a closed cycle and is very effective in the absorption of solar energy in the UV, because no net loss of components is involved. The four reactions 1.26 - 1.29 have different characteristic times. If an atomic oxygen atom is produced by Eq. 1.26, reactions 1.27 and 1.28 cycle many times before reaction 1.29 can take place. Reactions 1.27 and 1.28 rapidly convert O into ozone and vice versa so one can talk about an aggregation of species which is then called odd oxygen O_x. The lifetime of odd oxygen is short in comparison with that of its individual members or O_2. This pseudo steady-state concentration, which can be seen to be in photochemical equilibrium, is only produced by reaction 1.26 and destroyed by reaction 1.29. Reaction 1.26 denotes the process of photolysis of O_2 in the Herzberg continuum near 242 nm, whereas Eq. 1.28 reflects the absorptive behavior of ozone in the Hartley and Huggins band near 310 nm.

Production and Destruction Rates

The rates of ozone formation depend on latitude, altitude, and season. As a function of a different impact of solar radiation and the solar zenith angle, in equatorial regions the ozone production is highest and increases with increasing altitude, however regions with highest ozone formation (equatorial regions about 40 km altitude) do not correspond to regions with highest ozone concentrations (northern latitudes). At higher

latitudes with large abundances of ozone, the production takes place even higher than near the equator.

The rate of destruction of ozone in Eq. 1.29 is given by

$$\left.\frac{d[\mathrm{O_3}]}{dt}\right|_{-} = -j_3[\mathrm{O_3}], \tag{1.30}$$

a Lagrangian derivative of the ozone number density. Destruction and production coefficients are here and subsequently denoted by j's and k's. The production rate of ozone in Eq. 1.27 is

$$\left.\frac{d[\mathrm{O_3}]}{dt}\right|_{+} = k_2[\mathrm{O_2}][\mathrm{O}][\mathrm{M}], \tag{1.31}$$

which furthermore allows for a description of net production of ozone

$$\left.\frac{d[\mathrm{O_3}]}{dt}\right|_{\pm} = k_2[\mathrm{O_2}][\mathrm{O}][\mathrm{M}] - j_3[\mathrm{O_3}]. \tag{1.32}$$

Due to photochemical equilibrium the left hand side vanishes and we find

$$j_3[\mathrm{O_3}] = k_2[\mathrm{O_2}][\mathrm{O}][\mathrm{M}], \tag{1.33}$$

leading to a characterization of a ratio of odd oxygen members

$$\frac{[\mathrm{O}]}{[\mathrm{O_3}]} = \frac{j_3}{k_2[\mathrm{O_2}][\mathrm{M}]}. \tag{1.34}$$

With increasing altitude M decreases and $[\mathrm{O}]/[\mathrm{O_3}]$ becomes larger. Thus atomic oxygen in favored at higher altitudes and ozone at lower heights. Equally to Eq. 1.34 one can find rates for the production and destruction of odd oxygen yielding

$$j_2[\mathrm{O_2}] = k_3[\mathrm{O}][\mathrm{O_3}]. \tag{1.35}$$

The equilibrium number density of ozone is obtained by eliminating [O] in Eqs. 1.34 and 1.35

$$[\mathrm{O_3}] = [\mathrm{O_2}]\left(\frac{k_2 j_2}{k_3 j_3}[\mathrm{M}]\right)^{\frac{1}{2}}. \tag{1.36}$$

While the ozone production cycle has only a small set of reactions, the depletion of ozone is far more complex due to the existence of a number of processes by involving free radicals such as hydrogen, nitrogen, and chlorine [*Seinfeld and Pandis* (1998), *Fabian and Singh* (1999)]. The Chapman mechanism is a good approximation to a comprehensive understanding of ozone chemistry but it turns out that it overestimates the actual ozone density in the upper stratosphere, and that ozone is underestimated in the lower stratosphere. Free radicals, produced by photodissociation of reservoir species often of tropospheric origin, are found to destroy ozone in catalytic cycles. Hence we introduce an additional process to the ozone destruction of the form

$$\begin{aligned} \mathrm{X} + \mathrm{O_3} &\rightarrow \mathrm{XO} + \mathrm{O_2} \\ \mathrm{XO} + \mathrm{O} &\rightarrow \mathrm{X} + \mathrm{O_2}, \end{aligned} \tag{1.37}$$

where X stands for a free radical and acts as a catalyst which does not get consumed in the reaction. For X we can find several species, such as H, OH, NO, Cl, or Br satisfying Eqs. 1.37.

HO_x Chemistry

The free radicals that can participate in this cycle are H, OH, and HO_2, which supersede X in Eqs. 1.37. Depending on altitude and the particular concentration, one species is favored and the reaction with odd oxygen, important at altitudes above 40 km only, is found to be

$$\begin{aligned} H + O_3 &\rightarrow OH + O_2 \\ OH + O &\rightarrow H + O_2, \end{aligned} \tag{1.38}$$

whereas below 40 km we get

$$\begin{aligned} OH + O_3 &\rightarrow HO_2 + O_2 \\ HO_2 + O &\rightarrow OH + O_2. \end{aligned} \tag{1.39}$$

The upper reactions do not necessarily need the form of Eqs. 1.37 and thus we can find for the upper stratosphere

$$\begin{aligned} OH + O &\rightarrow H + O_2 \\ H + O_2 + M &\rightarrow HO_2 + M \\ HO_2 + O &\rightarrow OH + O_2, \end{aligned} \tag{1.40}$$

which converts two odd oxygens into an even oxygen. Below 30 km no atomic oxygen is needed in the reaction and ozone gets destroyed via

$$\begin{aligned} OH + O_3 &\rightarrow HO_2 + O_2 \\ HO_2 + O_3 &\rightarrow OH + 2O_2. \end{aligned} \tag{1.41}$$

NO_x Chemistry

The free radicals NO_x can efficiently convert odd oxygen into even oxygen through the catalytic cycle

$$\begin{aligned} NO + O_3 &\rightarrow NO_2 + O_2 \\ NO_2 + O &\rightarrow NO + O_2, \end{aligned} \tag{1.42}$$

which results in a net effect of

$$O_3 + O \rightarrow 2O_2. \tag{1.43}$$

This closed cycles leaves NO and NO_2 unchanged, so many ozone molecules can be destroyed by one nitric oxide. Nitric oxide is known to be produced by natural processes as well as by anthropogenic interaction via, e.g., by-products of inefficient combustion. The principal source of NO in the stratosphere constitutes through the process

$$NO_2 + O \rightarrow 2NO, \tag{1.44}$$

where NO_2 is a species with a photochemical lifetime of order of 100 years. In the lower stratosphere with higher ozone abundances there exists another NO_x cycle

$$\begin{aligned} NO + O_3 &\rightarrow NO_2 + O_2 \\ NO_2 + O_3 &\rightarrow NO_3 + O_2 \\ NO_3 + h\nu &\rightarrow NO + O_2. \end{aligned} \tag{1.45}$$

Several NO compounds are capable of participating in the reaction remaining in photochemical equilibrium. As already denoted for odd oxygen, we find a family of chemicals forming odd nitrogen

$$NO_x = N + NO + NO_2 + NO_3 + 2N_2O_5 + HNO_4, \tag{1.46}$$

which reacts with other families such as O_x.

ClO_x Chemistry

Atomic chlorine is produced by nature through photodissociation of methyl chloride CH_3Cl (cf. Tab. 1.4), which is the largest natural source of ozone-depleting chlorine compounds. It accounts for about 15% of the present atmospheric chlorine content, where the remaining chlorine originates from man-made sources. The chemical, produced by ocean processes and fungal action on rotting wood, is believed to have been present in higher concentrations in pre-industrial times, when additional anthropogenic sources such as CFCs were absent. The CFCs lifetimes are sufficiently large to reach stratospheric heights, where they are photodissociated by

$$\begin{aligned} CFCl_3 + h\nu &\rightarrow CFCl_2 + Cl \\ CF_2Cl_2 + h\nu &\rightarrow CF_2Cl + Cl \end{aligned} \tag{1.47}$$

and chlorine radicals are released. The chlorine atom is highly reactive and is capable of destroying several ozone molecules on a small time scale via

$$\begin{aligned} Cl + O_3 &\rightarrow ClO + O_2 \\ ClO + O &\rightarrow Cl + O_2. \end{aligned} \tag{1.48}$$

It furthermore reacts with other species on varying times scales and an introduction of a so-called odd chlorine

$$Cl_x = Cl + ClO + HOCl \tag{1.49}$$

is therefore convenient. The odd chlorine and odd nitrogen family can interact with each other and form a high potential for ozone depletion.

Br_x Chemistry

A fourth cycle with potential to deplete ozone includes bromine, which has a similar cycle like chlorine.

$$\begin{aligned} BrO + ClO &\rightarrow Br + Cl + O_2 \\ Br + O_3 &\rightarrow BrO + O_2 \\ Cl + O_3 &\rightarrow ClO + O_2. \end{aligned} \tag{1.50}$$

Bromine, which has a large anthropogenic source budget of about 60%, has no stable reservoir and thus it is released rapidly to the atmosphere. It is as 50 times more effective in ozone destruction than chlorine and couples the chlorine and the bromine cycle.

1.4.2 The Ozone Hole

Chlorofluorocarbons (CFCs) were developed in the 1930s to replace refrigerants such as chloromethane, carbon tetrachloride, isobutane, and propane which were considered unsafe. With the Montreal protocol and its amendments CFCs were withdrawn from the market and primarily replaced by hydrofluorocarbons (HFCs) and hydrochlorofluorocarbons (HCFCs), all fulfilling the basic properties of low-flammability, low toxicity and a short environmental lifetime. A list of so-called ozone depletion potentials (ODP) (cf. Tab. 1.4) was calculated and reflects the influence of former and newly designed chemical species on ozone. Since the 1950s production and emission of CFCs increased

Chemical Formula	**Compound**	**ODP**
$CFCl_3$	CFC-11	1.000
CF_2Cl_2	CFC-12	0.820
$CFCl_2CF_2Cl$	CFC-113	0.900
CF_2ClCF_2Cl	CFC-114	0.850
CF_2ClCF_3	CFC-115	0.400
CCl_4		1.200
CH_3CCl_3		0.120
CF_2HCl	HCFC-22	0.004
CF_3CHCl_2	HCFC-123	0.014
CF_3CHFCl	HCFC-124	0.030
CH_3CFCl_2	HCFC-141b	0.100
CH_3CF_2Cl	HCFC-142b	0.050
$CF_3CF_2CHCl_2$	HCFC-225ca	0.020
CF_2ClCF_2CHFCl	HCFC-225cb	0.020
CH_3Br		0.640
CF_3Br	H-1301	12.000
CF_2ClBr	H-1211	5.100
CF_2Br_2	H-1202	0.300
CF_2BrCF_2Br	H-2402	6.200
CH_3Cl		0.020

Table 1.4. Ozone Depletion Potentials (ODP)

rapidly with the spread of refrigeration and the new usage of propellants in aerosol sprays. By the early 1970s CFCs had already become ubiquitous trace gases in the troposphere. The potential of chemicals emitted on the Earth's surface contributing to the stratospheric ozone depletion depends on how many of those get already destroyed in the troposphere. In 1974 Molina and Rowland [*Molina and Rowland* (1974), *Rowland and Molina* (1975)] were the first to point out, that man-made chlorofluorocarbons ($CFCl_3$ and CF_2Cl_2) have no sink in the troposphere and due to their stability diffuse unchanged to the stratosphere, where they photolyse and free chlorine radicals. This was a hypothesis that could not be tested due to the lack of appropriate atmospheric models and insufficient computer power. In 1985 [*Farman et al.* (1985)] there was

presented the first evidence of ozone depletion in the Antarctic during austral spring due to the growths of chlorine in the stratosphere. This observation, now called the ozone hole, took the scientific community by surprise. Models were thought to be well advanced in the explanation of stratospheric transport and chemistry. The observed ozone depletion took place much lower in the atmosphere than at expected heights of ∼40 km.

Each winter near the poles a pronounced circumpolar wind system builds up due to the rotation of the Earth and a poleward flow of air. The so-called polar vortex confines the air to move to the poles, where, because of the lack of solar heating in winter, very cool temperatures can be observed. This situation clearly favors a depletion of ozone via several positive feedback reactions. The vortex in southern polar regions is nearly zonal and much more stable than found in the northern hemisphere. Due to orography the northern polar vortex often breaks down through planetary waves and thus temperatures do not decline to values which increases the formation of critical aerosols and subsequent large scale destruction of ozone.

In spring the Antarctic stratosphere warms up later and cold temperatures favoring the formation of clouds persist longer. Aerosols found in the stratosphere may build so-called polar stratospheric clouds (PSCs), which in the Antarctic reach a fractional coverage of up to 50%. The crucial role of PSCs is the ozone depletion by heterogeneous chlorine activation on PSC surfaces. PSCs are known to increase the speed of certain reactions that is much higher than in the gas phase alone. Consistent with the observed ozone depletion, PSCs shift the catalytic destruction of ozone from the upper stratosphere to heights between 10 and 20 km. Two major types of PSCs were originally distinguished by lidar measurements [*Browell et al.* (1990)]. Type II is identified with water ice and is only very rarely observed in the Arctic, whereas the composition and phase of type I PSCs are still under discussion. From remote sensing and *in situ* measurements, several sub-types are distinguished due to their polarization and backscattering behavior. It is believed that if temperatures decrease below 196 K one finds the threshold of the formation of type I PSCs, which then goes along with a sharp increase of chlorine monoxide and provides the environment of accelerated ozone destruction.

2

Atmospheric Remote Sensing

Observables of the atmosphere can be measured in various ways. Generally we can distinguish between *in situ* and remote sensing measurements. *In situ* measurements, where observations are taken at the exact instrument position, are typically found for meteorological parameters, such as temperature and wind. Remote sensing, in turn, is defined as the acquisition of information about an object without being in physical contact with it. Measurements are made by acquiring information of effects imposed by the object on its surrounding field. The term remote sensing most commonly stands for measurements in the electromagnetic spectrum, ranging from radio waves to gamma rays. A general discussion concerning remote sensing techniques can be found in, e.g., [*Elachi* (1987), *Rees* (2001), *Huffmann* (1992)].

2.1 History of Remote Sensing

Remote sensing as a technology started with the first photographs in the early nineteenth century. Nowadays several techniques are in use like inserting radar systems into space, proliferating of weather satellites, launching a series of satellites to monitor the Earth's atmosphere and environment by using, e.g., radio, microwave, infrared, visible, or ultraviolet sensors, and deploying a variety of sensors to gather imagery and other data of planets and astronomical bodies.

Remote sensing above the atmosphere originated at the dawn of the space age. The power and capability of launch vehicles was a big factor in determining which remote sensors could be placed as part of the payload. Especially in the last 30 years satellite measurements have become an important technique for monitoring the Earth's atmosphere. Small sounding rockets, such as the Wac Corporal, the Viking, and Aerobee series were developed and launched by the military in the mid of the 20th century. These rockets, while not attaining orbit, contained automated still or movie cameras that took pictures as the vehicles ascended. In these early days there were many variants of sounding rockets, along with those being groomed for eventual insertion of objects into orbit. The two heavily used launch vehicles in the U.S. space program

have been the Atlas and Delta rockets, each having been upgraded over the last 30 years. Another example is the Saturn V rocket famous for launching the Apollo Moon missions and the Skylab. The U.S. Air Force's primary launch vehicle is the Titan. Another frequently used launch vehicle is the Space Transport System (STS), more commonly known as the Space Shuttle. Other nations have built their own vehicles for various purposes. Examples are the successful European Ariane 4 or the much newer Ariane 5 rocket (well known for failing with Artemis, but bringing Envisat into its designated orbit without problems), operating out of Arianespace in French Guiana. Russia has contributed with remote sensing instruments launched by, e.g., the Proton and the Soyuz rockets, achieving a high launch success rate in over 800 flights.

2.2 In situ vs. Remote Sensing Measurements

Ground-based stations, measuring local meteorological parameters, are distributed all over the world and thus form a basis for the gain of daily down to hourly comprehensive weather data. If we are interested in the vertical distribution of, e.g., temperature or humidity we may use balloon-borne instruments, transmitting data back to Earth via radio signals. Regular ascents of radio-sondes provide a dense network (chiefly over North America, Europe, and some parts of Asia) of data points with high vertical resolution for tropospheric temperature profiles. Research balloons and aircrafts are limited in their vertical range. They can cover the whole troposphere and the low stratosphere by measuring *in situ*. For sampling the air above this layer rockets are in use, where measurements are taken by the instruments when they descent through the atmosphere with a parachute.

Measurements can all be taken in the vicinity of the instruments and thus are termed *in situ*. An alternative method is the so-called remote sensing measurement which is characterized by the fact, that the measurement takes place at a different location from that of the instrument. Remote sensing applications are found in ground-based, in balloons, aircraft, and spacecraft systems. Nowadays satellite remote sensing is already the most elaborated and most advanced technique in the observation of the Earth. Actual and future remote sensing measurements by satellites are and will be the main input into our weather and climate models. Tab. 2.1 gives an overview of parameters measured by *in situ* and by remote sensing measurements.

Compound	**In Situ Methods**	**Remote Sensing Methods**
O_3	UV absorption, chemiluminescence	UV, IR, and microwave spectroscopy, LIDAR
O_2	mass spectroscopy	IR spectroscopy
NO	chemiluminescence	IR spectroscopy
NO_2	photolysis, chemiluminescence	visible and IR spectroscopy
H_2O	frost point hygrometer, Lyman-α absorption	IR and microwave spectroscopy, Raman LIDAR, filter spectroscopy
Cl, ClO	resonance fluorescence	microwave spectroscopy

Table 2.1. List of *in situ* and remote sensing techniques for the measurement of some important atmospheric gases (cf. [*Brasseur et al.* (1999)]).

Each of these techniques has further advantages and disadvantages. *In situ* measurements have high resolutions and samples can always be taken at the exact same positions which makes long term trend studies easily possible. Such measurements are often a lot cheaper and easier to establish than remote sensing measurements, but *in situ* measurements are often costly compared to the scientific output of the experiment. *In situ* measurements are very localized and often regions of special scientific interest are not covered very well (e.g., the temperature distribution over the Pacific Ocean or the Antarctica, where only a few radio-sonde measurements are taken regularly). Nonetheless *in situ* measurements are indispensable in the validation of remote sensing products. Temperature measurements by radio-sondes are still contributing to data assimilation systems.

Remote sensing measurements can have excellent global coverage with cycles of two or three days for sampling the same regions, but profiles are always somewhat blurred over hundreds of kilometers in the horizontal and over several kilometers in the vertical. Moreover, remote sensing measurements call for sophisticated numerical inversion systems, where indirect measurements of parameters of interest are to be retrieved. This implies an interpretation of statistical entities and the knowledge of accurate measurement errors. Details about the statistical analysis of atmospheric parameters are given in Chapter 4.

2.3 Basics of Atmospheric Remote Sensing

There are two types of atmospheric remote sensing, namely passive and active sensing. Passive systems measure naturally occurring radiation, which are mostly electromagnetic rays coming from the Sun (UV, visible, and IR radiation) or from objects emitting thermal radiation, such as the Earth (cf. [*Huffmann* (1992)]). Lunar and stellar signals are also measured, having the disadvantage of relatively small intensities, but, especially in the case of stellar signals, providing radiation at wavelengths not emitted by the Sun and thus making a variety of, e.g., atmospheric chemical constituent measurements possible. Active systems in turn, can emit signals at very well defined wavelengths which are then analyzed by a receiving instrument. In practice active instruments are only restricted by the transparency of the Earth's atmosphere.

These techniques of atmospheric remote sensing can be further divided into four general categories, which are governed by scattering, emission, absorption, and refraction.

The approach to scattering is to capture the signal backscattered from the Earth's surface, or from particles (e.g., aerosols) in the air between the Earth's surface and the instrument. Incoming radiation may be recorded by direct nadir-looking instruments or by instruments measuring at angles different from the incident rays (e.g., the radar backscatter instrument WS on ERS for wind measurement (http://earth.esa.int/ers/ws, November 2004), or an instruments for ozone monitoring such as the total ozone mapping spectrometer (TOMS) (http://toms.gsfc.nasa.gov, November 2004). The source of radiation is mostly the Sun, but remote sensing by scattering instruments can also be done with man made signals by active systems.

In the case of emission the source of radiation is the atmosphere itself and the sensor measures the spectral characteristics and the intensity of the emitted radiation.

An example instrument is the Infrared Atmospheric Sounding Interferometer (IASI) on METOP measuring the infrared spectrum emitted by the Earth. IASI will provide improved infrared soundings of temperature profiles in the troposphere and lower stratosphere, moisture profiles in the troposphere, as well as some of the chemical components playing a key role in the climate monitoring, global change, and atmospheric chemistry [*Weisz* (2001), *Schwärz* (2004)].

In absorptive occultation techniques one measures the changes of a signal after propagating through the atmosphere along the line-of-sight. The signal source can be the Sun, as the most illuminous visual natural object, the moon, stars, and several man made transmitters in the radio or radar wavelength region. Solar occultation is performed by, e.g., The Stratospheric Aerosol and Gas Experiment (SAGE) (cf., e.g., [*Chu et al.* (1989), *McCormick et al.* (1989), *Fussen* (1998), *Fussen et al.* (1998)]). This instrument provides unique measurements of temperature in the stratosphere and mesosphere and profiles of trace gases such as ozone, water vapor, and nitrogen dioxide, which play significant roles in atmospheric radiative and chemical processes. Another example for a solar occultation instrument is the Sun Monitoring and Atmospheric Sounder (SMAS) sensor concept [*Rehrl* (2000), *Rehrl and Kirchengast* (2004)]. The far most treated and in detail discussed occultation instrument in this thesis is GOMOS onboard Envisat (cf. Section 3.3). GOMOS exploits stellar occultation data to retrieve atmospheric constituent profiles like ozone. As application of the stellar occultation approach, the measurement of ozone was also done by [*Riegler et al.* (1996)] with the ORA-3 satellite. In more recent times extinctive and refractive stellar occultation was combined and analyzed on a proof-of-concept basis with the MSX/UVISI experiment [*Yee et al.* (2002)].

Absorptive occultation techniques are highly complementary to the information in refractive occultation data provided by GNSS radio occultation [*Kursinski et al.* (1997)]. Instead of recording transmissions passing the atmosphere, here phase delays of signals in wavelengths of meters are measured and inverted to bending angle profiles, thus leading to temperatures (cf. Section 4.5).

2.4 Stellar Occultation

Here we want to treat the occultation technique [*Yee et al.* (2004)] which is of major importance in this thesis. Occultation techniques have been used for many years to study the Earth's atmosphere, the other planets in the solar system, and their satellites. The techniques are generally based upon relative measurements. The stellar occultation technique has the significant advantage that an absolute estimate of the molecule density is obtained from the ratio of two measurements taken with the same instrument within a few seconds. This makes the method inherently self-calibrating, since even if the spectral sensitivity of the instrument is changing with time, the ratio will be measured correctly. This protection against long-term drifts is ideal for the study of atmospheric trends. Although easy to implement in principle, technical constraints have existed, however, occultation techniques have proven to be an excellent concept of exploring the overall structure of the terrestrial and planetary atmospheres.

2.4.1 A Comparison of Stellar to Solar and Lunar Occultations

When having a look on occultation techniques, stellar occultation has several advantages in comparison to solar or lunar occultation. A satellite in a low Earth orbit makes approximately 14 revolutions in one day which theoretically gives 28 occultations (14 sunrises and 14 sunsets) for the solar occultation case. Lunar occultation has the same number of possible measurements. In turn, stellar occultation has hardly no natural limit concerning the number of measurement. Measurements can be made from virtually anywhere looking to the Earth's limb. The only real constraints are technical realizations of the instrument possibly reducing the number of occultation events.

A theoretical study [*Hays and Roble* (1968)] demonstrated that the extinctive stellar occultation technique could be a powerful tool for remotely sensing the Earth's atmosphere. Measurements at broad wavelength bands at high spectral resolution are needed to separate the spectral signatures of the various atmospheric species. In order to track the star even in the presence of refraction, the instrument must have excellent stability and jitter compensation.

For an operation on very faint stars the technical constraint of a high signal-to-noise ratio has to be considered. The more faint stars are trackable the more measurements can be performed, which is especially interesting for having a great variety of stellar signals, each with a different visual star magnitude and star temperature. In turn, this makes the analysis of measurements a difficult task in order to handle variabilities in accuracy of the measurements. Depending on the obliquity (angle from an ideal vertical occultation) of the measurement, the quality of measured profiles moreover suffers from errors due to atmospheric turbulence.

The most limiting factor in stellar occultation is the weakness of the stellar fluxes compared to a rather constant solar flux. The telescope for collecting the signal has to be large in order to gain a high signal quality. A high-precision, two-axis system is needed to acquire and track the star as it sets through the atmosphere, including the apparent motion induced by refraction.

Solar occultations yield higher signal-to-noise ratios due to a high signal intensity of the Sun. Furthermore, solar occultations are generally immune to the effects of atmospheric emissions. However, in the lower atmosphere where refraction is significant, stellar occultations have the advantage that the refractive effects can be treated more easily for stars as a point source than for the Sun which is an extended source.

Other technical restrictions are due to bright limb occultations, occultations of faint stars, and the maximum time which passes between two consecutive measurements as well as the possibility of tracking stars in rising occultations. Bright limb occultations are in principle possible with GOMOS (cf. Section 3.3) where the measuring unit, a CCD, has extra lines for capturing strong light signals as originating from straylight. For bright limb occultation purposes the instrument has to have a very high signal-to-noise ratio in order to distinguish the star signal from the solar backscattered radiation.

Due to the self-calibrating nature of the stellar occultation measurements and the good global coverage by a multitude of available stars, it is possible to generate up to $\sim$ 400 profiles during 24 hours (see Fig. 2.1).

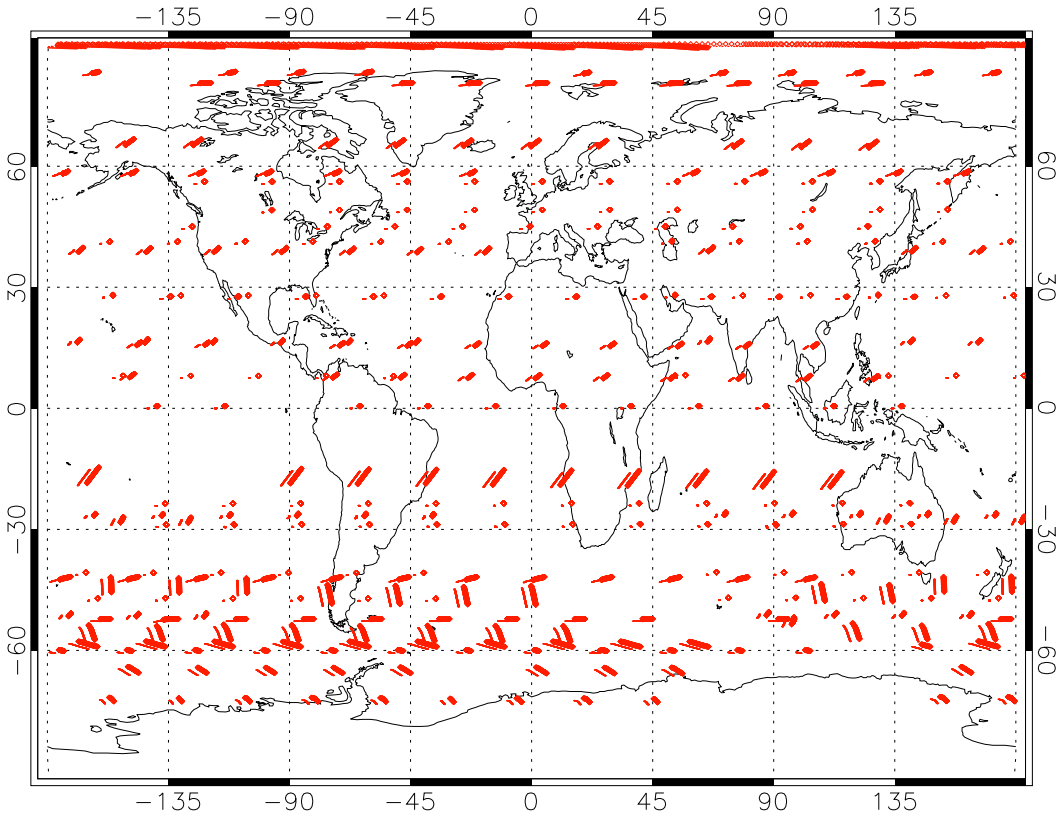

Figure 2.1. The distribution of GOMOS occultation events for a 24 hours period. Here 426 event locations are shown for September 03, 2003. High latitude profiles in this set are mostly measured under bright limb conditions. Low and mid latitude profiles are in turn gained by dark limb occultations.

2.4.2 Techniques for Stellar Occultation

The stellar occultation technique in general was first described by [*Hays and Roble* (1968)], who showed the possibility of using stars as a light source for extinction experiments. Five years later the first measurements of the Earth's atmosphere were performed when a spectrometer on the OAO-2 satellite was used to infer density profiles for O_2 and O_3 in the thermosphere and upper mesosphere. Extinctive stellar occultations have furthermore yielded densities for a number of species in the Earth's atmosphere [*Atreya* (1981), *Roscoe et al.* (1994)]. The technique has also been a primary means of probing the atmospheres of the other planets and their satellites.

In recent times Smith and Hunton [*Smith and Hunten* (1990)] showed a review of using absorptive occultations for planetary atmospheres. The investigation of the atmospheres of planets like Jupiter, Saturn, and Uranus (and some of its satellites) was primarily driven by such remote sensing techniques.

Extinctive Stellar Occultations

Two categories of occultations exist, which is the extinctive and the refractive measurement. In both, radiation from a source is affected by physical processes in the

atmosphere, and measurements of the outgoing signals are used to retrieve atmospheric properties.

The principles of extinctive stellar occultations are similar to those of classical absorption spectroscopy. As shown in Fig. 2.2 a star is used as the light source, a spectrometer serves as the detector, and the atmosphere along the line-of-sight acts as the absorbing medium. The spectrometer is often mounted on a spacecraft, and thus called

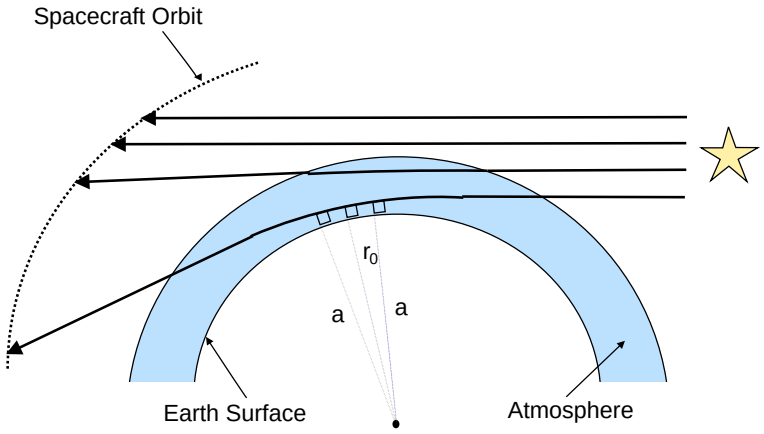

Figure 2.2. Stellar occultation geometry illustrating typical Envisat/GOMOS observations. Above the atmosphere rays coming from the star are straight lines. While the line-of-sight gets increasingly attenuated with decreasing heights, it also gets bended due to the higher air density. The tangent point radius is denoted by r_0 and a is the impact parameter, which is defined as the perpendicular distance between either of the ray asymptotes and the center of curvature.

space-borne, but may also be on the Earth's surface, on a balloon, or on an aircraft. Due to the fact that a satellite is outside the atmosphere, for limb-looking instruments the effective absorption path is double of that for nadir-looking sensors. The stellar signal passes through the atmosphere and is attenuated due to absorption or scattering by its constituents. Although the physical process involved is different, the net effect of extinction by scattering is equivalent to that by absorption. Absorption and scattering can be summarized by the term extinction. As the line-of-sight to the star moves deeper into the atmosphere, the light is, depending on the selected channel, progressively attenuated because the effective extinction path increases at the same time that the density of the extincting species changes. The ratio of the attenuated spectrum to the unattenuated spectrum, measured above the atmosphere, is referred to as the atmospheric transmission. The extinction cross sections of most species are wavelength dependent, thus spectral measurements of the transmission represent a measure of the relevant species.

The method of extinctive occultation is generally limited to high altitudes. Ozone and molecular oxygen absorb most of the UV radiation already at high altitudes before the signal could reach low atmospheric regions, thus giving low signal-to-noise ratio in the low stratosphere and troposphere. Atmospheric emissions (e.g., airglow) and ray bending are further limiting factors to high accuracy stellar occultation profiles at low altitudes. The separation from the stellar signal of radiation emitted into the ray path is not an easy task and must be treated carefully.

The opacity of the atmosphere in the visible and near infrared (NIR) is high in selected bands where the absorption coefficients are, due to a variety of electronic and vibrational processes, mainly related to water vapor and carbon dioxide. In the UV the opacity is chiefly due to the ozone layer in the upper atmosphere. In a spectral region where weak lines of the target species are obscured by much stronger lines of more abundant interfering species, the spectral resolution needs to be comparable to the width of the spectral line.

Refractive Stellar Occultations

Refractive stellar occultations occur because density gradients in the atmosphere lead to refraction, also called bending, of the incoming starlight. Signals are therefore following a curved path through the atmosphere. Measurements of the degree to which the path of the incoming starlight changes provide the bulk properties of the atmosphere (e.g., density, pressure, temperature). Already in 1904 the potential of refraction for studying planetary atmospheres was realized [*Pannekoek* (1904)], but it took almost fifty years that technology advancements allowed to verify the assumptions by useful observations.

The primary refractive stellar occultation technique is the photometric approach, which involves visible-light observations of the occultation of stars by a planetary atmosphere using ground, aircraft, or space-borne sensors. This approach has been first applied to the study of the atmospheres of other planets in our solar system. As a star passes behind a planet, light rays passing through deeper regions of the atmosphere are refracted more than rays at higher altitudes due to an increasing density. Incoming parallel light from the star is therefore diverged. On the sensor, the divergence appears as an attenuation of the light as a function of time. Photometric observations of this attenuation yield the so-called occultation light curve, which may be inverted to retrieve the atmospheric density, pressure, and temperature (cf. Section 4.5).

The first useful application of this technique was introduced by [*Baum and Code* (1953)], who determined the mean molecular weight of Jupiter's atmosphere from a stellar occultation. Since then numerous occultations of stars by other planets have been observed, and the technique has evolved into a powerful method for remotely probing planetary atmospheres.

Often, these photometric occultations yield light curves that exhibit rapid fluctuations in intensity. These fluctuations are caused by a refractive phenomenon known as scintillation (cf. Section 4.2), which arises from small-scale variations in the density profile. Such variations may be caused by atmospheric turbulence or by the presence of atmospheric waves. When combined with models of such variations, measurements of the scintillation have proven to be useful in retrieving small-scale atmospheric structures.

Refractive stellar occultations have been limited almost exclusively to the study of the other planets. The main reason for this is that the large distances involved allow for a greater separation of the diverging rays. Stellar intensity can therefore be measured more easily. At the same time, the choice of visible wavelengths for these occultations generally excludes the need to consider extinction of the starlight within the atmosphere itself.

However, the extinctive and refractive techniques are complementary, and a consideration of both processes allows for stellar occultation measurements to probe a larger altitude range more accurately than either one taken individually.

2.4.3 Orbit and Occultation Geometry

As we have seen in previous Sections, Earth orbiting satellites provide enormous possibilities for measurements on a global scale. Satellites have, depending on their scientific (or military) tasks, different orbit heights and different measurement geometries.

Geostationary satellites, for example, are orbiting at almost 36000 km over the equator, monitor the weather systems, and can provide information on tropospheric winds by tracking motions of clouds. The Meteosat Second Generation (MSG) satellite monitors a large portion of the Earth and their atmosphere from its position in geostationary orbit at 0° longitude.

Global satellite navigation systems typically operate at a Medium Earth Orbit (MEO) from almost 24000 km height above the Earth's surface. Europe's own global navigation satellite system Galileo, will be providing a highly accurate, guaranteed global positioning service under civilian control. It will be inter-operable with GPS and GLONASS, the two other global satellite navigation systems.

Another class of satellites, and for this work the far most important, are the so-called polar orbiting platforms. As a polar orbit one typically defines an inclination of nearly 90°. Satellites at a polar orbit complete up to 15 revolutions per day and thus measurements yield a good global coverage. The orbits are usually chosen to be phase-locked with the Sun, which is then called sun-synchronous. In a sun-synchronous orbit, each latitude is crossed twice at the same two local times.

Viewing Modes

Two viewing geometries are commonly in use. One system is known to be nadir viewing which means that instruments receive signals where the ray propagation is aligned parallel to the Earth's radius vector and look downward towards the Earth's surface. Nadir viewing measurements are used to capture radiation from a comparatively short path length of emitting gas, against the warm background of the Earth's surface and lower atmosphere, also emitting thermal radiation (e.g., the IASI instrument cf. Section 2.3).

The second viewing mode looks at the Earth's (or, e.g., planetary) limb with far longer path lengths along the line-of-sight. Measurements are made against the cold, in principle non-emitting, background space. The occultation geometry is shown in Fig. 2.3 for one bended ray. The Earth's radius is given by r_0, the impact parameter is denoted by a and the bending involved is expressed by the so-called total bending angle α. The impact parameter is defined as the perpendicular distance between the ray asymptote and the center of Earth. This states only for a spherically symmetric problem, where the equations for the ray geometry are much easier to solve. In the case of an ellipsoidal Earth model, the Earth center has no practical meaning and thus we introduce an expression for the center of curvature (or center of refraction) where we find a sphere being tangential to the Earth's ellipsoid. Spherical symmetry further implies that rays are lying in a plane (cf. [*Gorbunov and Sokolowsky* (1993)]).

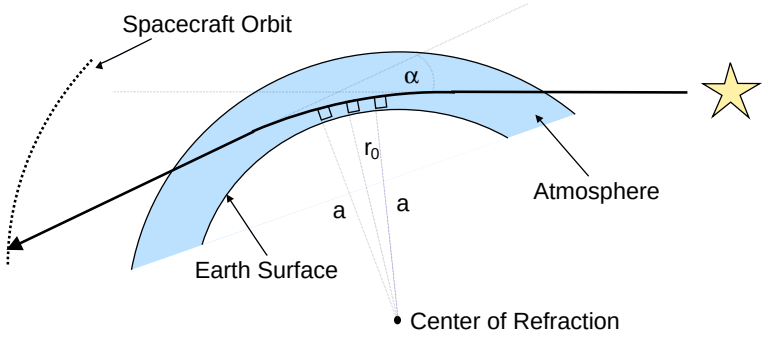

Figure 2.3. Ray bending where the corresponding angle is expressed by α.

In the approximation of geometrical optics for the propagation of electromagnetical signals, a ray passing through the atmosphere of varying refractive index n is determined by Fermat's principle of least time, where we want to find the minimum of an integral from n along the ray path. Locally we can apply Snell's law $n \sin \Phi = const.$ for rays changing their directions when going through a field of different refractive index, where Φ denotes the angle between the ray path and the gradient of the refractive index (cf. [*Born and Wolf* (1993)]).

3

The Envisat Polar Platform

3.1 History and Overview

Initially a Polar Orbiting Earth Observation Mission (POEM-1) was planned as a combined mission with instruments for scientific application, research, and operational meteorology. Planned to be the successor of ERS [*ESA* (2000)] it was designed for a polar platform. The development activities for the polar platform started in 1990, following the selection of the polar platform as a derivative of SPOT-4 (cf. http://spot4.cnes.fr, July 2004) by the council of the European Space Agency (ESA). At the Ministerial ESA council meeting in December 1993 POEM-1 was split into Envisat and METOP-1 [*Edwards and Pawlak* (2000)] and the development of the payload instruments for Envisat started. The information in this Section and Sections 3.2 and 3.3 was mainly drawn from [*ACRI S.A. et al.* (1998), *Bertaux et al.* (2001), *ESA* (2002)].

The Envisat satellite has an ambitious and innovative payload that will ensure the continuity of the data provided by the ERS satellites. Envisat data supports Earth science research and allows monitoring of the evolution of changes of the Earth's environment and climate. Furthermore, the data will facilitate the development of operational and commercial applications. Envisat is the so far largest satellite build within an ESA contract.

In March 2002, after several years of delay, an Ariane 5 heavy-lift launcher successfully injected Envisat (see Fig. 3.1), the advanced polar-orbiting Earth observation satellite, into its polar orbit. The satellite was lifted up to an altitude of around 800 km above the Earth's surface into a sun-synchronous orbit of 98.5° inclination and shall remain there operational for at least five years. The platform carries ten instruments on-board and provides measurements of the atmosphere, ocean, land, and ice. Amongst these instruments GOMOS, MIPAS, and SCIAMACHY (cf. Sections 3.3 and 3.2) are dedicated to the observation of physical and chemical processes in the Earth's atmosphere.

Another milestone in the story of a successful Envisat mission was achieved in spring 2003, when high rate data downloads from Envisat to its processing centers and to its

users was guaranteed in near real time. Artemis, the Advanced Relay Technology Mission, was brought to its assigned geostationary orbit after a 18-months recovery operation from an orbit far lower than intended. A new ion propulsion system, combined with innovative operations of its chemical thrusters raised the satellite to its nominal geostationary position at 21.5° East. Envisat transmits now about half of its sensor data in the Ka-band through Artemis straight to the Envisat data processing center at ESRIN, Italy, but data is also downloaded to the Envisat ground station and data processing centers in Kiruna, Sweden and Svalbard, Norway. The Envisat data downlink scenario was changed at the end of June 2004 in order to further increase the use of the Artemis data relay satellite. With Artemis, the Envisat data network has now been offered several important new capabilities.

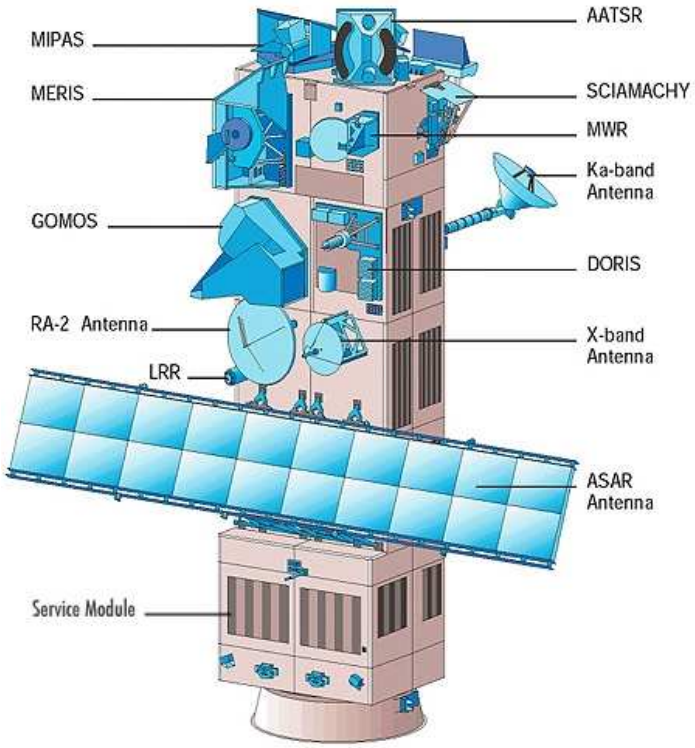

Figure 3.1. The Envisat satellite with all mounted instruments (http://envisat.esa.int, July 2004). The solar array is not shown.

The following list gives an overview of the Envisat instruments not to be discussed in more detail in Sections 3.2 and 3.3.

- **AATSR (Advanced Along Track Scanning Radiometer)**

  The prime scientific objective of the AATSR is to establish continuity of the ATSR-1 and ATSR-2 data sets of precise sea surface temperature (SST), thereby ensuring the production of an unique 10 year near-continuous data set at the levels of accuracy required (0.3 K or better) for climate research and for the community of operational as well as scientific users who have been developed through the ERS-1 and ERS-2 missions.

- **ASAR (Advanced Synthetic Aperture Radar)**

  The ASAR instrument, operating at C-band, ensures continuity with the image mode (SAR) and the wave mode of the ERS-1/2 AMI. It features enhanced capability in terms of coverage, range of incidence angles, polarization, and modes of operation. This enhanced capability is provided by significant differences in the instrument design: a full active array antenna equipped with distributed transmit/receive modules which provides distinct transmit and receive beams, a digital waveform generation for pulse chirp generation, a block adaptive quantization scheme, and a ScanSAR mode of operation by beam scanning in elevation.

- **DORIS (Doppler Orbitography and Radiopositioning Integrated by Satellite)**

  DORIS is a tracking system providing range-rate measurements of signals from a dense network of ground-based beacons. These data are precision processed on ground providing the satellite orbit with an accuracy of the order of centimeters.

- **LRR (Laser Retroreflector)**

  The LRR is mounted on a pillar attached to the nadir panel close to the RA-2 antenna. Its functions are a support-to-satellite ranging and the RA-2 altitude calibration. The LRR is a passive device which will be used as a reflector by ground-based SLR stations using high-power pulsed lasers.

- **MERIS (Medium Resolution Imaging Spectrometer)**

  The instrument MERIS measures the solar radiation reflected by the Earth, at a ground spatial resolution of 300 m, in 15 spectral bands, programmable in width and position, in the visible and near IR. MERIS allows global coverage of the Earth in 3 days.

- **MWR (Microwave Radiometer)**

  The main objective of the MWR is the measurement of the integrated atmospheric water vapor column and cloud liquid water content, as correction terms for the radar altimeter signal. In addition, MWR measurement data are useful for the determination of surface emissivity and soil moisture over land, for surface energy budget investigations to support atmospheric studies, and for ice characterization.

- **RA-2 (Radar Altimeter 2)**

  The RA-2 is an instrument for determining the two-way delay of the radar echo from the Earth's surface to a very high precision with less than a nanosecond. It also measures the power and the shape of the reflected radar pulses.

3.2 Atmospheric Chemistry Instruments

The understanding of actual atmospheric processes is of crucial importance to daily life and to future conditions on our home planet. The Earth's atmosphere cannot be seen as an isolated system, in contrary it interacts with the land mass, the ice sheets and the

oceans. Envisat accounts for that with three separated instruments covering complementary wavelength ranges, resolutions and observed parameters. GOMOS, MIPAS, and SCIAMACHY use different measurement techniques, which makes an intercomparison of results interesting. Possible special features in instrument design, measurement principles and retrieved quantities are highly transparent to the user of the end product. This Section introduces to the instrument design and the measurement principle of GOMOS and shortly outlines the MIPAS and the SCIAMACHY instrument.

3.2.1 GOMOS

The GOMOS instrument is of major importance for this thesis and thus discussed in a dedicated Section 3.3.

3.2.2 MIPAS

Like GOMOS the Michelson Interferometer for Passive Atmospheric Sounding (MIPAS) [*Fischer et al.* (2000)] is a complete new development. It is a Fourier transform spectrometer with a spectral range of 4.15 - 14.6 μm at a resolution of 0.2 nm for the measurement of high resolution gaseous emission spectra at the Earth's limb. One of the key features of the MIPAS instrument is the provision of measurements independent of solar illumination (day and night sensing) with a broadband coverage and high-spectral resolution ($\sim$ 60000 spectral data points). In the near to mid infrared many of the atmospheric trace-gases have important emission features and thus play a major role in atmospheric chemistry. The objective of MIPAS is the simultaneous and global measurement of geophysical parameters in the middle atmosphere. Stratospheric components like O_3, H_2O, CH_4, N_2O, and HNO_3 are determined. It enables the study of the chemical composition, the dynamics, and the radiation budget of the middle atmosphere. The horizontal resolution is found to be between 300 and 500 km along track. Another scientific goal of MIPAS is the measurement of precise temperature profiles. Thermal emissions in the infrared are very sensitive to temperature changes.

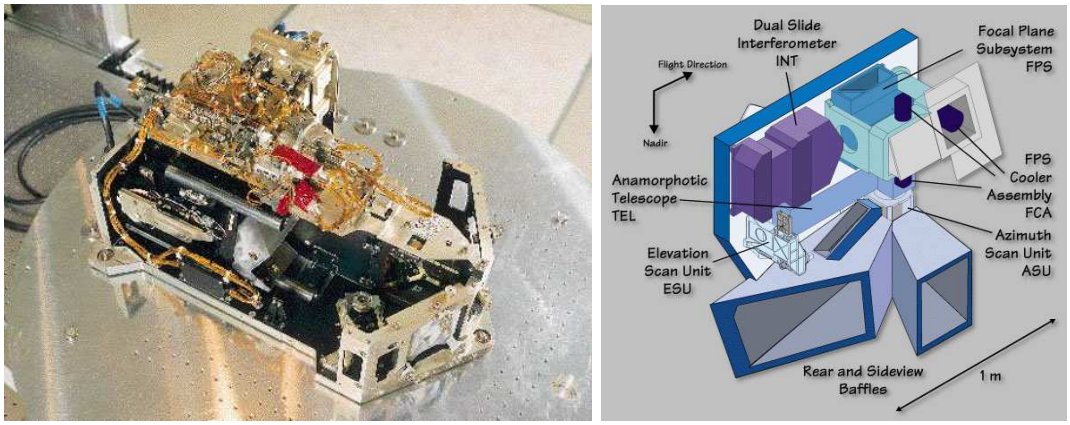

Figure 3.2. The MIPAS instrument with the optics module, installed at the anti-sunward extremity of Envisat (http://envisat.esa.int, July 2004).

3.2.3 SCIAMACHY

The instrument is designed and built as a joint German/Dutch project funded by the German (DLR, formerly DARA) and Dutch (NIVR) national space agencies, with a contribution from Belgium BIRA/IASB. SCIAMACHY the Scanning Imaging Absorption Spectrometer for Atmospheric Cartography [*DLR* (2000b)] is the enhanced successor of GOME [*DLR* (2000a)], which has been flying on ERS-2 since 21 April 1995. SCIAMACHY is designed to measure sunlight, transmitted, reflected, and scattered by the Earth's atmosphere or surface. Samples are taken in the ultraviolet, visible, and near infrared wavelength region from 240 - 2380 nm at a spectral resolution of 0.2 nm - 1.5 nm.

The nadir and limb viewing strategy of SCIAMACHY yields total column values as well as profiles for trace gases and aerosols in the stratosphere. Additionally, this enables estimates of global trace gas and aerosol content and distribution in the lower stratosphere and troposphere. With different viewing geometries the absorption, reflection and scattering characteristics of the atmosphere are determined by measuring the extraterrestrial solar irradiance and the upwelling radiance. The ratios of such irradiances and radiances are inverted into profiles of densities and distribution of atmospheric constituents such as O_3, NO_2, H_2O, N_2O, CO, CO_2, CH_4, ClO, OClO, BrO, H_2CO, SO_2, and aerosols, known to absorb or scatter light, as well as the reflectance of the Earth's surface. Furthermore pressure and temperature profiles as well as the cloud cover and the cloud top height are determined.

In nadir mode, the global distribution of total column values of the atmospheric trace gases and aerosols are observed. In this mode, the instrument is scanning across-track, with a swath width of 500 km with respect to the sub-satellite track. To obtain the altitude distribution of trace gases, SCIAMACHY performs observations in limb over an altitude range of 100 km, with a vertical resolution of 3 km. Starting at Earth's horizon, the atmosphere is scanned tangentially over a 1000 km wide swath. After each azimuth scan, the elevation is increased until the maximum altitude of 100 km is reached.

The measurements obtained from SCIAMACHY enable the investigation of a wide range of phenomena which influence atmospheric chemistry. Biomass burning, pollution, arctic haze, forest fires, dust storms, industrial plumes, and measurements in the stratosphere such as ozone chemistry, volcanic events, and solar proton events are recorded. The MIPAS and SCIAMACHY instruments simultaneously show how CFCs and other trace gases make their way up from the lower troposphere across the boundary of the stratosphere.

3.3 The GOMOS instrument

The Global Ozone Monitoring by Occultation of Stars instrument [*ACRI S.A. et al.* (1998), *Paulsen* (2000), *ESA* (2002)] is a completely new developed tool to investigate the Earth's atmosphere. It exploits stellar occultation in the ultraviolet, visible and the near infrared bands. GOMOS was first proposed in 1988 as an *Announcement of Opportunity* instrument dedicated to be a part of the Earth Observation Polar Platform Mission (cf. Section 3.1), the former name of Envisat. In 1992 it was decided that GOMOS will be developed as an ESA-funded instrument.

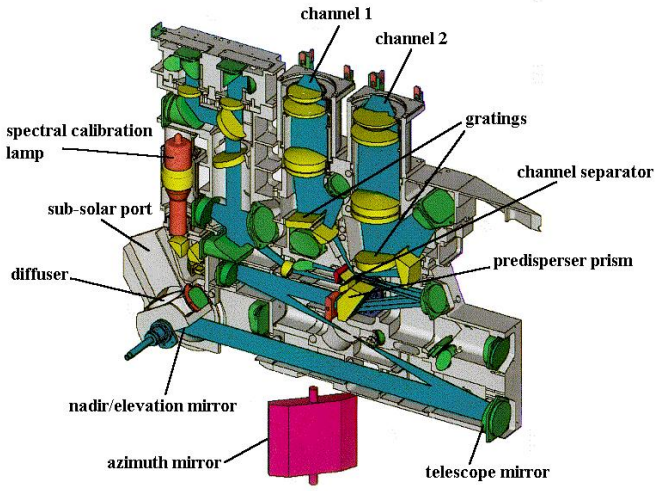

Figure 3.3. The SCIAMACHY instrument (http://www-iup.physik.uni-bremen.de, July 2004).

3.3.1 Scientific Objectives

Atmospheric chemistry is one of the key targets of the Envisat mission. Besides MIPAS and SCIAMACHY, GOMOS is an important instrument for ozone monitoring. Since there are about 400 stars to be used as light source, the stellar occultation technique has the potential to provide much more complete spatial coverage than available from solar occultations. Measurements at almost all latitudes are possible, even though the Envisat satellite has a polar sun-synchronous orbit.

The key scientific objective of the GOMOS instrument is the long-term monitoring of stratospheric and mesospheric vertical ozone distribution with global coverage, high vertical resolution, and long-term stability. In order to provide a seamless data stream to analyze the global ozone budget, GOMOS has a designated successor termed COALA (Calibration of Ozone through Atmospheric Limb Acquisitions). The COALA instrument, a smaller version of GOMOS, is presently being studied for operational ozone profile trend observation that uses the stellar occultation principle. Because of the good global coverage, GOMOS and COALA could prove to be the preferred solution for ozone profile monitoring.

The GOMOS ozone trend observations help to determine the degree of ozone loss in the Arctic under different meteorological conditions. An increased amount of data for determining ozone trend analysis can be used to monitor indicators for a beginning of expected recovery in ozone. As pointed out in the Section 1.4.1, nitrogen compounds, such as NO_2 and NO_3, play important roles in the chemistry relevant to ozone. The observations of NO_2 and NO_3 address, e.g., the abundance of lower stratospheric NO_2 (varies with aerosol loading) and the degree of denoxification/denitrification in Arctic winter as well as availability of NO_2 to deactivate ClO. Future NO_x observations are furthermore relevant to the ozone recovery. As NO_x dominates ozone loss on a global scale, NO_x observations are important to interpret ozone changes as halogens decrease.

Besides nitrogen compounds, the GOMOS instrument also observes OClO and BrO, key species in the polar ozone depletion processes (cf. Section 1.4.1). They can pos-

Figure 3.4. Artist impression of the GOMOS instrument (left panel). The GOMOS instruments before transportation from Matra Marconi Space in Toulouse to the test facility in Liege. The instrument is mounted on a stand with the optical unit on the top and the instrument electronic panel below, in basically the same configuration as on the spacecraft (right panel) (http://envisat.esa.int, July 2004).

sibly be detected with GOMOS if their concentrations increase. The measurement of aerosol extinction is an additional objective. Aerosols are known to provide surfaces for heterogeneous reactions, which can strongly affect the partitioning of chlorine and nitrogen compounds.

The observation of water vapor, another atmospheric key species measured by GOMOS, is fundamental to the budget of many trace gases in the stratosphere. It is therefore important to determine its three-dimensional distribution and long-term trends. Water vapor is measured in a NIR band. A second NIR band is dedicated to the retrieval of O_2 profiles. The O_2 measurements allow to relate all measurements of, e.g., ozone density to the air density to yield a mixing ratio, which is a quantity used in models. O_2 is a perfectly mixed gas and the air can be assumed to be in hydrostatic equilibrium. Therefore, its scale height is directly connected to the atmospheric temperature. Temperature and air density profiles are furthermore essential parameters for atmospheric dynamics, including the mixing of gases. The measurement of temperature is moreover needed for supporting the primary mission objective, ozone monitoring. The ozone cross-sections in the Huggins band are strongly dependent on the atmospheric temperature. Therefore, a long-term variation of UV absorption might be due to a temperature variation and could be wrongly attributed to an ozone variation. Complementary to this, a high-resolution temperature profile (cf. [*Theodore et al.* (2004)]) can be retrieved from atmospheric scintillations, which will be measured using two fast photometers sensitive in the blue and red, respectively.

3.3.2 Basic Instrumental Characteristics

The sensor provides data on trace gases such as ozone, NO_2, NO_3, BrO, OClO, as well as O_2 and water vapor. A special instrument design makes it possible to measure reference atmospheric profiles under dark, bright and twilight limb conditions obtaining very good global coverage with about 300 high-quality profiles per day and a minimum height resolution of about 1.7 km. GOMOS records the transmission of radiation passing the atmosphere along a path from the star to the instrument. The so-called

Band	Wavelength	Resolution	Main Usage
UV	250 - 375 nm	1.2 nm	O_3, NO_2, NO_3, OClO, BrO, Aerosol
VIS	405 - 675 nm	1.2 nm	O_3, NO_2, NO_3, OClO, BrO, Aerosol
IR 1	756 - 773 nm	0.2 nm	O_2, temperature
IR 2	926 - 952 nm	0.2 nm	H_2O
Photometer 1	470 - 520 nm	50.0 nm	turbulence, scintillations, temperature
Photometer 2	620 - 700 nm	50.0 nm	turbulence, scintillations, temperature

Table 3.1. Wavelength ranges and main usage of channels for the Envisat/GOMOS instrument [*ESA* (2002)].

spectrometer A measures ozone, NO_2, NO_3, BrO, and OClO within a wavelength range from 250 - 675 nm and provides a resolution of 1.2 nm. The spectrometers B1 and B2 are sensitive within 756 - 773 nm and 926 - 952 nm, respectively, with 0.2 nm resolution, and are designed to measure O_2 and water vapor (cf. Tab. 3.1 and Tab. 3.2). GOMOS, once fixed on a star, measures transmitted stellar light. During a setting event, due to the motion of the satellite, the line-of-sight descends through the atmosphere, while the signal gets increasingly attenuated.

The instrument ensures high data quality obeying the principle of selfcalibration (normalized intensities), wherefore instrumental long-term drifts can be largely neglected. GOMOS faces other problems due to the fact that the measured stellar light is occasionally a subject to perturbations from other light sources. Scattered solar light under bright limb conditions, lunar radiation or light coming from auroral emissions into the atmosphere may dominate the stellar signal, which in turn makes an estimation of such radiation indispensable. Also signal scintillations due to the turbulent atmosphere can be challenging and have to be estimated properly. The main spacecraft resource requirements of the instrument are shown in Tab. 3.3.

A special frame-transfer CCD has been developed to meet the needs of the GOMOS mission. This is a low-noise and radiation-hardened CCD sensitive from UV to NIR with the main requirements and the resulting technological and design choices summarized in Tab. 3.4. The performance of the CCD puts a technical constraint on the selection of the star signal, which has to be a stable flux at visual magnitude brighter than 5 with a star temperature range of favorably 3000 - 30000 K. By observing about 30 stars per orbit GOMOS can produce as much data daily as 360 separate ground stations.

Apart from the two spectrometers GOMOS is equipped with two fast photometers (1 kHz sampling) which account for measuring fast scintillations in the atmosphere. As a side product, but now reviewed for the next few months, photometer data can be used to get high resolution temperature profiles (HRTP) via time delay measurements of the red and the blue photometer lines.

The high sensitivity requirement down to 250 nm has been a significant design driver leading to an all-reflective optical system design for the UVVIS part of the spectrum and to functional pupil separation between the UVVIS and the NIR spectral regions, but no dichroic separation of UV was done. Due to the requirement of operating on very faint stars down to magnitude five, the sensitivity requirement to the instrument is very high. Consequently, a large telescope with 30 cm $\times$ 20 cm aperture had to be used to collect sufficient signal, and detectors with high quantum efficiency and very low noise had to be developed to achieve the required signal-to-noise ratios. In addition, a

Requirement description		Design driver for
Occulting stars characteristics	Visual magnitude range: -1.6 $\leq m \leq$ 4 for stars with 30000 K and 3000 K temperature respectively	• High sensitivity and dynamic range requirements for the star tracker • High sensitivity and dynamic range spectrometer detectors (especially in the UV) • Large telescope and high transmission optics needed to collect sufficient signal from the faint stars
Spectral range of the spectrometer	UV: 250 - 375 nm UV: 405 - 675 nm IR 1: 756 - 773 nm IR 2: 926 - 952 nm	• Wide spectral range, high transmission optics • Functional pupil separation between UVVIS and NIR • Very strict contamination control to avoid UV sensitivity degradation • Broadband sensitive and low noise detectors with high sensitivity in the UV • High NIR sensitivity
Spectral sampling	UVVIS: 0.3 nm IR: 0.05 nm	• Large sensors ($\sim$ 2500 used pixels on four sensors each 1500 pixels wide) • High dispersion, high efficiency gratings
Spectral resolution	UVVIS: 1.2 nm IR: 0.2 nm	• High imaging quality optics • Very high pointing system stability requirements
Spectral stability knowledge in dark limb	UVVIS: 0.07 nm IR: 0.016 nm	• Star tracker and pointing system
Photometer spectral windows and sampling rate	PM1: 470 - 520 nm PM2: 650 - 700 nm 1 kHz sampling rate	• Fast (1 kHz), high sensitivity detectors
Short term radiometric stability	1%	• Spatially uniform detectors and very high pointing stability
Linearity	1%	• High detector and electronic chain linearity (very challenging for the extremes of the dynamic range)
Pointing stability	Better than 40 μrad peak to peak	• High speed, high accuracy closed-loop pointing system
Number of occultations per orbit	45 on average, e.g., approximately 920000 occultations during planned mission	• Challenging requirement for the star pointing mechanism in terms of long term performance and reliability
Angular coverage	–10° - +90° with respect to the flight direction. Thus, large instrument angular range observability	• Large total angular travel range for the mechanism

Table 3.2. Instrumental properties of GOMOS (http://envisat.esa.int, July 2004).

Property	Value
Instrument mass	175 kg
Instrument power consumption	200 W
Data rate to satellite	226 kbit/s

Table 3.3. Main spacecraft resource requirements for the GOMOS instrument [*ESA* (2002)].

Parameter	Requirement	Selected technology
Spectral range	250 - 952 nm	Thinned, backside illuminated, anti-reflection coated CCD
Quantum efficiency	250 - 350 nm: 20% 500 - 675 nm: 60% 952 nm: 20%	See above
Dark current at 20° C	< 25 pAcm^{-2}	Inverted mode operation (MPP)
Linearity	better than 0.5%	Special design of the output stage
Geometrical design of the CCD	2×143 lines and 1353 columns with 20×27 μm pixels	

Table 3.4. Technical parameters of the GOMOS CCD, its requirements, and the selected design (http://envisat.esa.int, July 2004).

slitless spectrometer design had to be chosen, in order to use the entire star signal. For this reason a high performance pointing system is used to keep the star image fixed at the input of the spectrometers in order not to degrade the spectral resolution and the spectral stability. Achieving a high signal-to-noise ratio when observing the very weak star signal embedded in strong surrounding atmospheric background and stabilizing the star image in spite of the satellite disturbances, were major engineering challenges for the GOMOS design.

3.3.3 The Telescope and the Optics

The telescope, the optics, all sensors, and their associated front-end electronics are mounted on a thermally controlled optical bench. This telescope and optical bench assembly (TOBA) and the steering front mechanism (SFM) are mounted via a GOMOS-interface structure (GIFS) to the spacecraft. The entire spacecraft and the external GOMOS instrumentation, the so-called optomechanical assembly (OMA), is covered by an optomechanical cover responsible for protecting the instrument from light, coming from a different direction other than the defined angular range, and for ensuring a stable, defined thermal environment. The OMA is connected to the instrument electronics consisting of the sensor detection electronics, the redundant instrument control unit, and the redundant mechanism drive electronics in the payload equipment bay of the satellite via a dedicated harness. An overview of the optical design of GOMOS is shown in Fig. 3.5.

An optical beam dispatcher (OBD) splits the light coming from the telescope and provides the signal for the UVVIS and NIR spectrometers and the two redundant star trackers. The signal collected by the NIR subpupil is subsequently dichroically split between the NIR spectrometer and two photometers. A two-stage steering front mechanism moving a 40 cm $\times$ 30 cm flat mirror is used to point the line-of-sight

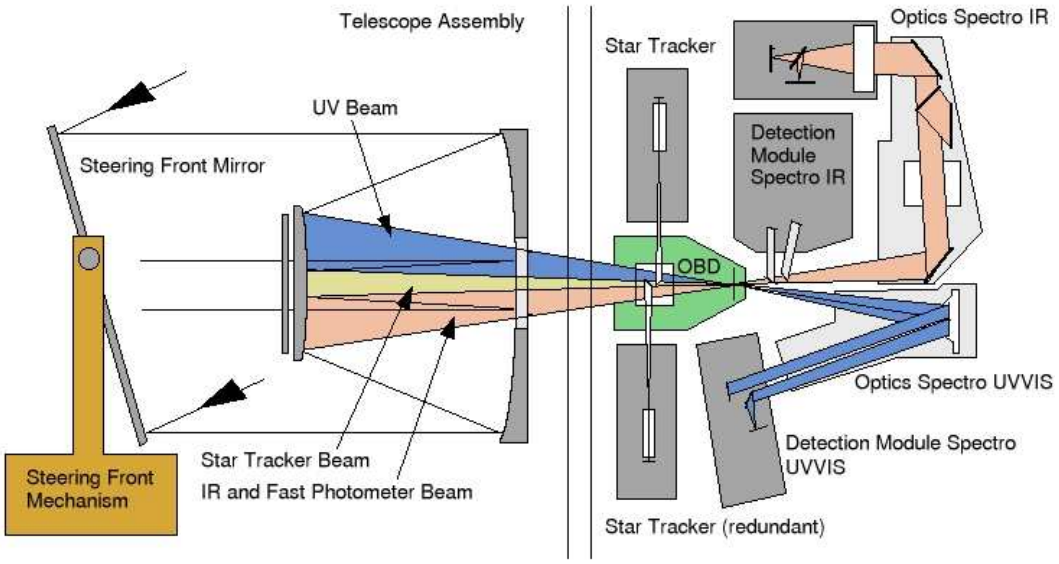

Figure 3.5. An overview of the GOMOS telescope and optical beam assembly (TOBA). The optical design is based on a telescope which bundles incoming light for the optical beam dispatcher (OBD). The OBD splits the signal and feeds the UVVIS spectrometer, the IR spectrometer, the two photometers channels as well as the nominal and the redundant star tracker (http://envisat.esa.int, July 2004).

towards the selected star and to track it with very high accuracy as it sets through the atmosphere. A coarse steering mechanism, in azimuth only, steers the mirror coarsely towards the occulting stars within a 100° angular range, while an azimuth and elevation fine-steering mechanism with a range of approximately 4° is performing the acquisition, centering, and tracking of the star as it sets through the atmosphere.

The azimuth coarse-pointing mechanism is using a ball-screw drive, while the fine-steering stages are using voice-coil actuators. The fine-steering stages, together with the mirror, are inertially mounted so that spacecraft microvibrations are not transmitted to the line-of-sight. Additionally, electrodynamical dampers are used for microvibration damping. The control bandwidth of the mirror is approximately 5 Hz. The main requirements, together with the resulting technological and design choices, are summarized in Tab. 3.5.

The science data electronics (SDE) is the CCD sensor control and signal conditioning unit. It controls a total of eight CCDs (two for the UVVIS spectrometer, two for the NIR spectrometer, two for the fast photometers, and two for the nominal and for the redundant star tracker). This unit has a high degree of programmability.

During the star occultation measurement, three bands of the spectrometer CCDs are read out. They contain the star, the upper, and the lower background spectrum. The typically seven lines of these bands are binned out in the output register of the CCD before reading. The position, the width, and the separation of these bands are all programmable. This gives a high degree of flexibility in optimizing the detection performance to specific observation objectives. During specific monitoring modes, the CCDs are read out in unbinned mode, and the integration times are programmable between 0.25 s and 10 s.

Parameter	Requirement	Selected technology
Angular range (optical)	100°	Two-stage (coarse + fine) design
Open loop pointing accuracy	better than ±0.02° bias and ±0.01° dynamics	High resolution Inductosyn angular sensors (1 LSB = 0.0009°)
Torque (acceleration) resolution	5 μNm	Voice-coil actuators together with high linearity electronics
Microvibration rejection	3 μrad residual above 10 Hz	Three-axis, frictionless mirror mounting
Number of angular travel cycles	$> 1.5\times10^6$ of 70° average	

Table 3.5. The requirements and the technical realizations of the steering front mechanism (SFM). The mirror can move within an angular range of 100°, from –10° - +90°, for coarse and fine steering (http://envisat.esa.int, July 2004).

The sequencing of the star tracker CCD is adapted dynamically to the different phases of star detection, centering, and tracking as follows. In the initial phase of star detection, the SDE detects the coordinates of the most-illuminated pixel of the CCD using a programmable integration between 5 ms and 50 ms, depending on the star magnitude. As soon as the star has been detected, a 10 × 10 pixel window centered around the star is read out with programmable integration times between 5 ms and 10 ms. This window follows the star as the tracking system centers the star in the field of view. As soon as the star is centered, the read out window collapses to 8 × 8 pixels and the read out frequency is set to 100 Hz with 5 ms or 10 ms integration times. The analog signal conditioning consists of low noise, programmable gain channels. The analog to digital conversion is done with 12 bit ADCs.

The GOMOS telescope has a rectangular aperture of 30 cm × 20 cm. It has to operate in a 0.6° field of view and has to have very good transmission in the 250 - 952 nm range. The small allowable volume (inter-mirror distance < 250 mm) coupled with high-quality imaging and stability requirement, and coupled with the high stiffness requirement (first eigenmode above 180 Hz) were very challenging. A Cassagrain design based on aspheric primary and secondary mirrors, and based on a carbon fiber reinforced plastic (CFRP) structure has been chosen. The main telescope requirements, together with the resulting technological and design choices, are summarized in the Tab. 3.6.

3.3.4 Operational Modes

The main mode of operation of GOMOS is the occultation mode. During this mode the instrument is, as a result of a macrocommand, autonomously acquiring and tracking stars as they set through the atmosphere. The sensors are operated in binning mode for the star band and for the upper and lower background bands. The width and the separation and position of these bands can be programmed. In this way optimum alignment can be ensured over the instrument lifetime and the signal-to-noise ratio can be optimized. The occultation mode has a specific submode called fictive star submode. In this submode the instrument is scanning the limb along a programmable

Parameter	Requirement	Selected technology
Field of view	0.6°	Cassagrain design
Optical transmission	> 82% between 250 nm and 500 nm > 92% between 500 nm and 952 nm	Al coated UVVIS subpupil and Ag coated NIR subpupil
Intermirror distance stability	better than 10 mm	coefficient of thermal expansion and coefficient of moisture expansion compensated CFRP structure
Imaging quality	UVVIS: 25 mm @ 85% encircled energy NIR: 30 mm @ 85% encircled energy	Cassagrain design with aspheric primary and secondary mirrors

Table 3.6. The technical requirements of the GOMOS telescope (http://envisat.esa.int, July 2004).

trajectory as if a star was present. This submode can be used for limb sounding under bright limb conditions. In addition to the occultation mode, the GOMOS design supports three other modes, called monitoring modes, which enable in orbit monitoring and recalibration of important instrument performance parameters used in the ground processing. These monitoring modes are listed in more detail in Tab. 3.7.

GOMOS Mode	Description
The uniformity mode	The CCD sensors are read out in a non-binned, i.e., pixel by pixel, mode. Depending on weather, the instrument is pointed towards dark space or towards uniform limb, the dark current or the photoresponse uniformity of the CCD sensors is characterized. In this mode the tracking function is disabled. The spectrometer integration time is programmable in the range of 0.25 s to 10 s.
The spatial spread mode	The instrument operates as in the uniformity mode, but with the tracking function active. Thus, the optical transfer function of the instrument can be monitored in this mode by observing a star outside the atmosphere.
The linearity mode	The sensors are operated in binned mode as in occultation mode but with variable integration times (in the range 0.25 s to 10 s). This mode is used to monitor the linearity of the detection chains during the instrument lifetime by observing stars outside the atmosphere with variable integration times.

Table 3.7. The GOMOS monitoring modes which exists besides the nominal occultation mode used for probing the star signals [*ESA* (2002)].

3.3.5 The GOMOS Star Catalogue

The star catalogue contains information related to all the stars of the general Hipparcos star catalogue up to visual magnitude $m_v = 4.5$ (898 stars), 7 planets (Mercury, Venus,

Mars, Jupiter, Saturn, Uranus, Neptune), the Moon, and a set of dark areas. The Level 1b processing only uses a few variables written in the star catalogue (cf. Tab. 3.9). Tab. 3.8 shows a list of actually measured stars with $0 \leq m_v \leq 4$. In our analysis of GOMOS measurements we only used data correspondent to signal occultation by stars listed in Section C.2.

Magnitude	**Number of Stars**
$m_v \leq 0$	4
$0 < m_v \leq 1$	11
$1 < m_v \leq 2$	34
$2 < m_v \leq 3$	120
$3 < m_v \leq 4$	340

Table 3.8. Number of stars with appendant visual magnitudes m_v to be selected by the GOMOS instrument [*ESA* (2002)].

GOMOS Star Catalogue Information
Number of targets in the Star Catalogue
Star identifier number in the GOMOS catalogue
Right ascension decimal degrees (J2000)
Declination decimal degrees (J2000)
Visual magnitude
Type of variability (information added to the star name)
Parallax
Proper motion in right ascension
Proper motion in declination
Radial velocity
Star name in the BSC catalogue
Effective temperature

Table 3.9. The GOMOS star catalogue description and information included in the level 1b data processing (http://envisat.esa.int, July 2004).

3.3.6 The GOMOS Products

Like for all instruments on Envisat, the GOMOS products are grouped due to their processing levels and labeled as follows.

- **Level 0:** Time corrected raw measurement data
- **Level 1b:** Geolocated calibrated engineering data
- **Level 2:** Geophysical products

Level 1b and level 2 data are here given in a more detailed list (cf. Tab 3.10) as they were processed by our retrieval scheme.

Product	Product Description
GOM_TRA_1P	Geolocated Calibrated Transmission Spectra
GOM_LIM_1P	Geolocated Calibrated Background Spectra (Limb)
GOM_NL__2P	GOMOS Temperature and Atmospheric Constituents Profiles
GOM_EXT_2P	GOMOS Residual Extinction
GOM_RR__2P	GOMOS Extracted Profiles for Meteo Users

Table 3.10. GOMOS level 1b/2 data products in detail as processed by our retrieval scheme [*ESA* (2002)].

Level 0 Products

The GOMOS level 0 data splits into two products each containing data for a full orbit. One product is for nominal occultation instrument operation, where sensor data is recorded and the other when GOMOS is switched into calibration mode. In calibration mode the instrument acquires data which is needed for gaining operational parameters.

Level 1b Products

Level 1 data is divided into level 1a and level 1b products. Level 1a is data coming from level 0 after being sorted and filtered by low-level quality checks. The basic product of the level 1b processing is the atmospheric transmission in the UVVIS and near IR. Stellar occultation with GOMOS provides self-calibrated data where slow changing radiometric drifts can be removed, though several other effects have to be taken into account separately. The level 1b processing also includes the correction for instrumental effects such as CCD dark charge, cosmic rays, nonlinearity, and straylight. Furthermore the stellar light has to be separated from the limb and a precise geolocation of the measurements with the knowledge of the corresponding refractivity is achieved. Tab. C.1 summarizes the data acquisition of the level 1b processing stage. The sampling rate of 2 Hz for the reference atmospheric profiles and errors corresponds to a minimum vertical resolution of 1.7 km depending on the obliquity of the measurement. In the level 1b data processing several operations are performed and listed below.

- **Reference star spectrum**

  The spectrum is obtained once per occultation by averaging five spectra obtained at the beginning of the occultation. The averaging ensures a low noise level which can be further improved by including more spectra. The acquisition of the star spectrum may encounter some problems due to the absorption of light by noctilucent clouds between 80 and 85 km tangent height. Auroral emission may contribute to the star spectrum measurement as well.

- **Reference atmospheric profile**

  The profile is retrieved from meteorological analysis of ECMWF data and combined with MSISE90 profiles. The computation of the refracted ray path is performed with a 2 Hz sampling where the combined atmospheric profiles serves as background information.

- **Full transmission spectra and covariance**

  With a 2 Hz sampling the transmission profile from each height is divided by the reference star spectrum. The transmission output in the level 1b product is termed as full product with several correction effects lacking. Such effects are the scintillation, the dilution, and the chromatic refraction which are identified in the level 2 data processing. In this thesis these corrections are performed as well (cf. Section 4.2) in order to ensure an optimal retrieval performance. In the level 1b processing each spectrum is re-sampled on the wavelength pixel grid of the reference star spectrum. The covariance, which is the variance of each pixel signal, is computed from the analysis of the signal-to-noise ratio (SNR).

- **Central background estimate and error**

  This is the estimated background contribution, measured with 2 Hz sampling, to the total signal in the central band which was subtracted to yield the pure stellar signal.

- **Photometers data and error**

  The photometer data is sampled with 1 kHz and is the count of measured electrons coming from the CCD. The signal can be used to correct for scintillation effects, as well to retrieve high resolution (40 Hz) temperature profiles (HRTP). Figs. 3.9 and 3.10 show two examples of photometer data for a bright star in dark limb condition with a good quality signal and a dim star in bright limb condition with decreased signal quality.

- **SFA angle measurements**

  The SFA data is the angle in elevation and azimuth where the star image is captured. The mirror moves with a sampling rate of 5 Hz and provides a coarse tracking of the star image.

- **SATU data**

  With 100 Hz sampling rate the star images is kept inside the center position of the mirror. The SATU therefore enables to find the pointing error as well as to determine where the signal of different wavelengths hit the mirror.

- **Wavelength assignment of the spectra**

  For a given measurement of the transmission the wavelength is read from the center of each pixel with 2 Hz sampling.

- **Geolocation and error**

  The position of Envisat and the position of the tangent point along the line-of-sight is sampled with 4 Hz.

- **Limb product**

  This product measures the background with 2 Hz sampling. The profile is derived by two external bands of the CCD, representing a corrected and an uncorrected measure for straylight.

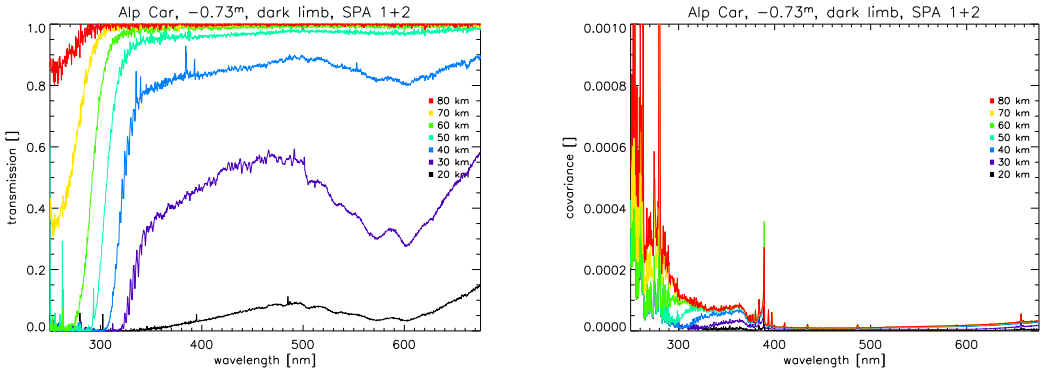

Figure 3.6. Real transmissions and covariances from GOMOS level 1b data. The spectrometer A covers the wavelength range from 250 - 650 nm, which serves as input for the retrieval of ozone, NO_2, NO_3, OClO, and BrO.

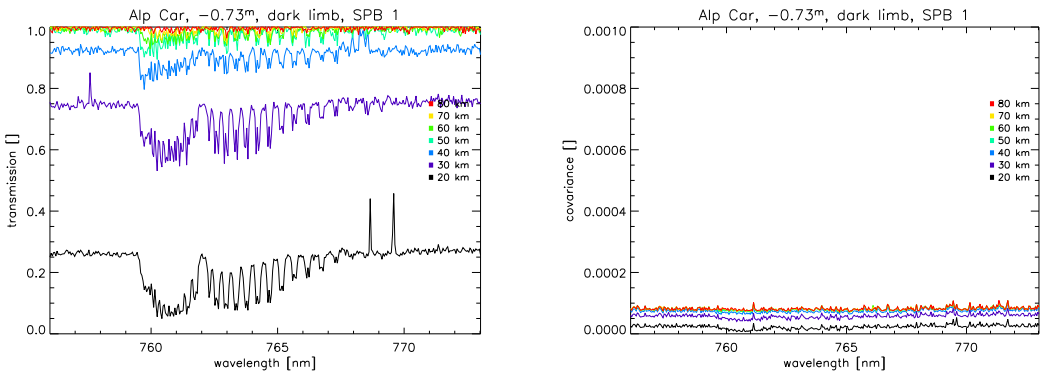

Figure 3.7. Real transmissions and covariances from GOMOS level 1b data. The spectrometer B1 covers the wavelength range from 756 - 773 nm, which serves as input for the retrieval of O_2.

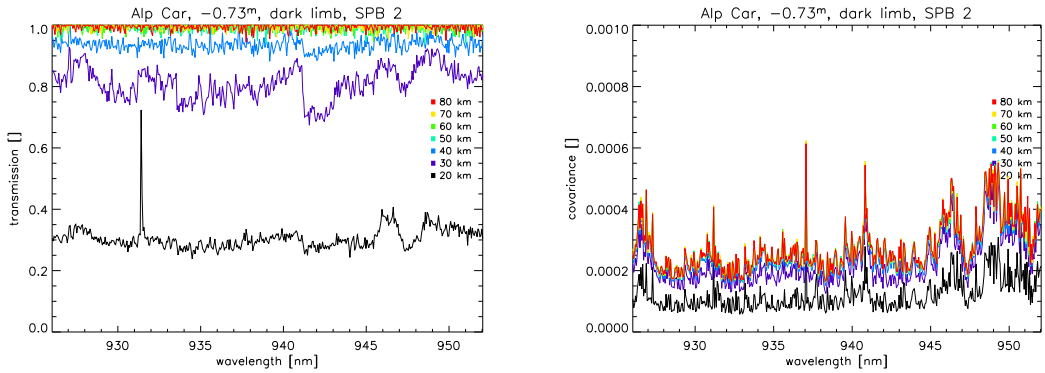

Figure 3.8. Real transmissions and covariances from GOMOS level 1b data. The spectrometer B2 covers the wavelength range from 926 - 952 nm, which serves as input for the retrieval of water vapor.

As listed in Tab. C.1 the level 1b data product contains, as major information, transmission and covariance profiles from spectrometer A and B (see Figs. 3.6, 3.7, and 3.8), which are used to retrieve the target species of the GOMOS mission.

Before a measurement can be taken, a nominal wavelength assignment is carried out by using auxiliary calibration data and then the spectral shifts in the CCD, caused by vibrations and imperfect tracking, are identified by incorporating 100 Hz SATU star tracker data. Fig. 3.11 is showing SATU data for two different stars with different magnitudes (-1.44^m and 2.36^m) under dark and bright limb conditions. The accuracy in the high stratosphere for the tracking of dim stars is significantly degraded to errors of $\sim$2 μrad, whereas bright stars are tracked within $\sim$1 μrad. In the low stratosphere and down to the upper troposphere the star tracking accuracy is further decreased due to increasing atmospheric turbulence and scintillation effects. The error can reach values of $\sim$30 μrad.

Level 2 Products

- **Line density product**

  Coming from the spectral inversion, the integrated line density product is delivered for ozone, NO_2, NO_3, O_2, H_2O, and air. It is a best fit to the spectral transmission. Line densities may be directly used for level 3 products (not provided by ESA) such as ozone and NO_2 trend profiles, having a major scientific impact.

- **Local density product**

  Under the assumption of a local spheric problem, this is the output of the vertical retrieval of line densities.

- **Aerosol product**

  The aerosol density is a special product in that sense that the extinction wavelength dependence may vary during one occultation. For each measured transmission an extinction coefficient at a reference wavelength is computed and also

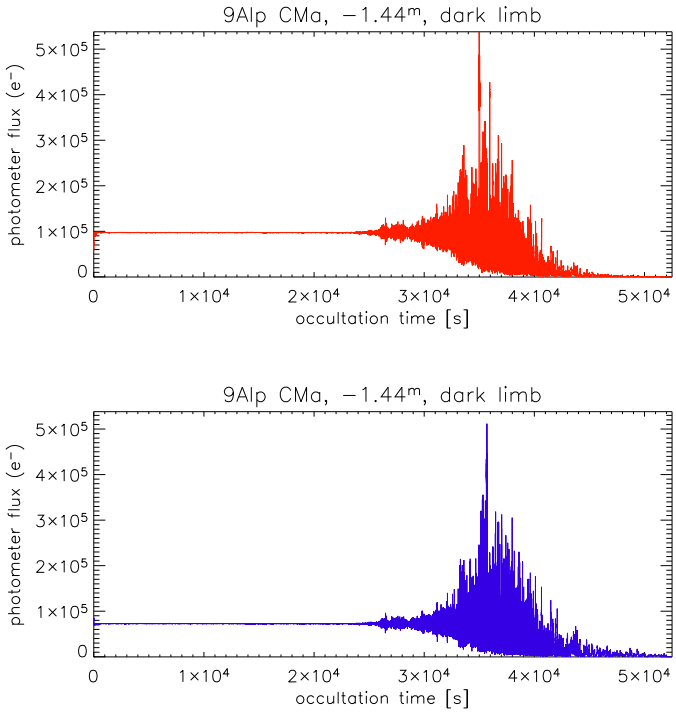

Figure 3.9. Red and blue GOMOS photometer lines for a bright star (-1.44^m) in dark limb conditions. The red signal (upper panel) has a higher photometric flux than the blue one (lower panel).

the three coefficients of a second degree polynomial fit. The optical thickness is given at the reference wavelength and with the three coefficients the calculation of the optical thickness at all wavelengths is enabled.

- **Turbulence product**

  For the analysis of the two fast photometers the tangent altitude of the line-of-sight is retrieved as well as the vertical profiles of density, pressure, and temperature with 40 Hz sampling rate. The turbulence product is gained by the time delay analysis of the peaks of the red and blue photometer line which is then converted into refraction angles (cf. [*Theodore et al.* (2004)]).

- **Geolocation and atmospheric product**

  The geolocation data is gained as explained for the level 1b data product. With pressure and temperature, here two additional profiles are stored, one coming from external sources and the other one derived by GOMOS algorithms.

- **Accuracy estimate product**

  For the spectral inversion the χ^2 is given. The 12 × 12 matrix corresponds to six atmospheric gas species, five aerosol parameters and one spare matrix element. The vertical inversion, including an additional covariance matrix, denotes the vertical correlation of products.

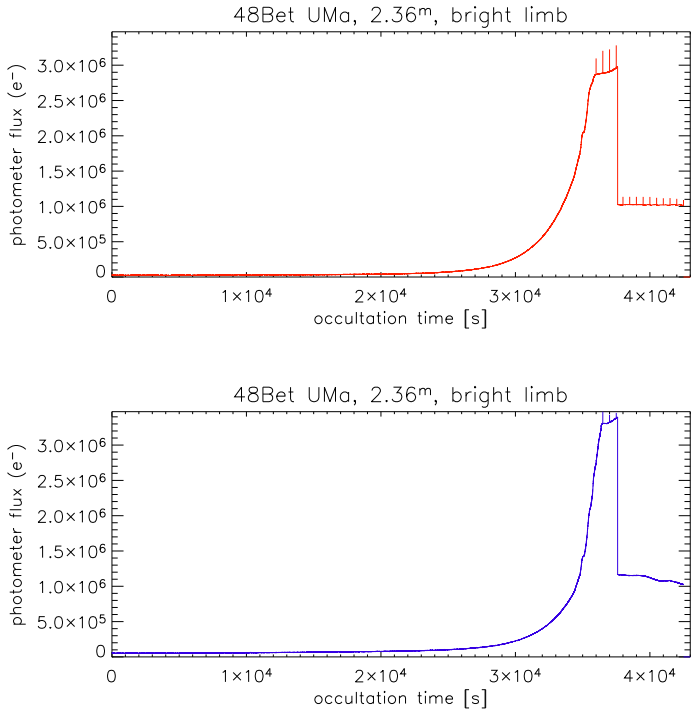

Figure 3.10. Red and blue GOMOS photometer lines for a dim star (2.36^m) in bright limb conditions. The red signal (upper panel) has a higher photometric flux than the blue one (lower panel).

- **Residual extinction product**

  The spectral transmission is produced with a correction for scintillation and refractive dilution effects. Together with the forward model one can compare the transmission and find if their differences are pure random in the wavelength distribution or if a bias is observed. These results as well ease the comparison of GOMOS products to off-line processing products.

- **Near real time meteo product**

  Some profiles of the level 2 product are delivered to various meteorological offices and users, as so-called Fast Delivery Products, available within three hours of reception by ground stations. The GOMOS processing is mainly identical to the standard processing. The main difference is that the external atmospheric data are predictions, while the standard processing is based on an *a posteriori* analysis.

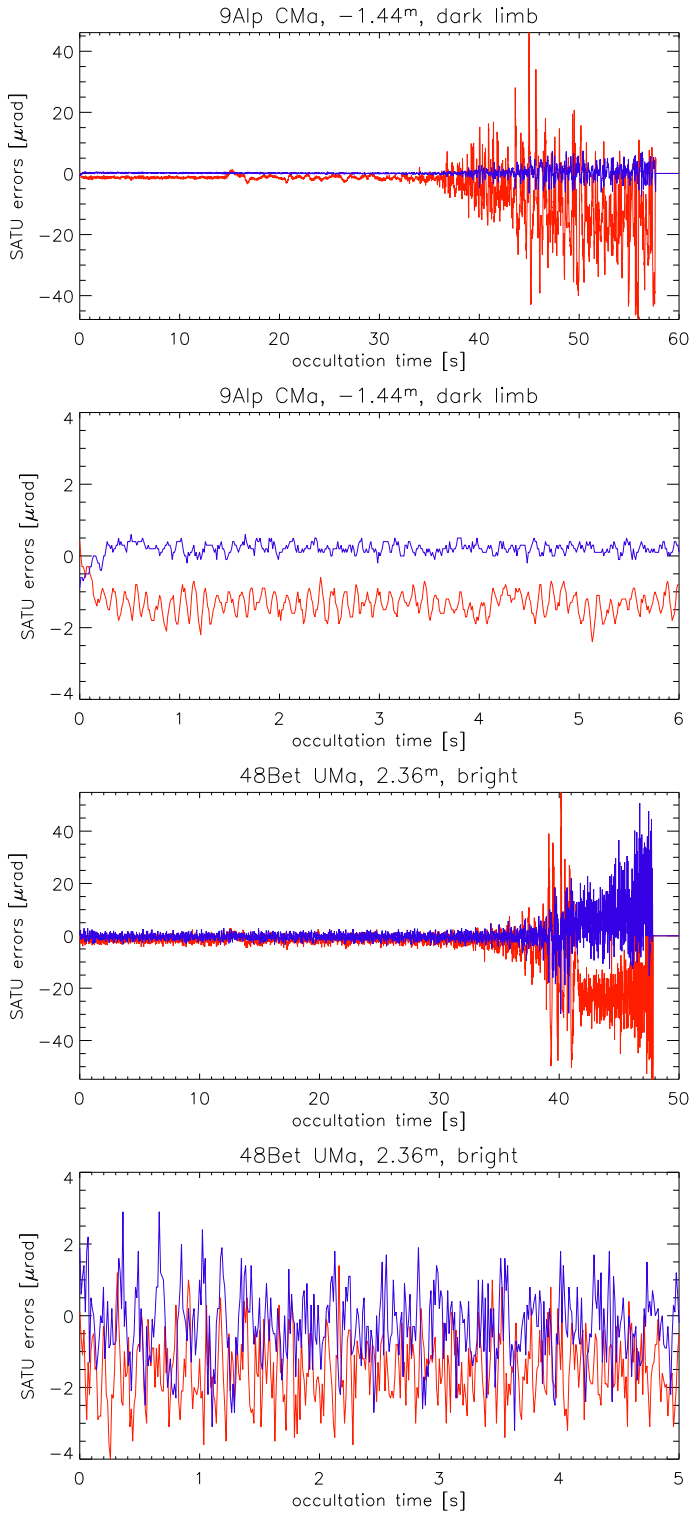

Figure 3.11. Star tracker errors (SATU) shown for a bright star (-1.44^m) in dark limb (upper two panels) and for a dim star (2.36^m) in bright limb (lower two panels) conditions for a whole occultation event and zoomed occultation time. The red lines (lower values) denote the elevation errors, while the blue lines (higher values) represents the azimuth errors.

4

Retrieval Algorithms and Statistics

This Chapter introduces in detail the forward model setup and the inversion scheme for the retrieval of temperature and ozone profiles from GOMOS star tracker and transmission data, respectively. A simulation study was performed for both, temperature and ozone, in order to ensure having a robust model for the application of real data. The real data inversion for ozone was enhanced by adding NO_2 and forming a joint retrieval for these two species. Here NO_2 is a side product and primarily serves to increase ozone retrieval quality in the lower stratosphere, but some few graphs evince the possibility of a NO_2 retrieval within the selected inversion scheme. For a more detailed description on error characterization and statistics we refer to, e.g., [*Rodgers* (1976), *Rodgers* (1990), *Rodgers* (2000), *Lang and Pucker* (1998), *Storch and Zwiers* (1999)]. More details on the operational GOMOS algorithm can be found in, e.g., [*Bertaux et al.* (2001), *ESA* (2002)].

4.1 Occultation Geometry and Forward Model Setup

A formulation of an appropriate signal propagation geometry is of major importance in order to develop a realistic forward model procedure. We use a realistic and fast raytracing algorithm, which solves the refractive raypath problem

$$\frac{d^2\mathbf{x}}{d\tau} = n(\mathbf{x})\nabla n(\mathbf{x}) \tag{4.1}$$

with the star and the satellite position as boundary conditions. The $n(\mathbf{x})$ denotes the refractivity field of the used atmospheric model (e.g., MSISE90 [*Hedin* (1983), *Hedin* (1987), *Hedin* (1991)]), while $d\tau$ is the along-ray arc length divided by the refractivity n. Once the occultation geometry is determined, we set up the calculation of the simulated atmospheric transmission.

The spectrometer A on the GOMOS instrument provides transmission data from 250 - 375 nm and 405 - 675 nm at a spectral sampling of ~ 0.3 nm. This gives more than 1000 channels for observations in the UVVIS. In the method presented here only a few

available channels were selected by empirical arguments and tests on the algorithm. The selection turned out to be the best one in terms of saving computing time and assuring a high information content. The selected channels were chosen to give a good signal response in the Hartley and Huggins band and as well in the Chappuis band, which is especially important for low stratospheric ozone retrieval. The wavelengths set selected for presentation in this thesis contains 14 channels

$$\lambda \in [260, 280, 288, 295, 302, 309, 317, 328, 334, 337, 340, 343, 600, 605]\,, \tag{4.2}$$

where numbers are given in [nm].

The atmospheric transmission is defined by Beer-Bouguer-Lambert's law (cf. Eq. 1.19), at each wavelength λ of interest, as

$$T_\lambda = \frac{I_\lambda(s)}{I_\lambda(0)} = e^{-\tau_\lambda}, \tag{4.3}$$

where

$$\tau_\lambda = \int_{s_1}^{s_2} \sum_i n_i(s')\sigma_{i\lambda}(s')ds' \tag{4.4}$$

is the corresponding optical thickness. The transmission T_λ is a ratio of the radiation intensity measured in the atmosphere, $I_\lambda(s)$, relative to the one, $I_\lambda(0)$, measured outside the atmosphere. Building ratios of intensities is moreover the only possibility of handling the acceptance and the retrieval of several different star signals all having different reference spectra. The integral is now carried out along a refracted ray path s from the star s_1 to the sensor s_2. In our context the number densities n_i and the cross sections $\sigma_{i\lambda}$ are associated with the species ozone, NO_2 and NO_3, respectively. In order to reflect the bulk medium, especially important in the lower stratosphere, a factor for the air density with the Rayleigh scattering cross section was introduced as well. The wavelength dependent Rayleigh scattering cross section for air reads (cf. [*Thomas and Stamnes* (1999)])

$$\sigma_{\lambda,\mathrm{ray}} = \lambda^{-4} \sum_{i=0}^{3} a_i \lambda^{-2i} \times 10^{-28}, \tag{4.5}$$

where σ is given in [cm^2] and the coefficients a_i are listed in Tab. 4.1. The formula is valid for a wavelength range of 205 - 1050 nm.

Parameter	**Value**
a_0	3.9729066
a_1	4.6547659×10^{-2}
a_2	4.5055995×10^{-4}
a_3	2.3229848×10^{-5}

Table 4.1. Parameter for the calculation of the Rayleigh cross sections.

The present forward model is a best estimate physical realization of the current atmospheric state. Due to an actual low stratospheric aerosol concentration a term representing the corresponding signal extinction, the so-called Mie scattering, was neglected. Aerosol cross sections can be approximated by Ångströms law

$$\sigma_{\lambda,\mathrm{mie}} = \frac{\sigma_0}{\lambda}, \tag{4.6}$$

where $\sigma_0 = 3 \times 10^{-7}$ cm^2.

The modeled transmission is further improved by an integration over adjacent channels. The channel integrated transmission takes into account a line spreading of the measured signal and therefore leads to a correlation of neighboring channels. The resulting signal is weighted by a normed Gaussian convolution function W and the new transmission is then expressed by

$$T_{\lambda,\mathrm{ch}} = \frac{1}{\Delta\lambda} \int_{\Delta\lambda} T_{\lambda_0} W(\lambda - \lambda_0) d\lambda. \tag{4.7}$$

A resulting modeled transmission for 14 channels is shown in Fig. 4.1, where transmissions are accepted for processing if they lie within a threshold of $0.01 < T_\lambda < 0.99$.

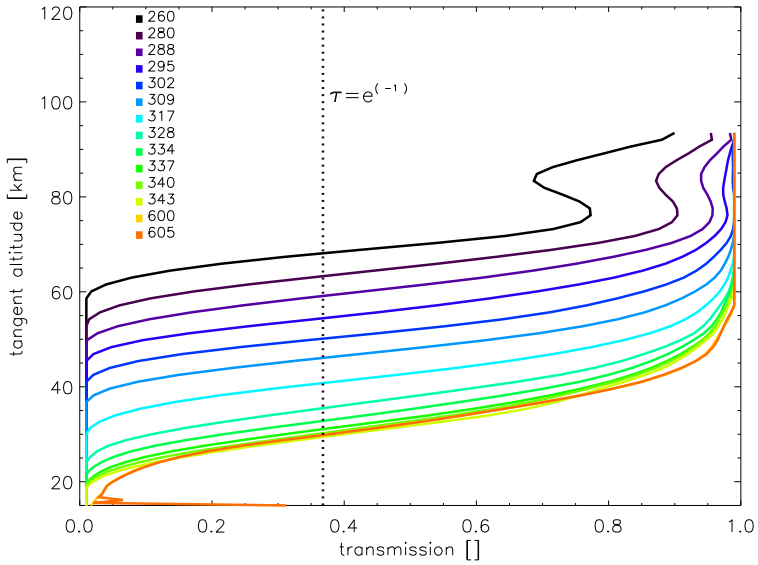

Figure 4.1. Simulated atmospheric transmissions for 14 selected wavelengths forming the basis of the forward model. The shown transmissions are convoluted by a Gaussian weighting function in order to reflect a correlation between adjacent channels.

For each tangent height, an integration over occultation time is neglected here due to the fact that the atmosphere can be considered as constant for, e.g., air and ozone density. Small scintillation structures are modeled neither, but real transmissions are corrected for such effects as discussed in Section 4.2. A further integration over a finite field of view has not to be carried out, which is in turn indispensable for solar, lunar or planetary occultations. In stellar occultation the signal can be seen as a point source, whereas, e.g., the Sun has to be regarded as a disk emitting light.

4.2 The Real Transmission: Scintillation and Dilution

The transmission measured by GOMOS is not only dependent on absorbing atmospheric constituents. It is additionly dependent on refraction effects of the air along the line-of-sight. In the previous Section 4.1 we have already taken into account a coefficient for

Rayleigh scattering for the simulated transmission, but here the observed transmission is also modulated by scintillation and dilution effects. In order to meet the premises of an accurate retrieval scheme, GOMOS transmissions have therefore to be corrected for these effects. The following method was developed for the operational GOMOS retrieval [*Bertaux et al.* (2001), *ESA* (2002)] and is adapted here for our needs.

Scintillations are rapid variations in apparent position, brightness, or color of a distant luminous object, viewed through the atmosphere. If the object lies outside the Earth's atmosphere, as in the case of stars and planets, the phenomenon is termed astronomical scintillation, while for objects lying within the atmosphere, the phenomenon is called terrestrial scintillation. Almost all scintillation effects are caused by anomalous refraction occurring in rather small parcels or strata of air, whose temperatures and densities differ slightly from those of their surroundings. Wind motions transport such air through the line-of-sight and produce the irregular fluctuations characteristic of scintillation. Scintillation effects are always much more pronounced near the horizon than near the zenith. Parcels of the order of only centimeters to decimeters are believed to produce most of the scintillatory irregularities in the atmosphere.

The so-called refractive dilution has its origin in the change of the propagation direction of the ray while passing the atmosphere. This effect is related to the density gradient in the atmosphere causing a larger deflection to a grazing ray compared to rays with larger impact parameters. Both effects, the signal scintillation and the refractive dilution, are chiefly noticeable in the lower stratosphere and in the troposphere.

We assume that the effects on the transmission by scintillation and dilution can be split into two independent terms

$$T_{sd}(t,\lambda) = T_s(t)T_d(t,\lambda). \tag{4.8}$$

The scintillation component T_s is modeled by incorporating GOMOS level 1b photometer data which is discussed in more technical detail in Section 3.3. We assume that the red photometer band has a high signal-to-noise ratio and is the less extinctive available photometer component. All high frequency fluctuations are believed to have their origin in scintillation effects, while fluctuations in the structure of vertical measured profiles only effect the low frequency part of the signal. The scintillation transmission (see Fig. 4.2) is now calculated by

$$T_s(t) = \frac{I_{ph}(t)}{\bar{I}_{ph}(t)}, \tag{4.9}$$

where $I_{ph}(t)$ are the electron counts of the red photometer and $\bar{I}_{ph}(t)$ is smoothed with a moving average as discussed in Section 4.3.

The component T_d for the dilution (see Fig. 4.3), is estimated by an exploitation of bending angles α gained by GOMOS level 1b SFA/SATU data. The mean dilution is modeled by using the so-called phase screen approximation where a three-dimensional atmosphere is replaced by a screen located a the tangent point. The bending due to atmospheric refraction now takes place at the screen and the transmission part due to refractive dilution is then given by

$$T_d(t,\lambda) = \frac{1}{1 + L\left|\frac{d\alpha(t,\lambda)}{dt}\right|}, \tag{4.10}$$

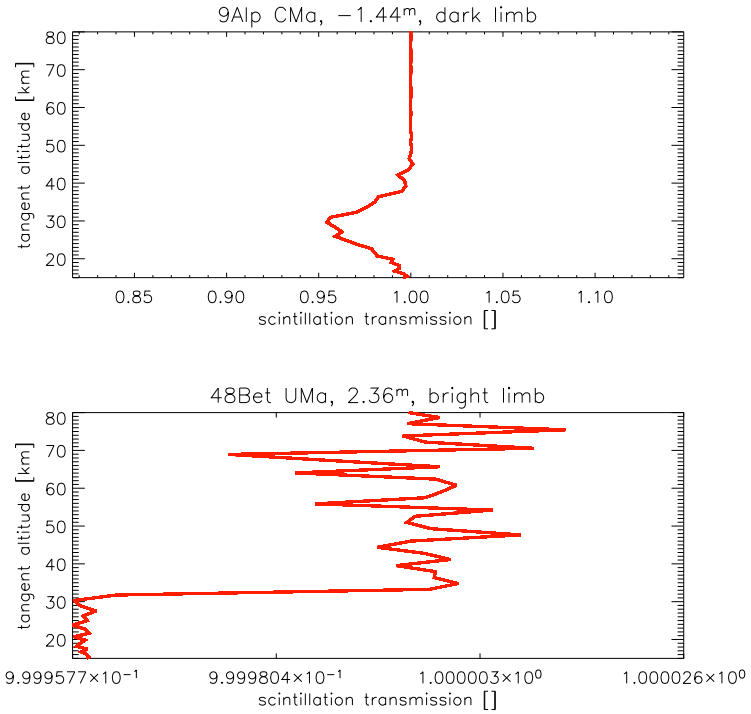

Figure 4.2. The so-called scintillation transmission T_s for an occultation of a star with -1.44^m in dark limb condition (upper panel) and for a star with 2.36^m in bright limb condition (lower panel).

where t is the occultation time and L denotes the distance from Envisat to the tangent point. The resulting observed and corrected transmission is expressed by

$$T_c(t,\lambda) = \frac{T_o(t,\lambda)}{T_{sd}(t,\lambda)} \tag{4.11}$$

and serves as the input (also termed "true") transmission into the optimal estimation scheme, discussed in Section 4.4.1.

A third effect caused by refraction is the so-called chromatic refraction [*Edlen* (1953)] leading to a spatial separation of rays with different wavelengths. A measurement of a stellar spectrum through the atmosphere therefore cannot be attached with an unique ray connecting the satellite and the star. The refractive effects discussed here are not only restricted to the stellar occultations in the Earth's atmosphere, but in fact they have also been detected in measurements of stellar occultations of planetary atmospheres. In this thesis we neglect the chromatic refraction in the first place and assume that the refractive index of air is independent on wavelength. The constituent profiles vary too weakly along tangent altitude changes due to small differences of the path length for different wavelengths.

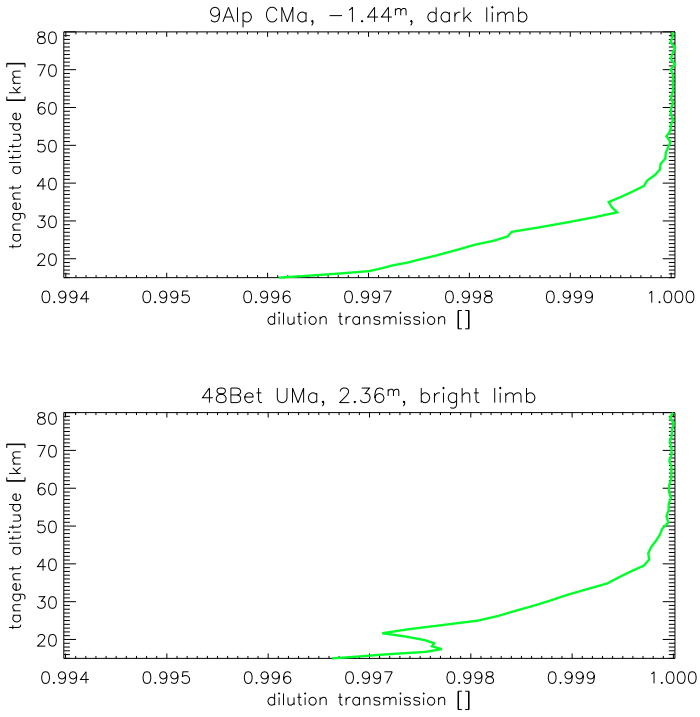

Figure 4.3. The dilution factor T_d contributing to a total correction of measured GOMOS transmissions for an occultation of a star with -1.44^m corresponding to a star temperature of 11000 K in dark limb condition (upper panel) and for a star with 2.36^m corresponding to a star temperature of 10600 K in bright limb condition.

4.3 Moving Average and Bias Correction

Once we have selected an optimal set of profiles based on arguments drawn in Section 4.1, we had to smooth transmission data for better retrieval performance. A moving average calculation was performed for every height step in the profile. A given sequence for one selected wavelength λ and height level i dependent transmissions $\{T_{\lambda i}\}_{i=1}^{N}$ is replaced by a new sequence of smoothed transmissions $\{(T_s)_{\lambda i}\}_{i=1}^{N-n+1}$ with

$$(T_s)_{\lambda i} = \frac{1}{\sum_n k_n} \sum_{j=i}^{i+n-1} k_j T_{\lambda j}. \tag{4.12}$$

The average was taken by n subsequences of $T_{\lambda j}$ each weighted with different k_j. In general moving averages are given with equal weights. Here the weights were chosen such that $\sum_n k_n = 1$. For a subsequence of $n = 5$ we find weights with $k_n = \frac{1}{10}[1, 2, 4, 2, 1]$, where k_3 can always be seen as the weight for the original T_i before taking the mean.

After a real transmission profile has been smoothed, it was then compared to a modeled transmission profile and corrected for large biases. This correction is found by averaging the difference (modeled vs. real transmission) profile over all heights. These biases exist due to a different forward model realization. Neglecting the majority of measured (and modeled beforehand) transmissions is intrinsic to our model, where we

only select a small subset of available data. A further reason why we observe deviations from measured transmission lies in the physics of the forward model itself, where, e.g., Mie scattering was not considered for this study. Nonetheless, after correcting for inherent forward model biases the results show improved behavior.

4.4 Ozone Retrieval

Having a forward model established, we have to find an inverse connection between measurements (transmission data) and targeted state (ozone profile) of the atmosphere. In the case presented here, ozone and NO_2 are retrieved simultaneously, forming a joint retrieval. The enhancement of the inversion scheme by incorporating other trace gases (e.g., NO_3, BrO, and OClO) targeted in the operational GOMOS retrieval is possible, but not investigated here. The measured transmission contains information of the density of the absorbing species and of the atmospheric refraction. To proceed from the transmission function one can find a solution for, e.g., the ozone density, by first separating the absorbing species by a spectral inversion and then perform a vertical inversion via an Abel transform. This is known as the so-called two-step retrieval and is realized in the GOMOS operational processing. Performing such a retrieval includes several restrictions one has to be aware of. Due to a line-by-line vertical retrieval, a correlation of adjacent vertical lines is not given any more after the spectral inversion. This is not observed in nature, where depending on altitude and selected wavelength the bending of rays and thus the absorption of light by target species has a vertical correlation. This feature can be handled by an one-step inversion by first performing a vertical retrieval [*Vanhellemont et al.* (2004)]. In the case of GOMOS this would include an inversion of large matrices (containing all wavelengths), which is then time consuming but can be processed in a proper way.

4.4.1 Retrieval Algorithm: Optimal Estimation

Here we use a different approach to the inversion of atmospheric species densities. Discrete inverse theory provides a framework [*Rodgers* (1976), *Rodgers* (1990), *Rodgers* (2000)], where the forward model $\mathbf{F}(\mathbf{x})$ can be seen as an algebraic mapping of the state space into the measurement space. The physics of the measurement is approximated by the forward model and we generally find

$$\mathbf{y} = \mathbf{F}(\mathbf{x}) + \boldsymbol{\varepsilon}, \tag{4.13}$$

where $\boldsymbol{\varepsilon}$ represents the measurement error of the forward model. Some problems can be linearized by making a Taylor expansion on Eq. 4.13 and by neglecting higher terms than of order one. We introduce an operator $\mathbf{K}$, which here will be the Jacobian matrix (weighting function matrix) with the dimension $m \times n$ for m measurements and n elements of the state vector. The forward model then reads

$$\mathbf{y} = \mathbf{K}\mathbf{x} + \boldsymbol{\varepsilon}. \tag{4.14}$$

The sensitivity of the measured transmissions $\mathbf{y}$ to the state $\mathbf{x}$, the ozone density profile, can be interpreted as "weighting functions" represented by the rows of $\mathbf{K}$

$$\mathbf{k}_i = \left(\frac{\partial y_i}{\partial x_1}, \ldots, \frac{\partial y_i}{\partial x_j} \right). \tag{4.15}$$

Numerically the coefficients of the Jacobian matrix are approximated by a perturbation of species densities with $\pm 5\%$ and then performing a forward model calculation, which gives the corresponding $\mathbf{y}$. In theory the perturbation should only be performed at the exact height level under consideration, but in the GOMOS case that has given a very low signal response. We therefore introduced a correlation by perturbing over three adjacent heights which gives a significantly higher signal and forms the basis for an accurate retrieval procedure.

Because of the generally non-linear Eq. 4.13, it is obvious that a straightforward solution for $\mathbf{x}$ by direct inversion is not feasible. The direct inverse mapping, if $\mathbf{K}(\mathbf{x}) = \mathbf{K}\mathbf{x}$ (e.g., linearity applies), would be

$$\mathbf{x}_r = \mathbf{K}^{-g}\mathbf{y}, \tag{4.16}$$

where $\mathbf{K}^{-g}$ denotes a general inverse matrix and $\mathbf{x}_r$ is the retrieved state (cf. Section B.1). As the problem of interest here is ill-posed at high altitudes due to low signal-to-noise ratio (it may also be over-determined if we use more measurements than unknown states; $m > n$), we cannot directly employ Eq. 4.16 but rather constrain the solution by incorporating sensible *a priori* information. The Bayesian approach is the method of choice to solve such inverse problems perturbed by noise, where we have rough but reliable prior knowledge of the behavior of a state of interest. We can enhance this prior knowledge in a consistent way by incorporating the measurements. Imperfect prior knowledge can be quantified as a probability density function (*pdf*) over the state space, whereas an imperfect (due to errors) measurement is quantified by a *pdf* over the measurement space. Bayes' theorem (cf. Tab. B.2) tells, how the measurement *pdf* maps into the state space and can be combined with prior knowledge.

If the problem is only moderately non-linear we can use a Gauss-Newton method (omitting small residual terms from Newtonian iteration, when applying on non-linear cases) for an iterative approach to find an optimal solution. Assuming Gaussian probability distributions and a linearized forward model, the primary task of a retrieval method is to find a state by satisfying optimal criteria from an ensemble of states which agree with the measurement within experimental errors. An overview of different cases of inverse problems is given in Tab. B.1 which has been adapted from [*Fehmers* (1996)].

Here we make use of a fast converging iterative optimal estimation algorithm,

$$\mathbf{x}_{i+1} = \mathbf{x}_{ap} + \mathbf{S}_i \mathbf{K}_i^T \mathbf{S}_\varepsilon^{-1} \Big[(\mathbf{y} - \mathbf{y}_i) + \mathbf{K}_i (\mathbf{x}_i - \mathbf{x}_{ap}) \Big] \tag{4.17}$$

with the associated retrieval error covariance matrix

$$\mathbf{S}_i = \left(\mathbf{K}_i^T \mathbf{S}_\varepsilon^{-1} \mathbf{K}_i + \mathbf{S}_{ap}^{-1} \right)^{-1}. \tag{4.18}$$

In Eq. 4.17, $\mathbf{x}_{i+1}$ is the retrieved, $\mathbf{x}_{ap}$ the *a priori* profile, $\mathbf{y}$ the measurement vector, and $\mathbf{y}_i = \mathbf{K}(\mathbf{x}_i)$ the forward-modeled measurement vector. Key ingredients of Eq. 4.18

are the *a priori* covariance matrix $\mathbf{S}_{ap}$ and the measurement error covariance matrix $\mathbf{S}_{\varepsilon}$ (see below). The Jacobian (weighting) matrix $\mathbf{K}_i$ represents the mapping involved. Index i is the iteration index, which is started by using $\mathbf{x}_0 = \mathbf{x}_{ap}$.

The ray tracer-simulated actual transmission measurements $\mathbf{y}$, are superimposed by stochastic error realizations $\boldsymbol{\varepsilon}$, gained via application of the error pattern method (cf. [*Rodgers* (2000)]), and are consistent with the $\mathbf{S}_{\varepsilon}$ matrix. The error pattern method is outlined below by using the *a priori* covariance matrix $\mathbf{S}_{ap}$. The forward-modeled measurement vector estimate at any iteration step i, $\mathbf{y}_i = \mathbf{K}(\mathbf{x}_i)$, is used without modification, however.

The number of needed iteration steps for Eq. 4.17 is found by a calculation of the cost function

$$\chi_i^2 = (\mathbf{y} - \mathbf{y}_i)^T \mathbf{S}_{\varepsilon}^{-1} (\mathbf{y} - \mathbf{y}_i) + (\mathbf{x}_i - \mathbf{x}_{ap})^T \mathbf{S}_{ap}^{-1} (\mathbf{x}_i - \mathbf{x}_{ap}) \tag{4.19}$$

at each iteration step i. The cost function χ_{i+1}^2 at iteration step $i+1$ has always to be smaller than χ_i^2. The minimum criterion is met if χ_i^2 is smaller than the number of selected channels. If this criterion is not reached the retrieval stops per definition after 10 iterations.

We can further identify so-called error characterization functions. The partial derivative of the inverse model with respect to the measurements gives

$$\begin{aligned} \mathbf{G}_i &\equiv \frac{\partial \mathbf{x}_i}{\partial \mathbf{y}_i} \\ &= \left(\mathbf{K}_i^T \mathbf{S}_{\varepsilon}^{-1} \mathbf{K}_i + \mathbf{S}_{ap}^{-1}\right)^{-1} \mathbf{K}_i^T \mathbf{S}_{\varepsilon}^{-1} \\ &= \mathbf{S}_i \mathbf{K}_i^T \mathbf{S}_{\varepsilon}^{-1}, \end{aligned} \tag{4.20}$$

the gain (or contribution) matrix for the i-th iteration. The columns of $\mathbf{G}_i$ are termed the gain functions and denote the contributions of each measurement to the retrieved state. For precise measurements and large errors in the prior state this leads to a large gain, in turn imperfect measurements with large errors together with an accurate prior knowledge yield small values in the gain matrix.

Another quantity, termed as the averaging kernel or model resolution matrix, is the partial derivative of the retrieved state with respect to the true state

$$\mathbf{A}_i \equiv \frac{\partial \mathbf{x}_i}{\partial \mathbf{x}} = \mathbf{G}_i \mathbf{K}_i. \tag{4.21}$$

The rows of $\mathbf{A}$ are called the averaging kernels and reflect how an element of a true state is reproduced by the estimated state. In an ideal inversion case, all elements of an estimated state have their origin in a corresponding true state, thus leading to $\mathbf{A} = \mathbb{1}$. When we look at different hight levels, averaging kernels encounter a peak with a certain FWHM denoting the spatial resolution of the observing system and therefore provide a characterization of the relationship of the retrieved to the true state.

4.4.2 Error Covariance Specifications

A priori Covariance Matrix

For the elements of $\mathbf{x}_{ap}$ we considered typical errors expected in prior ozone and NO_2 profiles and assumed uncertainties of 30% and 40%, respectively, for the diagonal elements. Off-diagonal elements can be modeled in different ways. Typical drop-off correlation functions are of Gaussian

$$(S_{ap})_{ij} = \sigma_i \sigma_j \exp\left[-\frac{(z_i - z_j)^2}{L^2}\right], \tag{4.22}$$

or of exponential type

$$(S_{ap})_{ij} = \sigma_i \sigma_j \exp\left[-\frac{|z_i - z_j|}{L}\right] \tag{4.23}$$

(see Fig. 4.4), where z_i and z_j denote the height levels between which the covariance is expressed, and where L denotes a correlation length set to 6 km in order to reflect the fact that prior profiles are usually fairly smooth at scales smaller than the atmospheric scale height. Measured ozone profiles may in turn show strong laminar structures with much smaller scales. The standard deviation σ_i at a specific height level corresponds to $\sigma_i = (\mathbf{S}_{ap})_{ii}^{1/2}$. In our case we have chosen to formulate correlations by Eq. 4.23, where the resulting matrix in a joint retrieval notation has the form

$$\mathbf{S}_{ap} = \begin{pmatrix} \mathbf{S}_{ap}^{O_3} & \mathbf{0} \\ \mathbf{0} & \mathbf{S}_{ap}^{NO_2} \end{pmatrix}. \tag{4.24}$$

An example of an ozone covariance matrix with $\sigma = 30\%$ and $L = 6$ km is shown in Fig. 4.4.

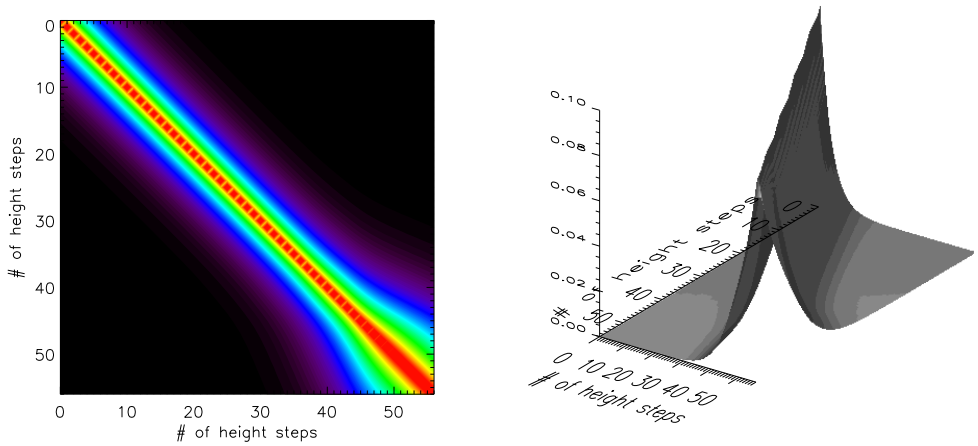

Figure 4.4. Typical *a priori* ozone covariance matrix with $\sigma = 30\%$, correlation length $L = 6$ km and exponential drop-off correlations.

Error Covariance Matrix

The $\mathbf{S}_\varepsilon$ matrix was designed by adopting a 1% standard error at unity transmission and increasing errors with decreasing transmissions y_i according to the square-root law (photon detection noise), e.g.,

$$(\mathbf{S}_\varepsilon)_{jj} = \frac{0.01}{\sqrt{y_j}}. \tag{4.25}$$

No interchannel correlation was assumed, thus the off-diagonal elements were set to zero. These error assumptions roughly reflect the measurement error specifications of the GOMOS sensor [*Bertaux et al.* (2001)].

Error Pattern Method

The method was applied for the calculation of *a priori* and measurement error vectors in general, but for simplicity reasons it is only outlined in the notation of the *a priori* profile.

The *a priori* profiles $\mathbf{x}_{ap}$ where derived by superimposing on the "true" state $\mathbf{x}$ error realizations consistent with the *a priori* error covariance matrix $\mathbf{S}_{ap}$. For this purpose we exploit the fact that one can decompose $\mathbf{S}_{ap}$ (e.g., [*Rodgers* (2000)]) into so-called error patterns obeying $\mathbf{e}_i = \sqrt{\lambda_i}\ \mathbf{l}_i$. The error patterns $\mathbf{e}_i$ (see Fig. 4.5) are the eigenvectors $\mathbf{l}_i$ of $\mathbf{S}_{ap}$ weighted by the square-root of the eigenvalues λ_i. In order to construct $\mathbf{x}_{ap}$ statistically consistent with $\mathbf{S}_{ap}$, one adds an error vector

$$\boldsymbol{\varepsilon}_\mathrm{e} \equiv \sum_i a_i \mathbf{e}_i \tag{4.26}$$

to the "true" state $\mathbf{x}$, where the scalar coefficients a_i are normal random deviates drawn from a normalized (zero mean and unit variance) Gaussian distribution. The method

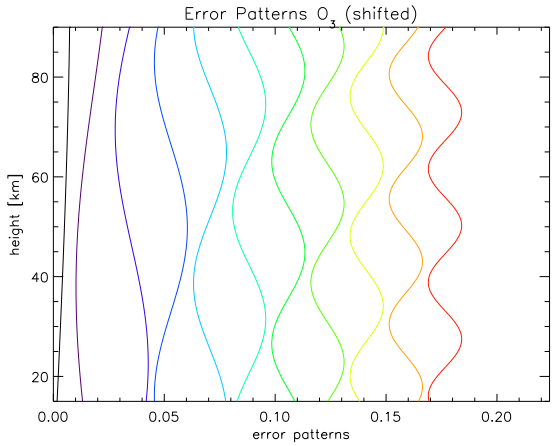

Figure 4.5. An example of error patterns (scaled eigenvectors) for an ozone *a priori* covariance matrix.

can be verified by reconstructing a so-called empirical error covariance matrix $\mathbf{S}_\mathrm{e}$ by

forming the expectation value

$$\mathbf{S}_\mathrm{e} = \left\langle \boldsymbol{\varepsilon}_\mathrm{e} \boldsymbol{\varepsilon}_\mathrm{e}^T \right\rangle \tag{4.27}$$

$$= \frac{1}{n} \sum_{j=1}^{n} \boldsymbol{\varepsilon}_{j,\mathrm{e}} \boldsymbol{\varepsilon}_{j,\mathrm{e}}^T \tag{4.28}$$

of an ensemble of realizations. This is illustrated in Fig. 4.6 for $n = 100$ randomly generated errors and for $n = 10000$ error realizations, respectively. The original matrix can thus be reconstructed by an infinite number of contributing random errors to $\mathbf{S}_\mathrm{e}$

$$\mathbf{S} = \lim_{n \to \infty} \frac{1}{n} \sum_{j=1}^{n} \boldsymbol{\varepsilon}_{j,\mathrm{e}} \boldsymbol{\varepsilon}_{j,\mathrm{e}}^T. \tag{4.29}$$

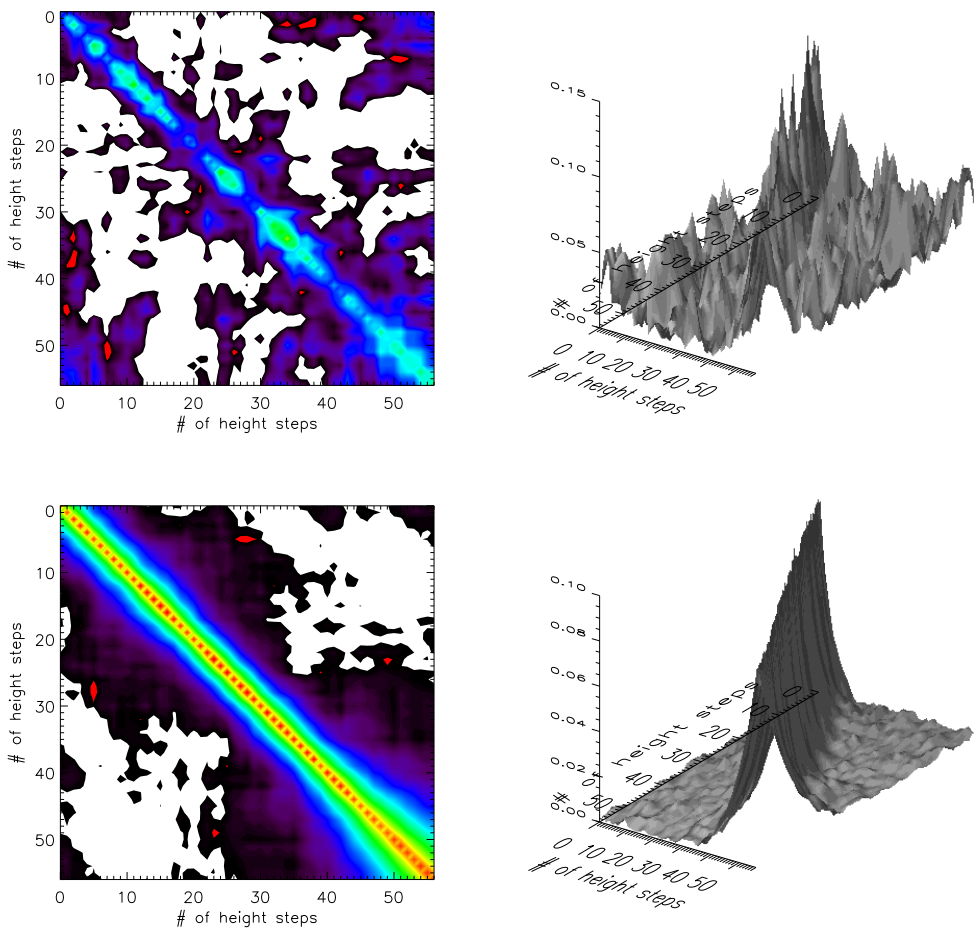

Figure 4.6. Empirical *a priori* ozone covariance matrix with $\sigma = 30\%$, correlation length $L = 6$ km and exponential drop-off correlations after 100 (upper panel) and 10000 (lower panel) iterations.

4.4.3 Error Correlation and Resolution

At each step of iteration of Eq. 4.17 we computed several characterization functions. For one selected simulation event at 38° latitude (see Figs. 5.1 and 5.3) we retrieved ozone profiles and determined the retrieval correlation matrix $\mathbf{S}_i$ and the averaging kernel matrix $\mathbf{A}_i$. The rows of $\mathbf{S}_i$ are called the retrieval error correlation functions, while the rows of $\mathbf{A}_i$ are so-called averaging kernel functions. Representative height levels were selected at above tropopause, at the stratopause, and in the high stratosphere. The functions generally peak at the height levels corresponding to the matrix diagonal and indicate that at the height grid used here (1.5 - 2 km sampling) error correlation between levels are negligible and the resolution essentially matches the sampling.

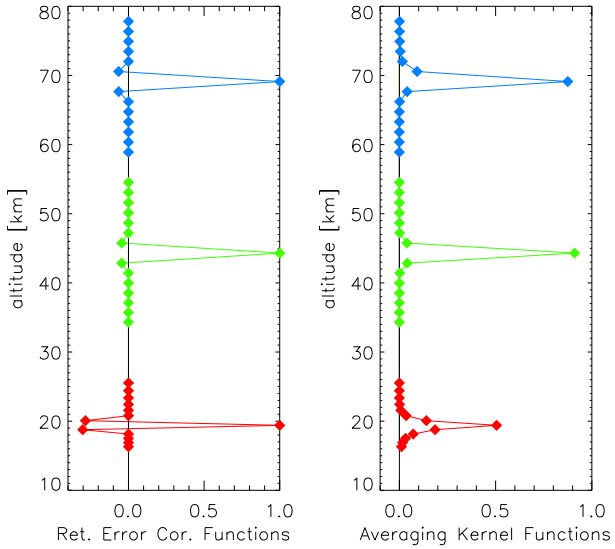

Figure 4.7. Retrieval error correlation functions (rows of $\mathbf{S}_i$) and averaging kernel functions (rows of $\mathbf{A}_i$) for representative heights at 20, 45 and 70 km for one selected simulated retrieved ozone profile at 38° latitude.

4.5 Temperature Retrieval

The GOMOS temperature retrieval follows a method which was shortly outlined in the previous Section. Instead of introducing a third matrix, besides ozone and NO_2, for a joint retrieval, temperature profiles are inverted by an Abel transform. Light coming from, e.g., stellar sources undergo a refractive bending before the signal gets measured by the instrument. The degree of refraction is a measure for the atmospheric density, pressure, and temperature, respectively.

GOMOS derived bending angles have their origin in an exploitation of the elevation movement of the star tracking unit (SFA/SATU). The SFA/SATU tracks the star image on its way down trough the atmosphere during data acquisition for a setting event. The whole CCD can move within an elevation angle of $61.7° - 69°$ and $11° - 91°$ in the azimuthal direction with a sampling rate of 10 Hz for the SFA. The star image

is kept inside the CCD with a sampling of 100 Hz and errors of ± 10 μrad from the central position. The measured elevation angles are compared to an unrefracted ray, measured outside the atmosphere and thus giving a bending angle profile.

For the derivation of refractivity profiles from bending angles and impact parameters using the Abel transform, we assume spherical symmetric conditions. In nature this is not the case and therefore we have to find a correction for an ellipsoidal shape of the Earth. The center of curvature is no longer the Earth center. A better approximation to real conditions can be achieved by finding a sphere which is tangential to the ellipsoid at the profile location. The new center of curvature is now the center of a sphere and bending angles and impact parameters can subsequently be found for a spherical symmetry.

In theory one can now start with the calculation of the refractive index, which is the next step in the temperature retrieval procedure. Bending angles at high altitudes, due to small refraction, are typically generated by differences of very small numbers. Measurement errors and errors of discretization further decrease the quality of bending angle profiles. The signal-to-noise ratio in the measured bending angle profile becomes less than unity at altitudes above $\sim$ 40 km. Due to the application of the Abelian integral, errors in the bending angle profile at high altitudes propagate down through all height steps and thus also low altitude temperature profiles suffer from an inappropriate initialization value [*Syndergaard* (1999)]. A sensible use of good-quality bending angle data for high-altitude initialization is therefore needed and realized by the introduction of the statistical optimization technique.

A further modification of the bending angle profile, as may be applied in radio occultation (cf. [*Kursinski et al.* (1997)]) is of no importance to GOMOS measurements. In radio occultation, due to the selected wavelength in the order of meters, a ionospheric correction is necessary and thus is an important issue. Rays in the optical, UV, and NIR wavelength range are not affected by the ionosphere and thus a correction can be neglected.

4.5.1 Statistical Optimization

The statistical optimization [*Sokolovsky and Hunt* (1996)] optimally combines measured and background (*a priori*) bending angle profiles leading to the most probable bending angle profile. An optimal solution is found via

$$\alpha_{opt} = \alpha_b + \mathbf{B}\left(\mathbf{B} + \mathbf{O}\right)^{-1}\left(\alpha_o - \alpha_b\right), \tag{4.30}$$

where α_b is the background and α_o the observed bending angle profile, respectively. The matrices $\mathbf{B}$ and $\mathbf{O}$ express the background and the observation error covariances, respectively. Similar to Eq. 4.23 we define

$$B_{ij} = \sigma_i \sigma_j \exp\left[-\frac{|a_i - a_j|}{L}\right], \tag{4.31}$$

with impact parameters a at different height levels i and j. The correlation length L was set to 6 km for $\mathbf{B}$, while we find $L = 1$ km appropriate for $\mathbf{O}$, using the same form as Eq. 4.31. As a background profile we chose a CIRA-86 climatology. Background errors (such as σ_i and σ_j) were assumed to be 20% in line with radio occultation literature (e.g.,

[*Healy* (2001), *Gobiet and Kirchengast* (2002)]). The observation errors were estimated from the root-mean-square deviation of the observed data from the background at high altitudes (70 - 80 km), where noise dominates the measured signal. More details on the statistical optimization scheme used here are found in, e.g., [*Gobiet and Kirchengast* (2002), *Gobiet et al.* (2004a), *Gobiet et al.* (2004b), *Gobiet and Kirchengast* (2004)].

4.5.2 Abel Transform

Once we have a total bending angle profile α and accompanying impact parameters a we can formulate an Abel integral equation [*Bronstein et al.* (1993)] connected to the logarithm of the refractive index n. An inverse Abel transform [*Fjeldbo et al.* (1971)] has to be carried out in order to find an expression of the refractive index as a function height.

In a spherically symmetric atmosphere the ray path is symmetrical about the tangent point and we find

$$\alpha = 2a \int_{r=r_t}^{r=\infty} \frac{1}{\sqrt{(nr)^2 - a^2}} \frac{d\left(\ln(n)\right)\, dr}{dr}, \tag{4.32}$$

where a denotes the impact parameter, r is the radius integrated from the tangent point location r_t to ∞. After substituting $x = r\, n(r)$ and multiplying both sides with the kernel $\left(a^2 - a_0^2\right)^{-1/2}$ we get

$$\begin{aligned}
\int_{a=a_0}^{a=\infty} \frac{\alpha\, da}{\sqrt{a^2 - a_0^2}} &= \int_{a=a_0}^{a=\infty} \frac{2a\, da}{\sqrt{a^2 - a_0^2}} \left[\int_{x=a}^{x=\infty} \frac{1}{\sqrt{\left(x^2 - a^2\right)}} \frac{d\ln(n)\, dx}{dx} \right] && (4.33)\\
&= \int_{x=a_0}^{x=\infty} \frac{d\ln(n)\, dx}{dx} \left[\int_{a=a_0}^{a=x} \frac{2a\, da}{\sqrt{\left(a^2 - a_0^2\right)\left(x^2 - a^2\right)}} \right] && (4.34)\\
&= \pi \int_{x=r_0 n(r_0)}^{x=\infty} \frac{d\ln(n)\, dx}{dx} && (4.35)\\
&= -\pi \ln\left(n(r_0)\right), && (4.36)
\end{aligned}$$

where the order of integration and the integration limits are changed in Eq. 4.33. The inner integral is solved by the introduction of substituting parameters. The left hand side of Eq. 4.33 and the final right hand side of Eq. 4.36 give the classical Abel transform equation

$$n(r_0) = \exp\left[-\frac{1}{\pi} \int_{a_0}^{\infty} \frac{\alpha(a)\, da}{\sqrt{a^2 - a_0^2}} \right]. \tag{4.37}$$

If $\alpha(a)$ is given, Eq. 4.37 can be inverted numerically

$$n(r_0) = \exp\left[\frac{1}{\pi} \int_{\alpha=\alpha(a_0)}^{\alpha=0} \ln\left(\frac{a(\alpha)}{a_0} + \sqrt{\left(\frac{a(\alpha)}{a_0}\right)^2 - 1} \right) d\alpha \right], \tag{4.38}$$

written here in a favorable form for numerical use by avoiding poles (e.g. cf. [*Steiner* (1998), *Foelsche* (1999)]). The $\alpha(a_0)$ and a_0 are the bending angle and impact parameter associated with radius r_0, the bottom height of the Abelian integration extending over the height domain above r_0.

4.5.3 Density, Pressure, and Temperature

Parameters of the neutral atmosphere, such as density ρ, pressure p, and temperature T can now be derived from a given refractive index n or the refractivity N which is be expressed by

$$N(z) = (n(z) - 1) \times 10^6, \tag{4.39}$$

where z denotes the height above the Earth's surface. In general there are dry and moist contributions to the refractivity, but GOMOS measurements seldom reach tropospheric heights, where moisture is measurable and thus we can find an expression for the dry refractivity

$$N = k_1 \frac{p}{T}, \tag{4.40}$$

with $k_1 = 77.65$ K/hPa. Neglecting the small effects of non-ideal gas behavior the ideal gas law states

$$\begin{aligned} \rho_d(z) &= \frac{p}{T}\frac{m_d}{R^*} \\ &= \frac{m_d}{R^* k_1} N(z) \\ &= b_1 N(z), \end{aligned} \tag{4.41}$$

where the constant $b_1 = 4.4892 \times 10^{-3}$ kg/m^3.

The pressure profiles can be derived from the density profiles by applying the hydrostatic equation, which states that the downward orientated gravitational force F on an air parcel must equate the upward forces due to pressure gradients. We thus find

$$dF = -\rho g(z, \varphi)\, dx\, dy\, dz \tag{4.42}$$

and the pressure follows with

$$dp = -\rho g(z, \varphi)\, dz, \tag{4.43}$$

which is the net force per area. The acceleration of gravity g can accurately be derived by [*Press* (1993)]

$$g(z, \varphi) = 9.806(1 - 0.0026\ \cos 2\varphi)(1 - 3.1 \times 10^{-7} z). \tag{4.44}$$

The pressure profile is then obtained by integrating Eq. 4.43, where we generally start at the top of the atmosphere and perform the integration downward

$$p(z) = \int_z^\infty g(z', \varphi')\rho(z')dz'. \tag{4.45}$$

The top of the atmosphere is mostly defined at a height of 120 km with a pressure of $p \simeq 0$. Initialization errors decrease exponentially with the scale height of the atmosphere as the integration moves deeper into the atmosphere.

The temperature profile can be subsequently derived from p and N by the application of the equation of state (cf. Eq. 4.40).

4.5.4 Joint Temperature and Atmospheric Constituents Retrieval

In this thesis we have chosen to retrieve atmospheric constituent profiles (ozone and NO_2) in a joint retrieval and separately invert bending angles into temperatures with an Abel transform. For these retrieval schemes, as discussed in Sections 4.4 and 4.5, there exist several ideas for enhancements. In general, ozone cross sections, as used in the forward model, are temperature dependent (see Fig. 4.8) which obviously makes an ozone retrieval dependent on the temperature distribution along the line-of-sight. Our model accounts for this fact, though our selected channels for the retrieval are mostly outside a strong temperature dependence for ozone cross section, as is found within a wavelength range of 350 - 450 nm. A joint retrieval including also temperature, thus having three products included in the retrieval matrices, would give best results in such wavelength regions (cf., e.g., [*DeMajistre and Yee* (2002)]).

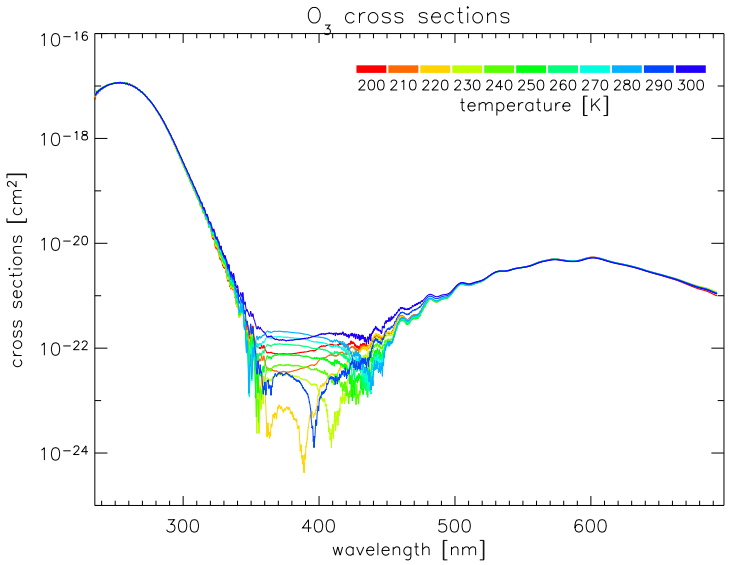

Figure 4.8. Temperature dependent ozone cross sections for typical GOMOS wavelengths between 250 and 700 nm.

A second enhancement to the constituent retrieval process is the actual use of retrieved temperature data and modification of the atmospheric background (refractivity, density) as seen by the forward model. This was investigated and we concluded that the quality of temperature profiles, gained by our SFA/SATU based inversion scheme, is not good enough to have a positive effect on the constituent retrieval. In turn, high resolution temperature profiles from GOMOS photometer data have the capability to provide accurate information on the state of the atmosphere at the time of measurement of transmission spectra.

4.6 Error Statistics Setup

In general, an error analysis and characterization of atmospheric profile retrievals is an important task for every sensor. Bayesian optimal estimation provides a very suitable

framework for this purpose also in case of occultation data (cf. [*Rieder and Kirchengast* (2001a), *Rieder and Kirchengast* (2001b), *Steiner and Kirchengast* (2004a), *Steiner and Kirchengast* (2004b)]).

Here we give an introduction into error statistics applied throughout this thesis (cf. [*Lang and Pucker* (1998), *Storch and Zwiers* (1999)]). We assume having a set of measurements $\mathbf{x}_i$ out of an ensemble $\mathbf{x}$ of possible states in a system of interest, then we can find estimators of several statistical properties like the mean value, the variance, and the standard deviation. Estimators are mere functions and random variables itself and depend on the variability of the sampling. In general such quantities are moments of distributions of random variables.

An appropriate estimator for the mean value (first moment) and for the variance (second moment) can be found with

$$\hat{\mathbf{x}} \equiv \frac{1}{n}\sum_{i=1}^{n}\mathbf{x}_i, \quad \hat{\boldsymbol{\sigma}}^2 \equiv \frac{1}{n}\sum_{i=1}^{n}\left(\mathbf{x}_i - \hat{\mathbf{x}}\right)^2. \tag{4.46}$$

Having defined such estimators we can now find equivalent definitions for differences of profiles

$$\Delta\mathbf{x} = \mathbf{x}_m - \mathbf{x}_r, \tag{4.47}$$

where $\mathbf{x}_m$ represents the measurement and $\mathbf{x}_r$ a corresponding reference profile. Here entities are more generally given in a vector notation due to the fact that we are looking at vertical distributions of geophysical quantities.

We are now interested in expectation values of our estimators in Eq. 4.46. The expectation value of $\hat{\mathbf{x}}$ is

$$\langle\hat{\mathbf{x}}\rangle = \frac{1}{n}\sum_{i=1}^{n}\langle\mathbf{x}_i\rangle = \langle\mathbf{x}\rangle \equiv \mu_{\mathbf{x}}, \tag{4.48}$$

while for the variance follows

$$\langle\hat{\boldsymbol{\sigma}}^2\rangle = \frac{1}{n}\sum_{i=1}^{n}\left\langle\left(\mathbf{x}_i - \hat{\mathbf{x}}\right)^2\right\rangle = \boldsymbol{\sigma}_{\mathbf{x}}^2 - \boldsymbol{\sigma}_{\hat{\mathbf{x}}}^2 = \frac{n-1}{n}\boldsymbol{\sigma}_{\mathbf{x}}^2, \tag{4.49}$$

where $\boldsymbol{\sigma}_{\mathbf{x}}^2$ and $\boldsymbol{\sigma}_{\hat{\mathbf{x}}}^2$ are the variances for $\mathbf{x}$ and $\hat{\mathbf{x}}$, respectively. Obviously Eq. 4.49 does not appropriately represent the expected mean value for the variance. We therefore have to correct Eq. 4.49 by the factor $n/(n-1)$.

Superseding now $\mathbf{x}_i$ in Eq. 4.46 by $\Delta\mathbf{x}$ we obtain an estimator for a so-called bias profile

$$\hat{\mathbf{b}} \equiv \frac{1}{n}\sum_{i=1}^{n}\Delta\mathbf{x}. \tag{4.50}$$

Applying this to Eqs. 4.46 and 4.49 we find

$$\hat{\mathbf{s}}^2 \equiv \frac{n}{n-1}\hat{\boldsymbol{\sigma}}^2 = \frac{1}{n-1}\sum_{i=1}^{n}\left(\Delta\mathbf{x} - \hat{\mathbf{b}}\right)^2, \tag{4.51}$$

where $\hat{\mathbf{s}}$ is an estimator of the standard deviation of a bias-free profile

$$\mathbf{x}_f = \Delta\mathbf{x} - \hat{\mathbf{b}}. \tag{4.52}$$

More generally one can now define an error covariance matrix

$$\mathbf{S} = \frac{1}{n-1}\sum_{i=1}^{n}\mathbf{x}_f\mathbf{x}_f^T, \tag{4.53}$$

where the diagonal elements are variances at different height levels k, while off-diagonal elements stand for covariance elements. Another quantity often used is the root-mean-square error (rms)

$$\mathbf{r} = \sqrt{\hat{\mathbf{b}}^2 + \hat{\mathbf{s}}^2}. \tag{4.54}$$

Finally we define an error correlation matrix

$$\mathbf{R} \rightarrow R_{kl} = \frac{s_{kl}}{\sqrt{s_{kk}s_{ll}}}, \tag{4.55}$$

where off-diagonal elements denote vertical error cross-correlations. Values of one of the correlation matrix $\mathbf{R}$ correspond to full correlation, while zero off-diagonal values indicate no correlation. In the latter case the diagonal elements are all one and $\mathbf{R} = \mathbb{1}$, the unit matrix.

5

Validation Setup and Retrieval Results

This Chapter is dedicated to a resume of IGAM retrieval schemes setups for ozone and temperature profiles, with Envisat/GOMOS input data. We developed a joint ozone and NO_2 inversion scheme based on GOMOS transmission data, processed with an optimal estimation technique by incorporating *a priori* information. In a second task we set up a temperature retrieval by exploiting GOMOS SFA/SATU mirror data. Mirror data was converted into bending angles and then optimized at high altitudes by applying the statistical optimization approach. Such optimized bending angles were used to calculate density, pressure, and temperature profiles.

For both retrieval routines (joint ozone-NO_2 and temperature) real GOMOS data were available in more day ensembles for the years 2002 and 2003.

5.1 Setup for Ozone Retrieval

5.1.1 Ozone Validation Setup

For our joint ozone and NO_2 retrieval we have chosen an optimal estimation scheme by incorporating prior knowledge. Reliable *a priori* information was taken from AFGL-TR-86 data (FASCODE model) (cf., e.g., [*Anderson et al.* (1995)]) profiles. Retrieved ozone profiles are validated with operational GOMOS level 2 data as well we show a comparison with ECMWF analysis data. ECMWF analysis data for ozone is known to have biases (cf., e.g., [*Nett* (2002), *Dethof* (2004), *Bracher et al.* (2004)]), nevertheless if one would subtract an ECMWF/ozone - IGAM/ozone bias, profile validation shows good results.

NO_2 profiles are retrieved as a side-product, helping the ozone retrieval algorithm to gain performance in height and wavelength ranges, where signal absorption by NO_2 is comparable to the effects by ozone. The processing chain is purely optimized for ozone and thus the NO_2 retrieval produces profiles not considered for validation. Future

optimizations will make a full joint ozone-NO_2 retrieval possible, by, e.g., modifying the Jacobian matrix, or new channel selections by carefully looking at the information content. A detailed discussion of NO_2 retrieval processes is therefore beyond the scope of this thesis.

In this Section we summarize the results of a feasibility study for an ozone retrieval algorithm. We show pure simulated data and results of an exploitation of GOMOS real transmission data. Ozone profiles from real data are validated with GOMOS operational level 2 data and with ECMWF analysis data.

For the IGAM ozone retrieval, GOMOS transmission spectra and geolocation data were taken and processed with an optimal estimation technique (cf. Section 4.4). The forward model and its derivative are iteratively called and form the core of the retrieval. For initialization of the iteration we choose the *a priori* profile. The model is capable of processing real and simulated data, where the latter provided a basis for the feasibility of the whole scheme. Once we were convinced in the simulated model [*Retscher et al.* (2002)] it had to be adapted in order to accept non-smoothed transmission data input.

5.1.2 Test of Setup: Simulated Ozone Retrieval

We first prepared a simulation study on ozone and NO_2 data by using an end-to-end simulator (EGOPS [*Kirchengast* (1998), *Kirchengast et al.* (2002)]) providing quasi-true Envisat orbits, geodetical positions of Envisat as well as the approximated position of an occulted sample star. We selected simulated occultation events (see Fig. 5.1) and compared single profiles and errors. As well we performed error statistics, as outlined in Section 4.6, with 100 profiles contributing. The star image was modeled in a simplified manner only providing light at different wavelengths, where a further dependence of the model on the star temperature or the obliquity of the occultation was not considered.

Day		**Latitude**
September	2001, 15	$\sim 50°$
March	2002, 06	$\sim 38°$
May	2002, 25	$\sim 18°$
November	2003, 12	$\sim 70°$

Table 5.1. Simulated occultation events for four selected days in the years 2001, 2002, and 2003 at four different latitudes.

Physical interpretations and realizations of scintillation and dilution effects were here neglected in the first place, but resulting modeled transmissions account for these effects with an imposed random error (forward model error gained by the error pattern method cf. Section 4.4.1) with reasonable size of $\sim 1\%$.

The $\mathbf{S}_{ap}$ were chosen to have a standard deviation of 30% for ozone and 40% for NO_2, respectively. The error characteristic, the random errors for the forward model and for *a priori* data, were designed as outlined in Section 4.4.1. As a basis for quasi-true and *a priori* ozone and NO_2 number densities we used CIRA-86 and MSISE-90 data. Cross sections were taken from the official temperature dependent GOMOS cross section database.

The main reason why NO_2 was included into our retrieval scheme is given by its high absorption of the star image in wavelength regions between 350 and 450 nm. This coin-

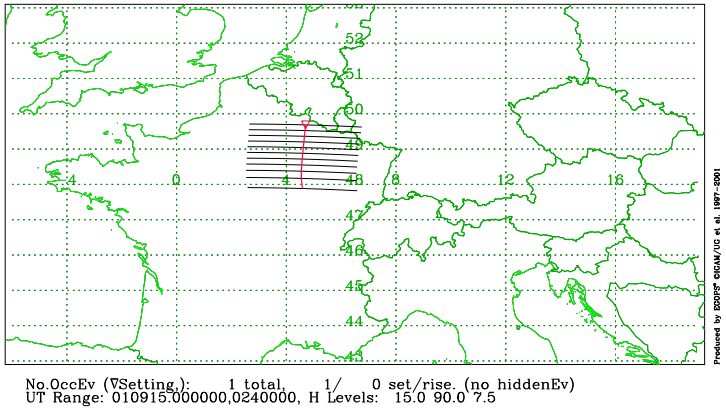

Figure 5.1. Test occultation event shown with 7.5 km spacing between rays from 15 to 90 km along the tangent point trajectory in nadir view over north-eastern France and southern Belgium. The bundle of parallel lines illustrates the raypaths for ±150 km about the tangent point, roughly reflecting the horizontal resolution of the occultation data.

cides with the region of low signal absorption by ozone. Fig. 1.5 shows ozone and NO_2 absorption coefficients for all GOMOS wavelengths. The forward model also includes absorption coefficients from NO_3 and refraction coefficients from air (see Fig. 1.6). Our simulated joint ozone-NO_2 retrieval perfectly reflects the effects of the NO_2 interference in this regime, nevertheless in this validation setup NO_2 was not retrieved with considerable quality.

In this simulation study we restricted ourselves to include a small set of well selected wavelength channels perfectly placed to cover ozone absorption bands [*Salby* (1995)] such as the Hartley (200 - 310 nm), the Huggins (310 - 400 nm), and the Chappuis band (400 - 850 nm), which is especially important for absorptions below 25 km. Our set of channels (260, 280, 288, 295, 302, 309, 317, 328, 334, 337, 340, 343, 600, and 605 nm) therefore provides the maximum possible information coming from the measurement by simultaneously reducing the elapsed time to retrieve one profile.

Simulated data were used to show whether the algorithm meets the requirements we defined. A carefully selected set of artificial data will give visibility to possible leaks in the understanding of the chosen retrieval process. Figs. 5.2 to 5.5 clearly point out the basic capability of the algorithm to be used for operational data.

Here we have selected four single events and present ozone profiles and its corresponding errors. We furthermore perform error statistics for all four single events by choosing 100 randomly initiated profiles calculated for the same occultation location. Bias profiles and the bias ± standard deviations $\hat{\mathbf{b}} \pm \hat{\mathbf{s}}$ are shown. All four profiles show excellent behavior regardless of the chosen latitude. The bias profiles for all four simulated profiles show errors almost always lying below 1% for heights between 20 and 70 km. Below this height region the bias increases to 2%. Above 70 km the profiles tend to have biases greater than 5% reflecting effects of low star light absorption and thus low signal response in the Jacobian matrix. Due to the low signal the *a priori* profile with 30% error has more effects on the retrieved profiles. The standard deviations of these profiles are below 3% from 30 to 70 km and increases to 7% at $\sim$ 20 km.

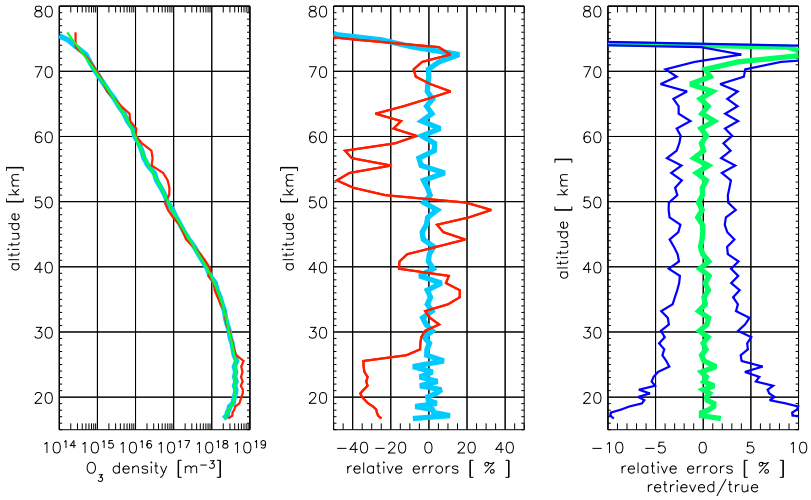

Figure 5.2. Simulated single ozone profile (left panel) and corresponding errors (mid panel) for an event located at $\sim 50°$ latitude. The blue line denotes the retrieved profile, the green line (almost not visible) is the "true" profile, and the red line is the *a priori* profile. In the error plot the blue line is the retrieved/"true" error while the red lines denotes the retrieved/*a priori* error. The right panel shows statistical errors with 100 profiles contributing, where the green line is the bias profile and the enveloping blue lines are the bias ± standard deviation.

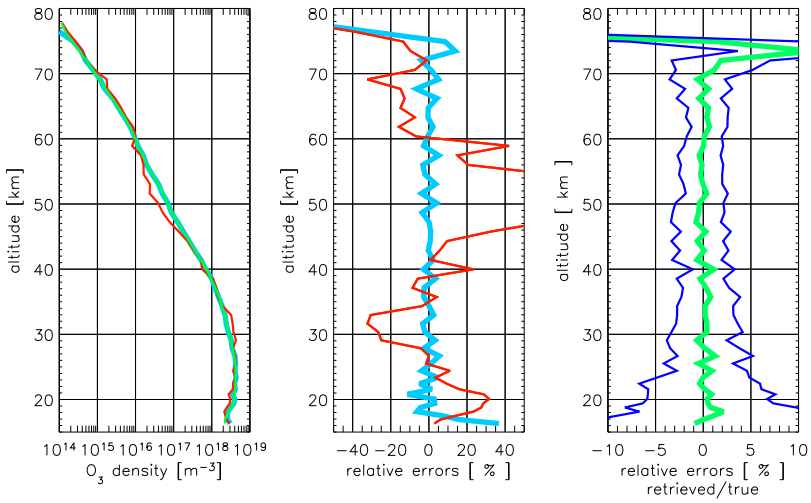

Figure 5.3. Simulated single ozone profile (left panel) and corresponding errors (mid panel) for an event located at $\sim 38°$ latitude. The right panel shows statistical errors with 100 profiles contributing. For further description of the graphs see caption of Fig. 5.2.

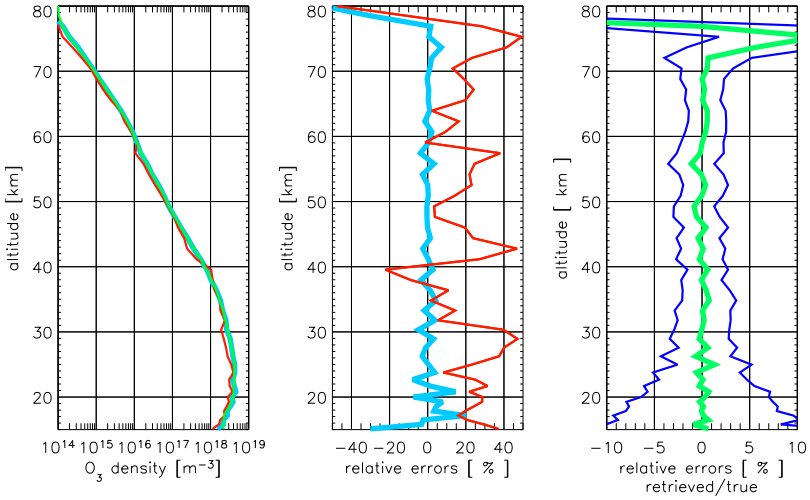

Figure 5.4. Simulated single ozone profile (left panel) and corresponding errors (mid panel) for an event located at $\sim 18°$ latitude. The right panel shows statistical errors with 100 profiles contributing. For further description of the graphs see caption of Fig. 5.2.

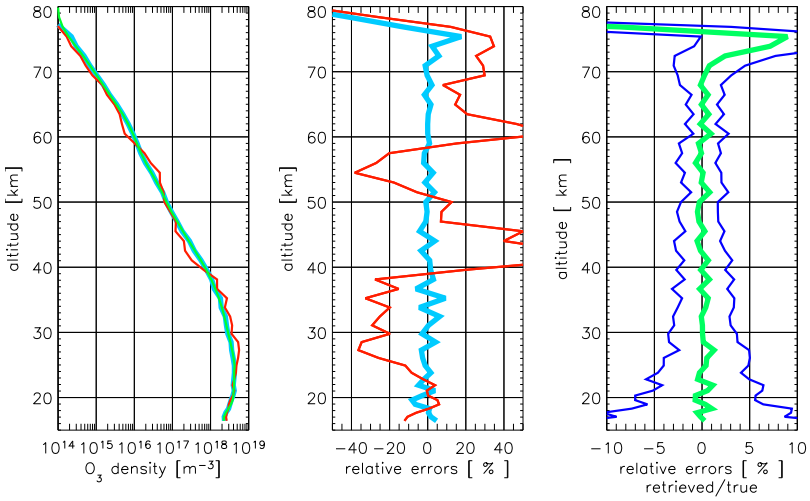

Figure 5.5. Simulated single ozone profile (left panel) and corresponding errors (mid panel) for an event located at $\sim 70°$ latitude. The right panel shows statistical errors with 100 profiles contributing. For further description of the graphs see caption of Fig. 5.2.

5.2 Real Ozone Profile Retrieval Validation (set 2002)

For the retrieval of real ozone and NO_2 profiles we used official GOMOS level 1b and level 2 data, which were provided by ACRI-ST in Sophia Antipolis, France. ACRI-ST is one of four (ACRI-ST, SA/CNRS, FMI, IASB) expert support laboratories (ESL) for the GOMOS instrument. The data were then reprocessed with the so-called BEAT-software (cf. http://www.science-and-technology.nl/beat/, July 2004), which is now available for reading raw data as well as displaying graphs of measured data. BEAT is an ESA-funded software tool developed to ease the life for users of Envisat atmospheric instruments data (GOMOS, MIPAS, and SCIAMACHY) as well as data from GOME on ERS-2, the predecessor instrument of SCIAMACHY.

The GOMOS data products are stored in several files shown in Tab. 3.10, where we used `GOM_TRA_1` and `GOM_NL__2` products corresponding to our previously (cf. Section 3.3.6) introduced notation of GOMOS level 1b and level 2 data.

This thesis summarizes retrieved data for two different sets listed in Tab. 5.2 and Tab. 5.5. One set contains data from an official GOMOS validation period in 2002, while the second set uses data of 2003 (cf. Section5.2), where operational data has been further improved in quality. Here we reduced the set of available data due to large errors

Periods with GOMOS data	
September	2002, 20 - 27
October	2002, 11 - 13
December	2002, 02

Table 5.2. For the year 2002 data GOMOS data were available in September, October, and December.

in level 1b transmissions and reference level 2 ozone data. Such errors significantly diminish the performance of our retrieval. The remaining transmission profiles where first selected by arguments of an optimal set of wavelengths (cf. Section 5.1.2) and then adapted to our needs of retrievals for upper and lower stratospheric ozone profiles. Real transmissions were smoothed by running averages (cf. Section 4.3) and then corrected for scintillation and refractive dilution effects (cf. Section 4.2), which has a significant impact on the lower stratospheric ozone retrieval profiles.

The quality of transmission data is further strongly dependent on the star magnitude, the star temperature, and the obliquity of the occultation. Light coming from bright stars is able to penetrate the Earth's atmosphere down to lower heights than light stemming from weak stars. In general the penetration depth of light into the atmosphere is known to be wavelength dependent. In our analysis we find an ozone retrieval dependence mostly on the star temperature. Stars with temperatures between 8000 and 11000 K clearly favors our retrieval where the corresponding maximum of the Planck function lies within the UV wavelength range. This is reflected by a large number (passing the quality check) of contributing profiles in the error statistics of stars like Sirius (-1.44^m, 11000 K), Fomalhaut (1.16^m, 9700 K) and δ Velorum (1.95^m, 10600 K).

In this Section we give a selection of ozone profiles validated with GOMOS level 2 data and then sorted by different star magnitudes and periods. Tab. 5.3 and Tab. 5.7 summarize all available profiles and outliers for all latitudes with corresponding star

magnitudes and star temperatures as well as the wavelength $\lambda_{\max}$, where the Planck function B_ν (cf. Eq. 1.25) given in [μm] has a maximum $\lambda_{\max} = 2898\, T^{-1}$.

ECMWF T511L60 analysis data were taken for the same period, where GOMOS data were available. ECMWF T511L60 ozone data allows for a comparison with GOMOS ozone data up to around 60 km. Ozone is fully integrated into the ECMWF forecast model and analysis system as an additional three-dimensional model and analysis variable similar to humidity. The forecast model includes a prognostic equation for the ozone mass mixing ratio with a parameterization of sources and sinks of ozone.

Period	**Latitude**	$\mathbf{x_{acc}}$	$\mathbf{x_{out}}$
2002-09-20 – 2002-12-02	all	371	25
2002-09-20 – 2002-12-02	low	93	1
2002-09-20 – 2002-12-02	mid	226	24
2002-09-20 – 2002-12-02	high	52	0
2002-09-20 – 2002-09-27	all	307	22
2002-09-20 – 2002-09-27	low	65	0
2002-09-20 – 2002-09-27	mid	198	22
2002-09-20 – 2002-09-27	high	44	0
2002-10-11 – 2002-10-13	all	35	3
2002-10-11 – 2002-10-13	low	13	1
2002-10-11 – 2002-10-13	mid	22	2
2002-10-11 – 2002-10-13	high	–	–
2002-12-02 – 2002-12-02	all	29	0
2002-12-02 – 2002-12-02	low	15	0
2002-12-02 – 2002-12-02	mid	6	0
2002-12-02 – 2002-12-02	high	8	0

Table 5.3. Number of processed and accepted profiles $\mathbf{x}_{\text{acc}}$ contributing to the error statistics and not considered outliers $\mathbf{x}_{\text{out}}$. The profiles listed here are measured under dark limb conditions. The outliers are identified as profiles with errors larger than 50% between 30 and 60 km altitude.

Fig. 5.6 shows single profiles and errors from two selected events in the year 2002. The profiles are validated with operational GOMOS ozone and with ECMWF analysis data. Single profiles, validated with GOMOS level 2 data, tend to have errors of up to 10% between 30 and 70 km and increasing ones below and above this height region. Errors from the ECMWF validation show a clear bias of about −30%. This bias is known to be in the ECMWF product (cf., e.g., [*Nett* (2002), *Dethof* (2004), *Bracher et al.* (2004)]). Nevertheless a profile validation with ECMWF can be useful, if the observed biases behave almost equally throughout our profile validation.

$m_{\mathbf{v}}$	$T_{\mathbf{star}}$ [**K**]	$\lambda_{\mathbf{max}}$ [**nm**]	$\mathbf{x_{acc}}$	$\mathbf{x_{out}}$
–1.44	11000	263.45	58	0
–0.73	7000	414.00	56	0
0.40	6500	445.84	68	0
1.16	9700	298.76	85	0
1.50	26000	111.46	18	0
1.73	15200	190.65	33	0
1.95	10600	273.39	26	1
2.15	2800	1035.0	22	0
2.44	20000	144.90	3	0
2.65	15200	190.65	5	0
2.76	30000	96.600	6	0
2.90	9300	311.61	10	2
3.03	26000	111.46	6	0

Table 5.4. Total retrieved and accepted ozone profiles $\mathbf{x}_{\mathrm{acc}}$ and outliers $\mathbf{x}_{\mathrm{out}}$ for visual star magnitude m_{v} and the star temperature T_{star} in the validation period 2002. The λ_{max} denotes the maximum of the Planck function B_ν at given temperature. The outliers are identified as profiles with errors that are larger than 50% between 30 and 60 km altitude.

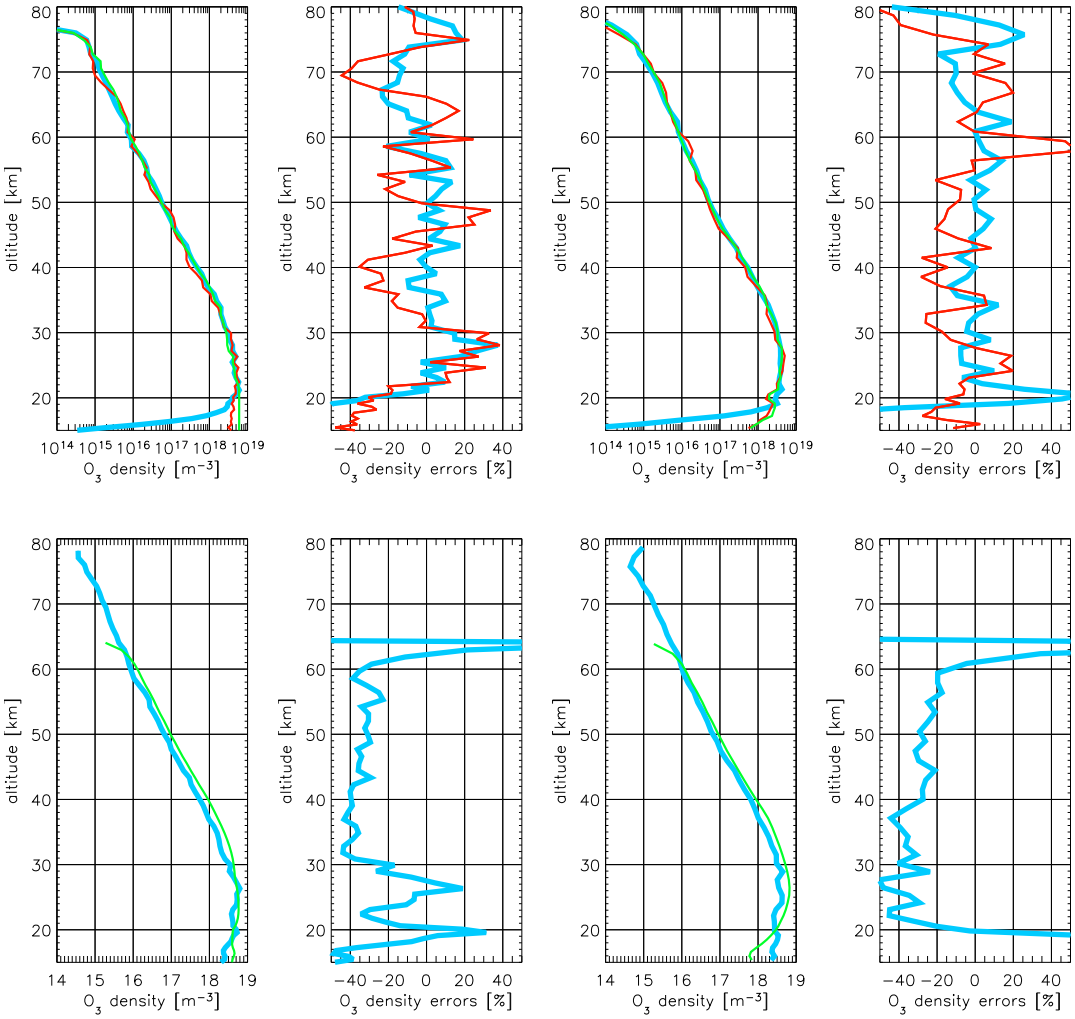

Figure 5.6. Two selected ozone and corresponding error profiles validated with operational GOMOS level 2 profiles are shown in the upper panel. The two left plots correspond to a star with -1.44^m and the two right plots are results from a star with -0.73^m. The ozone densities are shown in a log plot, where the heavy light blue line denotes the retrieved profile, the small green line is the reference GOMOS level 2 profile, and the light red line represents *a priori* data. The errors for the validation with GOMOS level 2 data profiles are given with a heavy light blue line while errors to the *a priori* profiles are given with light red lines. In the lower panel we show two selected ozone and corresponding error profiles validated with ECMWF analysis data. The ozone densities are shown in a log plot, where the heavy light blue line denotes the retrieved profile (as in the upper panel) and the small green line is the reference ECMWF analysis profile. The errors for the validation with ECMWF analysis profiles are given with a heavy light blue line.

5.2.1 Validation with globally distributed profiles

Here we present the statistics of a selection of globally distributed occultation events separated by date and latitude regimes. The latitude regimes are divided into low (0° – 30°), mid (30° – 60°), and high (60° – 90°) latitudes. Such a selection is especially useful for looking at ozone trends in the high latitude profiles where the ozone density is significantly diminished. Large scale stratospheric ozone depletion is mostly reported from high latitudes, where meteorological conditions favor depletion processes (cf. Section 1.4).

In the following graphs (see Figs. 5.7 to 5.10) the heavy green line denotes the bias profile $\hat{\mathbf{b}}$, while the enveloping fine blue lines are the bias $\pm$ standard deviation profile $\hat{\mathbf{b}} \pm \hat{\mathbf{s}}$. The sets include occultations of stars between -1.44^m and 3.03^m. Stars with magnitudes greater than 3.03^m show significantly larger errors and are not considered. We apply an outlier correction, by not considering profiles with errors larger than 50% between altitudes of 30 and 60 km.

As in the single profile statistics, here we see good retrieval performance at all latitude regions, where biases are found $\sim$ 5% from 25 - 65 km. Below 25 km we find slightly increasing biases. Above 65 km most profiles tend to negative biases with values of 20% at 70 km. This reflects the fact that data measured at such altitudes have small transmission values and large fluctuations, which affect the retrieval quality. The standard deviation is at $\sim$ 20% for plots in September and October. Plots from December have a smaller standard deviation with $\sim$ 15%, though only a few profiles are considered in the statistics.

Errors in the validation with ECMWF profiles are, as already denoted for single profiles, large and lie around -30%. Especially low and mid latitude profiles from September and October have a strong signal in the stratosphere at $\sim$ 25 km with a changing bias to positive values.

Fig. 5.7 shows the overall plots from all available occultation data. No significant differences for systematic deviations in latitude selected profiles are found, but ECMWF validation at high latitudes has an almost constant bias. The profiles validated with GOMOS level 2 data and selected by periods (see Figs. 5.8, 5.9, and 5.10) have almost constant values of bias and standard deviation as denoted above.

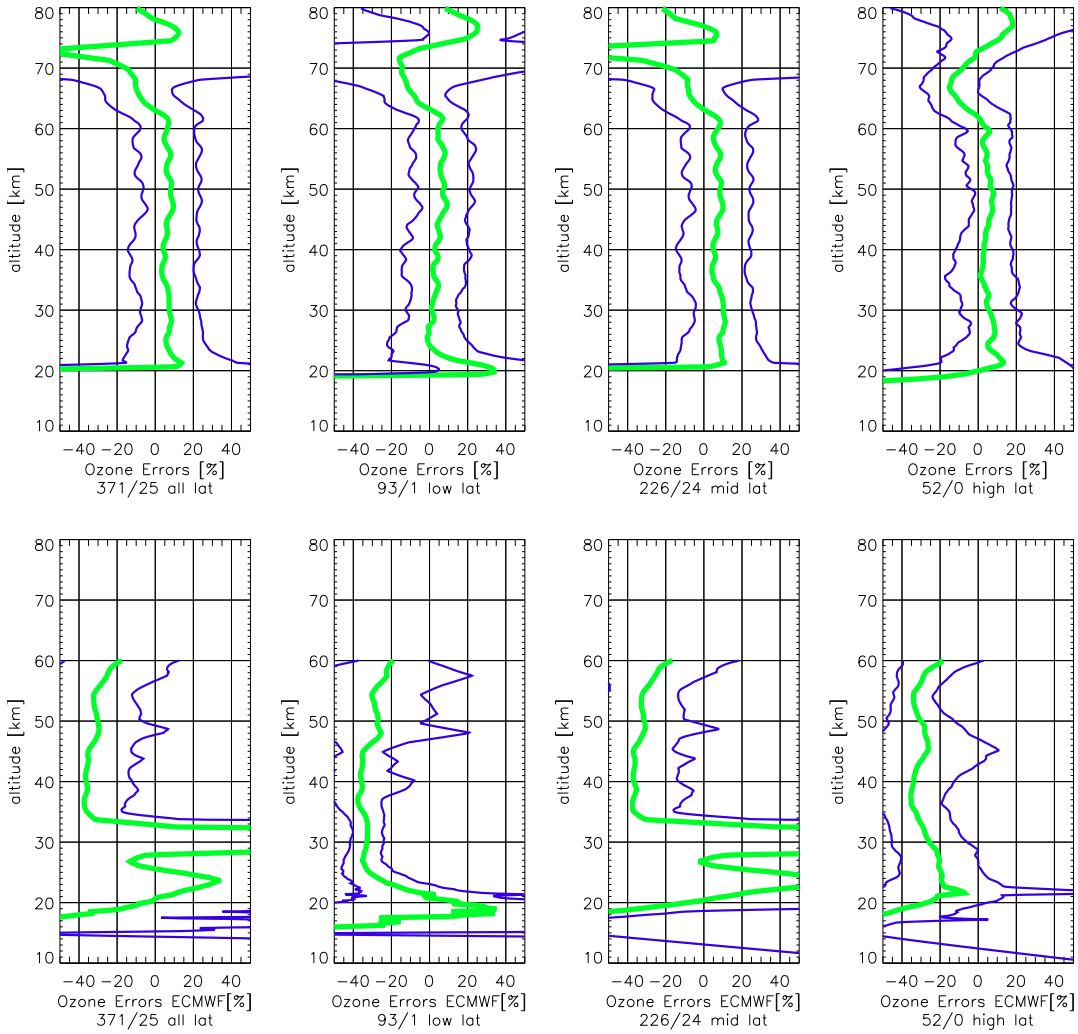

Figure 5.7. Ozone error statistics for more day ensembles in the period 2002-09-20 – 2002-12-02 (whole set 2002). In the upper panels we present profiles validated with GOMOS level 2 files and in the lower panels we validate with ECMWF analysis data. From the left, the first panel shows the overall profile, the second, third, and fourth panel show the low, mid, and high latitude selected profiles. The heavy green line denotes the bias profile $\hat{\mathbf{b}}$, while the enveloping fine blue lines are the bias $\pm$ standard deviation profile $\hat{\mathbf{b}} \pm \hat{\mathbf{s}}$. To each error profile contributes a certain number of available files passing the quality check. This is given below each plot where on the left one finds the number of accepted profiles and the right number denotes the outliers.

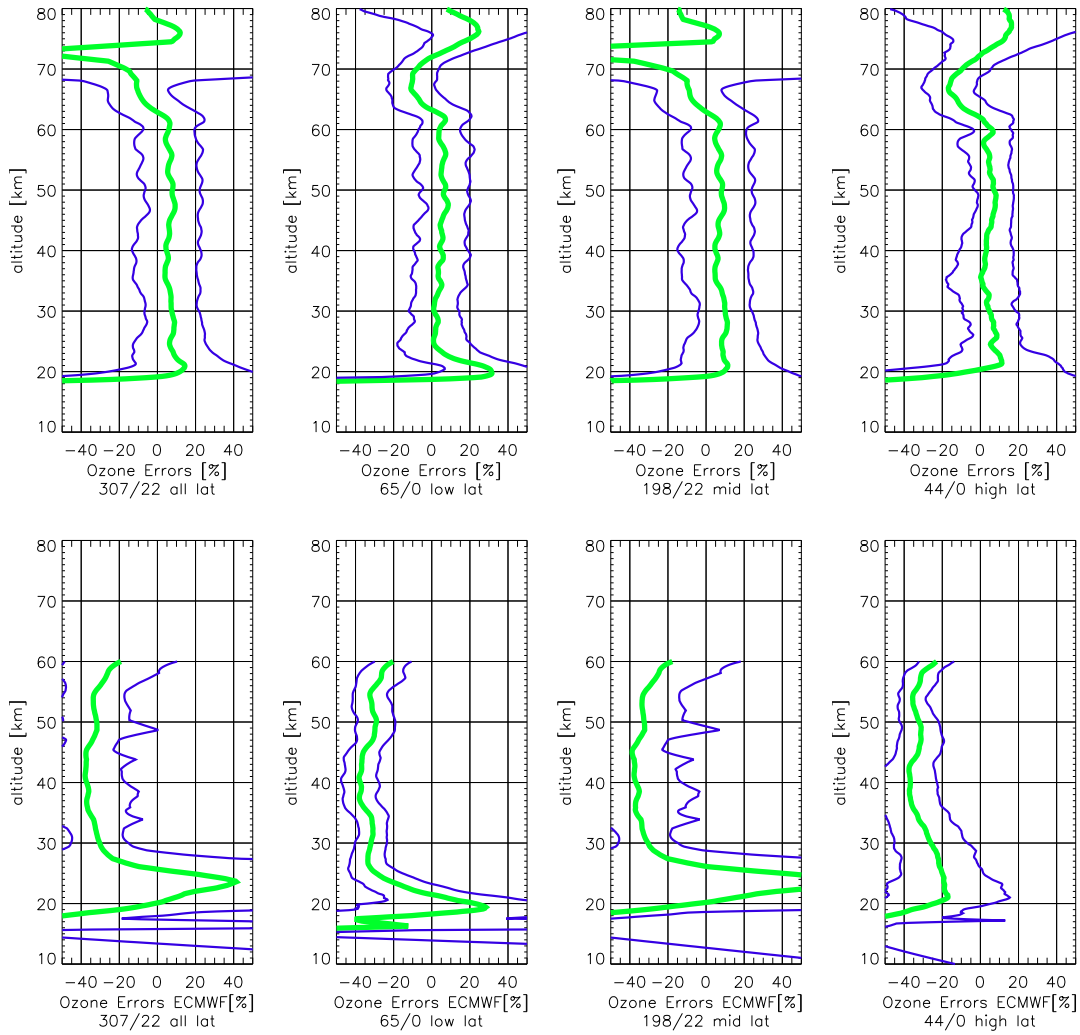

Figure 5.8. Ozone error statistics for more day ensembles in the period 2002-09-20 – 2002-09-27 (whole set Sep. 2002). For further description of the graphs see caption of Fig. 5.7.

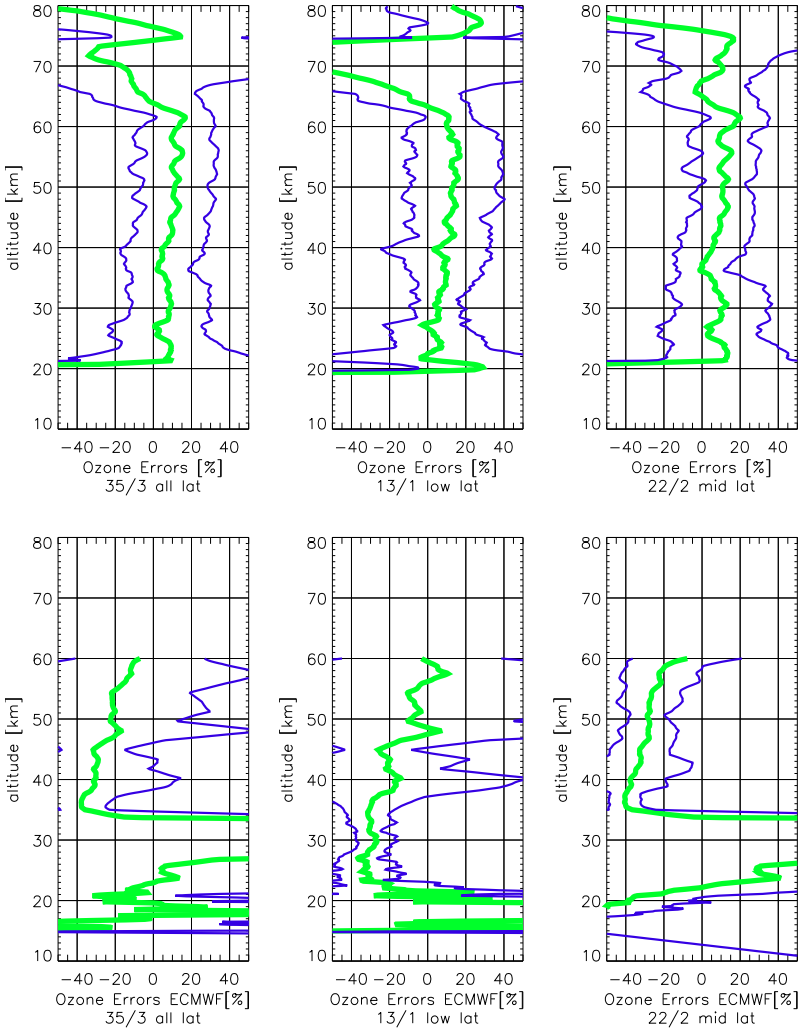

Figure 5.9. Ozone error statistics for more day ensembles in the period 2002-10-11 – 2002-10-13 (whole set Oct. 2002). For further description of the graphs see caption of Fig. 5.7.

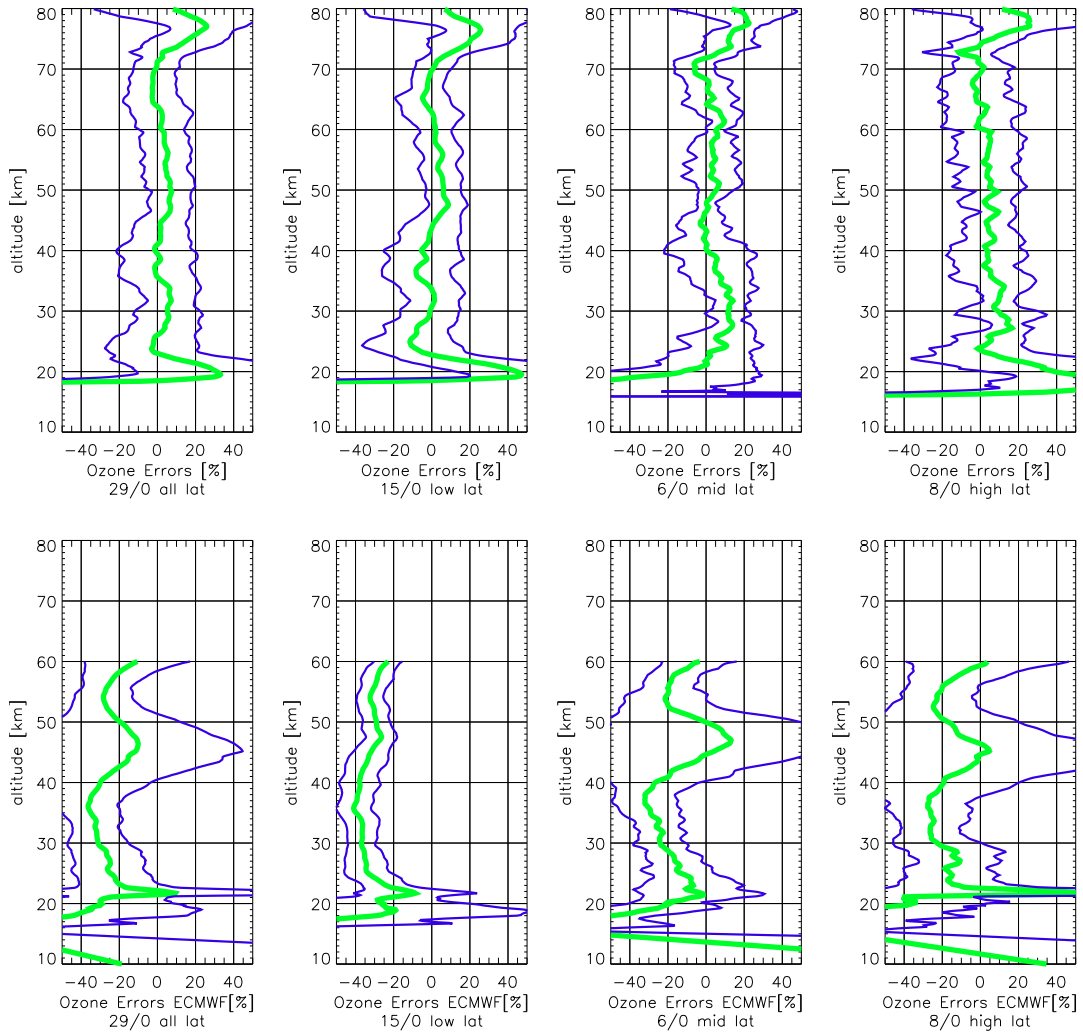

Figure 5.10. Ozone error statistics for a singe day ensemble on 2002-12-02 (whole set Dec. 2002). For further description of the graphs see caption of Fig. 5.7.

5.2.2 Ozone Profiles and Errors at different Star Magnitudes

In the previous Section we analyzed profiles accumulated from different stars, sorted by latitude regimes and available periods in the data. Here we look at the profile validation with GOMOS level 2 and ECMWF analysis data, where our retrieved ozone profiles are sorted by star magnitudes and their corresponding temperatures.

The plots (see Figs. 5.11, 5.12, and 5.13) clearly show a star magnitude and temperature dependence for all latitude regimes. For bright stars with high temperatures the ozone retrieval works best and biases between 20 and 65 km height are below 10%, for some special (bright) stars even below 5%. As already noted in Section 5.2.1, below and above this altitude region errors increase independent of the selected star. Standard deviations are mostly found below 15% from 20 km up to 65 km.

In the upper stratospheric regime, errors significantly rise due to a high signal (transmission $T \simeq 1$) throughout all wavelengths, which in turn makes it difficult to see clear ozone absorption structures. From the ozone layer peak ($\sim$ 25 km) downwards the star signal diminishes quickly which results in low signal-to-noise ratios and large fluctuations in the ozone profile.

In detail, there is an explicit difference in the retrieval quality when we look at error profiles from different stars. Bright stars with magnitudes -1.44^m, -0.73^m, 0.40^m, 1.16^m, 1.50^m, and 1.73^m show a constant positive bias from 20 to 65 km. In theory the star with 1.93^m and a temperature of 10600 K should give good results in the Hartley and Huggins band, but biases lie at $> 15\%$, which possibly can be explained by large covariances in the transmission measurement. Dim stars with magnitudes 2.65^m, 2.76^m, 2.90^m, and 3.03^m have changing biases from negative values between 20 and 40 km and positive values from 40 to 70 km. A bad example was chosen as well. The star with magnitude 2.15^m and a temperature of only 2800 K is obviously too dim and too cold in order to give good retrieval results from 30 km upwards.

Validation with ECMWF profiles is done with the same data set as discussed for the validation with GOMOS operational data. As mentioned in the previous Section, almost all profiles have a large -30% bias, but some profiles have interesting features. For the star -1.44^m the bias goes from almost -40% at high altitudes to about 10% in the low stratosphere. The ECMWF profile there has a tendency to overestimate the ozone density, which is not seen in other profiles.

A direct comparison of GOMOS level 2 and ECMWF data is not given here, but can be estimated qualitatively. GOMOS profiles optimally reach heights of more than 80 km, but in this validation set we can only use data up to $\sim$ 60 km, which is the maximum height level available for ECMWF data. For convenience of comparison with simulated data (same altitude range), the plots are given from 15 to 80 km.

In the following graphs the heavy green line denotes the bias profile $\hat{\mathbf{b}}$, while the enveloping fine blue lines are the bias $\pm$ standard deviation profile $\hat{\mathbf{b}} \pm \hat{\mathbf{s}}$.

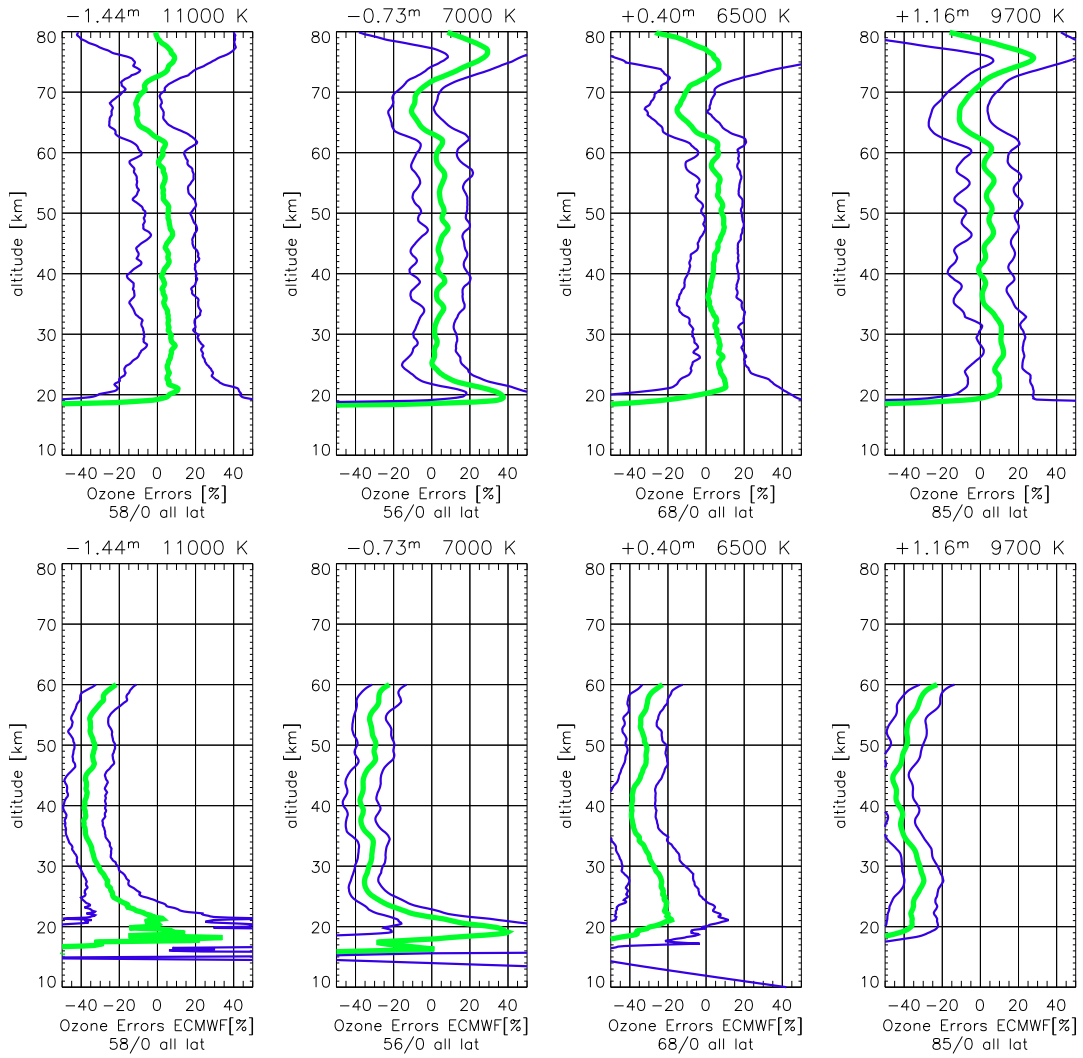

Figure 5.11. Ozone error statistics for more day ensembles in the period 2002-09-20 – 2002-12-02 (whole set 2002). In the upper panels we present profiles validated with GOMOS level 2 files and in the lower panels we validate with ECMWF analysis data. From the left to the right, the panels show data for selected stars with visual magnitudes -1.44^m, -0.73^m, 0.40^m, and 1.16^m as well as corresponding star temperatures. The heavy green line denotes the bias profile $\hat{\mathbf{b}}$, while the enveloping fine blue lines are the bias $\pm$ standard deviation profile $\hat{\mathbf{b}} \pm \hat{\mathbf{s}}$. To each error profile contributes a certain number of available files passing the quality check. This is given below each plot where on the left one finds the number of accepted profiles and the right number denotes the outliers.

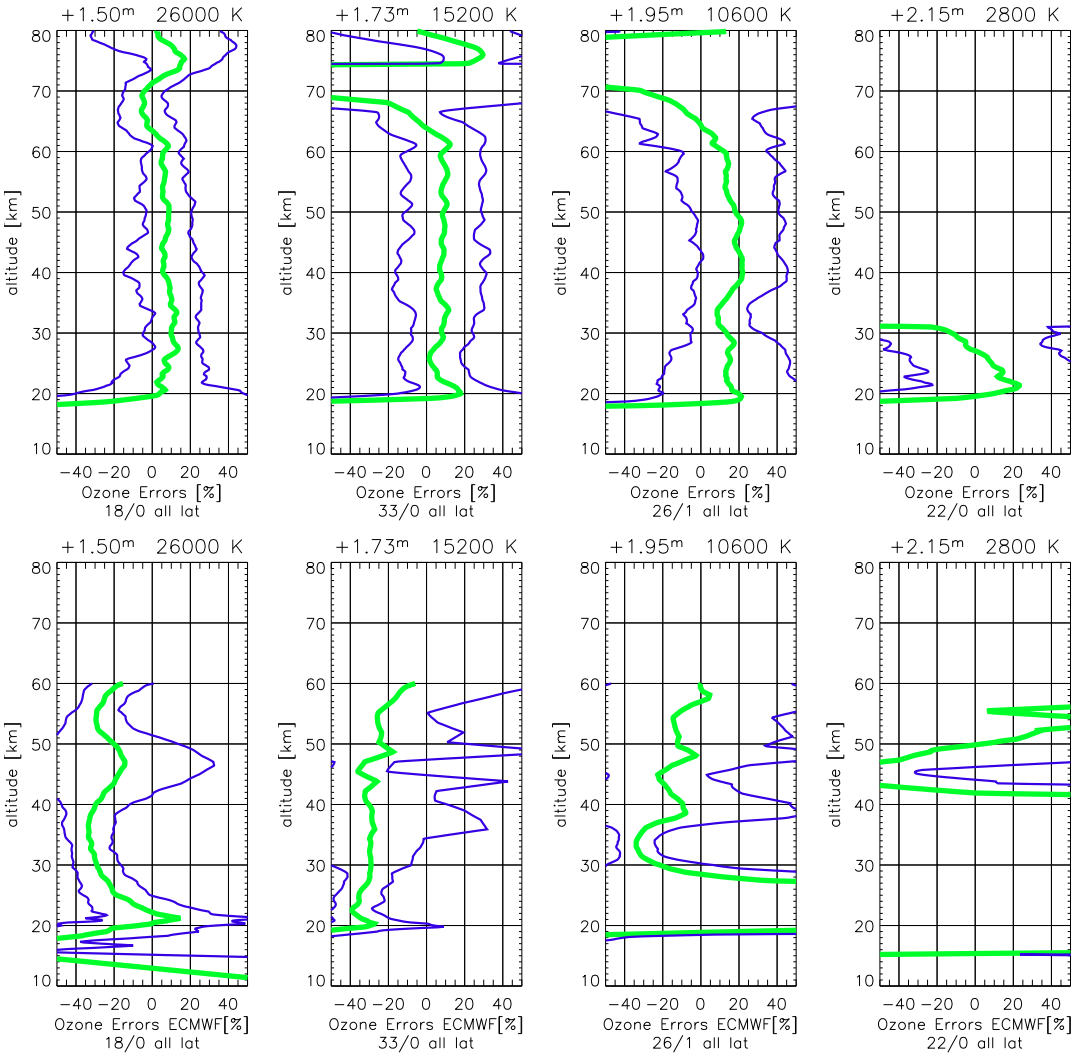

Figure 5.12. Ozone error statistics for more day ensembles in the period 2002-09-20 – 2002-12-02 (whole set 2002). In the upper panels we present profiles validated with GOMOS level 2 files and in the lower panels we validate with ECMWF analysis data. From the left to the right, the panels show data for selected stars with visual magnitudes 1.50^m, 1.73^m, 1.95^m, and 2.15^m as well as corresponding star temperatures. For further description of the graphs see caption of Fig. 5.11.

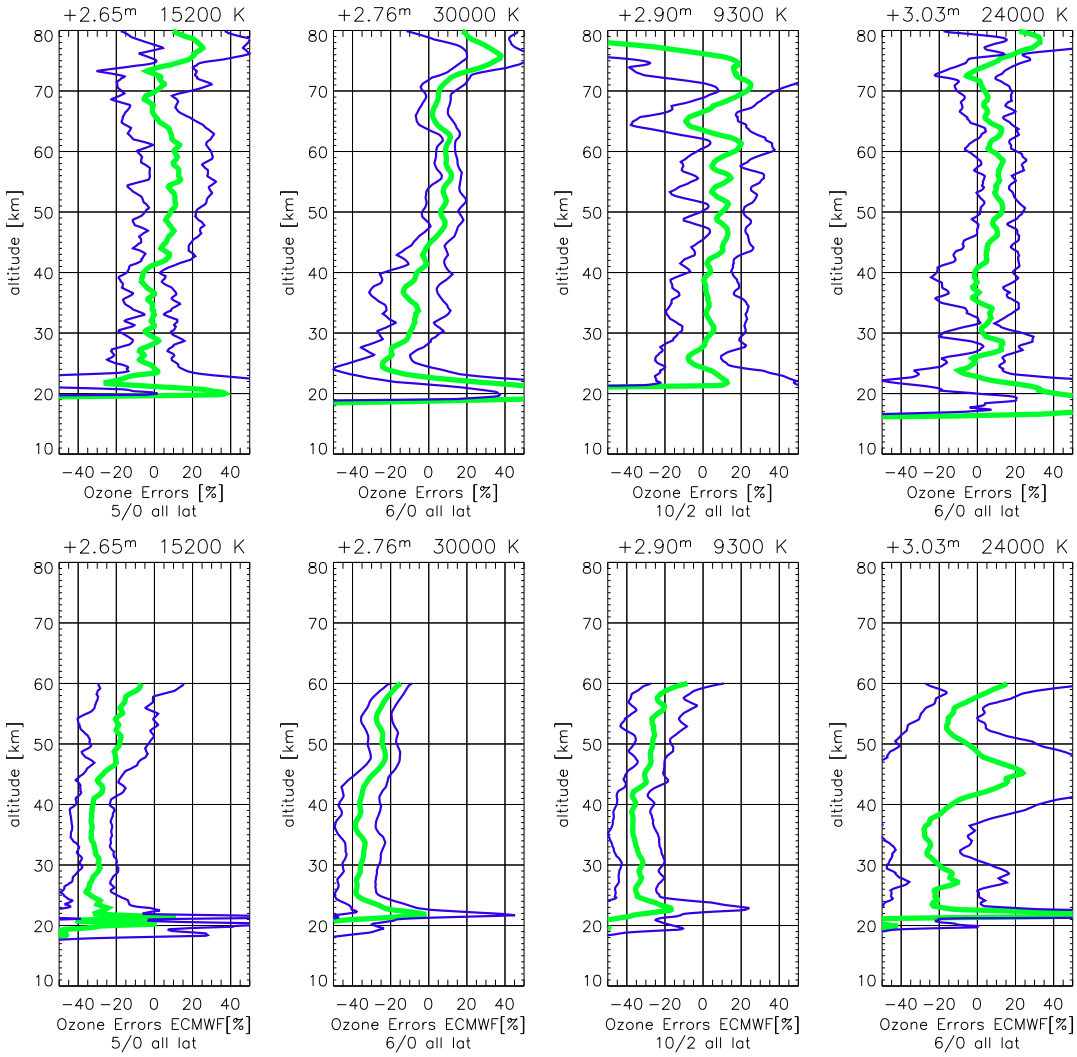

Figure 5.13. Ozone error statistics for more day ensembles in the period 2002-09-20 – 2002-12-02 (whole set 2002). In the upper panels we present profiles validated with GOMOS level 2 files and in the lower panels we validate with ECMWF analysis data. From the left to the right, the panels show data for selected stars with visual magnitudes 2.65^m, 2.76^m, 2.90^m, and 3.03^m as well as corresponding star temperatures. For further description of the graphs see caption of Fig. 5.11.

5.3 Real Ozone Profile Retrieval Validation (set 2003)

In this Section we perform a validation study for ozone retrieval data from our algorithm validated with operational GOMOS level 2 and ECMWF data. The validation period was September 2003. In order to see changes in retrieval quality during one month we have selected three subsets, each collecting profiles from 10 consecutive days.

The total set of available retrieved data were corrected in the way that profiles with errors larger than 50% between 30 and 60 km are identified as outliers and not considered in the overall plots.

Most of the arguments discussed in Section 5.2 are valid as well here. For the data set from 2003 the operational GOMOS ozone retrieval software was updated by several enhancements, now having increased data quality. In the data set analyzed here we find occultations under dark and bright limb conditions. The set of 2002 was purely dark limb occultation and thus we chiefly perform our validation with dark limb occultations. The GOMOS instrument is capable to measure data under bright limb conditions as well, by switching to an alternative occultation mode. Nevertheless, bright limb occultations suffer from high signal fluctuations and diminished data quality. This data set has a large number of bright limb occultations, but only available for a narrow range of star temperatures. An explicit discussion of the possibility to retrieve GOMOS profiles in bright limb occultations with our algorithm must therefore be postponed.

ECMWF data were taken from T42L60 analysis fields, providing data up to 60 km and having a good enough horizontal resolution for validation with retrieved ozone data from our algorithm.

Set	Period with GOMOS data
total	September 2003, 01 - 30
subset1	September 2003, 01 - 10
subset2	September 2003, 11 - 20
subset3	September 2003, 21 - 30

Table 5.5. For the year 2003 GOMOS data were exclusively available in September. Error statistic was performed for the total set and for three subsets, where data were selected for three ten-day ensembles.

As for the data set in 2002, here we show single profiles and errors (see Fig. 5.14) for two selected events in the year 2003. The profiles are validated with operational GOMOS level 2 ozone data. Single profiles from both profiles with -1.44^m have errors of only 5% between 30 and 70 km. Both profiles show a drift to (negative and positive) larger errors in the low altitudes. Profiles with -0.73^m have errors of up to 10% between 30 and 70 km and increase below and above this height region.

5.3.1 Validation with globally distributed profiles

In this Section we present the error statistics of a selection of globally distributed occultation events separated by date and latitude regimes. The latitude regimes are divided into low (0° – 30°), mid (30° – 60°), and high (60° – 90°) latitudes. Such a selection is especially useful for looking at ozone trends in the high latitude profiles where the ozone density is significantly diminished. Especially in this set of data, in

Period	Latitude	$\mathbf{x_{acc}}$	$\mathbf{x_{out}}$
2003-09-01 – 2003-09-30	all	1150	431
2003-09-01 – 2003-09-30	low	308	29
2003-09-01 – 2003-09-30	mid	830	249
2003-09-01 – 2003-09-30	high	21	144
2003-09-01 – 2003-09-10	all	361	74
2003-09-01 – 2003-09-10	low	53	0
2003-09-01 – 2003-09-10	mid	308	71
2003-09-01 – 2003-09-10	high	–	–
2003-09-11 – 2003-09-20	all	350	90
2003-09-11 – 2003-09-20	low	121	4
2003-09-11 – 2003-09-20	mid	228	68
2003-09-11 – 2003-09-20	high	–	–
2003-09-21 – 2003-09-30	all	439	267
2003-09-21 – 2003-09-30	low	134	25
2003-09-21 – 2003-09-30	mid	394	110
2003-09-21 – 2003-09-30	high	20	123

Table 5.6. Number of processed and accepted profiles $\mathbf{x}_{\mathrm{acc}}$ contributing to the error statistics and not considered outliers $\mathbf{x}_{\mathrm{out}}$. The profiles listed here are measured under dark limb conditions. The outliers are identified as profiles with errors larger than 50% between 30 and 60 km altitude. For some subsets high latitude profiles and outliers are not detected due to only a small set of available data.

contrary to the set 2002, we have very few high latitude occultations under dark limb conditions.

In the following graphs (see Figs. 5.15 to 5.18) the heavy green line denotes the bias profile $\hat{\mathbf{b}}$, while the enveloping fine blue lines are the bias $\pm$ standard deviation profile $\hat{\mathbf{b}} \pm \hat{\mathbf{s}}$. The sets include occultations of stars between magnitudes -1.44^m and 3.03^m. Stars with magnitudes greater than 3.03^m show significantly larger errors and are not considered. We apply an outlier correction by not considering profiles with errors larger than 50% between altitudes of 30 and 60 km.

Like in the single profile calculation we see good retrieval performance in the overall plot (whole September 2003) for the low and mid latitude regions, where biases are found at $\sim 5\%$ from 25 - 65 km. Below 25 km the bias in the low latitude overall profile tends to 0%, whereas the mid latitude profile retrieval stops at about 26 km. The overall high latitude profile has very few contributors (and a large number of outliers) to the statistics, nevertheless from 20 km to 38 km the bias profiles changes from positive to negative values while the standard deviation of $\sim 40\%$ reflects the contribution of dim and cold stars. Above 65 km most profiles tend to negative biases with values of 10% at 70 km.

A direct overall comparison of profile statistics from 2003 to comparable profile statistics from 2002 shows no significant gain in data quality. The low and mid latitude profiles even tend to have the same shape for bias and standard deviation profiles. As already mentioned above the overall high latitude profile cannot be compared due to the lack of good quality measurements in the set of 2003.

The data in the set 2003 were split into three subsets. Occultations in the first and second set (first and second ten days in September) show at all latitudes slightly better performance than in the third set. In the latter more dim stars contribute to the error

$m_{\mathbf{v}}$	$T_{\mathbf{star}}$ [K]	$\lambda_{\mathbf{max}}$ [nm]	$\mathbf{x_{acc}}$	$\mathbf{x_{out}}$
–1.44	11000	263.45	137	0
–0.73	7000	414.00	146	0
0.10	14000	207.00	3	2
1.16	9700	298.76	306	0
1.50	26000	111.46	56	0
1.69	30000	96.60	8	0
1.73	15200	190.65	112	2
1.86	4100	706.82	98	2
1.95	10600	273.39	112	5
1.97	28000	103.50	3	11
2.03	4500	644.00	12	143
2.20	4400	658.63	4	158
2.25	30000	96.60	3	0
2.39	4500	644.00	7	77
2.44	20000	144.90	22	0
2.49	26000	111.46	68	6
2.65	15200	190.65	23	0
2.82	5800	499.65	9	0
2.92	7200	402.5	23	17
3.03	26000	111.46	6	0

Table 5.7. Total retrieved and accepted ozone profiles $\mathbf{x}_{\mathrm{acc}}$ and outliers $\mathbf{x}_{\mathrm{out}}$ for visual star magnitude m_{v} and the star temperature T_{star} in the validation period 2003. The maximum wavelength λ_{max} denotes the maximum of the Planck function B_ν at given temperature. The outliers are identified as profiles with errors that are larger than 50% between 30 and 60 km altitude.

statistics and thus the bias increases, especially in the mid latitude profile.

Errors in the validation with ECMWF profiles are, as already denoted for single profiles, large and lie around -30%. A strong signal at $\sim$ 25 km at low and mid latitude profiles, as seen in the set 2002, is not observed here at large extent. The low latitude profile in the third set 2003 has a peak, where negative biases go to small positive biases at 20 km height. The far most largest peak observed is found in the high latitude profile in the third set (mostly influencing the overall plot) where a strong positive bias around 25 km is found, pointing to significantly degraded data quality.

Fig. 5.15 shows the overall plots from all available occultation data. No significant differences for systematic deviations in latitude selected profiles are found, but ECMWF validation at high latitudes has an almost constant bias. The profiles validated with GOMOS level 2 data and selected by periods (see Figs. 5.16, 5.17, and 5.18) have almost constant values of bias and standard deviation.

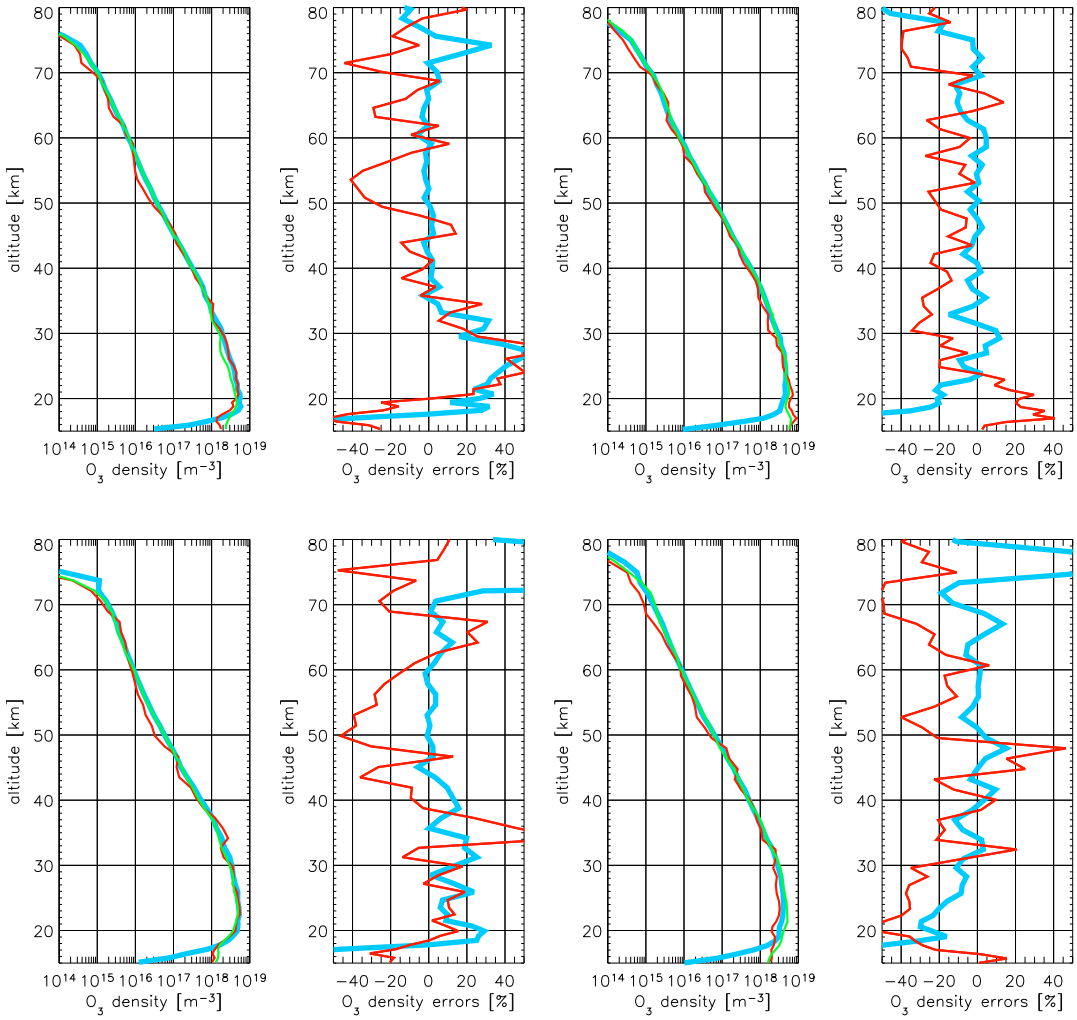

Figure 5.14. Four selected ozone and corresponding error profiles validated with operational GOMOS level 2 profiles. The upper panel corresponds to a stars with -1.44^m and the lower panel shows retrieval results from stars with -0.73^m. The ozone densities are shown in a log plot, where the heavy light blue line denotes the retrieved profile, the small green line is the reference GOMOS level 2 profile and the light red line represents *a priori* data. The errors for the validation with GOMOS level 2 data profiles are given with a heavy light blue line while errors to the *a priori* profiles are given with light red lines.

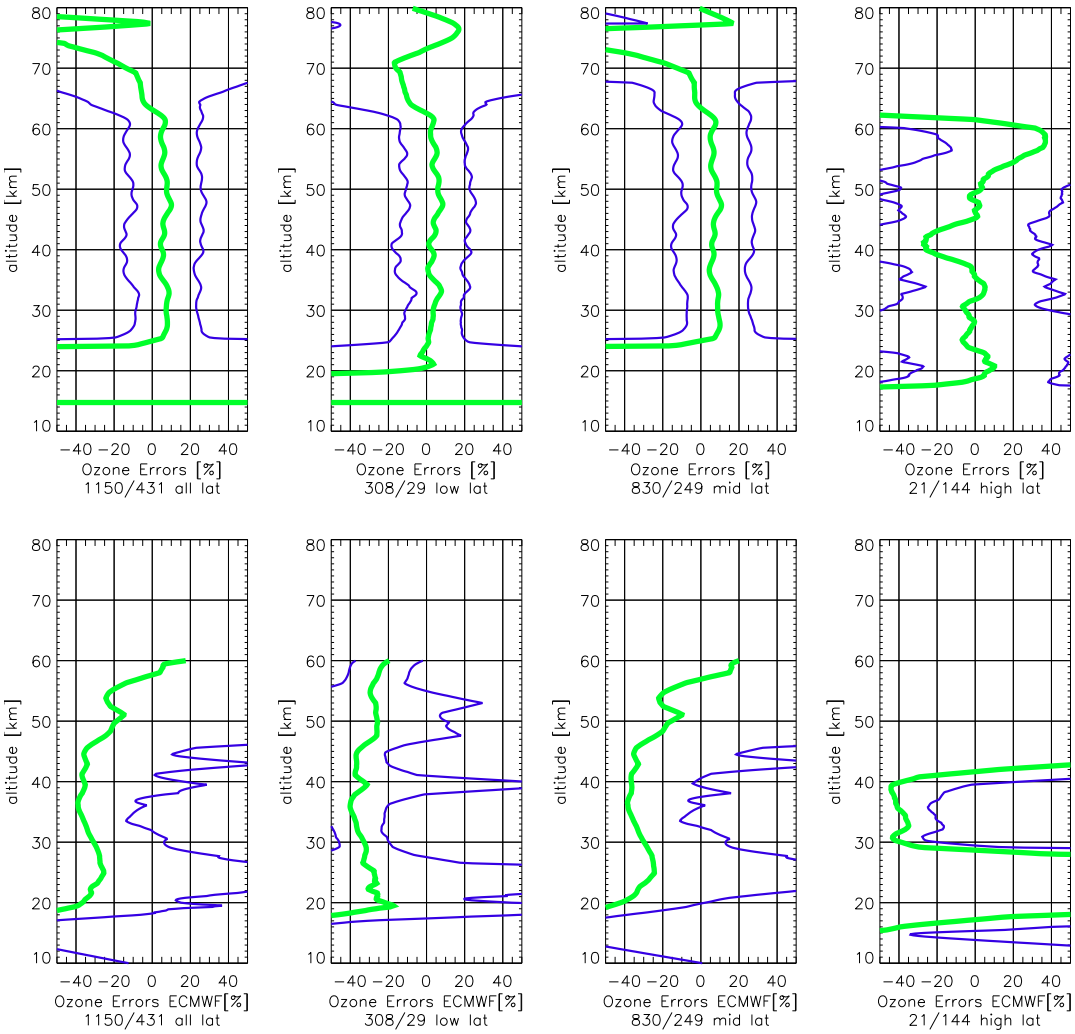

Figure 5.15. Ozone error statistics for more day ensembles in the period 2002-09-01 – 2002-09-30 (whole set 2003). In the upper panels we present profiles validated with GOMOS level 2 files and in the lower panels we validate with ECMWF analysis data. From the left, the first panel shows the overall profile, the second, third, and fourth panel show the low, mid, and high latitude selected profiles. The high latitude profile here was calculated with the outlier correction turned off. The heavy green line denotes the bias profile $\hat{\mathbf{b}}$, while the enveloping fine blue lines are the bias $\pm$ standard deviation profile $\hat{\mathbf{b}} \pm \hat{\mathbf{s}}$. To each error profile contributes a certain number of available files passing the quality check. This is given below each plot where on the left one finds the number of accepted profiles and the right number denotes the outliers.

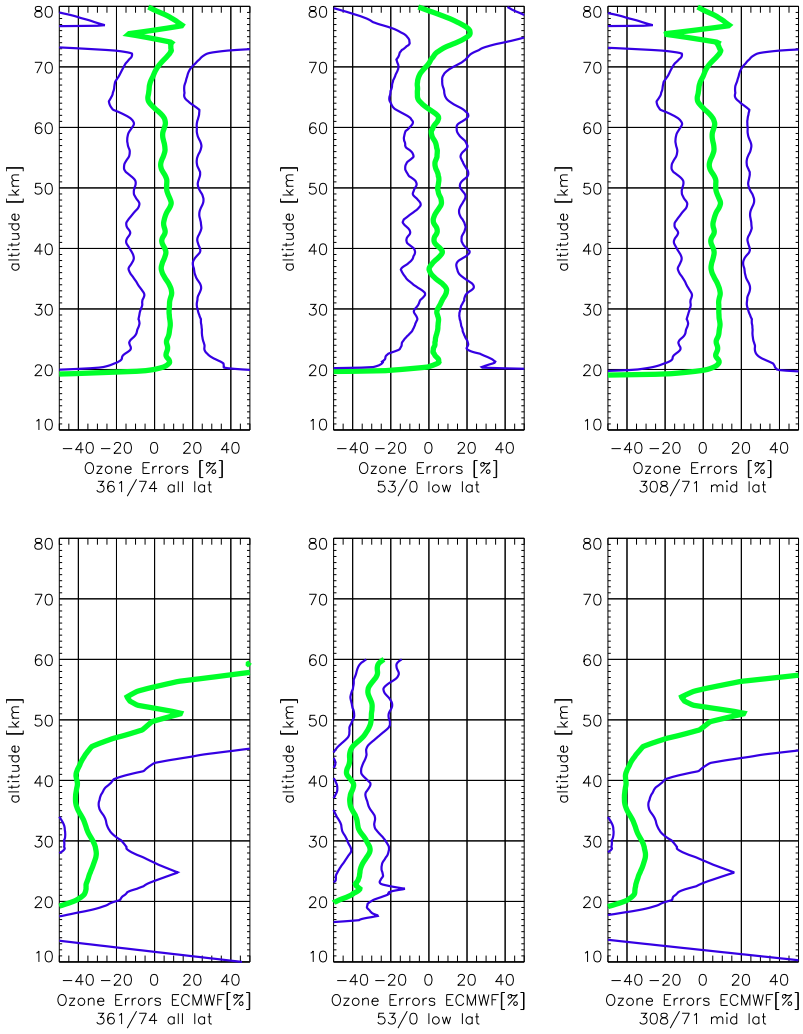

Figure 5.16. Ozone error statistics for ten day ensembles in the period 2002-09-01 – 2002-09-10. In the upper panels we present profiles validated with GOMOS level 2 files and in the lower panels we validate with ECMWF analysis data. For further description of the graphs see caption of Fig. 5.15.

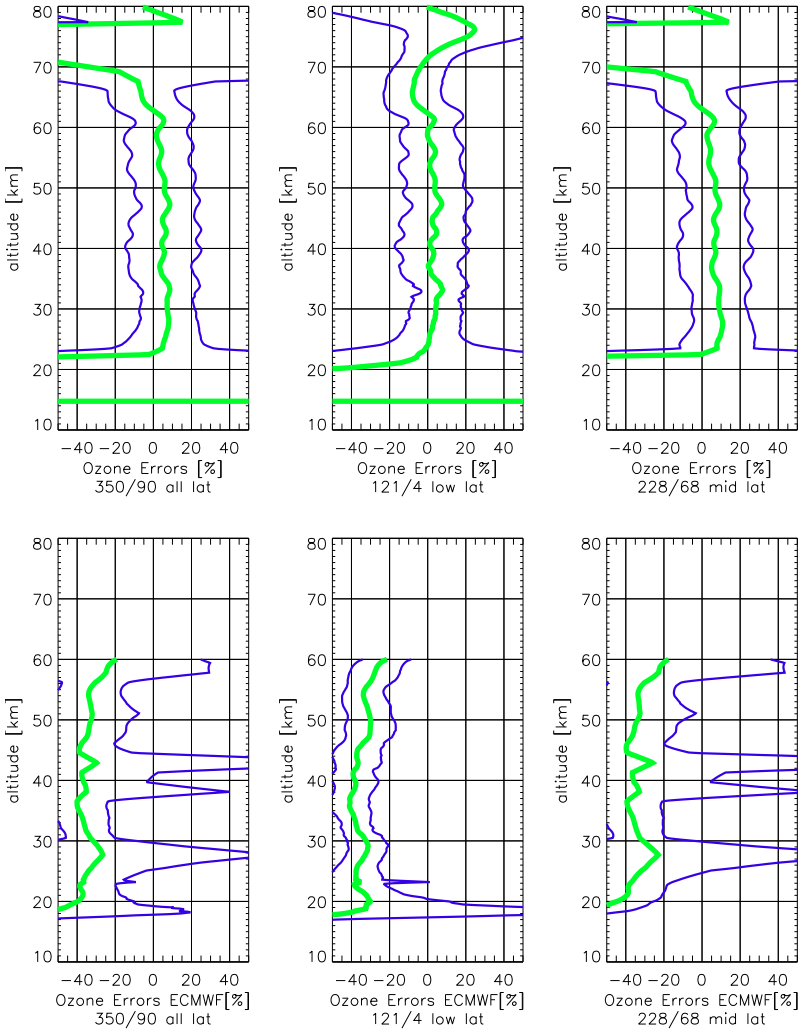

Figure 5.17. Ozone error statistics for ten day ensembles in the period 2002-09-11 – 2002-09-20. In the upper panels we present profiles validated with GOMOS level 2 files and in the lower panels we validate with ECMWF analysis data. For further description of the graphs see caption of Fig. 5.15.

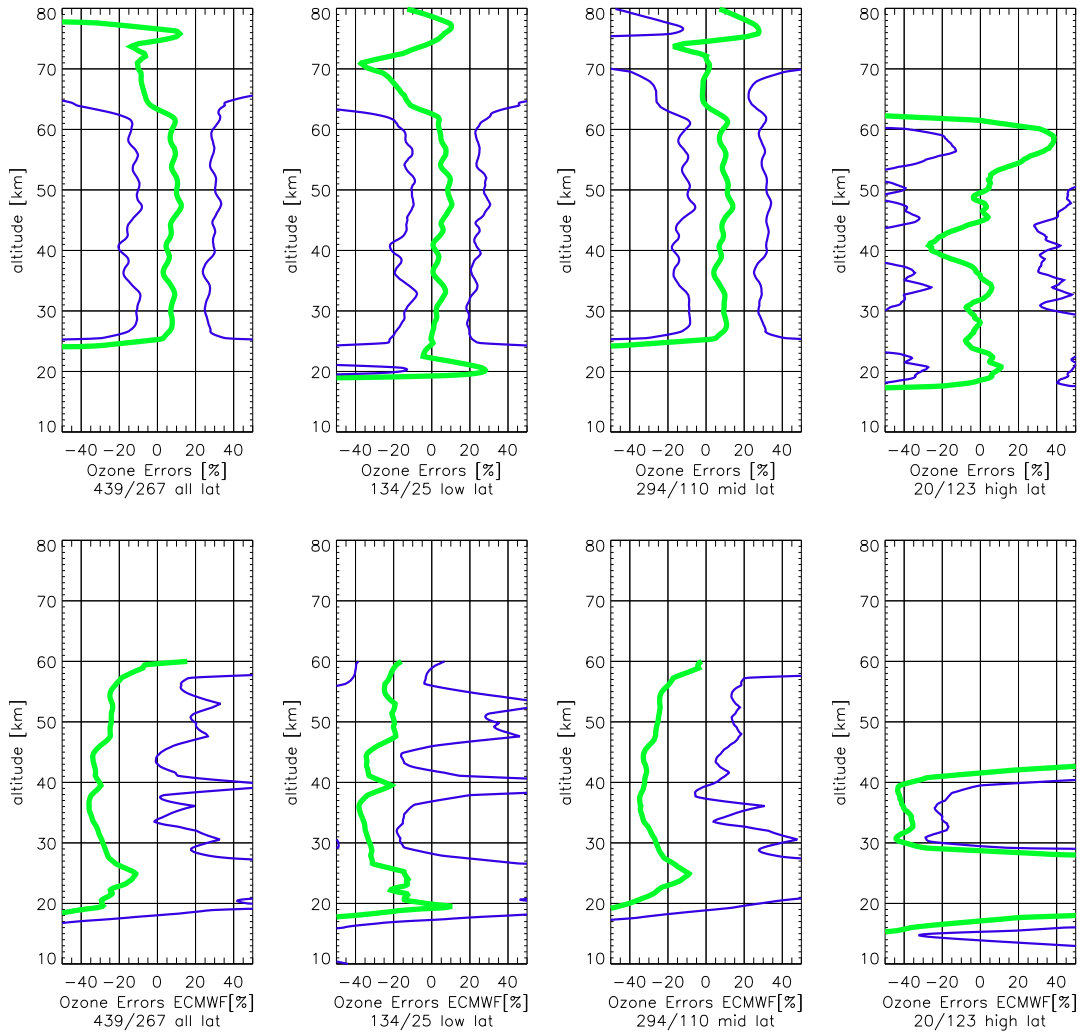

Figure 5.18. Ozone error statistics for ten day ensembles in the period 2002-09-21 – 2002-09-30. In the upper panels we present profiles validated with GOMOS level 2 files and in the lower panels we validate with ECMWF analysis data. For further description of the graphs see caption of Fig. 5.15.

5.3.2 Ozone Profiles and Errors at different Star Magnitudes

In the previous Section we analyzed profiles accumulated from different stars, sorted by latitude regimes and introduced periods in the data set 2003. Here profiles are sorted by star magnitude and temperature and validated with GOMOS level 2 and ECMWF analysis data.

The plots shown here (see Figs. 5.19 to 5.23) confirm which we have already seen in the set 2002. Bright stars with high temperatures perform best for an ozone retrieval. In this set we have 20 stars instead of 12 as in the set of 2002, where more than half meet the criteria of excellent stars for our needs. In detail, the stars with -1.44^m, -0.73^m, 1.16^m, 1.50^m, 1.69^m, 1.73^m, 1.95^m, 1.97^m, 2.25^m, 2.44^m, and 2.65^m have small biases down to 5% at altitudes between 25 and 65 km. Due to the fewer data at low stratospheric heights the biases increase there. Most of these stars emit light in the UV (e.g., class A and B stars). Due to strong absorption by ozone in the low and mid stratosphere, light does not reach heights below 25 km. A star with 2.20^m having its $\lambda_{\max}$ in the Chappuis band gives good retrieval results even down to 10 km. In this set we observe that stars with occultations with a higher obliquity (angle from the vertical), having more than double of measured height steps, show smaller biases and standard deviations than the typical hot stars, but have a large number of detected outliers. Stars with very oblique occultations have magnitudes 0.10^m and 2.25^m with temperatures 15000 K and 30000 K (hottest star in the total set), respectively. The star with 0.10^m has small standard deviations at high altitudes down to 40 km, but suffer from few contributions to the statistics at mid and low heights. The very hot star 2.25^m has a standard deviation of only 5% at low and mid altitudes with increasing values from 50 km upwards.

Examples with very bad retrieval quality are shown as well. The star with 2.83^m, called β Hydri, should in theory give good retrieval results down to the low stratosphere, but transmission data exhibit too large errors and thus a good quality retrieval was not possible.

ECMWF validation shows which was already seen in the overall plots in the previous Section. The typical peak, as observed in the set 2002, is not observed here in general, nevertheless some stars have positive values in the bias profile. A very special feature is observed for the star with 2.65^m having a strong tendency to positive biases at the altitude of the ozone layer. Light coming from this star is only measured at $\sim 28^\circ$ and around $\sim 3^\circ$latitude, thus all being low latitude occultation profiles.

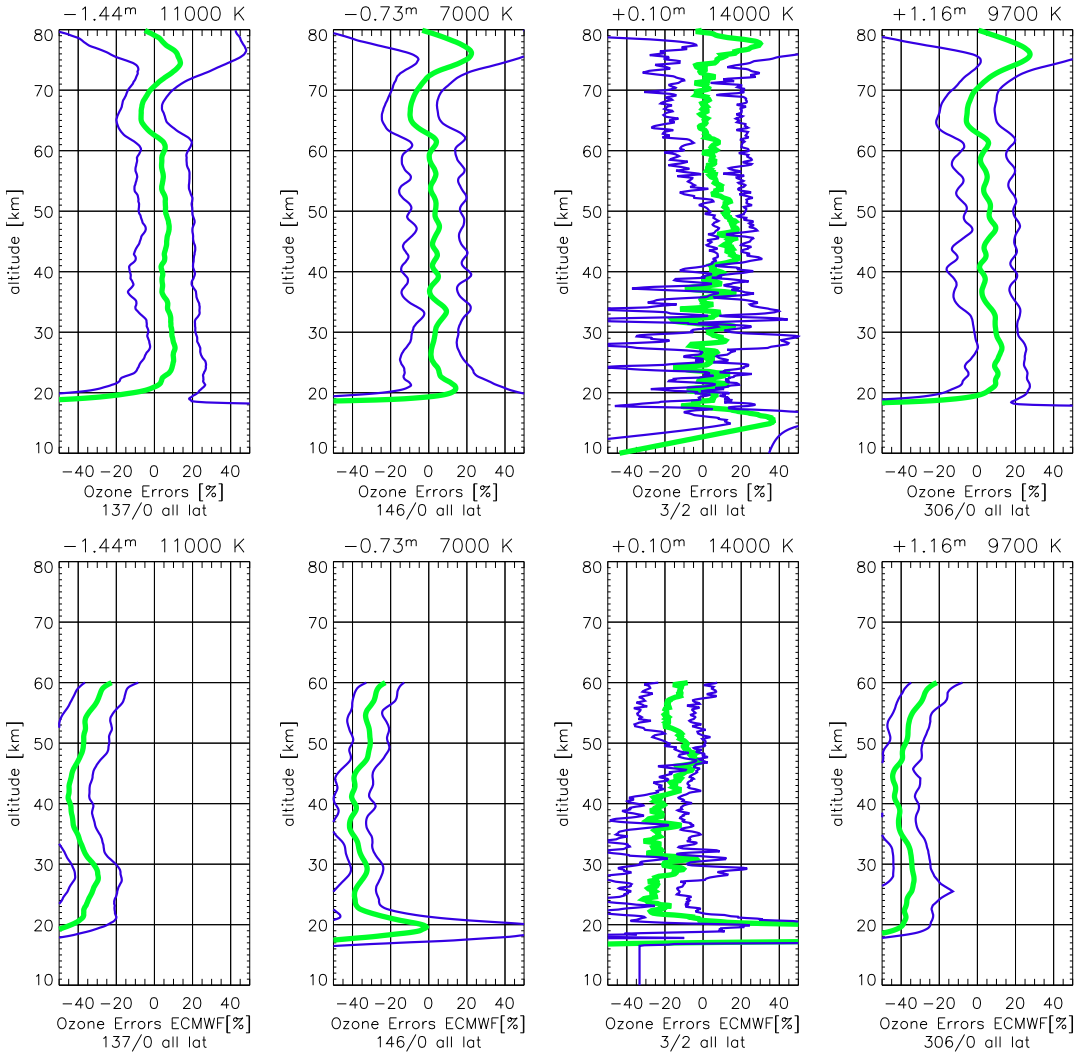

Figure 5.19. Ozone error statistics for more day ensembles in the period 2003-09-01 – 2003-09-30 (whole set 2003). In the upper panels we present profiles validated with GOMOS level 2 files and in the lower panels we validate with ECMWF analysis data. From the left to the right, the panels show data for selected stars with visual magnitudes -1.44^m, -0.73^m, 0.01^m, and 1.16^m as well as corresponding star temperatures. The heavy green line denotes the bias profile $\hat{\mathbf{b}}$, while the enveloping fine blue lines are the bias $\pm$ standard deviation profile $\hat{\mathbf{b}} \pm \hat{\mathbf{s}}$. To each error profile contributes a certain number of available files passing the quality check. This is given below each plot where on the left one finds the number of accepted profiles and the right number denotes the outliers.

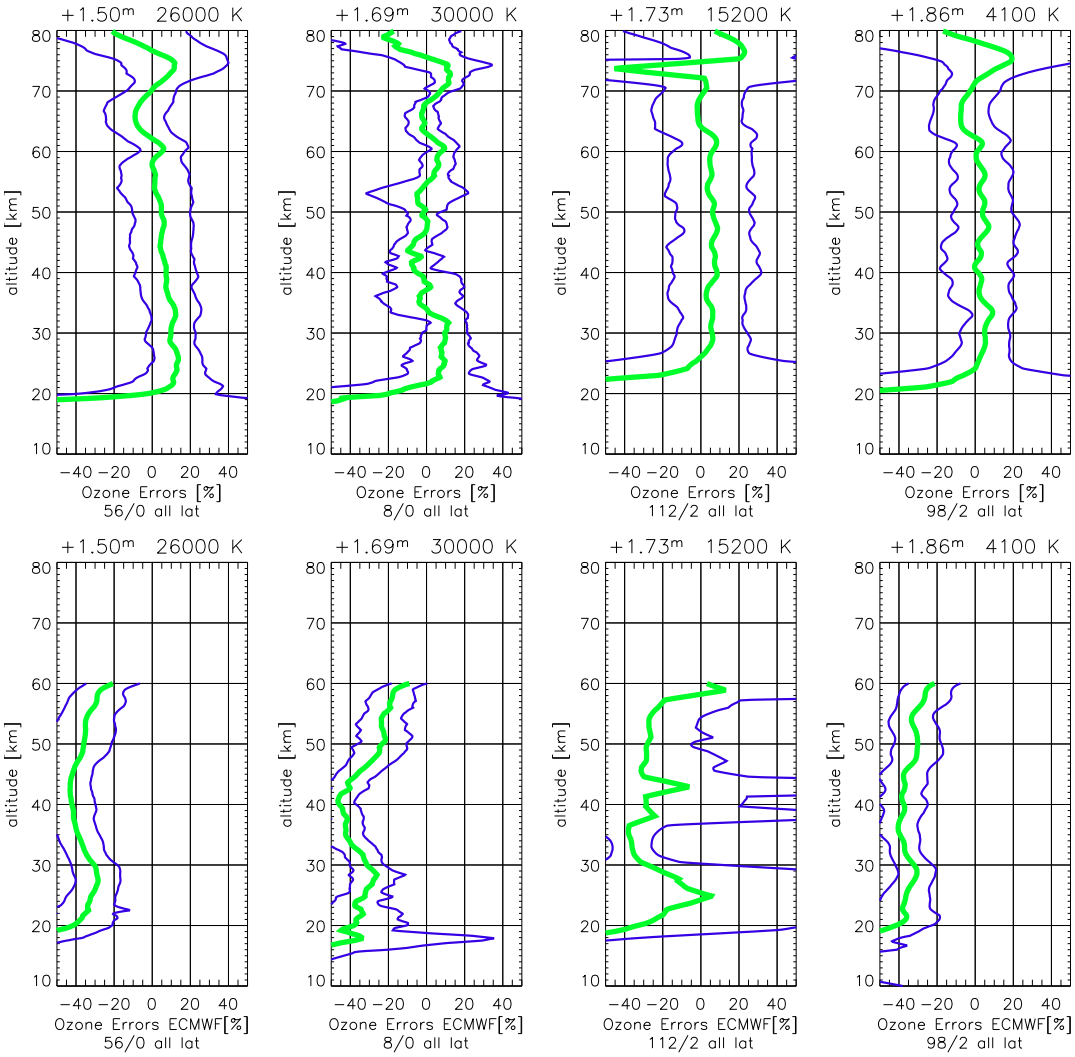

Figure 5.20. Ozone error statistics for more day ensembles in the period 2003-09-01 – 2003-09-30 (whole set 2003). In the upper panels we present profiles validated with GOMOS level 2 files and in the lower panels we validate with ECMWF analysis data. From the left to the right, the panels show data for selected stars with visual magnitudes 1.50^m, 1.69^m, 1.73^m, and 1.86^m as well as corresponding star temperatures. For further description of the graphs see caption of Fig. 5.19.

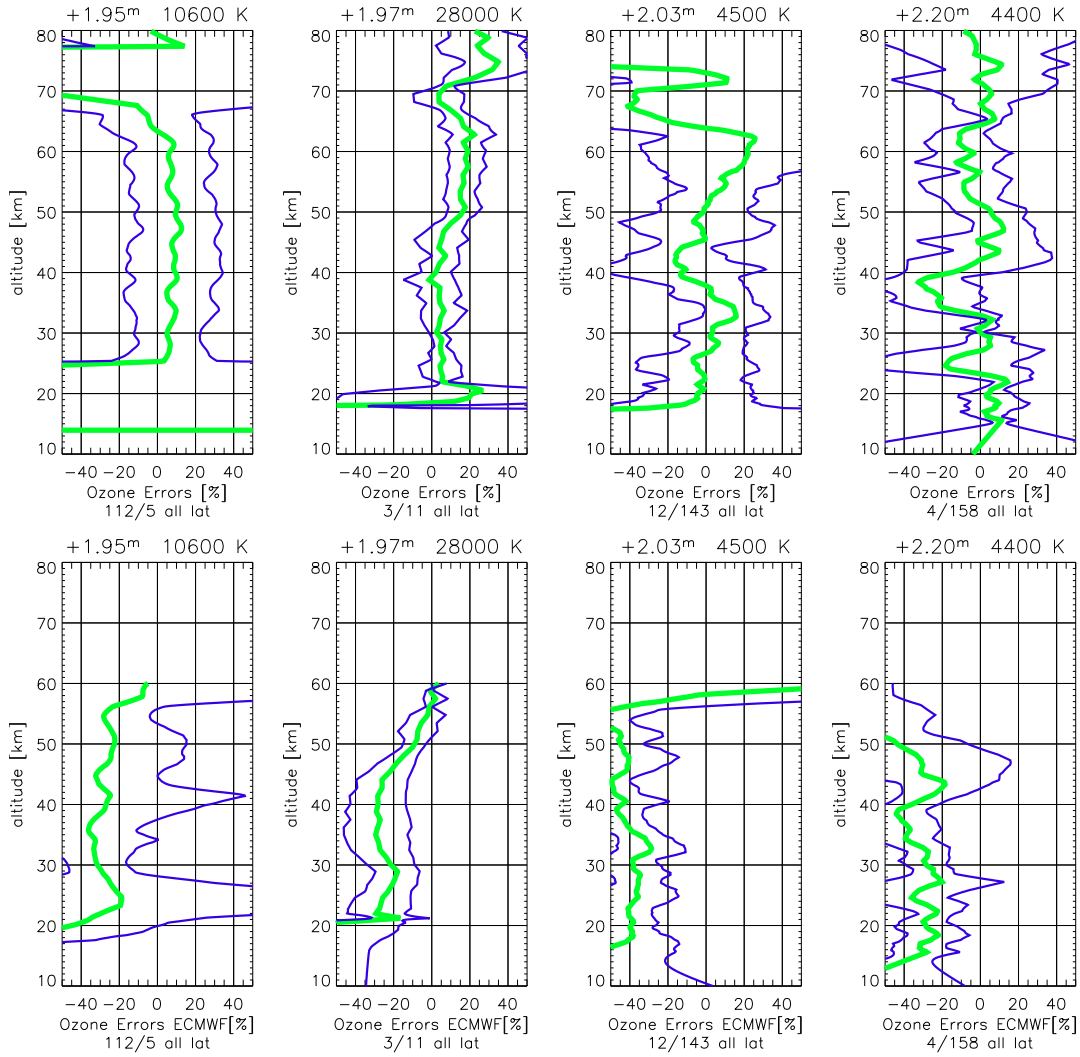

Figure 5.21. Ozone error statistics for more day ensembles in the period 2003-09-01 – 2003-09-30 (whole set 2003). In the upper panels we present profiles validated with GOMOS level 2 files and in the lower panels we validate with ECMWF analysis data. From the left to the right, the panels show data for selected stars with visual magnitudes 1.95^m, 1.97^m, 2.03^m, and 2.20^m as well as corresponding star temperatures. For further description of the graphs see caption of Fig. 5.19.

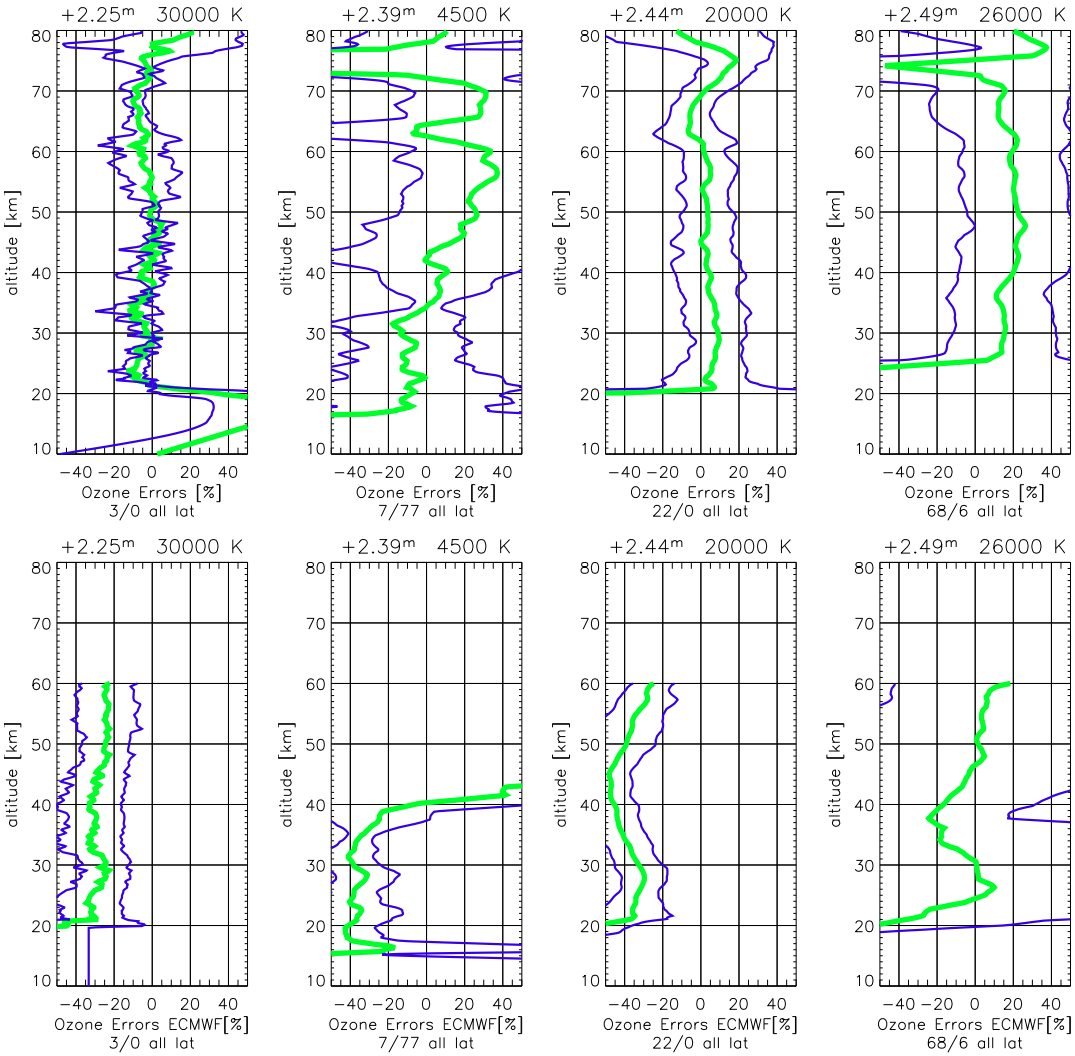

Figure 5.22. Ozone error statistics for more day ensembles in the period 2003-09-01 – 2003-09-30 (whole set 2003). In the upper panels we present profiles validated with GOMOS level 2 files and in the lower panels we validate with ECMWF analysis data. From the left to the right, the panels show data for selected stars with visual magnitudes 2.25^m, 2.39^m, 2.44^m, and 2.49^m as well as corresponding star temperatures. For further description of the graphs see caption of Fig. 5.19.

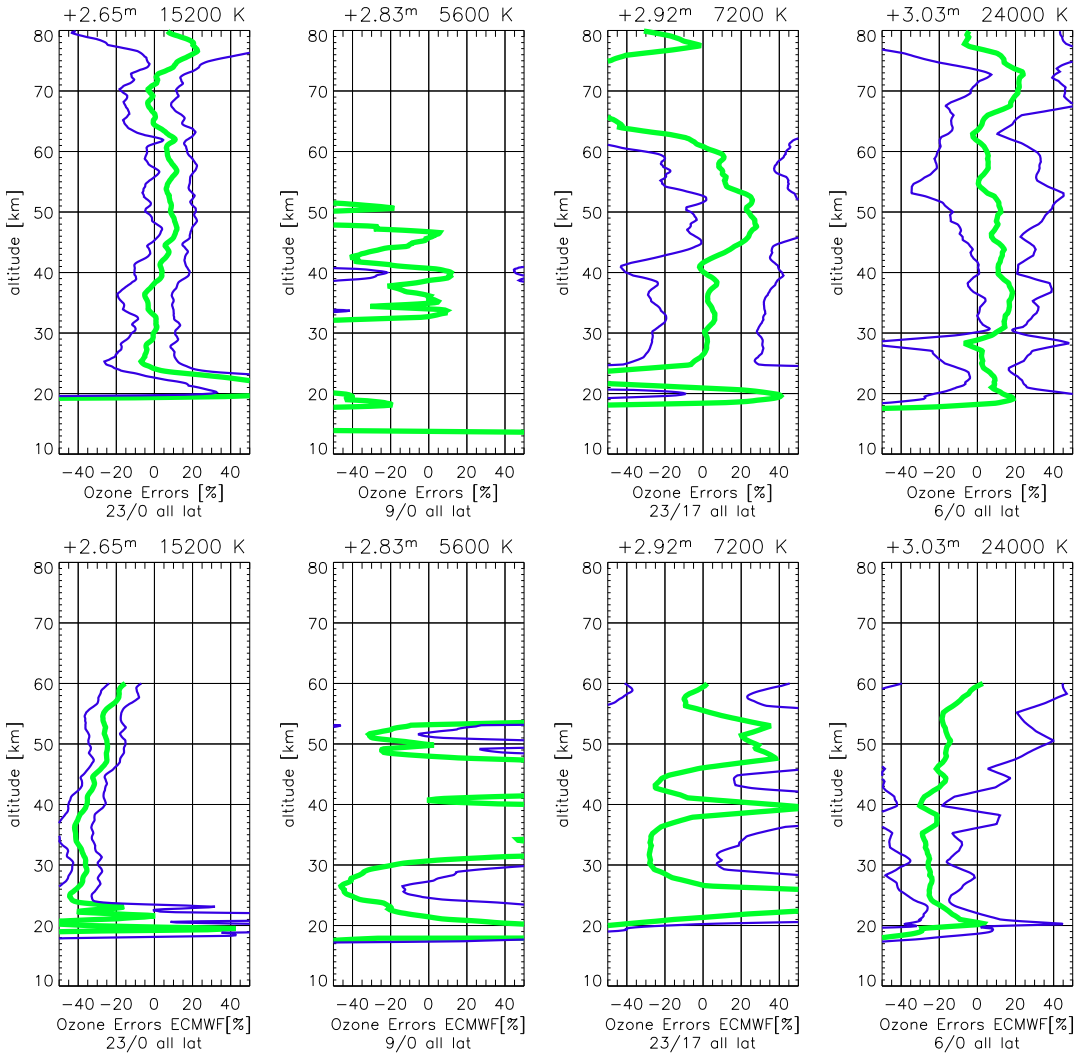

Figure 5.23. Ozone error statistics for more day ensembles in the period 2003-09-01 – 2003-09-30 (whole set 2003). In the upper panels we present profiles validated with GOMOS level 2 files and in the lower panels we validate with ECMWF analysis data. From the left to the right, the panels show data for selected stars with visual magnitudes 2.65^m, 2.83^m, 2.92^m, and 3.03^m as well as corresponding star temperatures. For further description of the graphs see caption of Fig. 5.19.

5.4 Temperature Retrieval & Validation Setup

5.4.1 Setup for Temperature Retrieval

This Section is dedicated to a summary of temperature retrieval results based on GOMOS level 1b data. The retrieval routines follow an inversion scheme the core of which is an Abel transform. Major parts of the programming logic, connected to simulated temperature profiles with MSISE-90 background data, are provided by EGOPS [*Kirchengast et al.* (2002)], an end-to-end simulation software developed and maintained at IGAM, University of Graz.

After a simulated temperature retrieval we exploit real bending angles from GOMOS. A main focus lies on the comparison of GOMOS level 1b data with CHAMP/RO, MIPAS, and ECMWF analysis data for selected days in the years 2002 and 2003.

As a starting point for the retrieval, we take GOMOS SFA/SATU internal mirror position data (cf. Section 3.3.6) and convert them into bending angles [*Sofieva et al.* (2003), *GOMOS-ESL* (1999)], by taking differences of an almost unrefracted ray above the atmosphere and measured refracted rays inside the atmosphere. GOMOS SFA data is available in 10 Hz and 100 Hz SATU errors, which is a higher sampling rate than the reference tangent point location with 2 Hz. In order to upgrade to 10 Hz, which works best for our EGOPS retrieval routines, we had to interpolate GOMOS tangent point locations.

The temperature retrieval follows a new approach for occultations in the optical spectral range, but is a method well known in the Radio Occultation (RO) community. Once we have bending angles exploited from real measurements, data was statistically optimized (cf. Section 4.5.1) and then used to gain refractivity and temperature profiles via Abel transform (cf. Section 4.5.2).

5.4.2 Test of Setup: Simulated Temperature Retrieval

Simulated bending angle and temperature profiles, produced by EGOPS, are prepared and used as *a priori* (background) data. Two realizations of temperature profiles based on bending angles with and without statistical optimization are shown in Fig. 5.24. The two profiles differ from each other in the randomly selected initialization error vector. Errors are assumed to be ~ 3 μrad at 10 Hz for bending angles, which corresponds to a downgrade from $\sim 10\mu$rad at 100 Hz operational SATU errors. In Fig. 5.24 one perfectly finds the influence of optimized bending angle data on the temperature retrieval. Non-optimized temperature profiles are shown with dotted lines, where temperature errors exceed 5 K at already 30 km, while the error for optimized temperatures (solid line) remains below 5 K up to almost 45 km. The black line denotes the "true" profile, which is the unperturbed temperature, obtained with the assumption of no error in the bending angle profile.

5.5 Real Temperature Retrieval Validation (set 2002)

In the temperature retrieval simulation (previous Section) we have shown the influence of bending angle optimization on corresponding temperatures. In this Section we discuss the results of our real GOMOS SFA/SATU data temperature re-

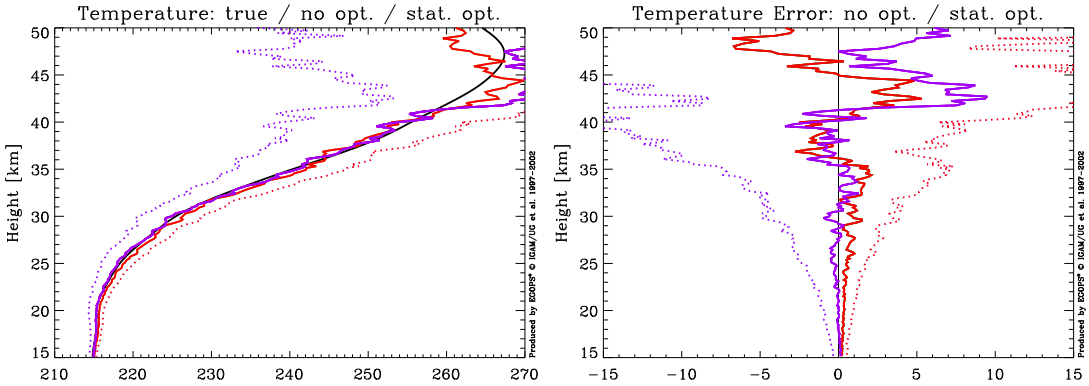

Figure 5.24. Two realizations of temperature profiles with (solid lines) and without (dotted lines) statistical optimization applied, where the smooth solid black line is the "true" profile (left). Corresponding errors (difference retrieved minus "true") of the two error realizations of temperature profiles with and without statistical optimization applied (right).

trieval (cf. [*Retscher et al.* (2004)]). Statistically optimized bending angles from GOMOS SFA/SATU data lead to temperature profiles and are then compared to CHAMP level 2, ECMWF T511L60 analysis, and MIPAS level 2 data. For this analysis, the *Geo Forschungs Zentrum* (GFZ) in Potsdam provided CHAMP data, which were further retrieved and analyzed by IGAM in order to gain temperature profiles. The *Institut für Meteorologie und Klimaforschung* (IMK) in Karlsruhe provided preprocessed MIPAS temperature data. Both data packages were validated with ECMWF data and published in [*Gobiet et al.* (2004b)].

As already found for the ozone retrieval, the results of a GOMOS temperature retrieval strongly depends on the selected star and its magnitude as well as on its corresponding temperature. In general one finds for bending angles and temperatures that a low star magnitude, favorably below 0, allows for retrievals into the troposphere down to heights of around 5 km, which is the theoretical minimum of GOMOS occultation data.

In our selected set of data, bending angles were available for the period given in Tab. 5.2 and for 20 selected stars. The GOMOS occultation events nicely cover different latitude regions (see Fig. 5.25), but especially in the high altitude region there is clear need for more occultation data.

We first present a selection of bending angle error and temperature profiles from eight different stars (see Figs. 5.26 and 5.27). Bending angle data for hot stars (cf. Section C.2) show a better performance than for cold stars and the corresponding temperatures have errors mostly below 5 K from 20 to 40 km. Temperature profiles for non-optimized bending angle profiles have errors larger than 5 K from already 25 km upwards.

After processing all GOMOS bending angle data and retrieved temperature profiles data was validated with CHAMP, MIPAS, and ECMWF data and separated into three latitude regions. Tab. 5.8 and 5.13 show latitude separated sets of total available data, as well as coincidences between GOMOS and these products. The coincidence interval is defined such that compared temperature profile must lie within 300 km of distance and the occultation time shall not differ by more than 3 hours. The error statistics was

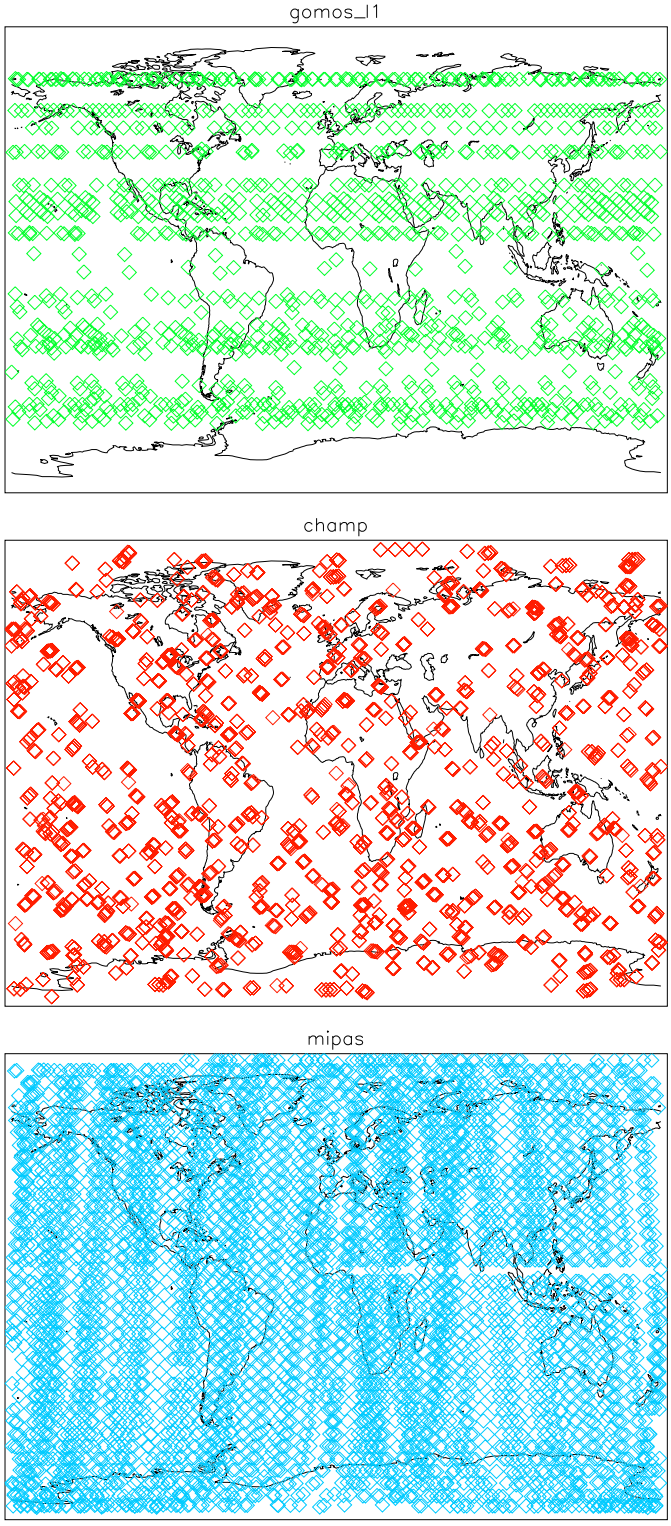

Figure 5.25. Locations where GOMOS (upper panel), CHAMP (mid panel), and MIPAS (lower panel) measurements were performed. The plots displays 1719, 3729, and 6754 occultation profiles, respectively. Data was available for days: September 20 - 27, October 11 - 13, and December 2, 2002. ECMWF profiles were taken at the same time and location as data was available for GOMOS.

Profiles	low	mid	high	all
GOMOS	698	699	322	1719
CHAMP	1159	1423	1147	3729
MIPAS	2188	2210	2356	6754
ECMWF	698	699	322	1719

Table 5.8. Numbers of profiles in total sets of available GOMOS, CHAMP, MIPAS, and ECMWF data in the period September 20 - 27, October 11 - 13, and December 2, 2002. The sets were separated into low, mid, and high latitude regions. An overall count is given as well.

Profiles	Coincidences
GOMOS – CHAMP	74
GOMOS – MIPAS	198
GOMOS – ECMWF	1719

Table 5.9. Numbers of coinciding profiles in total sets of available GOMOS, CHAMP, MIPAS, and ECMWF data in the period September 20 - 27, October 11 - 13, and December 2, 2002.

corrected for outliers by not considering profiles with errors larger than 20% between altitudes of 20 and 30 km.

Temperature profiles validated with CHAMP, MIPAS, and ECMWF data are furthermore sorted into different latitude regimes and star magnitudes. Tab. 5.10 and Tab. 5.11 summarize all available profiles and outliers for all latitudes with corresponding star magnitudes and star temperatures as well as the wavelength $\lambda_{\max}$, where the Planck function B_ν (cf. Eq. 1.25) given in [μm] has a maximum at $\lambda_{\max} = 2898\, T^{-1}$.

Products	Latitude	$\mathbf{x_{acc}}$	$\mathbf{x_{out}}$
GOMOS – CHAMP	all	49	7
GOMOS – CHAMP	low	8	1
GOMOS – CHAMP	mid	15	6
GOMOS – CHAMP	high	26	0
GOMOS – MIPAS	all	123	1
GOMOS – MIPAS	low	66	1
GOMOS – MIPAS	mid	30	0
GOMOS – MIPAS	high	27	0
GOMOS – ECMWF	all	954	98
GOMOS – ECMWF	low	286	7
GOMOS – ECMWF	mid	432	55
GOMOS – ECMWF	high	236	36

Table 5.10. Number of processed and accepted profiles $\mathbf{x}_{\text{acc}}$ contributing to the error statistics and not considered outliers $\mathbf{x}_{\text{out}}$. The profiles listed here are measured under dark limb conditions. The outliers are identified as profiles with errors larger than 20% between 20 and 30 km altitude.

5.5.1 Validation with globally distributed profiles

The GOMOS level 1b data product is separated into three latitude regions, low (0°to ± 30°), mid (±30°to ± 60°), and high (±60°to ± 90°) in order to account for different

m_{v}	T_{star} [K]	λ_{max} [nm]	$\mathbf{x}_{\mathrm{acc,ch}}$	$\mathbf{x}_{\mathrm{out,ch}}$	$\mathbf{x}_{\mathrm{acc,mi}}$	$\mathbf{x}_{\mathrm{out,mi}}$	$\mathbf{x}_{\mathrm{acc,ec}}$	$\mathbf{x}_{\mathrm{out,ec}}$
–1.44	11000	263.45	1	0	20	0	79	0
–0.73	7000	414.00	1	0	–	–	60	0
0.40	6500	445.84	6	0	–	–	60	22
0.45	24000	120.75	6	0	42	0	78	0
1.16	9700	298.76	6	0	–	–	86	0
1.50	26000	111.46	–	–	–	–	12	3
1.73	15200	190.65	2	0	–	–	25	0
1.86	4100	706.82	–	–	10	0	33	0
1.95	10600	273.39	2	0	–	–	19	0
2.03	4500	644.00	10	0	27	0	104	0
2.15	2800	1035.00	–	–	–	–	23	0
2.44	20000	144.90	–	–	–	–	3	0
2.65	15200	190.65	–	–	–	–	1	0
2.80	6900	420.00	6	0	8	0	32	19
2.85	8900	325.61	4	0	4	0	63	2
2.87	4100	706.82	–	–	–	–	26	0
2.89	3000	966.00	4	0	–	–	34	21
2.90	9300	311.61	–	–	–	–	8	0
3.00	13100	221.22	6	0	–	–	21	7
3.03	26000	111.46	–	–	–	–	2	2

Table 5.11. Total retrieved and accepted temperature profiles $\mathbf{x}_{\mathrm{acc}}$ and outliers $\mathbf{x}_{\mathrm{out}}$ for visual star magnitude m_{v} and the star temperature T_{star} in the validation period 2002. The profiles are separated by a validation with CHAMP (ch), MIPAS (mi), and ECMWF (ec) profiles. The maximum wavelength λ_{max} denotes the maximum of the Planck function B_ν at given temperature. The outliers are identified as profiles with errors that are larger than 20% between 20 and 30 km altitude. This table only includes all shown plots, but some stars are missing due to bad data quality.

mean states of the atmosphere at different latitudes. A global set of retrieved data is given as well, where dependences on different latitude regions of the quality of an overall profile can be seen. GOMOS SFA/SATU (level 1b) data in general suffers from different influences. SFA/SATU data often show much larger errors than primarily assumed. The data set, which was provided for this study, only includes a small set of occulted stars, which makes it especially difficult to ensure good retrieval quality at high latitudes (see Fig. 5.28).

For this thesis we first validated GOMOS temperature profiles with CHAMP data. Phase delays from the CHAMP level 2 (version 2) data served as input into our retrieval [*Gobiet et al.* (2004b)], which had ECMWF data as background information. Once atmospheric profiles were retrieved we separated our data set (like for GOMOS) into three latitude regions. The success of ionospheric corrections can be seen much better when looking at latitude subsets. Low latitudinal effects such as the equatorial anomaly, the spherical assymetry and small scale structures cause perturbations in the RO profile. In turn dry conditions in the high-latitude troposphere favor a good quality RO retrieval, but have only minor influences in the comparison to GOMOS data. GOMOS data in the selected subset seldom reaches tropospheric heights with reasonably quality. From 3724 CHAMP profiles we found 74 profiles, where our coincidence intervals with GOMOS data were reached.

In Fig. 5.29 GOMOS level 1b data is validated with CHAMP level 2 data at altitudes between 20 and 35 km. The high latitude bias profile $\hat{\mathbf{b}}$ is shifted to positive values for altitudes below 25 km, while the standard deviation is < 5 K. This is due to the fact that only a small set of GOMOS data with very few selected stars for occultation was available. For altitudes higher than 25 km a negative bias of up to 2 K was found. At mid and high latitudes $\hat{\mathbf{b}}$ has a negative deviation below 25 km and performs similar to the high latitude sample. The global ensemble clearly averages over negative and positive drifts below 25 km and a positive tendency in $\hat{\mathbf{b}}$ can be seen.

For the comparison of GOMOS SFA/SATU data to ECMWF data we chose co-located vertically distributed temperatures and refractivity profiles from the nearest analysis time of 6-hourly ECMWF operational analysis data. The data fields were retrieved from ECMWF corresponding to the T511L60 spectral resolution with 60 height levels and spherical harmonics truncation 511, which results in a latitudinal/longitudinal resolution of 0.351°.

Compared to the GOMOS-CHAMP validation Fig. 5.30 shows similar results. At high latitudes and altitudes between 20 and 35 km one can see the deviation to positive values of $\hat{\mathbf{b}}$ even clearer. Due to interpolations, the profiles here look more smoothed than in the GOMOS – CHAMP validation. For altitudes higher than 25 km a negative bias of > 2 K was found. At mid and high latitudes $\hat{\mathbf{b}}$ has a positive deviation below 25 km and performs equally to the high latitude sample.

From a total of 6754 available operational MIPAS occultation profiles we had to reduce the set (see Fig. 5.28) by selecting days, where GOMOS data was available in good quality. After applying coincidences criteria (300 km distance and 3 hours between two occultation events) we could identify 198 profiles for our validation study. Details on the MIPAS retrieval scheme can be found in [*Fischer et al.* (2000)]. MIPAS measurements were taken between 6 and 70 km height at a resolution of 3 km. The horizontal resolution lies between 300 and 500 km along track.

The validation with MIPAS data (see Fig. 5.31) reveals once again the structure of retrieved GOMOS temperature profiles as already seen in the previous validation sets with CHAMP and ECMWF analysis data. In Fig. 5.31 we find small biases below 1.5 K in the low latitude regime. In the mid and high latitudes, biases increase while standard deviations remain below 4 K. At high latitudes, the dominant effect is an increasing bias with decreasing altitude. The global ensemble performs equal to the ECMWF validation profiles and shows temperature biases of less than 2 K throughout the displayed regions.

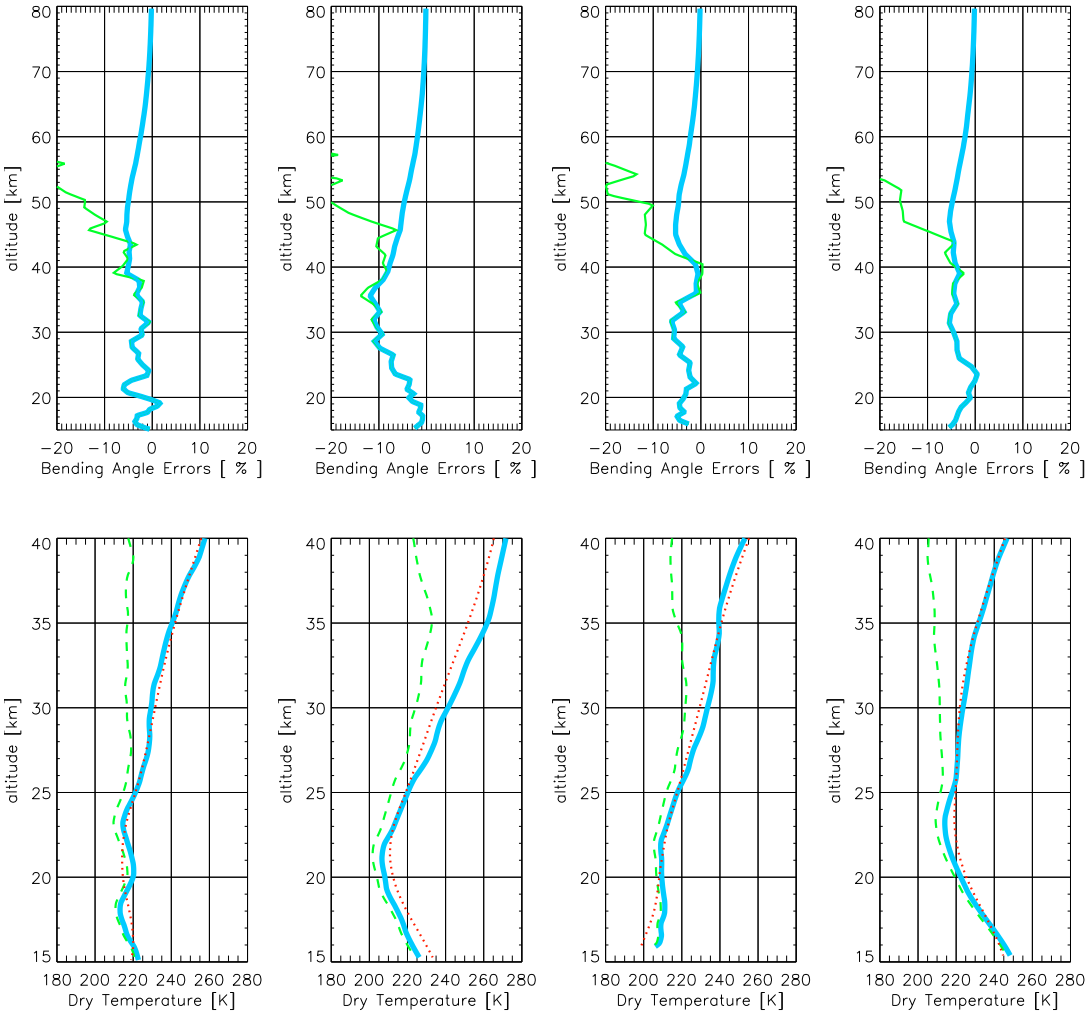

Figure 5.26. Relative bending angle errors profiles (upper panel) and corresponding temperatures (lower panel) for four different stars with -1.44^m, 0.40^m, 0.45^m, and 1.16^m. Heavy light blue lines denote statistically optimized profiles. Light red dotted lines are *a priori* profiles, while light green solid and dashed lines are measured profiles without statistical optimization.

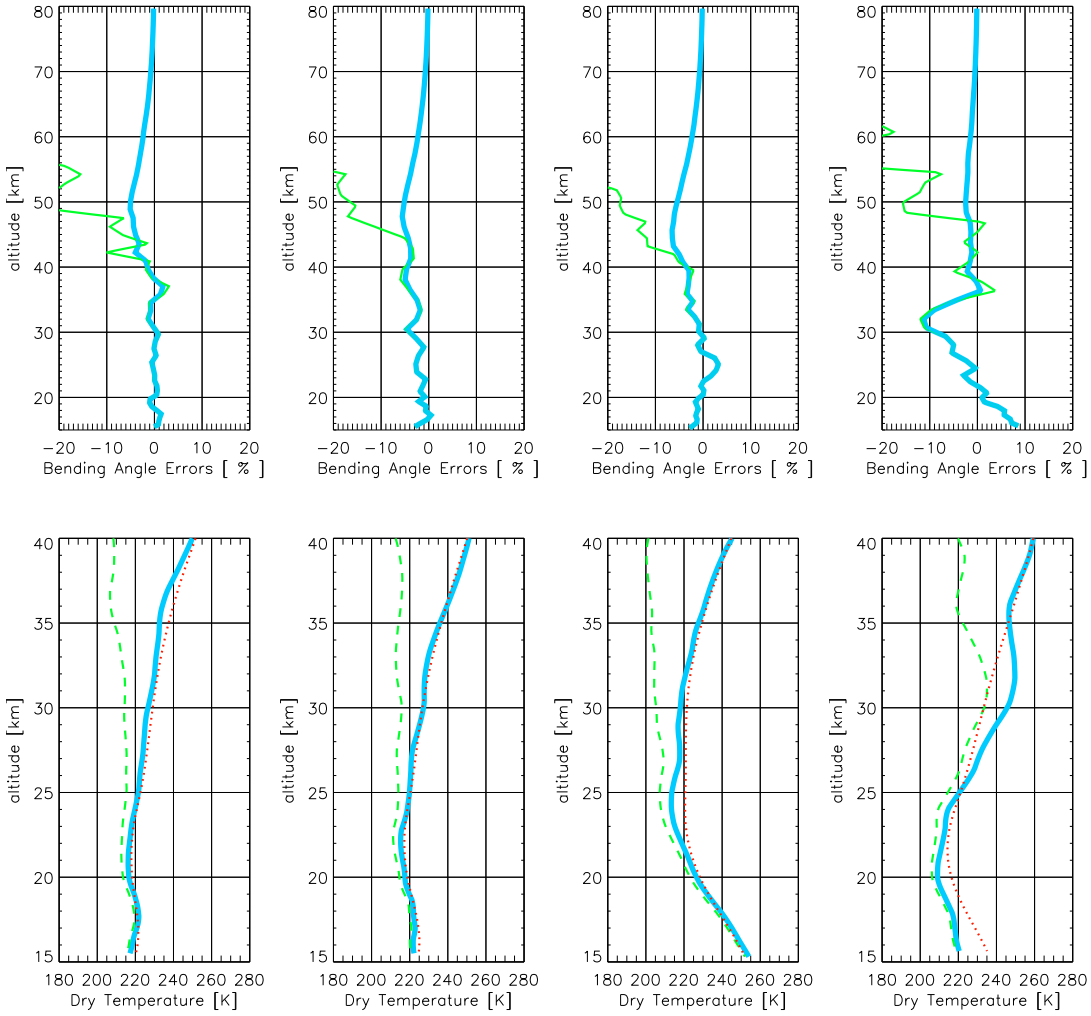

Figure 5.27. Relative bending angle errors profiles (upper panel) and corresponding temperatures (lower panel) for four different stars with 1.50^m, 1.73^m, 2.03^m, and 2.80^m. Heavy light blue lines denote statistically optimized profiles. Light red dotted lines are *a priori* profiles, while light green solid and dashed lines are measured profiles without statistical optimization.

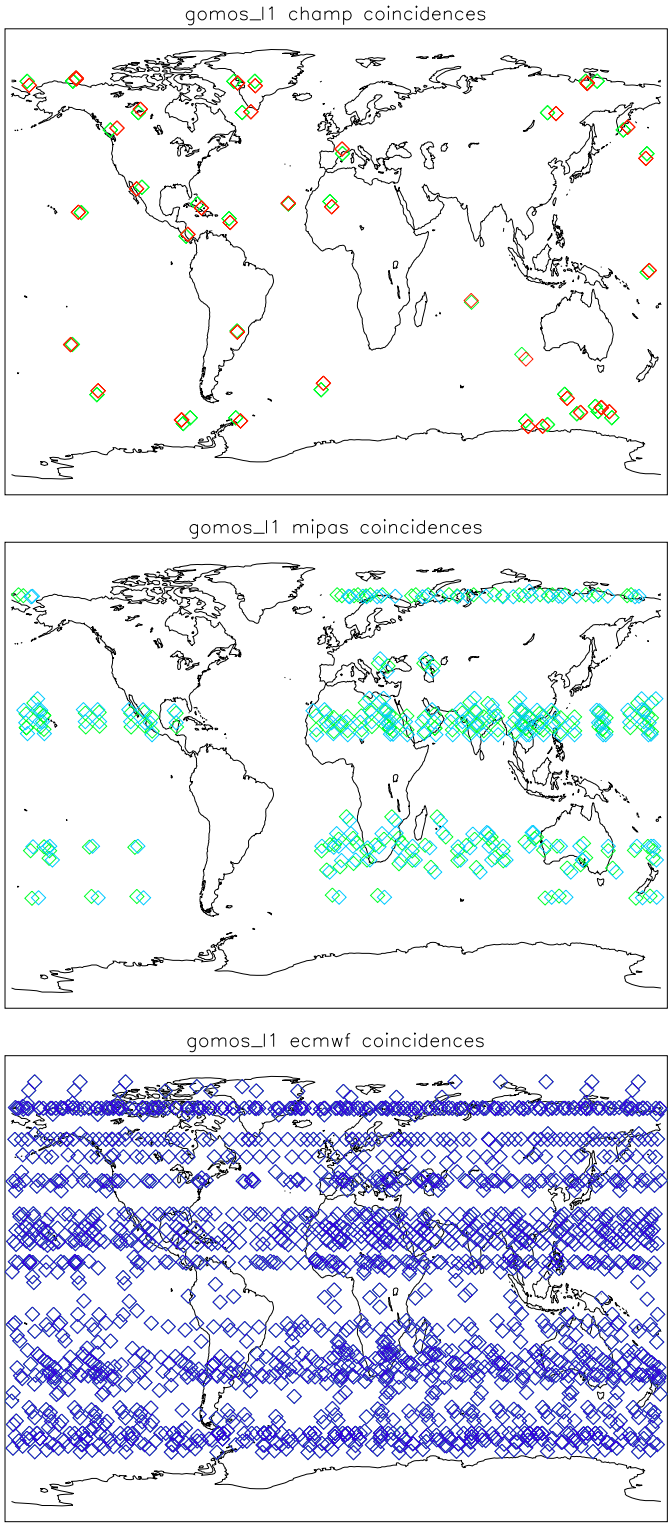

Figure 5.28. Coincidences for GOMOS to CHAMP (upper panel), GOMOS to MIPAS (mid panel), and GOMOS to ECMWF (lower panel) measurements within an interval of 300 km and 3 hours. In this set we find 74, 198, and 1719 coinciding profiles, respectively. ECMWF profiles were generally taken at the same time and location where GOMOS data was available, but sometimes there was more than one occultation fulfilling the coincidence criteria.

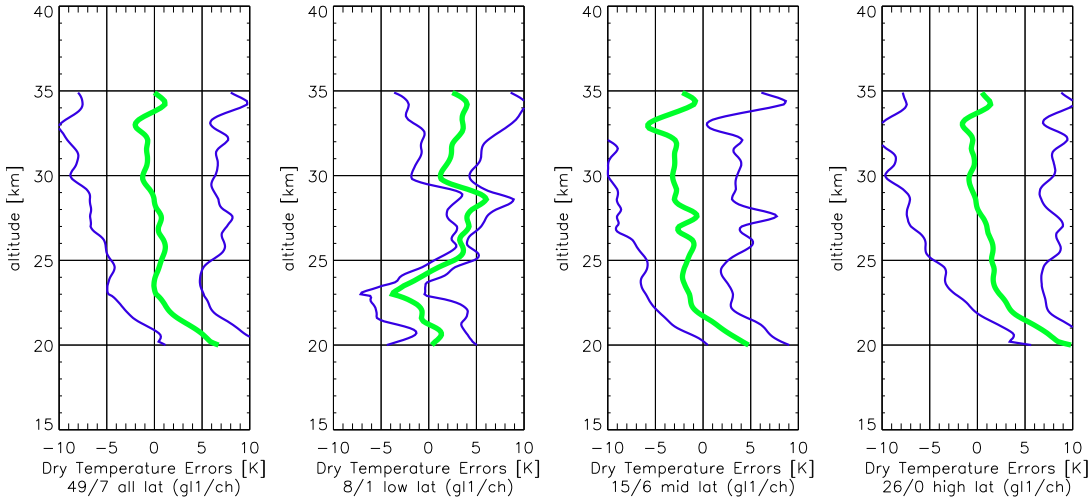

Figure 5.29. Temperature error statistics for more day ensembles in the period 2002-09-20 – 2002-12-02 (whole set 2002). We present profiles validated with CHAMP GPS profiles, which fulfill the coincidence criteria. From the left, the first panel shows the overall profile, the second, third, and fourth panel show the low, mid, and high latitude selected profiles. The heavy green line denotes the bias profile $\hat{\mathbf{b}}$, while the enveloping fine blue lines are the bias $\pm$ standard deviation profile $\hat{\mathbf{b}} \pm \hat{\mathbf{s}}$. To each error profile contributes a certain number of available files passing the quality check. This is given below each plot where on the left one finds the number of accepted profiles and the right number denotes the outliers.

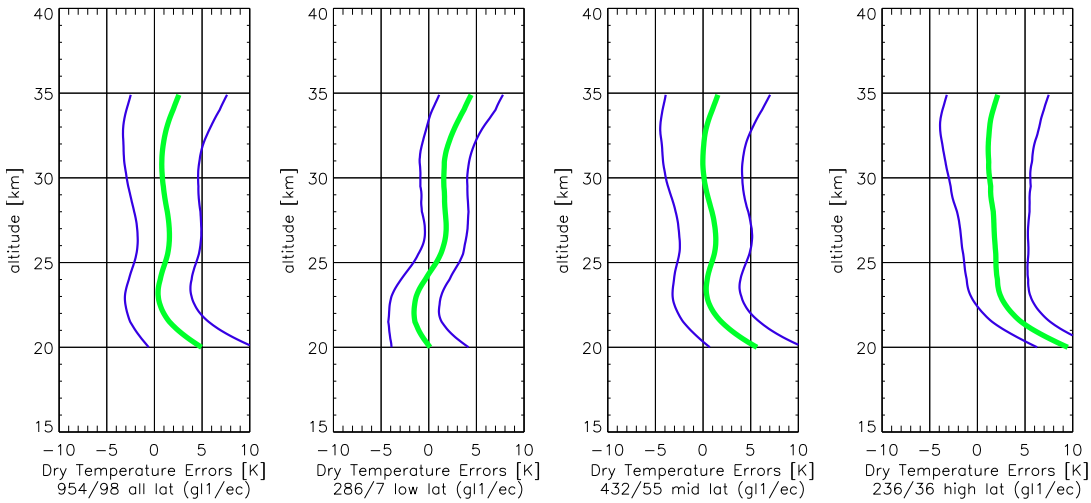

Figure 5.30. Temperature error statistics for more day ensembles in the period 2002-09-20 – 2002-12-02 (whole set 2002). We present profiles validated with ECMWF analysis profiles, which fulfill the coincidence criteria. For further description of the graphs see caption of Fig. 5.29.

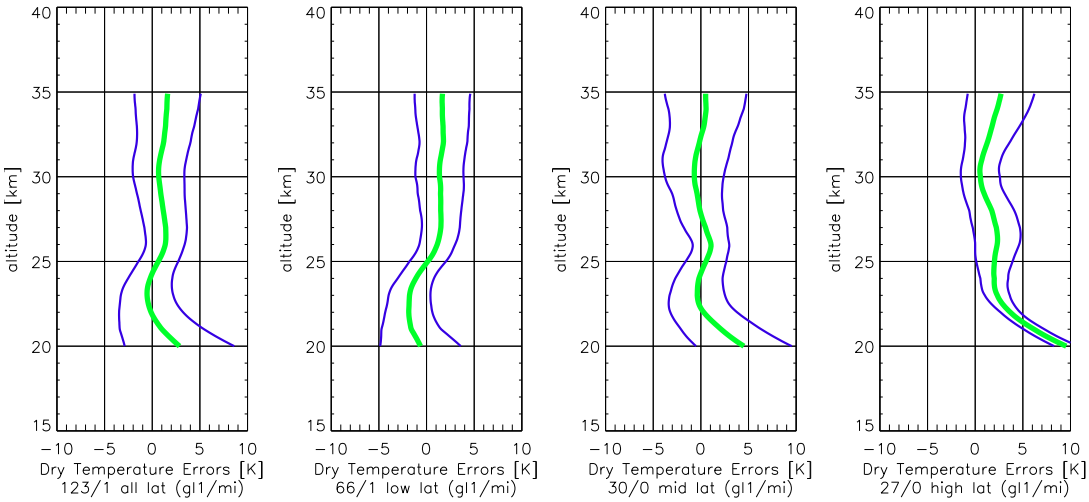

Figure 5.31. Temperature error statistics for more day ensembles in the period 2002-09-20 – 2002-12-02 (whole set 2002). We present profiles validated with Envisat/MIPAS profiles, which fulfill the coincidence criteria. For further description of the graphs see caption of Fig. 5.29.

5.5.2 Temperature Profiles and Errors at different Star Magnitudes

As in the previous Section, we here compare GOMOS profiles validated with CHAMP, MIPAS, and ECMWF, but in this Section we sort the results by star magnitude and its corresponding temperature.

GOMOS – CHAMP validation profiles (see Figs. 5.32 and 5.33) often suffer from not enough profiles contributing to the statistics. Only 12 different stars could be determined, where a validation between these two products was available. Tab. 5.11 gives an overview of all available profiles in the validation with CHAMP, MIPAS, and ECMWF. One finds only a few profiles for the GOMOS – CHAMP validation and thus results have often larger error than one would expect from the conclusions in the previous Section. Especially bright stars (Sirius and Canopus) are underrepresented with only one (!) available profile. For those validation plots, where the bias remains reasonably limited (<5 K), there is a positive bias of about 2 K observed. Stars with magnitudes 0.45^m, 1.16^m, 1.95^m, and 2.03^m show a good performance. Typical not well behaving occultation profiles are found for stars with magnitudes 0.40^m, 2.80^m, 2.98^m, and 3.00^m, where relatively cold temperatures are the main factor for bad profile quality.

In the validation with MIPAS (see Fig. 5.34) the situation is a lot easier to analyze due to the fact that more coincidences are found with GOMOS occultation data. For the MIPAS validation six stars could be identified in the GOMOS data. Here we clearly find which was observed in the overall plots. There is a tendency to small (<2 K) or positive biases in all plots below 25 km. From 25 km upwards we mostly find small positive biases with <2 K and small standard deviations with <3 K.

The analysis of GOMOS – ECMWF products (see Figs. 5.35 to 5.37) is the most favorable one, because almost all stars available in the data set contribute to the statistics. We often found stars, as noted in Section 5.2, which are not considered in the GOMOS ozone retrieval due to bad data quality. This was due to a corrupted ozone inversion for several stars. Similarly some stars are not good for temperature retrieval and thus disregarded from the analysis. For a complete list of stars available within the whole thesis we refer to Section C.2.

All profiles in the validation set have a clear peak with a tendency to negative temperature biases at low altitudes between 20 and 25 km. Pointing data at these altitudes are degraded in quality due to the fact that the atmosphere becomes denser. Between 25 and 30 K the peaks are observed in the positive region of the error plot. This time very bright stars have much more deviation from the 0 K bias. Profiles from stars with 2.03^m and 2.85^m, which are mostly gained by high latitude occultations, have a positive bias of 3 K between 22 and 35 km. Below 22 km the profiles show the same drift to positive biases as already denoted above. Profiles where mid and high latitude occultations participate in the error statistics (0.40^m and 2.89^m) have a 4 K negative bias from $\sim$ 26 km upwards and show the same overall characteristic below 25 km as observed for all plots.

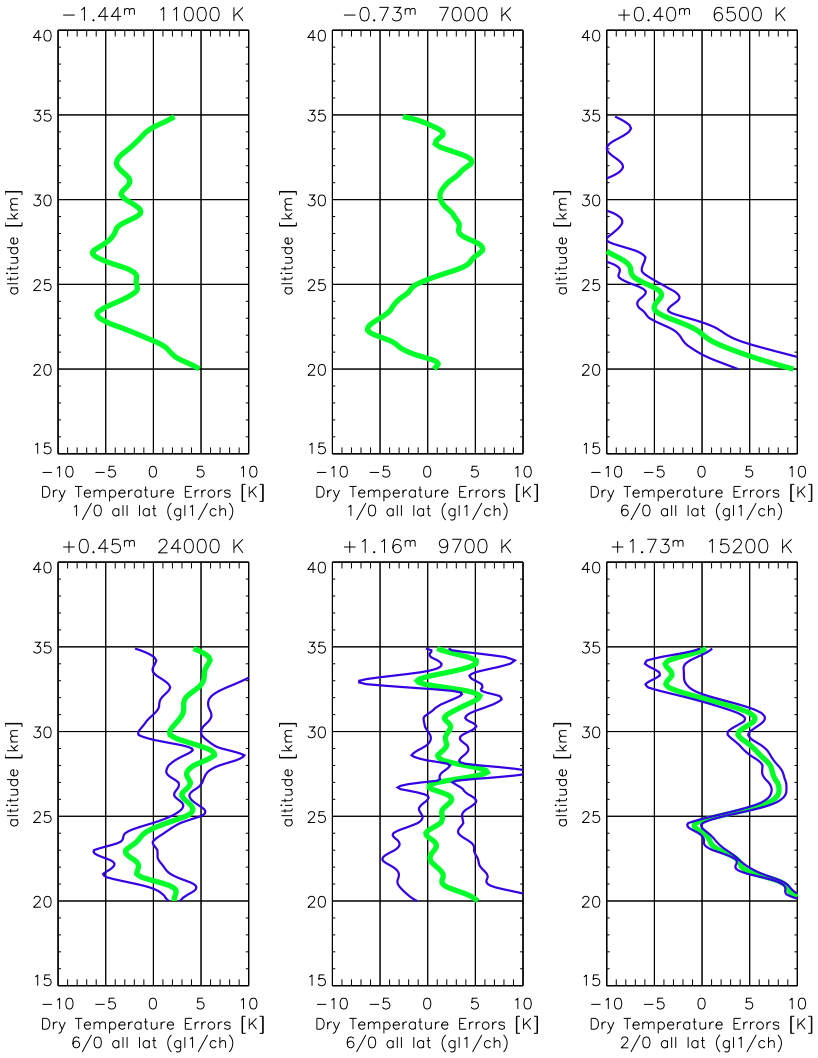

Figure 5.32. Temperature error statistics for more day ensembles in the period 2002-09-20 – 2002-12-02 (whole set 2002) validated with CHAMP GPS data. We show profiles for selected stars with visual magnitudes -1.44^m, -0.73^m, and 0.40^m in the upper panel and 0.45^m, 1.16^m, and 1.73^m in the lower panel, respectively. The heavy green line denotes the bias profile $\hat{\mathbf{b}}$, while the enveloping fine blue lines are the bias $\pm$ standard deviation profile $\hat{\mathbf{b}} \pm \hat{\mathbf{s}}$. To each error profile contributes a certain number of available files passing the quality check. This is given below each plot where on the left one finds the number of accepted profiles and the right number denotes the outliers.

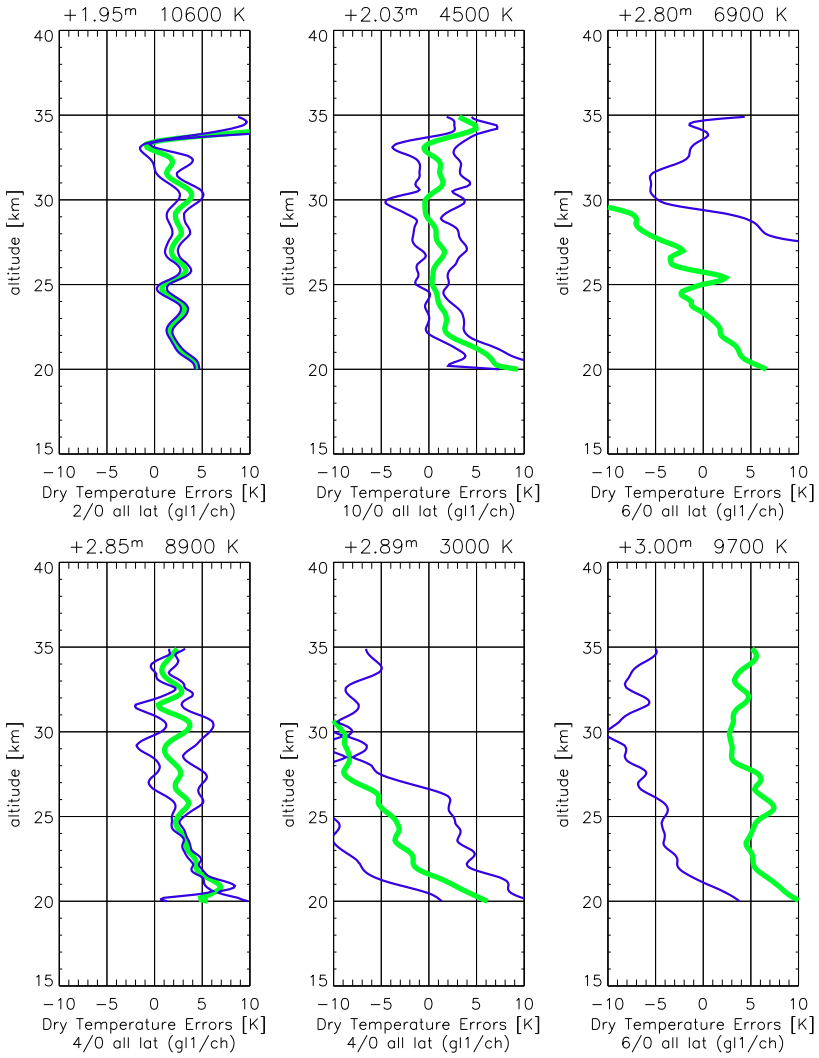

Figure 5.33. Temperature error statistics for more day ensembles in the period 2002-09-20 – 2002-12-02 (whole set 2002) validated with CHAMP GPS data. We show profiles for selected stars with visual magnitudes 1.95^m, 2.03^m, and 2.80^m in the upper panel and 2.85^m, 2.89^m, and 3.00^m in the lower panel, respectively. For further description of the graphs see caption of Fig. 5.32.

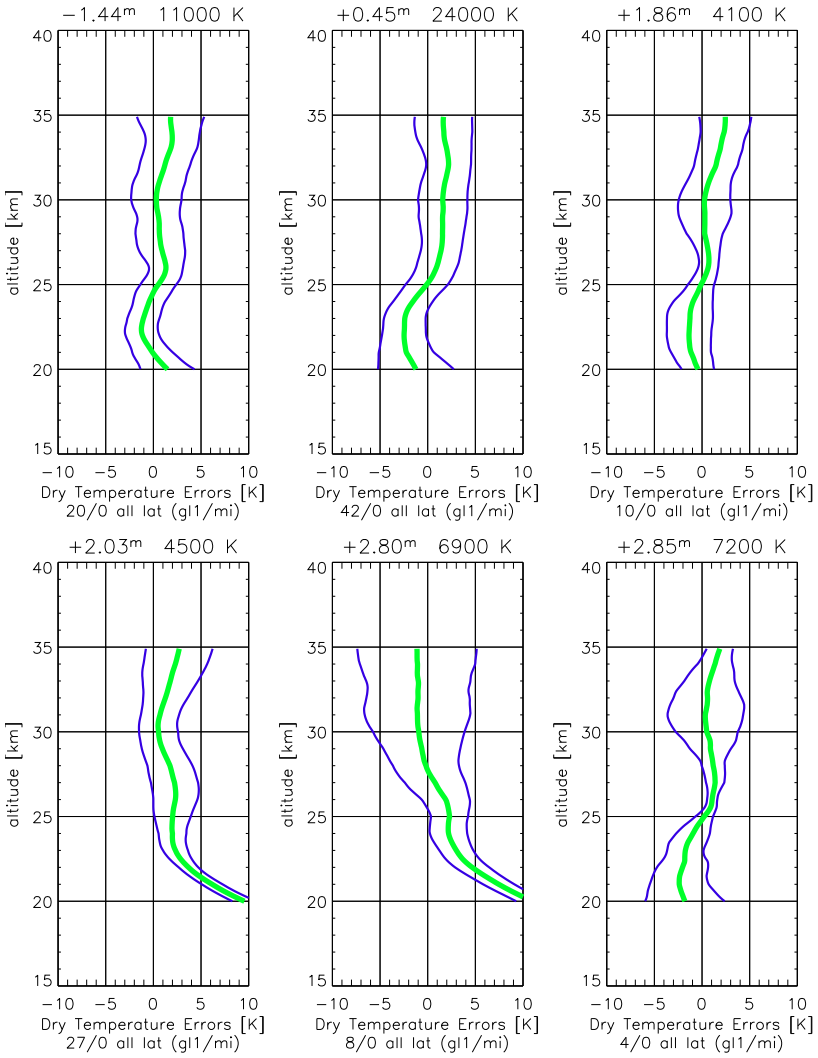

Figure 5.34. Temperature error statistics for more day ensembles in the period 2002-09-20 – 2002-12-02 (whole set 2002) validated with Envisat/MIPAS data. We show profiles for selected stars with visual magnitudes -1.44^m, 0.45^m, and 1.86^m in the upper panel and 2.03^m, and 2.80^m, and 2.85^m in the lower panel, respectively. For further description of the graphs see caption of Fig. 5.32.

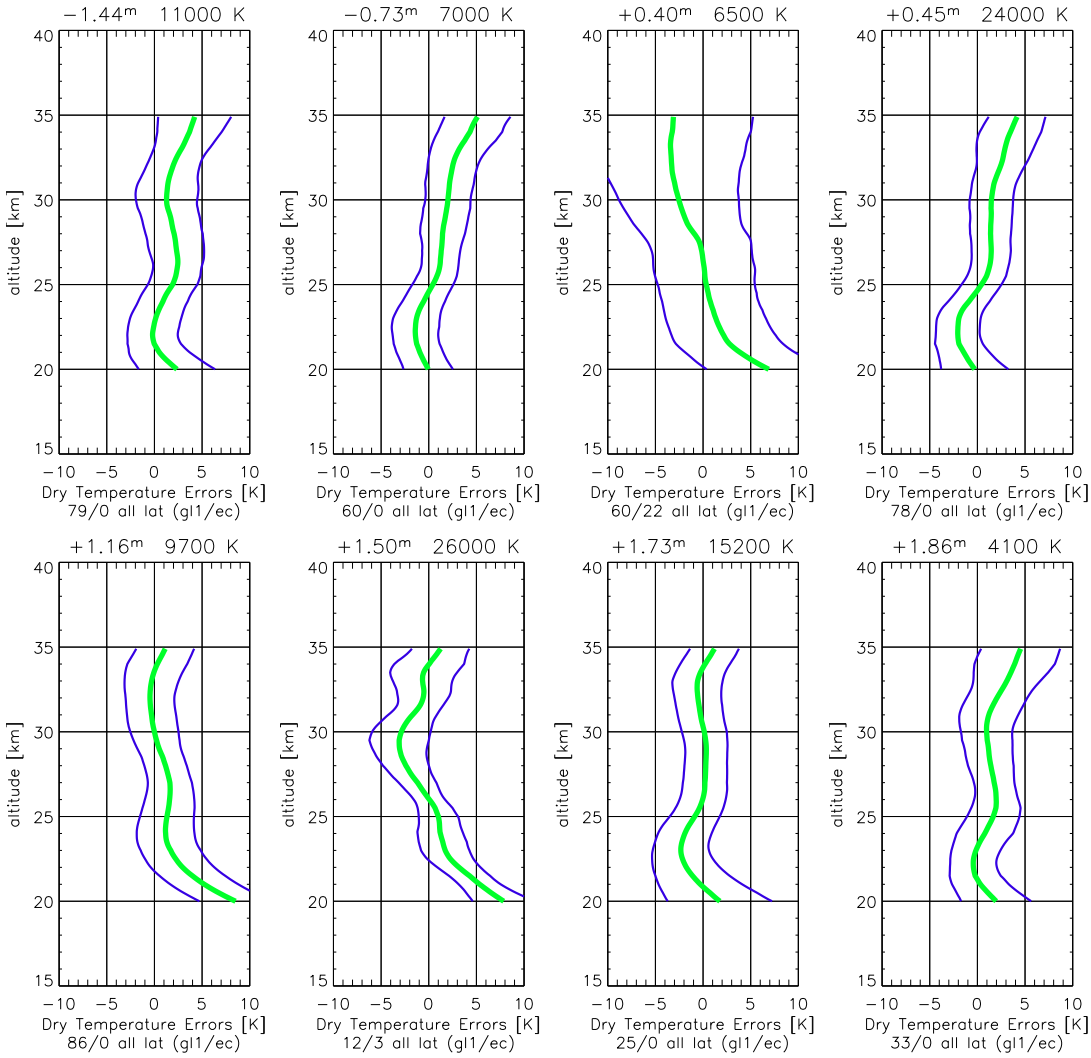

Figure 5.35. Temperature error statistics for more day ensembles in the period 2002-09-20 – 2002-12-02 (whole set 2002) validated with ECMWF analysis data. We show profiles for selected stars with visual magnitudes -1.44^m, -0.73^m, 0.40^m, and 0.45^m in the upper panel and 1.16^m, and 1.50^m, 1.73^m, and 1.86^m in the lower panel, respectively. For further description of the graphs see caption of Fig. 5.32.

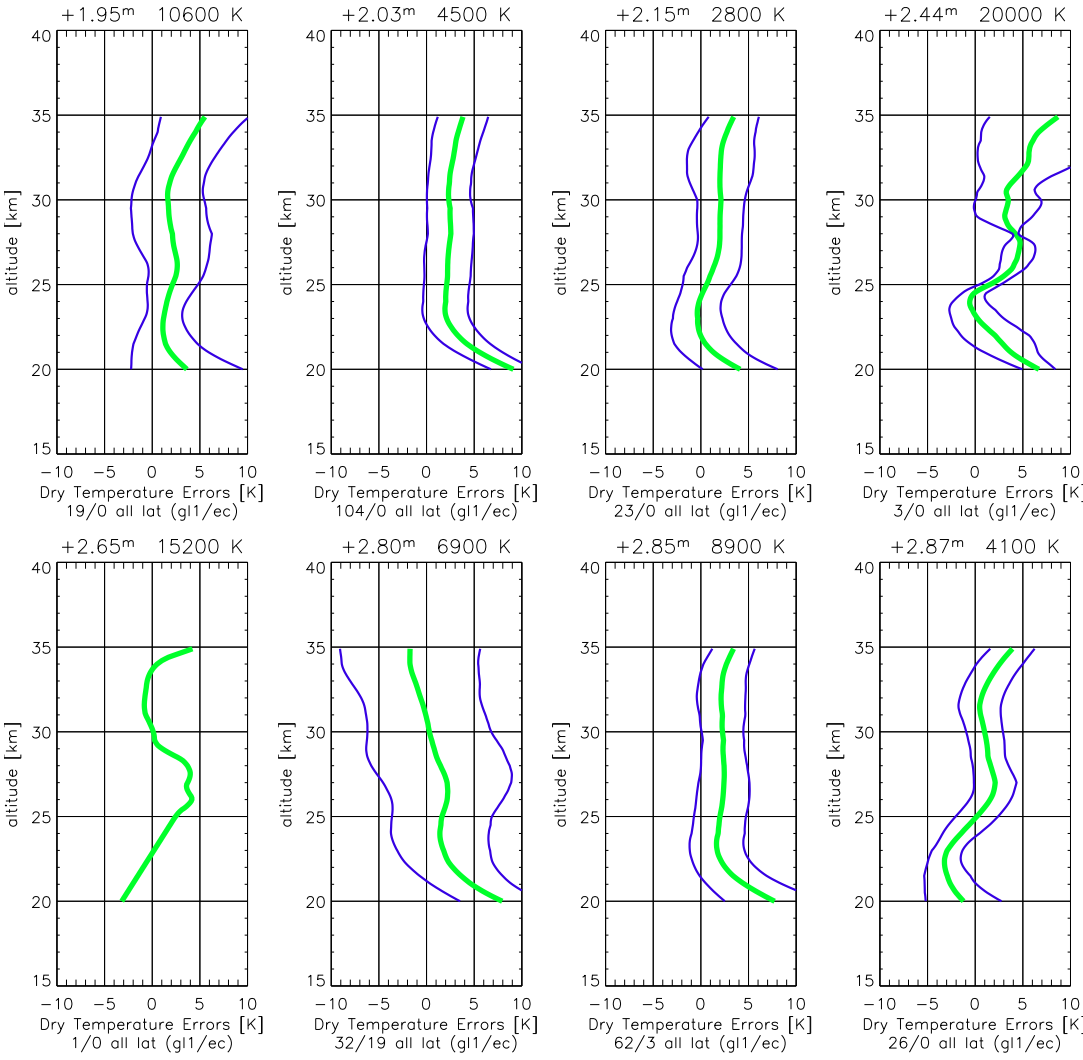

Figure 5.36. Temperature error statistics for more day ensembles in the period 2002-09-20 – 2002-12-02 (whole set 2002) validated with ECMWF analysis data. We show profiles for selected stars with visual magnitudes 1.95^m, 2.03^m, 2.15^m, and 2.44^m in the upper panel and 2.65^m, and 2.80^m, 2.85^m, and 2.87^m in the lower panel, respectively. For further description of the graphs see caption of Fig. 5.32.

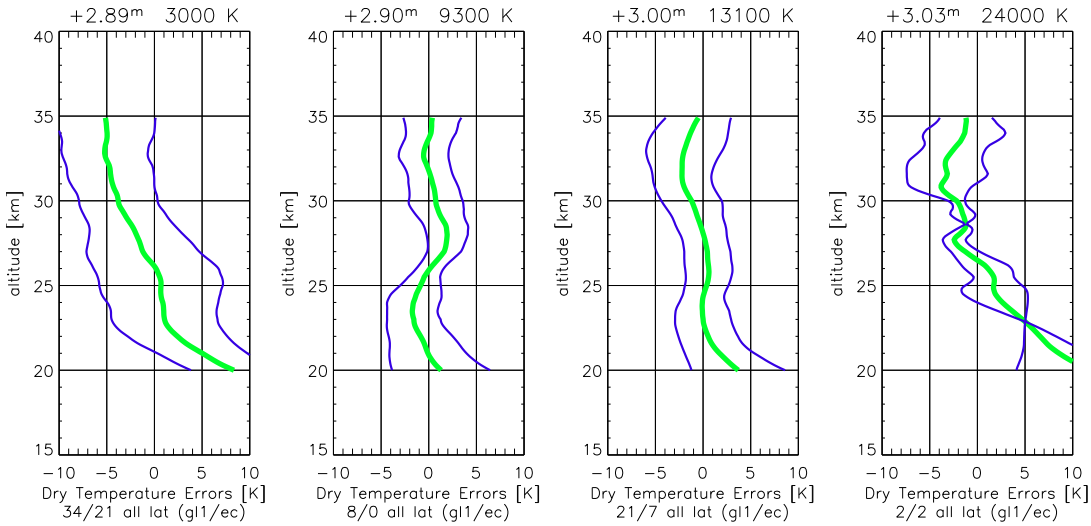

Figure 5.37. Temperature error statistics for more day ensembles in the period 2002-09-20 – 2002-12-02 (whole set 2002) validated with ECMWF analysis data. We show profiles for selected stars with visual magnitudes 2.98^m, 2.90^m, 3.00^m, and 3.03^m. For further description of the graphs see caption of Fig. 5.32.

5.6 Real Temperature Retrieval Validation (set 2003)

This Section is dedicated to the validation of temperature retrieval results from the period September 2003. Most of the conclusions drawn in Section 5.5 also apply here. In comparison to the set of year 2002, we have no MIPAS data available and thus only validate with CHAMP GPS and ECMWF analysis data. The GOMOS data set of 2003 contains a lot of dark and bright limb occultations, but only results for dark limb occultations are shown due to their better retrieval quality; bright limb data could not be processed with any satisfactory results with the present algorithm.

Mirror data from GOMOS in the set 2003 has undergone some changes compared to the profiles in the year 2002 set. SFA/SATU data is now stored in real angles, in turn in 2002 there were internal mirror positions used. The latter had to be converted into angles via a list of formulas given in [*GOMOS-ESL* (1999)]. A second change, not directly effecting the GOMOS product, is connected to malfunctions of the nominal star tracker in spring 2003 and thus leading to a switch to redundant electronics in July 2003. These two facts may influence our 2003 temperature retrieval and lead to results lacking the higher accuracy found in the 2002 data set.

From a total of over 9000 GOMOS profiles, about 4600 (cf. Tab. 5.12) were identified as dark limb occultations and about 2200 profiles could be processed successfully. Outliers are identified as profiles with errors larger than 20% between 20 and 30 km altitude. These profiles are used for the error statistics. A validation with CHAMP profiles was performed for 79 (cf. Tab. 5.9) coinciding profiles, which lie within 300 km of radius and the time of occultation does not differ by more than 3 hours. Fig. 5.38 illustrates the geographic distribution of the profile ensembles.

Profiles	**low**	**mid**	**high**	**all**
GOMOS	1554	2545	545	4644
CHAMP	1398	1341	1288	4027
ECMWF	1554	2545	545	4644

Table 5.12. Numbers of profiles in total sets of available GOMOS, CHAMP, and ECMWF data in the period September 01 - 30, 2003. The sets were separated into low, mid, and high latitude regions. An overall count is given as well.

Profiles	**Coincidences**
GOMOS – CHAMP	79
GOMOS – ECMWF	4644

Table 5.13. Numbers of coinciding profiles in total sets of available GOMOS, CHAMP, and ECMWF data in the period September 01 - 30, 2003.

As for the set 2002, here we also give a set of single profiles for bending angle errors and temperatures (see Fig. 5.39). We have also chosen some stars (1.16^m, 2.15^m, 2.80^m, and 3.00^m), which have large contributions to the error statistics.

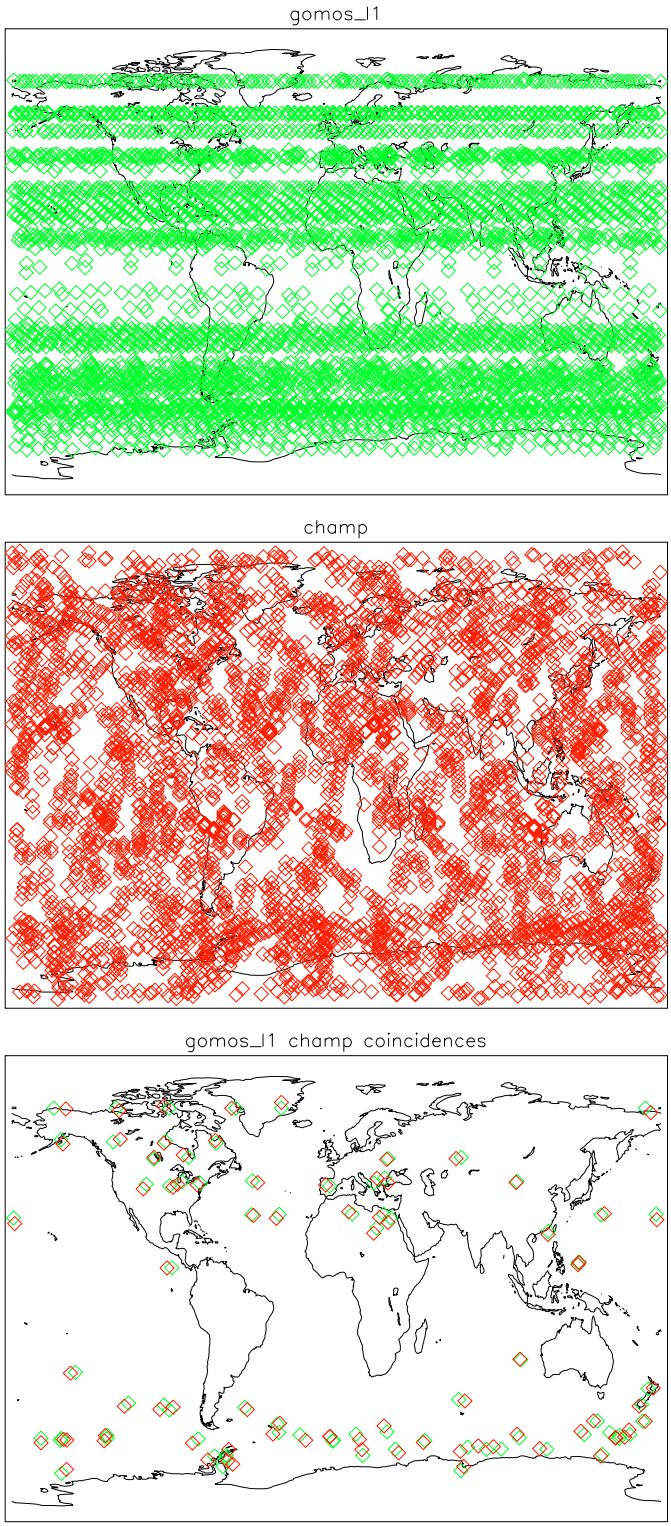

Figure 5.38. Locations where GOMOS (upper panel) and CHAMP (mid panel) measurements were performed. The plots displays 4644 and 4027 occultation profiles, respectively. Data was available for days: September 01 - 30, 2003. ECMWF profiles were taken at the same time and location as data was available for GOMOS. In the lower panel we find 79 coincidences for GOMOS to CHAMP measurements within an interval of 300 km and 3 hours.

Products	Latitude	$\mathbf{x_{acc}}$	$\mathbf{x_{out}}$
GOMOS – CHAMP	all	20	32
GOMOS – CHAMP	low	–	–
GOMOS – CHAMP	mid	19	16
GOMOS – CHAMP	high	1	14
GOMOS – ECMWF	all	1117	1144
GOMOS – ECMWF	low	–	–
GOMOS – ECMWF	mid	1082	724
GOMOS – ECMWF	high	35	421

Table 5.14. Number of processed and accepted profiles $\mathbf{x}_{\mathrm{acc}}$ contributing to the error statistics and not considered outliers $\mathbf{x}_{\mathrm{out}}$. The profiles listed here are measured under dark limb conditions. The outliers are identified as profiles with errors larger than 20% between 20 and 30 km altitude.

m_{v}	T_{star} [K]	λ_{max} [nm]	$\mathbf{x_{acc,ch}}$	$\mathbf{x_{out,ch}}$	$\mathbf{x_{acc,ec}}$	$\mathbf{x_{out,ec}}$
–1.44	11000	263.45	–	–	46	64
0.40	6500	445.84	1	7	54	220
1.16	9700	298.76	4	0	288	8
1.50	26000	111.46	–	–	30	29
1.73	15200	190.65	2	1	32	19
2.15	2800	1035.00	1	0	110	37
2.44	20000	144.90	–	–	6	15
2.80	6900	420.00	2	1	78	41
2.85	8900	325.61	–	–	1	14
2.89	3000	966.00	2	3	32	80
3.00	13100	221.22	2	0	117	27
3.03	26000	111.46	–	–	4	0

Table 5.15. Total retrieved and accepted temperature profiles $\mathbf{x}_{\mathrm{acc}}$ and outliers $\mathbf{x}_{\mathrm{out}}$ for visual star magnitude m_{v} and the star temperature T_{star} in the validation period 2003. The profiles are separated by a validation with CHAMP (ch) and ECMWF (ec) profiles. The maximum wavelength λ_{max} denotes the maximum of the Planck function B_ν at given temperature. The outliers are identified as profiles with errors that are larger than 20% between 20 and 30 km altitude. This table only includes all shown plots, but some stars are missing due to bad data quality.

5.6.1 Validation with globally distributed profiles

In the validation of GOMOS data for the year 2003, there is, compared to year 2002, a severe degradation of retrieval quality noticeable. The validation with CHAMP profiles (see Fig. 5.40) leads to positive biases of ~ 3.5 K at all altitude levels shown from 20 km up to 35 km. Mostly mid latitude profiles contribute to the overall error statistics, while only one (!) high latitude profile successfully passes the restrictions for an outlier correction. Profiles are marked as outlier, if the temperature errors exceed 20% between 20 km and 30 km altitude. Low latitude profiles are not retrieved with any reasonable quality and thus not shown.

Temperature profile validation with ECMWF (see Fig. 5.41) confirms, what we have seen for the GOMOS – CHAMP validation. The overall profiles have an equivalent structure, peaking to more negative biases at 27 km and tending to positive biases above and below. Due to the abundance of available data for validation a lot more

profiles contribute to a high latitude error profile statistics, though there is still a large number of outliers.

In general one observes larger standard deviations for both profile validations compared to the corresponding graphs in the year 2002 Section. Standard deviations in the year 2002 profile validation had sometimes values even below 3 K, which is not observed here; standard deviations lie at ~ 6 K. The results indicate that the year 2003 temperature profiles are, given the present performance achieved, not significantly accurate for practical utility in atmospheric research and applications. Still it will be valuable to re-check the performance of this data product also again in the future to see whether quality increases may be achieved.

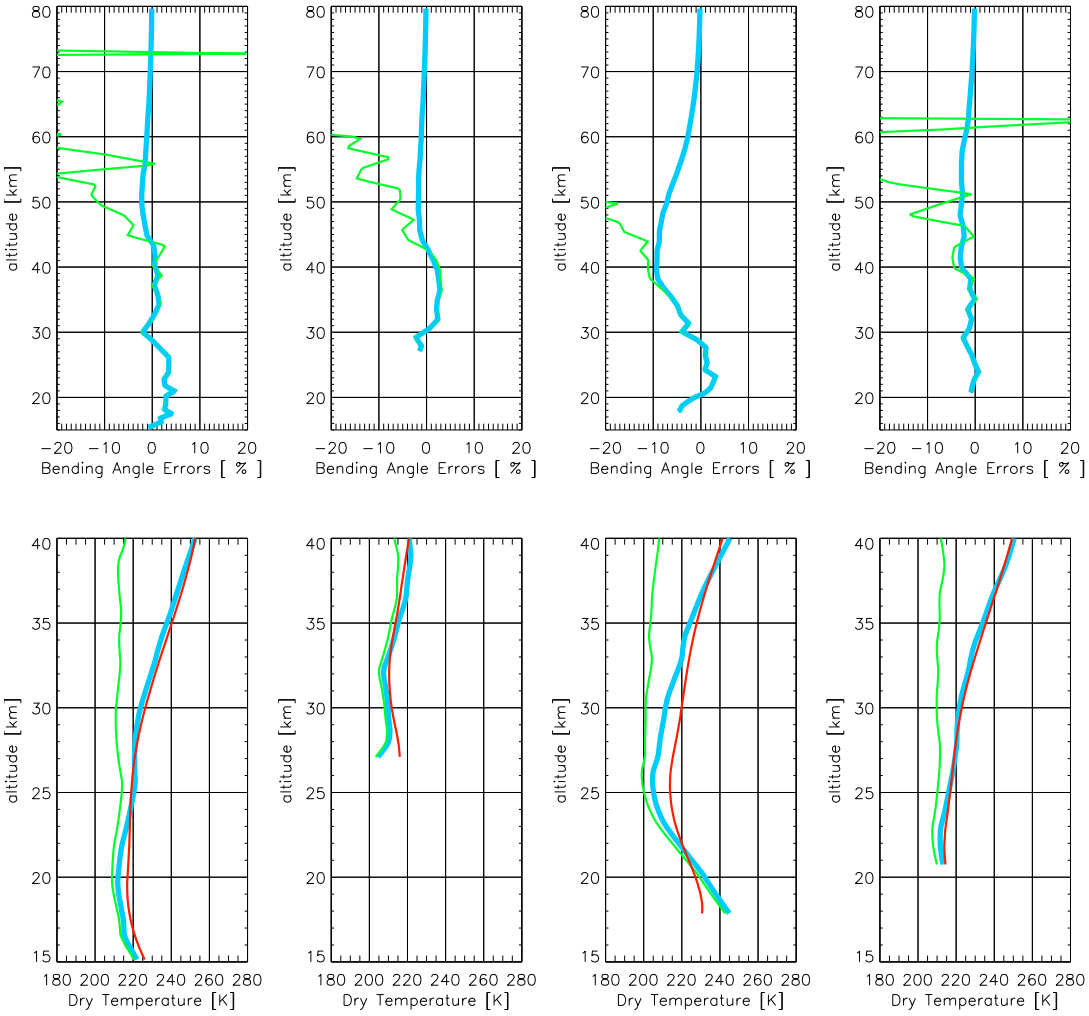

Figure 5.39. Relative bending angle errors profiles (upper panel) and corresponding temperatures (lower panel) for four different stars with 1.16^m, 2.15^m, 2.80^m, and 3.00^m. Heavy light blue lines denote statistically optimized profiles. Light red dotted lines are *a priori* profiles, while light green solid and dashed lines are measured profiles without statistical optimization.

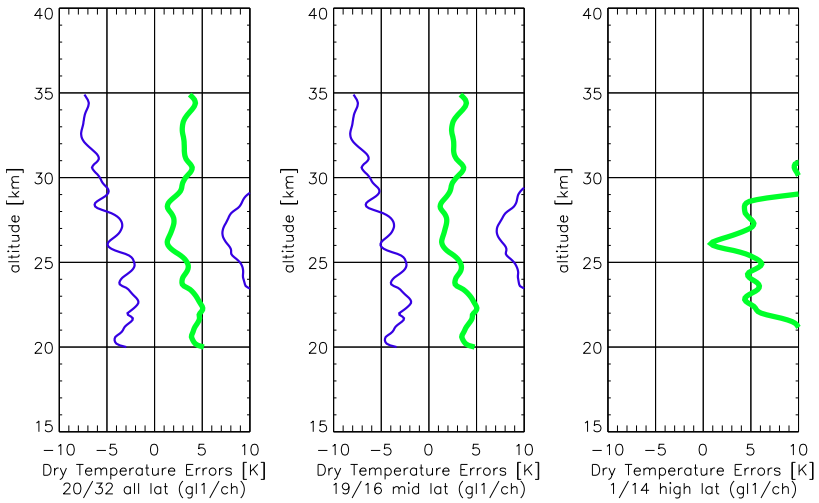

Figure 5.40. Temperature error statistics for more day ensembles in the period 2003-09-01 – 2003-09-30 (whole set 2003). We present profiles validated with CHAMP GPS profiles, which fulfill the coincidence criteria. From the left, the first panel shows the overall profile, the second and third panel show the mid and high latitude selected profiles. The heavy green line denotes the bias profile $\hat{\mathbf{b}}$, while the enveloping fine blue lines are the bias $\pm$ standard deviation profile $\hat{\mathbf{b}} \pm \hat{\mathbf{s}}$. To each error profile contributes a certain number of available files passing the quality check. This is given below each plot where on the left one finds the number of accepted profiles and the right number denotes the outliers.

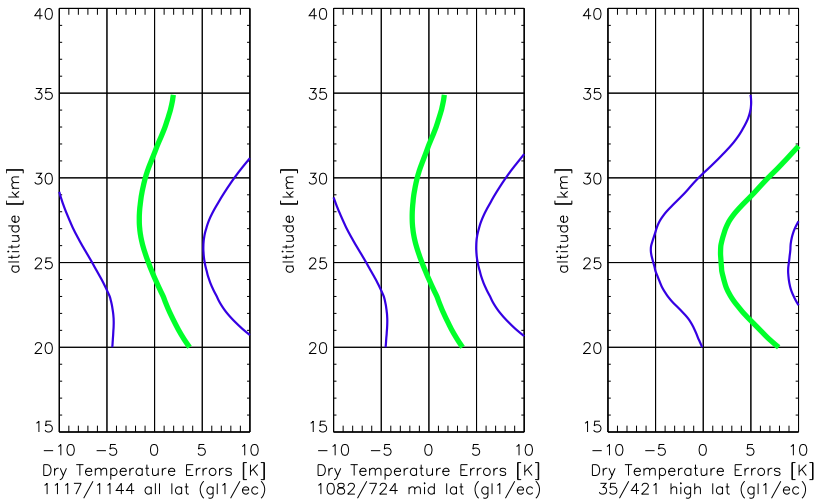

Figure 5.41. Temperature error statistics for more day ensembles in the period 2003-09-01 – 2003-09-30 (whole set 2003). We present profiles validated with ECMWF analysis profiles, which fulfill the coincidence criteria. For further description of the graphs see caption of Fig. 5.40.

5.6.2 Temperature Profiles and Errors at different Star Magnitudes

A selection of single stars for validation purposes was somewhat difficult due to the degraded quality in retrieval accuracy for the year 2003 data. Nevertheless some results from a validation with with CHAMP and ECMWF temperature profiles are shown to indicate the problems. Most of the stars available for temperature profiles where not accounted for, due to the fact that often bright limb occultations were performed. From a smaller set of dark limb occultation data, we could identify not more than twelve stars with some reasonable retrieval accuracy compared to 20 stars in the year 2002 set.

In the CHAMP validation (see Fig. 5.42 and 5.43) the set of data was further reduced due to few profile coincidences. Temperature validation for CHAMP data shows a strange behavior of almost all stars mainly originating from very few contributors to the statistics. Strong biases are observed for stars with magnitude 1.16^m, 1.73^m, 2.80^m, and 3.00^m. The profile with star magnitude 2.89^m is almost a complete outlier. Single profiles for magnitudes 0.40^m and 2.15^m provide evidently no serious ensemble of profiles for error statistics.

Profile validation with ECMWF data (see Fig. 5.44, 5.45, and 5.46) shows the capability of the temperature profile retrieval. Temperature validation for some stars stays in line with the results seen for the year 2002 validation. Well performing occultation results are given for stars with magnitude -1.44^m and 3.00^m. The profile statistics for star 2.80^m is almost better than for the year 2002. Profiles for stars 1.16^m and 2.89^m have small biases below 25 km, but severely loose accuracy above 27 km. The error profile statistics for star 3.03^m has a bias of ~ 4.5 K from 20 km up to 32 km, which is not observed in the year 2002 plot. There the bias was negative from 27 km upwards. Stars with 1.50^m and 2.15^m are connected to validation profiles with biases going from > 5 K at 20 km to values below –5 K above 28 km.

In summary, the results confirm from another perspective the findings of Section 5.6.1, that the year 2003 SFA/SATU data are poorer than the year 2002 ones. It will be investigated closer in the future under what conditions SFA/SATU based temperature retrievals might be of practical meteorological or climatological utility.

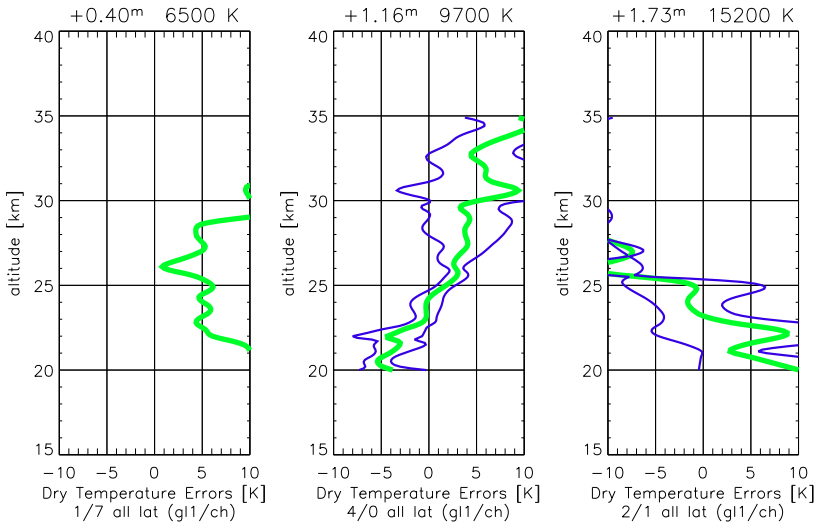

Figure 5.42. Temperature error statistics for more day ensembles in the period 2003-09-01 – 2002-09-30 (whole set 2003) validated with CHAMP GPS data. We show profiles for selected stars with visual magnitudes 0.40^m, 1.16^m, and 1.73^m. The heavy green line denotes the bias profile $\hat{\mathbf{b}}$, while the enveloping fine blue lines are the bias $\pm$ standard deviation profile $\hat{\mathbf{b}} \pm \hat{\mathbf{s}}$. To each error profile contributes a certain number of available files passing the quality check. This is given below each plot where on the left one finds the number of accepted profiles and the right number denotes the outliers.

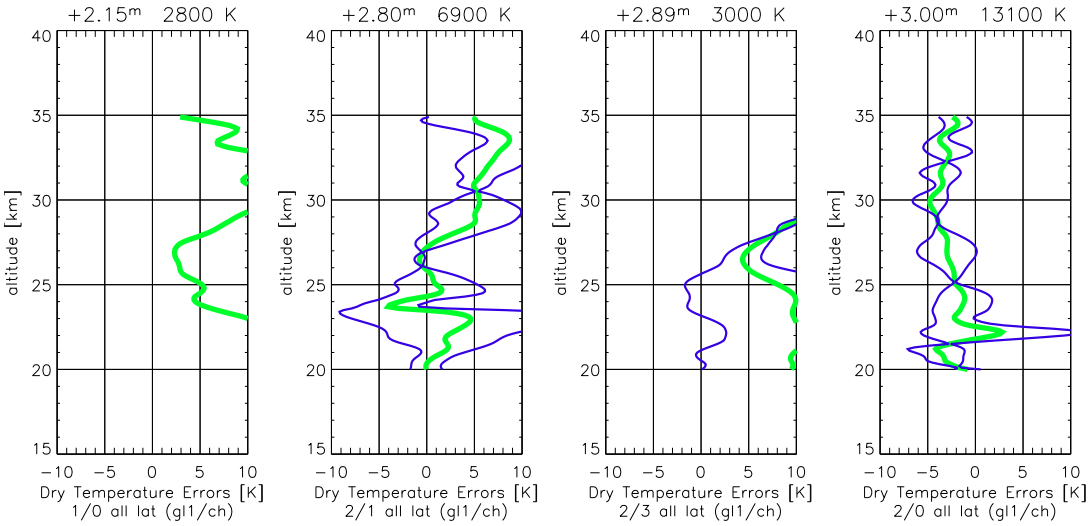

Figure 5.43. Temperature error statistics for more day ensembles in the period 2003-09-01 – 2002-09-30 (whole set 2003) validated with CHAMP GPS data. We show profiles for selected stars with visual magnitudes 2.15^m, 2.80^m, 2.89^m, and 3.00^m. For further description of the graphs see caption of Fig. 5.42.

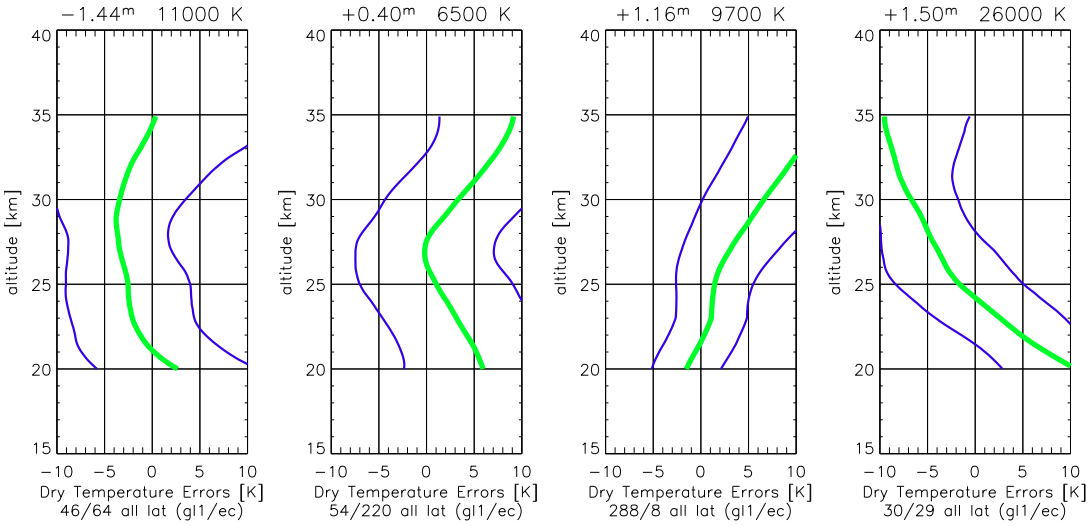

Figure 5.44. Temperature error statistics for more day ensembles in the period 2003-09-01 – 2002-09-30 (whole set 2003) validated with ECMWF analysis data. We show profiles for selected stars with visual magnitudes -1.44^m, 0.40^m, 1.16^m, and 1.50^m. For further description of the graphs see caption of Fig. 5.42.

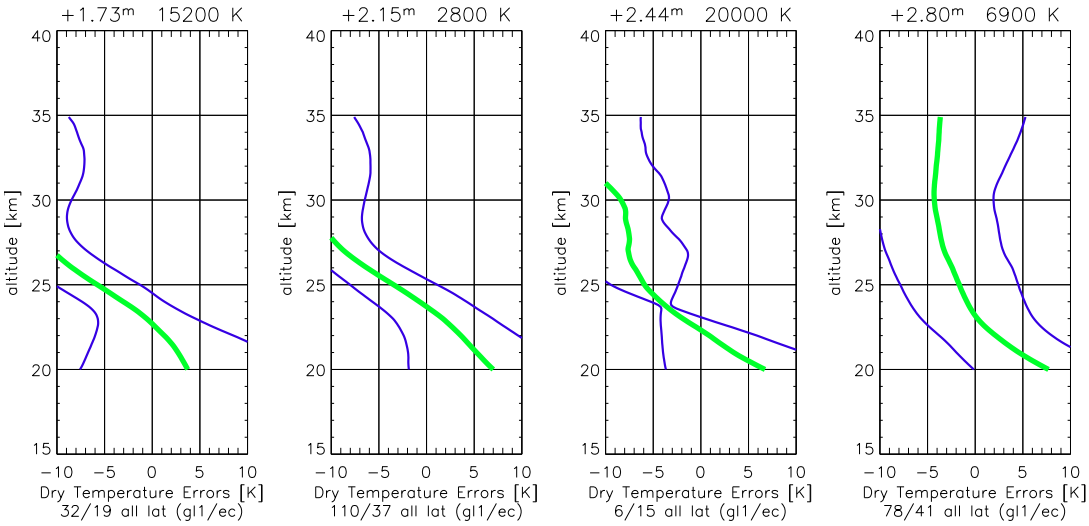

Figure 5.45. Temperature error statistics for more day ensembles in the period 2003-09-01 – 2002-09-30 (whole set 2003) validated with ECMWF analysis data. We show profiles for selected stars with visual magnitudes 1.73^m, 2.15^m, 2.44^m, and 2.80^m. For further description of the graphs see caption of Fig. 5.42.

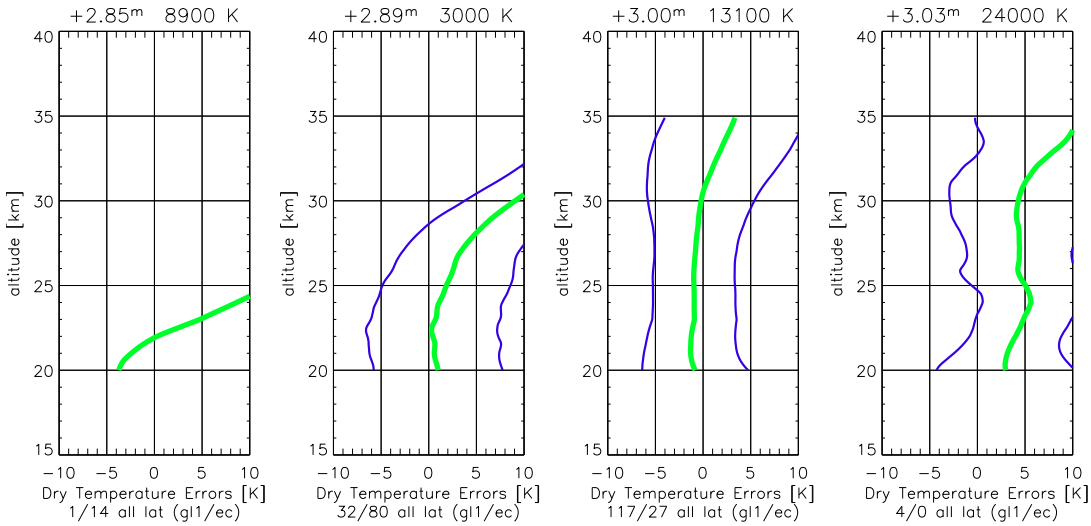

Figure 5.46. Temperature error statistics for more day ensembles in the period 2003-09-01 – 2002-09-30 (whole set 2003) validated with ECMWF analysis data. We show profiles for selected stars with visual magnitudes 2.85^m, 2.89^m, 3.00^m, and 3.03^m. For further description of the graphs see caption of Fig. 5.42.

Summary and Conclusions

This thesis was dedicated to an analysis of ozone and temperature profiles gained by measurements from the Envisat/GOMOS stellar occultation sensor. In addition a simulation study for both types of profiles was performed, confirming our adequate implementation of retrieval techniques.

The first Chapter dealt with details on atmospheric physics. It shows how the radiative transfer is connected to absorption, emission and scattering processes. As well we give an introduction to ozone physics and chemistry. The subsequent Chapter summarizes facts concerning atmospheric remote sensing techniques and details on stellar occultations are discussed. After a concise description of the Envisat satellite and its payload, especially the atmospheric chemistry instruments (GOMOS, MIPAS, and SCIAMACHY), we come to a precise illustration of selected retrieval algorithms and error statistics setup. Finally, a study on simulated ozone and temperature data is discussed as well as retrievals from Envisat/GOMOS real measurements.

Envisat is the so far largest European satellite for Earth observation purposes. It provides measurements on the land masses, the oceans, the ice sheets, and the atmosphere of our home planet. GOMOS, the Global Ozone Monitoring by Occultation of Stars instrument is one amongst three atmospheric instruments on-board Envisat. The instruments measure light coming from stellar sources in broad wavelength bands in the UV, visible, and IR and enable to invert it into geophysical products such as ozone and NO_2 profiles. We make use of the measured transmitted light through the atmosphere at selected wavelengths in the Hartley and Huggins as well as in the Chappuis band. The measured signals are inverted by our routines mainly into ozone profiles and validated with the operational GOMOS ozone product and with ECMWF analysis data.

We first built a realistic forward model representing the physical state of the atmosphere. An integral over the line-of-sight, connecting the star with the GOMOS instruments, was carried out by considering absorptive constituents such as ozone, NO_2 and NO_3 as well as a refractive component representing the bulk air. The forward model serves as input into our ozone retrieval process. The latter follows a so-called optimal estimation technique, which sensibly incorporates *a priori* information. The inversion scheme is an iterative process, starting with a first guess profile, and stops if a designated minimum in a cost function is obtained. The minimum is connected to the number of selected wavelengths and height levels. One focus in this thesis lies on an ozone profile retrieval, but the inversion routines for transmission data are also capable of retrieving NO_2 profiles in a joint retrieval.

Before transmission data could be incorporated into our inversion process, GOMOS-

measured level 1b data had to be reprocessed and corrected for scintillations and refractive dilution effects. Scintillations are rapid variations in apparent position, brightness, or color of a distant luminous object viewed through the atmosphere. The so-called refractive dilution has its origin in the change of the propagation direction of the ray while passing the atmosphere. This effect is related to the density gradient in the atmosphere causing a larger deflection to a grazing ray compared to rays with larger impact parameters. Both effects, the signal scintillation and the refractive dilution, are chiefly noticeable in the lower stratosphere and in the troposphere and degrades the signal coming from stellar sources.

The study of simulated ozone profiles was important for the extension to real measurements. In this simulation study we restricted ourselves to include a small set of well selected wavelength channels perfectly placed to cover ozone absorption bands. Our set of channels (260, 280, 288, 295, 302, 309, 317, 328, 334, 337, 340, 343, 600, and 605 nm) provides the maximum possible information coming from the measurement by simultaneously reducing the computational time to retrieve one profile. Simulated ozone retrieval profiles show excellent behavior throughout all high levels from 20 km up to 70 km. Error statistics was performed with 100 profiles contributing. Each of these profiles was constructed by imposing different initialization values for the optimal estimation scheme. Profile statistics is shown for four events at four different latitudes, all having biases smaller than 2% from 20 to 70 km.

Real transmission measurements were available for selected days in the year 2002 and 2003. Profile validations for both years show almost the same results. Ozone could be retrieved within a bias of $\sim 5\%$ from about 20 to 70 km. The small bias is due to the selected *a priori* error of 30%, were full linearity in the optimal estimation scheme for moderately non-linear systems is not given anymore. We could identify some special stars, where the ozone retrieval worked best. In general, bright stars with high temperature are preferred candidates of high quality ozone profiles down to the low stratosphere. Stars like Sirius with -1.44^m or Canopus with -0.73^m are examples of best behaving stellar light sources for a highly accurate ozone profile retrieval. Even dim, but at the same time hot stars with temperatures of up to 30000 K, show reliable results. In conclusion, the approach adopted for an efficient retrieval of ozone profiles has yielded encouraging results for simulated data up to high mesospheric regions. The application to real data clearly showed errors depending on transmission data quality and the selected star magnitude. Measured signals from good-quality stars enable to accurately see ozone structures. Comparisons with ECMWF ozone profiles show bias-type deviations of up to 30% throughout all latitude regions. These errors in the validation with ECMWF profiles have their origin in the ECMWF ozone analysis product itself.

A second focus in this thesis was the retrieval of temperature profiles from measurements of the star positions relative to the Envisat polar platform. So-called SFA/SATU star tracking data can be converted into bending angles and subsequently into density, pressure, and temperature profiles. Bending angles from GOMOS star tracker data (SFA/SATU) were not inverted directly. We first applied a so-called statistical optimization, thus leading to an overall bending angle profile, where *a priori* information especially at high altitude ensures a good temperature retrieval below 40 km. Bending angles at low altitudes mostly come from the measurement information. A best estimate bending angle profile is then inverted into a refractivity, density, pressure, and

temperature profile via an Abel transform.

Like for the GOMOS ozone retrieval, also here we first developed a simulation system for temperature profile retrieval, where results with high accuracy could be obtained. Based on some single profiles we show how *a priori* profiles increase the quality of retrieved temperature profiles at high altitudes.

As for transmission data, real bending angles were available for the same selected days in the year 2002 and 2003. Retrieved temperature profiles were validated with CHAMP GPS, Envisat/MIPAS (year 2002 only), and ECMWF analysis data. An overall plot for year 2002 data reveals the basic capability of using GOMOS SFA/SATU data for a temperature retrieval. Data validated with CHAMP has a exhibit positive bias of $\sim$ 5 K from 20 - 23 km, which decreases rapidly to values of $<$ 2 K from 23 - 35 km. The corresponding MIPAS and ECMWF validation results are even better, where biases especially in the low latitude profile stay below 2 K throughout the whole altitude range shown. As noted for the ozone retrieval, some stars provide signals which are preferred for our retrieval. In general, bright and hot stars lead to best results. Such stars have visual magnitudes of, e.g., -1.44^m, 0.45^m, or also 1.73^m, which is a dim but hot star.

A validation of year 2003 GOMOS bending angle data does not perform as good as expected, compared to the good results of the 2002 validation campaign. Temperature retrieval quality is severely degraded, which may have several reasons as follows. Mirror data from GOMOS in the set 2003 has undergone some changes compared to the profiles in the year 2002 set; SFA/SATU data is now stored in form of real angles, whereas in 2002 there were internal mirror positions used. A second change, not directly effecting the GOMOS product, is connected to malfunctions of the nominal star tracker, which led to switching to redundant electronics in July 2003. Nevertheless part of the profiles could be identified as reasonably good and are validated with CHAMP and ECMWF data. Biases are now seen even more clearly for the validation with CHAMP profiles, while the ECMWF validation has enough contributing profiles to the errors statistics that biases stay at values as seen for 2002 data. Some selected stars give results in the temperature retrieval validation with small biases of $\sim$ 2 K (e.g., hot star with 3.00^m).

In conclusion, we find that we have now a well-working retrieval algorithm with partially excellent performance depending on the validated year, latitude regime, and altitude region. In theory, density profiles, a pre-stage in the temperature retrieval process, can be used to update and improve the background refractivity fields required by the raytracing in the forward model. Such an exploitation of data would give the most accurate physical environment for an atmospheric constituent (e.g., ozone) retrieval. Also the temperature data can help in providing accurate temperature-dependent cross section values in the constituent retrieval process. Due to lacking high accuracy of density and temperature data we neglected this in the first place, but an investigation of a proper inclusion of such profiles is pending. High resolution temperature profiles from GOMOS photometer data may be an excellent candidate to increase atmospheric background data at the stage of raytracing and to optimize the accuracy of cross section values.

A validation with ozone from other Envisat atmospheric instruments such as MIPAS is a task for future enhancements of the validation scheme. Extending the measurement capabilities to lowest altitudes (below 20 km) is a further challenge at all wavelengths. The significance of the refractive effects in this region couples with the ever-decreasing

signal of the star to increase the difficulty of getting high enough signal-to-noise for accurate data to be obtained. Stellar occultation instruments will be required which have excellent throughput, sensitivity, and tracking capabilities.

A

Acronyms and Abbreviations

AATSR	Advanced Along Track Scanning Radiometer
ACRI-ST	ACRI-ST Observations de la Terre et Sciences de l'Environnement
AFGL	Air Force Geophysics Laboratory
AMI	Active Microwave Instrumentation
ARTEMIS	Advanced Relay and Technology Mission
ASA	Austrian Space Agency
ASAR	Advanced Synthetic Aperture Radar
BIRA	Belgisch Instituut voor Ruimte-Aëronomie
BASCOE	Belgian Assimilation System of Chemical Observations from Envisat
BEAT	Basic Envisat Atmospheric Toolbox
CCD	Charge-Coupled Device
CFC	Chlorofluorocarbons
CFRP	Carbon Fiber Reinforced Plastic
CHAMP	Challenging Minisatellite Payload
CIRA	Cooperative Institute for Research in the Atmosphere
CNRS	Centre National de la Recherche Scientifique
COALA	Calibration of Ozone through Atmospheric Limb Acquisitions
DARA	Deutsche Agentur für Raumfahrtangelegenheiten
DLR	Deutsches Zentrum für Luft- und Raumfahrt
DORIS	Doppler Orbitography and Radiopositioning Integrated by Satellite
DU	Dobson Unit
ECMWF	European Centre for Medium Range Weather Forecast
EGOPS	End-to-end Occultation Sounding Simulator
ERS	European Remote Sensing Satellite
ESA	European Space Agency
ESL	Expert Support Laboratory
EUV	Extreme Ultraviolet
FASCODE	Fast Atmospheric Signature Code
FMI	Finnish Meteorological Institute

FWHM	Full Width at Half Maximum
GFZ	Geo Forschungs Zentrum Potsdam
GIFS	GOMOS Interface Structure
GNSS	Global Navigation Satellite System
GOME	Global Ozone Monitoring Experiment
GOMOS	Global Ozone Monitoring by Occultation of Stars
GPS	Global Positioning System
HRTP	High Resolution Temperature Profiles
IGAM	Institut für Geophysik, Astrophysik und Meteorologie
IASB	Institut d'Aéronomie Spatiale de Belgique
IASI	Infrared Atmospheric Sounding Interferometer
IMK	Institut für Meteorologie und Klimaforschung
IR	Infrared
LEO	Low Earth Orbit
LTE	Local Thermodynamic Equilibrium
LRR	Laser Retroreflector
LSB	Least Significant Bit
LW	Longwave
MERIS	Medium Resolution Imaging Spectrometer
METOP	Meteorological Operational Satellite
MEO	Medium Earth Orbit
MIPAS	Michelson Interferometer for Passive Atmospheric Sounding
MSIS	Mass Spectrometer Incoherent Scatter
MSX	Midcourse Space Experiment
MUV	Middle Ultraviolet
MWR	Microwave Radiometer
NIVR	Nederlands Instituut voor Vliegtuigontwikkeling en Ruimtevaart
ODP	Ozone Depletion Potential
ORA	Occultation Radiometer
POEM	Polar-Orbit Earth Observation Mission
PSC	Polar Stratospheric Cloud
RA-2	Radar Altimeter 2
RO	Radio Occultation
RMS	rms or Root Mean Square
SA	Service d'Aéronomie
SAGE	Stratospheric Aerosol and Gas Experiment
SAR	Synthetic Aperture Radar
SATU	Star Acquisition and Tracking Unit
SCIAMACHY	Scanning Imaging Absorption Spectrometer for Atmospheric Chartography
SDE	Science Data Electronics
SFA	Steering Front Assembly
SLR	Satellite Laser Ranging

SMAS	Sun Monitor and Atmospheric Sounder
SNR	Signal-to-Noise Ratio
SPOT	Satellite/Systéme Probatoire/Pour l'Observation de la Terre
SST	Sea Surface Temperature
STS	Space Transport System
SW	Shortwave
TOMS	Total Ozone Mapping Spectrometer
U.S.	United States
UV	Ultraviolet
UVVIS	Ultraviolet and Visible
VAR	Variational
WS	Wind Scatterometer

B

Inverse Problem Methodology

B.1 Classification of Inverse Problems

In general a linear problem has a quadratic cost function term for the state vector, which leads to a linear solution of the problem. For a non-linear problem the forward model may be non-linear, or in the case the forward model is linear, a prior information constrains the problem and non-linearity is observed. A non Gaussian probability density function (*pdf*) will also lead to a non-linear problem. In general one can find a classification of linearity of inverse problems [*Rodgers* (2000)]:

- **Linear**

  The forward model can be found in the form $\mathbf{y} = \mathbf{K}\mathbf{x}$ and any *a priori* is Gaussian.

- **Nearly linear**

  A general non-linear problem, but a linearization by a prior state can be found. Problems are linear to the accuracy of the measurements, or to the accuracy of the solution within the normal range of variations of the state.

- **Moderately non-linear**

  A linearization is adequate for error analysis, but not for finding the solution.

- **Grossly non-linear**

  Problems are as well non-linear within the range of errors

An overview of inverse problems is given in Tab. B.1.

B.2 The Bayesian Approach

The Bayesian approach is a method to solve inverse problems perturbed by noise, where we have rough but reliable prior knowledge of the behavior of a state of interest. We can enhance this prior knowledge in a consistent way by incorporating measurements.

$\mathbf{A}$ is of full rank $\text{rank}(\mathbf{A}) = \min(m,n)$			$\mathbf{A}$ is rank deficient $\text{rank}(\mathbf{A}) < \min(m,n)$
m>n $\text{rank}(\mathbf{A}) = n$	m=n $\text{rank}(\mathbf{A}) = m = n$	m<n $\text{rank}(\mathbf{A}) = m$	m, n unordered $\text{rank}(\mathbf{A}) < \min(m,n)$
$\mathbf{Ax} = \mathbf{y}$ over-determined	$\mathbf{Ax} = \mathbf{y}$ even-determined	$\mathbf{Ax} = \mathbf{y}$ under-determined	$\mathbf{Ax} = \mathbf{y}$ under- or mixed-determined
$\nexists \mathbf{A}^{-1}$	$\exists \mathbf{A}^{-1}$	$\nexists \mathbf{A}^{-1}$	$\nexists \mathbf{A}^{-1}$
$\mathbf{A}^{-g} = \left(\mathbf{A}^T\mathbf{A}\right)^{-1}\mathbf{A}^T$	$\mathbf{A}^{-g} = \mathbf{A}^{-1}$	$\mathbf{A}^{-g} = \mathbf{A}^T\left(\mathbf{A}\mathbf{A}^T\right)^{-1}$	$\mathbf{A}^{-g} = \mathbf{V}\mathbf{\Lambda}^{-g}\mathbf{U}^T$
$\mathbf{A}^{-g}\mathbf{A} = I_n$ $\mathbf{A}\mathbf{A}^{-g} \neq I_m$	$\mathbf{A}^{-1}\mathbf{A} = I_n$ $\mathbf{A}\mathbf{A}^{-1} = I_m$	$\mathbf{A}^{-g}\mathbf{A} \neq I_n$ $\mathbf{A}\mathbf{A}^{-g} = I_m$	$\mathbf{A}^{-g}\mathbf{A} \neq I_n$ $\mathbf{A}\mathbf{A}^{-g} \neq I_m$
$\mathbf{x} = \mathbf{A}^{-g}\mathbf{y}$ least squares solution	$\mathbf{x} = \mathbf{A}^{-1}\mathbf{y}$ exact solution	$\mathbf{x} = \mathbf{A}^{-g}\mathbf{y}$ min norm solution	$\mathbf{x} = \mathbf{A}^{-g}\mathbf{y}$ least squares - min norm solution

Table B.1. An overview of inverse problems and their classifications. The general solution $\mathbf{A}^{-g}$ is given and $\mathbf{A}^{-1}$ and $\mathbf{A}^T$ denote the inverse and the transpose matrix, respectively (e.g., [*Fehmers* (1996)]).

Imperfect prior knowledge can be quantified as a *pdf* over the state space, whereas an imperfect measurement is quantified by a *pdf* over the measurement space. Bayes' theorem tells how the measurement *pdf* maps into the state space and combines with prior knowledge, according to a forward model $\mathbf{y} = \mathbf{F}(\mathbf{x}) + \varepsilon$ (cf. Section 4.4.1).

The scalar-valued *pdf* can be summarized as follows:

- $P(\mathbf{x})$

  as the prior *pdf* of the state $\mathbf{x}$. This means that the quantity $P(\mathbf{x})\mathrm{d}\mathbf{x}$ is the probability before the measurement that $\mathbf{x}$ lies in the multidimensional volume ($\mathbf{x}$, $\mathbf{x}$+d$\mathbf{x}$), expressing quantitatively our knowledge of $\mathbf{x}$ before the measurement is made. The $P(\mathbf{x})$ is normalized by $\int P(\mathbf{x})\mathrm{d}\mathbf{x} = 1$.

- $P(\mathbf{y})$

  as the prior *pdf* for the measurement, with a similar meaning. This is the *pdf* of the measurement before is is made.

- $P(\mathbf{x}, \mathbf{y})$

  as the joint prior *pdf* of $\mathbf{x}$ and $\mathbf{y}$. meaning that $P(\mathbf{x}, \mathbf{y})\mathrm{d}\mathbf{x}\mathrm{d}\mathbf{y}$ is the probability that $\mathbf{x}$ lies in ($\mathbf{x}$, $\mathbf{x}$+d$\mathbf{x}$) and $\mathbf{y}$ lies in ($\mathbf{y}$,$\mathbf{y}$+d$\mathbf{y}$)

- $P(\mathbf{y}|\mathbf{x})$

  as the conditional *pdf* of $\mathbf{y}$ given $\mathbf{x}$, meaning that $P(\mathbf{y}|\mathbf{x})\mathrm{d}\mathbf{y}$ is the probability that $\mathbf{y}$ lies in ($\mathbf{y}$, $\mathbf{y}$+d$\mathbf{y}$) when $\mathbf{x}$ has a given value

- $P(\mathbf{x}|\mathbf{y})$

  as the conditional *pdf* of $\mathbf{x}$ given $\mathbf{y}$, meaning that $P(\mathbf{x}|\mathbf{y})\mathrm{d}\mathbf{x}$ is the probability that $\mathbf{x}$ lies in ($\mathbf{x}$, $\mathbf{x}$+d$\mathbf{x}$) when $\mathbf{y}$ has a given value. This is the quantity of interest for solving the inverse problem.

We now refer to the *pdf* $P(\mathbf{x})$ which is given by the integral of the combined prior *pdf*, $P(\mathbf{x}, \mathbf{y})$, over all values of $\mathbf{y}$:

$$P(\mathbf{x}) = \int_{-\infty}^{\infty} P(\mathbf{x}, \mathbf{y}) d\mathbf{y}, \tag{B.1}$$

and $P(\mathbf{y})$ is found likewise by integrating over all $\mathbf{x}$. The conditional *pdf*, $P(\mathbf{x}|\mathbf{y})$, is proportional to the values of $P(\mathbf{x}, \mathbf{y})$ as a function of $\mathbf{x}$ for a given value of $\mathbf{y}$. The proportionality constant is normed by $\int P(\mathbf{x}|\mathbf{y}) d\mathbf{x} = 1$:

$$P(\mathbf{x}|\mathbf{y}) = \frac{P(\mathbf{x}, \mathbf{y})}{\int P(\mathbf{x}, \mathbf{y}) d\mathbf{x}} = \frac{P(\mathbf{x}, \mathbf{y})}{P(\mathbf{y})} \tag{B.2}$$

We can use similar arguments in order to show that $P(\mathbf{y}|\mathbf{x}) = P(\mathbf{x}, \mathbf{y})/P(\mathbf{x})$. By eliminating the combined prior *pdf* we obtain Bayes' theorem as the relationship between the two different conditional *pdf*'s

$$P(\mathbf{x}|\mathbf{y}) = \frac{P(\mathbf{y}|\mathbf{x}) P(\mathbf{x})}{P(\mathbf{y})}. \tag{B.3}$$

The posteriori *pdf* $P(\mathbf{x}|\mathbf{y})$ is the state for a given measurement. The prior knowledge $P(\mathbf{x})$ of the state is to be updated with the measurements. To get $P(\mathbf{y}|\mathbf{x})$, which describes the knowledge of $\mathbf{y}$ that is obtained if the state were $\mathbf{x}$, we only need the forward model and the statistical description of the measurement error. The only remaining quantity is the denominator, $P(\mathbf{y})$, which formally can be obtained by integrating $P(\mathbf{x}, \mathbf{y})$ over all $\mathbf{x}$. In practice, this is only a normalizing factor which is often not needed.

We now find a conceptual approach for solving the inverse problem defined by the Bayes' theorem:

- Before performing a measurement we have prior knowledge of the state expressed by a prior *pdf*.
- The measurement process is expressed by a forward model which maps the state space into the measurement space.
- Bayes' theorem provides us with a formalism to invert this mapping and calculate a posterior *pdf* by updating the prior *pdf* with a measurement *pdf*.

For more information on the relevance of the Bayesian approach in atmospheric remote sensing see, e.g., [*Rodgers* (1976)], [*Rodgers* (1990)], [*Rodgers* (2000)].

C

GOMOS Products and Star Names

C.1 GOMOS Data Products

Level 1b Data Product

Level 1b Product	**Sampling Rate**
Reference star spectrum	once per occultation
Reference atmospheric profile	2 Hz
Full transmission spectra and covariance	2 Hz
Central background estimate and error	2 Hz
Photometers data and error	1 kHz
SATU data	100 Hz
SFA angle measurements	5 Hz
Wavelength assignment of the spectra	2 Hz
Geolocation and error	4 Hz
Limb product	**Sampling Rate**
Upper and lower background spectra and error	2 Hz

Table C.1. GOMOS Level 1b and limb products [*ESA* (2002)].

Level 2 Data Product

Level 2 Product	**Contents**
Line density product	Line density of O_3, NO_2, NO_3, and error Line density of air and error Line density of O_2 and H_2O and error Line density of OClO and error
Local density product	Local density of O_3, NO_2, NO_3 and error Local density of air and error Local density of O_2 and H_2O and error Local density of OClO and error
Aerosol product	Extinction coefficient and error [km^{-1}] Spectral parameters of the extinction coefficient and error
Turbulence product	Tangent altitude including fluctuations High resolution vertical profile Local density
Geolocation and atmospheric profile	Position of the spacecraft and error Position of the tangent point of LOS and error Tangent point pressure and temperature (from external model) Local air density from GOMOS atmospheric profile and error Local temperature and error from GOMOS atmospheric profile
Accuracy estimate product	χ^2 final value Covariance matrix for line densities after spectral inversion Covariance matrix for local densities after vertical inversion
Residual extinction product	Transmission corrected for scintillation and dilution effects Transmission model function

Table C.2. GOMOS Level 2 products [*ESA* (2002)].

C.2 Star Names and Classifications

Star name				$m_{\mathbf{v}}$	$T_{\mathbf{star}}$ [K]	Spectral type	Latitude
Sirius	9	α	CMa	–1.44	11000	A1Vm	mid
Canopus		α	Car	–0.73	7000	A9II	low
Rigel	19	β	Ori	0.10	14000	B81ae	high
Procyon	10	α	CMi	0.40	6500	F5IV-V	mid/high
Achernar		α	Eri	0.45	24000	B3Vpe	low
Betelgeuse		α	Ori	0.87	3000	M2Iab	mid
Fomalhaut	24	α	PsA	1.16	9700	A3Va	mid
Adhara	21	ϵ	CMa	1.50	26000	B2II	mid
Alnilam	46	ϵ	Ori	1.69	30000	B0Ia	high
Al Na'ir		α	Gru	1.73	15200	B7IV	mid
Avior		ϵ	Car	1.86	4100	K3III+B2:V	low
		δ	Vel	1.95	10600	A1V	low/mid
Murzim	2	β	CMa	1.97	28000	TypeB1II-III	low/high
Diphda	16	β	Cet	2.03	4500	G9.5IIICH-1	high
		β	Gru	2.15	2800	M5III	mid
Alsuhail		λ	Vel	2.20	4400	K4.5Ib-II	mid
Mintaka	34	δ	Ori	2.25	30000	O9.5II	low
Ankaa		α	Phe	2.39	4500	K0III	mid
Aludra	31	η	CMa	2.44	20000	B5Ia	mid
		κ	Vel	2.49	26000	B2IV-V	mid
Phaet		α	Col	2.65	15200	B7IVe	low
		θ	Car	2.76	30000	B0Vp	low
	15	ρ	Pup	2.80	6900	F6IIpDel Del	mid
		β	Hyi	2.82	5800	G2IV	low
Deneb Algedi	49	δ	Cap	2.85	8900	Am	low/high
		α	Tuc	2.87	4100	K3III	low
Tejat Posterior	13	μ	Gem	2.89	3000	M3IIIab	mid/high
Acamar		θ^1	Eri	2.90	9300	A4III	mid
		υ	Car	2.92	7200	A6Ib	low
Al Dhanab		γ	Gru	3.00	13100	B8III	mid
	24	o^2	CMa	3.03	26000	B3Iab	high

Table C.3. Stars in the GOMOS star catalogue, which are used by our retrieval algorithm in order to gain ozone and temperature profiles. The stars are listed by the Flamsteed/Bayer designation (cf. [*The Stationary Office* (2003)]). Stars which are from spectral type A are typically favored in our ozone retrieval procedure. We give as well a column where one can find the latitude where GOMOS measures corresponding occultation profiles.

List of Figures

List of Tables

References

[*ACRI S.A. et al.* (1998)] ACRI S.A., et al., GOMOS High Level Algorithms Definition Document, *Tech. rep.*, ACRI S. A., France, Finnish Meteorol. Institute, Service d'Aronomie du CNRS, and Institut d'Aronomie Spatiale de Bruxelles, 1998, http://envisat.esa.int/support-docs/.

[*Anderson et al.* (1995)] Anderson, G., F. Kneizys, J. Chetwynd, J. Wang, M. Hoke, L. Rothman, L. Kimball, and R. McClatchey, FASCODE/MODTRAN/LOWTRAN: Past/Present/Future, *18th Ann. Rev. Conf. on Atm. Transmission Models*, 1995.

[*Andrews* (2000)] Andrews, D., *An Introduction to Atmospheric Physics*, Cambridge University Press, 2000.

[*Atreya* (1981)] Atreya, S., Measurement of Minor Species (H_2, Cl, O_3, NO) in the Earth's Atmosphere by the Occultation Technique, *Adv. Space Res.*, pp. 127–141, 1981.

[*Baum and Code* (1953)] Baum, W., and A. Code, A Photometric Observation of the Occultation of σ Arietis by Jupiter, *Astron. J.*, *58*, 108–112, 1953.

[*Bertaux et al.* (2001)] Bertaux, J., et al., Envisat/GOMOS An instrument for Global Atmospheric Ozone Monitoring, *Tech. rep.*, ESA Publication Division, 2001, sP-1244 'Envisat - GOMOS'.

[*Born and Wolf* (1993)] Born, M., and E. Wolf, *Principles of Optics*, Pergamon Press, Oxford, 1993.

[*Bracher et al.* (2004)] Bracher, A., K. Eichmann, C. von Savigny, and M. Weber, Ozone Distribution in the Arctic Winter/Spring 2002/2003 as Measured by GOMOS, MIPAS, and SCIAMACHY, in *Envisat Symposium 2004*, 2004.

[*Brasseur and Solomon* (1984)] Brasseur, G., and S. Solomon, *Aeronomy of the Middle Atmosphere*, D. Reidel Publishing Company, 1984.

[*Brasseur et al.* (1999)] Brasseur, G., J. Orlando, and G. Tyndall (Eds.), *Atmospheric Chemistry and Global Change*, Atmospheric and Space Science Series, Oxford Science Publications, 1999.

[*Bronstein et al.* (1993)] Bronstein, I., K. Semendjajew, G. Musiol, and H. Mülig, *Taschenbuch der Mathematik*, Verlag Harri Deutsch, 1993.

[*Browell et al.* (1990)] Browell, E., et al., Airborne Lidar Observations in the Wintertime Arctic Stratosphere: Polar Stratospheric Clouds, *Geophys. Res. Let.*, *19*, 385–388, 1990.

[*Chapman* (1930)] Chapman, S., A Theory of Upper Atmospheric Ozone, *Mem. R. Meteorol. Soc.*, *3*, 103–125, 1930.

[*Chu et al.* (1989)] Chu, W. P., M. McCormick, J. Lenoble, C. Brogniez, and P. Pruvost, SAGE II Inversion Algorithm, *J. Geophys. Res.*, *94*, 8339–8351, 1989.

[*Crutzen* (1970)] Crutzen, P., The Influence of Nitrogen Oxides on Atmospheric Ozone Content, *Q. J. R. Meteorol. Soc.*, *96*, 320–325, 1970.

[*DeMajistre and Yee* (2002)] DeMajistre, R., and J.-H. Yee, Atmospheric Remote Sensing Using A Combined Extinctive and Refractive Stellar Occultation Technique I. Inversion Method for Extinction Measurements, *J. Geophys. Res.*, *107*, 2002.

[*Dethof* (2004)] Dethof, A., Assimilation of ozone data in the ECMWF Integrated Forecast System, in *SPARC 2004*, 2004.

[*DLR* (2000a)] DLR, Product Specification Document of the GOME Data Processor, *Tech. rep.*, DLR, 2000a, eR-PS-DLR-GO-0016.

[*DLR* (2000b)] DLR, Envisat-1 SCIAMACHY ATBD, *Tech. rep.*, DLR, 2000b, eNV-ATB-SAO-SCI-2200-0003.

[*Edlen* (1953)] Edlen, B., The Dispersion of Standard Air, *J. Opt. Soc. Am.*, *43*, 339–345, 1953.

[*Edwards and Pawlak* (2000)] Edwards, P., and D. Pawlak, Metop: The Space Segment for Eumetsat's Polar System, *Tech. rep.*, ESA Publication Division, 2000.

[*Elachi* (1987)] Elachi, C., *Introduction to the Physics and Techniques of Remote Sensing*, Wiley Series in Remote Sensing, John Wiley and Sons, 1987.

[*Errera and Fonteyn* (2001)] Errera, Q., and D. Fonteyn, Four-dimensional Variational Chemical Assimilation of CRISTA Stratospheric Measurements, *J. Geophys. Res.*, *106*, 12,253–12,265, 2001.

[*ESA* (2000)] ESA, Further Achievements of the ERS Mission, *Tech. rep.*, ESA Publication Division, 2000, sP-1228 "ERS Further Achievements'.

[*ESA* (2002)] ESA, GOMOS Product Handbook, *Tech. rep.*, ESA Publication Division, 2002.

[*Fabian and Singh* (1999)] Fabian, P., and O. Singh (Eds.), *Reactive Halogen Compounds in the Atmosphere*, The Handbook of Environmental Chemistry, Springer, 1999.

[*Farman et al.* (1985)] Farman, J., B. Gardiner, and J. Shanklin, Large Losses of Total Ozone in Antarctica Reveal Seasonal ClO_x/NO_x interaction, *Nature*, *315*, 207, 1985.

[*Fehmers* (1996)] Fehmers, G., Tomography of the Ionosphere, Ph.D. thesis, Eindhoven University of Technology, The Netherlands, 1996.

[*Fischer et al.* (2000)] Fischer, H., et al., Envisat MIPAS, An Instrument for Atmospheric Chemistry and Climate Research, *Tech. rep.*, ESA Publication Division, 2000, sP-1299 'Envisat - MIPAS'.

[*Fjeldbo et al.* (1971)] Fjeldbo, G., V. Eshleman, and A. Kliore, The Neutral Atmosphere of Venus as Studied with the Mariner V Radio Occultation Experiments, *Astronomical Journal*, *76*, 123–140, 1971.

[*Foelsche* (1999)] Foelsche, U., Tropospheric Water Vapor Imaging by Combination of Ground-Based and Spaceborne GNSS Sounding Data, Ph.D. thesis, Institute for Geophysics, Astrophysics and Meteorology, University of Graz, Austria, 1999.

[*Fussen* (1998)] Fussen, D., A Critical Analysis of the Stratospheric Aerosol and Gas Experiment II Spectral Inversion Algorithm, *J. Geophys. Res.*, *103*, 8455, 1998.

[*Fussen et al.* (1998)] Fussen, D., E. Arjis, D. Nevejans, F. van Hellemont, C. Brogniez, and J. Lenoble, Validation of the ORA Spatial Inversion Algorithm with Respect to the Stratospheric Aerosol and Gas Experiment II Data, *App. Opt.*, *37*, 3121, 1998.

[*Gobiet and Kirchengast* (2002)] Gobiet, A., and G. Kirchengast, Sensitivity of atmospheric profiles retrieved from GNSS occultation data to ionospheric residual and high-altitude initialization errors, *Tech. rep.*, ESA/ESTEC No. 1/2002, 2002, institute for Geophysics, Astrophysics and Meteorology, University of Graz, Austria, 58 pp.

[*Gobiet and Kirchengast* (2004)] Gobiet, A., and G. Kirchengast, Advancements of Global Navigation Satellite System Radio Occultation Retrieval in the Upper Stratosphere for Optimal Climate Monitoring Utility, *J. Geophys. Res.*, *109*, 2004, in press.

[*Gobiet et al.* (2004a)] Gobiet, A., G. Kirchengast, J. Wickert, C. Retscher, D. Wang, and A. Hauchecorne, Evaluation of Stratospheric Radio Occultation Retrieval Using Data from CHAMP, MIPAS, GOMOS and ECMWF Analysis Fields, in *Earth Observation with CHAMP: Results from Three Years in Orbit*, edited by C. Reigber, H. Lühr, P. Schwintzer, and J. Wickert, pp. 531 – 536, Springer, 2004a.

[*Gobiet et al.* (2004b)] Gobiet, A., A. Steiner, C. Retscher, U. Foelsche, and G. Kirchengast, Radio Occultation Data and Algorithms Validation Based on CHAMP/GPS Data, *Tech. rep.*, Wiss. Bericht, No. 1/2004, 2004b, institute for Geophysics, Astrophysics and Meteorology, University of Graz, Austria.

[*GOMOS-ESL* (1999)] GOMOS-ESL, ENVISAT-1 Ground Segment GOMOS Level 1b Detailed Processing Model, *Tech. rep.*, ACRI, 1999.

[*Gorbunov and Sokolowsky* (1993)] Gorbunov, M., and S. Sokolowsky, Remote Sensing of Refractivity from Space for Global Observations of Atmospheric Parameters, *Tech. rep.*, Max-Planck-Institut, Hamburg, Germany, 1993, rep. No. 119, 58pp.

[*Hays and Roble* (1968)] Hays, P., and R. Roble, Stellar Spectra and Atmospheric Composition, *Journal of Atmospheric Science*, *25*, 1142, 1968.

[*Healy* (2001)] Healy, S., Smoothing Radio Occultation Bending Angles Above 40km, *Ann. Geophys.*, *19*, 459, 2001.

[*Hedin* (1983)] Hedin, A., A Revised Thermospheric Model Based on Mass Spectrometer and Incoherent Scatter Data: MSIS-83, *J. Geophys. Res.*, *88*, 10,170, 1983.

[*Hedin* (1987)] Hedin, A., MSIS-86 Thermospheric Model, *J. Geophys. Res.*, *92*, 4649, 1987.

[*Hedin* (1991)] Hedin, A., Extension of the MSIS Thermosphere Model into the Middle and Lower Atmosphere, *J. Geophys. Res.*, *96*, 1159, 1991.

[*Houghton et al.* (2001)] Houghton, J., et al. (Eds.), *Climate Change 2001: The Scientific Basis*, Cambridge University Press, 2001, contribution of Working Group I to the Third Assessment Report of the IPCC.

[*Huffmann* (1992)] Huffmann, R., *Atmospheric Ultraviolet Remote Sensing*, Academic Press, Inc, 1992.

[*Kirchengast* (1998)] Kirchengast, G., End-to-end GNSS Occultation Performance Simulator Overview and Exemplary Applications, *Wiss. Bericht, No. 2/1998,*, 1998, institute for Geophysics, Astrophysics and Meteorology, University of Graz, Austria.

[*Kirchengast et al.* (2002)] Kirchengast, G., J. Fritzer, and J. Ramsauer, End-to-end GNSS Occultation Performance Simulator Version 4 (EGOPS4) Software User Manual (Overview and Reference Manual), *Tech. rep.*, Technical Report ESA/ESTEC-3/2002, University of Graz, Austria, 2002, institute for Geophysics, Astrophysics and Meteorology, University of Graz, Austria, 472 pp.

[*Kursinski et al.* (1997)] Kursinski, E., G. Hajj, J. Schofield, R. Linfield, and K. Hardy, Observing the Earth's Atmosphere with Radio Occultation Measurements using GPS, *J. Geophys. Res.*, *102*, 23,429–23,465, 1997.

[*Lang and Pucker* (1998)] Lang, C., and N. Pucker, *Mathematische Methoden in der Physik*, Spektrum Akademischer Verlag GmbH, 1998.

[*McCormick et al.* (1989)] McCormick, M., J. Zawodny, R. Veiga, J. Larson, and P. Wang, An Overview of SAGE I and II Ozone Measurements, *Planetary Space Science*, *37*, 1567, 1989.

[*Molina and Rowland* (1974)] Molina, M., and F. Rowland, Stratospheric Sink for Chlorofluoromethanes: Chlorine Atomcatalyzed Destruction of Ozone, *Nature*, *249*, 810–812, 1974.

[*Nett* (2002)] Nett, H., MIPAS Validation Summary, *MIPAS Validation Review*, 2002.

[*Pannekoek* (1904)] Pannekoek, A., Über die Erscheinungen, welche bei einer Sternbedeckung durch einen Planeten auftreten, *Astron. Nachr.*, *164*, 5–10, 1904.

[*Paulsen* (2000)] Paulsen, T., GOMOS Level 1b/2 Algorithm Description Document for Enviview Pre-Release, *Tech. rep.*, ESA Doc. PO-TN-ESA-GM-1019, ESA/ESTEC, Noordwijk, Netherlands, 2000.

[*Peixoto and Ooort* (1992)] Peixoto, J., and A. Ooort, *Physics of Climate*, American Institute of Physics, 1992.

[*Press* (1993)] Press, C., *Handbook of Chemistry and Physics*, vol. 74, CRC press, 1993.

[*Rees* (2001)] Rees, W., *Physical Principles of Remote Sensing*, Cambridge University Press, 2001.

[*Rehrl* (2000)] Rehrl, C., Mesospheric Temperature and Ozone Sounding Based on Solar Occultation Data, Master's thesis, Institute for Geophysics, Astrophysics and Meteorology, University of Graz, Austria, 2000.

[*Rehrl and Kirchengast* (2004)] Rehrl, C., and G. Kirchengast, Mesospheric Temperature and Ozone Sounding by the SMAS Solar Occultation Sensor, in *Occultations for Probing Atmosphere and Climate*, edited by G. Kirchengast, U. Foelsche, and A. Steiner, pp. 333 – 342, Springer, 2004.

[*Retscher et al.* (2002)] Retscher, C., G. Kirchengast, and A. Hauchecorne, Middle Atmospheric Ozone Sounding by the Envisat/GOMOS Stellar Occultation Sensor, in *29th International Symposium on Remote Sensing of Environment*, edited by ISRSE, 2002.

[*Retscher et al.* (2004)] Retscher, C., G. Kirchengast, A. Gobiet, and A. Hauchecorne, Stratospheric Temperature and Ozone Sounding with Envisat/GOMOS Stellar Occultation, in *Occultations for Probing Atmosphere and Climate*, edited by G. Kirchengast, U. Foelsche, and A. Steiner, pp. 299 – 308, Springer, 2004.

[*Rieder and Kirchengast* (2001a)] Rieder, M., and G. Kirchengast, Error Analysis for Mesospheric Temperature Profiling by Absorptive Occultation Sensors, *Ann. Geophys.*, *19*, 71–81, 2001a.

[*Rieder and Kirchengast* (2001b)] Rieder, M., and G. Kirchengast, Error Analysis and Characterization of Atmospheric Profiles Retrieved from GNSS Occultation Data, *J. Geophys. Res.*, pp. 31,755–31,770, 2001b.

[*Riegler et al.* (1996)] Riegler, G., J. Drake, S. Liu, and R. Cicerone, Stellar Occultation Measurements of Atmospheric Ozone and Chlorine from OAO-3, *J. Geophys. Res.*, *81*, 4997, 1996.

[*Rodgers* (1976)] Rodgers, C., Retrieval of Atmospheric Temperature and Composition from Remote Measurements of Thermal Radiation, *Rev. Geophys.*, *14*, 609–624, 1976.

[*Rodgers* (1990)] Rodgers, C., Characterization and Error Analysis of Profiles Retrieved From Remote Sensing Measurements, *J. Geophys. Res.*, *95*, 5587–5595, 1990.

[*Rodgers* (2000)] Rodgers, C., *Inverse Methods for Atmospheric Remote Sounding: Theory and Practice*, World Scientific, Singapore, 2000.

[*Roscoe et al.* (1994)] Roscoe, H., et al., Using Stars for Remote Sensing of the Earth's Stratosphere, *App. Opt.*, *33*, 7126–7131, 1994.

[*Rowland and Molina* (1975)] Rowland, F., and M. Molina, Chlorofluoromethanes in the Environment, *Rev. Geophys.*, *13*, 1–35, 1975.

[*Salby* (1995)] Salby, M., *Fundamentals of Atmospheric Physics*, Academic Press, Inc, 1995.

[*Schwärz* (2004)] Schwärz, M., Joint Temperature, Humidity, Ozone, and Sea Surface Temperature Retrieval from Infrared Atmospheric Sounding Interferometer Data, Ph.D. thesis, Institute for Geophysics, Astrophysics and Meteorology, University of Graz, Austria, 2004.

[*Seinfeld and Pandis* (1998)] Seinfeld, J., and S. Pandis, *Atmospheric Chemistry and Physics*, Wiley-Interscience, 1998.

[*Smith and Hunten* (1990)] Smith, G., and D. Hunten, Study of Planetary Atmospheres by Absorptive Occultations, *Rev. Geophys.*, *28*, 117–143, 1990.

[*Sofieva et al.* (2003)] Sofieva, V., E. Kyrölä, M. Ferraguto, and G. C. team, From Pointing Measurements in Stellar Occultation to Atmospheric Temperature, Pressure and Density Profiling: Simulations and First GOMOS Results, in *Geoscience and Remote Sensing Symposium*, edited by I. International, vol. 5 of *IGARSS '03. Proceedings*, p. 2990, 2003.

[*Sokolovsky and Hunt* (1996)] Sokolovsky, S., and D. Hunt, Statistical Optimization Approach for GPS/Met Data Inversions, in *URSI GPS/Met Workshop*, Tuscon, Arizona, 1996.

[*Steiner* (1998)] Steiner, A., High Resolution Sounding of Key Climate Variables Using the Radio Occultation Technique, Ph.D. thesis, Institute for Geophysics, Astrophysics and Meteorology, University of Graz, Austria, 1998.

[*Steiner and Kirchengast* (2004a)] Steiner, A., and G. Kirchengast, Empirical Error Analysis for GNSS Radio Occultation Data Based on End-to-End Simulations, *J. Geophys. Res.*, 2004a, submitted.

[*Steiner and Kirchengast* (2004b)] Steiner, A., and G. Kirchengast, Ensemble-Based Analysis of Errors in Atmospheric Profiles Retrieved from GNSS Occultation Data, in *Occultations for Probing Atmosphere and Climate*, edited by G. Kirchengast, U. Foelsche, and A. Steiner, pp. 149 – 160, Springer, 2004b.

[*Storch and Zwiers* (1999)] Storch, H., and F. Zwiers, *Statistical Analysis in Climate Research*, Cambridge University Press, 1999.

[*Syndergaard* (1999)] Syndergaard, S., Retrieval Analysis and Methodologies in Atmospheric Limb Sounding Using GNSS Radio Occultation Technique, Ph.D. thesis,

Niels Bohr Institute for Astronomy, Physics and Geophysics, University of Copenhagen, 1999.

[*The Stationary Office* (2003)] The Stationary Office (Ed.), *The Astronomical Almanac*, U.S. Government Printing Office, 2003.

[*Theodore et al.* (2004)] Theodore, B., J. Vergely, F. Daulaudier, A. Hauchecorne, V. Sofieva, J. Tamminen, E. Kyrölä, and D. Fussen, Algorithms for the Estimation of High Resolution Temperature and Density Profiles from GOMOS measurements, *Tech. rep.*, ACRI-st, 2004, algorithm Theoretical Basis Document (ATBD).

[*Thomas and Stamnes* (1999)] Thomas, G., and K. Stamnes (Eds.), *Radiative Transfer in the Atmosphere and Ocean*, Atmospheric and Space Science Series, Cambridge University Press, 1999.

[*Vanhellemont et al.* (2004)] Vanhellemont, F., D. Fussen, and C. Bingen, Global One-step Inversion of Satellite Occultation Measurements: A Practical Method, *J. Geophys. Res.*, *109*, D09,306, 2004.

[*Visconti* (2001)] Visconti, G., *Fundamentals of Physics and Chemistry of the Atmosphere*, Springer, 2001.

[*Weisz* (2001)] Weisz, E., Temperature Profiling by the Infrared Atmospheric Sounding Interferometer (IASI): Advanced Retrieval Algorithm and Performance Analysis, *Wiss. Bericht, No. 2/2001*, 2001, institute for Geophysics, Astrophysics and Meteorology, University of Graz, Austria.

[*Yee et al.* (2004)] Yee, J.-H., R. Vervack, and R. DeMajistre, The Stellar Occultation Technique: Past Achievements, Recent Developments and Future Challenges, in *Occultations for Probing Atmosphere and Climate*, edited by G. Kirchengast, U. Foelsche, and A. Steiner, pp. 261 – 273, Springer, 2004.

[*Yee et al.* (2002)] Yee, J.-H., et al., Atmospheric Remote Sensing Using A Combined Extinctive and Refractive Stellar Occultation Technique I. Overview and Proof-of-concept Oberservations., *J. Geophys. Res.*, *107*, 4213, 2002.